EXPLORING CROSS-LAMINATED TIMBER USE FOR TEMPORARY MILITARY STRUCTURES: BALLISTIC CONSIDERATIONS

A Dissertation
Presented to
The Academic Faculty

by

Kathryn Purchase Sanborn, P.E.

In Partial Fulfillment
Of the Requirements for the Degree
Doctor of Philosophy in the
School of Civil and Environmental Engineering

Georgia Institute of Technology

May 2018

EXPLORING CROSS-LAMINATED TIMBER USE FOR TEMPORARY MILITARY STRUCTURES: BALLISTIC CONSIDERATIONS

Approved by:

Dr. Lauren K. Stewart, Co-Advisor
School of Civil and Environmental Engineering
Georgia Institute of Technology

Dr. Kimberly Kurtis
School of Civil and Environmental Engineering
Georgia Institute of Technology

Dr. T. Russell Gentry, Co-Advisor
School of Architecture
Georgia Institute of Technology

Dr. Daniel Castro-Lacouture
School of Building Construction
Georgia Institute of Technology

Dr. Lawrence Kahn
School of Civil and Environmental Engineering
Georgia Institute of Technology

Dr. Sheldon Jeter
School of Mechanical Engineering
Georgia Institute of Technology

Date Approved: March 30, 2018

To Marc, my rock, my inspiration, and my compass

ACKNOWLEDGEMENTS

This work would not have been possible without the assistance of many people along the way. The opportunity to pursue a PhD became a reality thanks to amazing mentors and educators in the Department of Civil & Mechanical Engineering at the United States Military Academy who made this all possible. I am grateful to COL Fred Meyer, COL Joseph Hanus and COL Brad Wambeke for all of their support, guidance and leadership. Dr. Chris Conley, who originally suggested I look at CLT, has been an invaluable sounding board, technical expert, facilitator and mentor to me for many years but especially these last three.

I am especially grateful to have had the guidance and support of my two advisors, Dr. Lauren Stewart and Dr. Gentry. Dr. Stewart took me on when she already had a full research group and has provided me with many opportunities and the support to complete this program. Dr. Gentry, who's MacGyver engineering skills are enviable, also added me to his already full plate without hesitation and has always found time to meet with me and provide assistance and guidance.

This work would not have been possible without the commitment of the other members of my committee, Dr. Lawrence Kahn, Dr. Kimberly Kurtis, Dr. Sheldon Jeter and Dr. Daniel Castro-Lacouture. Thank you for your time, your support and your feedback. I have thoroughly enjoyed working with all of you and I am extremely grateful to have such an amazing committee.

Many thanks to the U.S. Forest Service for the Wood Innovations Grant which contributed to the funding of this work. Additionally, a big thanks with several of the collaborators including Dr. Charles Randow at ARL, Dr. Bill Heard, Dr. Jesse Sherburn, Mr. Omar Flores, Mr. David Roman-Castro and Mr. Ricky Magee at ERDC, Mr. Robert Tudhope at SmartLam, Mr. Bill Tobin and Mr. Charles Stark at LendLease, and the folks at WoodWorks.

I have also had the help of many fellow students along the way. Huge thanks to Cadets Zade Koch and Andrew Valkenburg for their help with the ballistics tests at the range facilities. Many thanks to my CLT production crew that included CPT Brian Riser, Alex Herdt, Bennett Crawford, Justin Wilson and Daniel Rosborough. Danny also took on the monotonous task of hundreds of hardness test with no complaints and a smile – thank you. I am also sincerely appreciative for all the help and ideas Mr. Jake Tompkins provided to me at the Digital Fabrication Lab. It truly takes a village of support to crash a PhD to the three years the Army gave us (let alone two in one house!) and I am forever grateful to Genevieve Pezzola, Natalia Cardelino, Rebecca Nylen, Dr. Nan Gao, Dr. Giovanni Loreto for listening to my ideas and my venting tangents.

The true inspiration for this work is the Soldiers I have had the honor of serving with over the past 16 years. Despite our time at school removing us from the "regular" Army, I have been continuously motivated by the amazing men and woman who volunteer for our Army and have spent years away from their families and friends while living in temporary military structures. I truly hope my work can eventually benefit the lives of Soldiers someday in the future.

The love and support of my family is a constant in my life and I am forever grateful for the encouragement my parents have always provided to me. They instilled a work ethic in me at a young age that has helped present opportunities like earning my doctorate. My siblings' senses of humor and support have also been invaluable and kept me grounded. My in-laws have also provided unending support and encouragement to both Marc and I. I am forever grateful for an amazing family network in my life.

Finally, I want to thank Marc, my amazing husband for all of his love, support and encouragement. I would not have made it without his wisdom, Jedi Mathcad skills, Sketch-Up artistry and unmatched patience with me, all while working on his own research and dissertation. You make it look easy and provide me with daily motivation. This chapter of our journey has been a challenging but amazing one and I am so grateful to have you by my side and inspiring me daily.

TABLE OF CONTENTS

LIST OF TABLES

LIST OF FIGURES

LIST OF ABBREVIATIONS

AEC	Architecture, engineering and construction
AHP	Analytical hierarchy process
AITC	American Institute of Timber Construction
ANSI	American National Standards Institute
AP	Armor piercing
APA	Engineered Wood Association
ARL	Army Research Laboratory
ASD	Allowable stress design
ASHRAE	American Society of Heating, Refrigerating and Air-Conditioning Engineers
ASTM	American Society for Testing and Materials
AT	Antiterrorism
BCR	Benefit-cost ratio
CERL	Construction Engineering Research Laboratory, U.S. Army Corps of Engineers
CLT	Cross-laminated timber
CMU	Concrete masonry unit
CNC	Computer Numerical Controlled
DFL	Digital Fabrication Laboratory
DLA	Defense Logistics Agency
DoD	Department of Defense
ECLT	Enhanced cross-laminated timber
ECU	Environmental control unit
EMC	Equilibrium moisture content
ERDC	Engineer Research and Development Center, U.S. Army Corps of Engineers
FML	Full metal jacket

FPCON	Force Protection Condition
FRP	Fiberglass reinforced plastic
FSP	Fragment simulating projectile
FST	Fuzzy Set Theory
HEL	Hugoniot elastic limit
HVAC	Heating, ventilation, and air conditioning
IBC	International Building Code
IIC	Impact Insulation Class
JSP	Jacketed soft point
LOP	Level of Protection
LRFD	Load factor and resistance design
LRHV	Long rifle high velocity
LSL	Laminated strand lumber
LVL	Laminated veneer lumber
MSE	Mean squared error
MSR	Machine stress rated
NASA	National Aeronautics and Space Administration
NDS	National Design Specification for Wood Construction
NGO	Non-governmental organization
NIJ	National Institute of Justice
NLT	Nail-laminated timber
OSB	Oriented strand board
P-I	Probability-impact
PSL	Parallel strand lumber
PVB	Polyvinyl butyral
RHA	Rolled homogenous armor
RN	Round nose
SCL	Structural composite lumber
SDOF	Single-degree-of-freedom

SHPB	Split-Hopkinson pressure bar
SIP	Structural Insulated Panels
SMART	Simplified Multi-Attribute Radar Tool
SPF	Spruce Pine Fir
SPF-S	Spruce Pine Fir-South
STC	Sound Transmission Class
SWC	Semi-wadcutter
SYP	Southern Yellow Pine
TRANSCOM	U.S. Transportation Command
UFC	Unified Facilities Criteria
UHMWPE	Ultra-high-molecular-weight polyethylene
UL	Underwriters Laboratory
USDA	U.S. Department of Agriculture
USMA	United Stated Military Academy

LIST OF SYMBOLS

A	area
a	acceleration
a_{char}	effective char depth
A_{cs}, A_i	cross-section area
b	waveform parameter
b_i	width of individual layer
c	damping
C_D	load duration factor
C_d	drag coefficient
C_e	equivalent pressure reduction factor
chrono	chronograph
CoV	coefficient of variation
CP	complete penetration
D, d	diameter
E	modulus of elasticity
e	target thickness
E_0	modulus of elasticity for longitudinal layers
E_{90}	modulus of elasticity for transverse layers
E_f	final energy
E_i	initial energy
EI	bending stiffness
EI_{app}	apparent stiffness
EI_{eff}	effective bending stiffness
E_{min}	modulus of elasticity for beam and column stability
F	force
f_b	characteristic bending strength

F_b	allowable bending stress
f_c	characteristic compressive strength
F_c	allowable compressive stress
$F_{c\perp}$	compression perpendicular to grain, $F_{c,90}$
fps	feet per second
F_s	allowable interlaminar (rolling) shear stress
f_s	characteristic interlaminar (rolling) shear strength
f_t	characteristic tensile strength
F_t	allowable tensile stress
f_v	characteristic shear strength
F_v	allowable shear stress
G_0	shear modulus parallel to the wood grain
Gaeff	effective shear stiffness
GPa	gigapascals
Gr	specific gravity
G_R	rolling shear modulus, perpendicular to the wood grain
h	relative humidity
H	hardness
h	target thickness
$h_{lam,}\, h_i$	lamination thickness
h_{panel}	entire thickness of panel
I	impulse
i	specific impulse
I_e	equivalent impulse
I_i	second moment of area, area moment of inertia
in.	inch(es)
i_r	reflected impulse
J	joules
k	stiffness

KE	kinetic energy
K_L	equivalent load factor
K_{LM}	load-mass factor
K_M	equivalent mass factor
K_S	constant related to influence of shear deformation based on load and end conditions
K_S	equivalent stiffness factor
ksi	kips per square inch
L	Longitudinal
L_1, L_2	distances used in striking velocity estimate
L_{eff}	effective length of the penetrator
L_p	panel height
M	moisture content
m	mass
m/s	meters per second
M_{dyn}	dynamic moment capacity
MPa	megapascal
ms	millisecond
N	number of samples
n_{lam}	number of charred laminations
P	pressure; depth of penetration
p_0	ambient pressure
pcf	pound per cubic foot
p_i	incident pressure
PP	partial penetration
p_{peak}^-	peak negative pressure
p_{peak}^+	peak positive pressure
p_r	peak reflected pressure
p_s	stagnation pressure
psi	pound per square inch

p_{so}	peak static overpressure
q	dynamic pressure
R	Radial
R_d	standoff distance
R_t	resisting stress of target
R_u	elastic resistance
S_{eff}	effective section modulus
Subscript 0 (ex. $F_{b,0}$)	value for parallel to the major strength direction of CLT, for strength/stress values
Subscript 90 (ex. $F_{b,90}$)	value for perpendicular to the major strength direction of CLT, for strength/stress values
t	time
T	Tangential
$t_{arrival}$	time of arrival
t_c	clearing time
T_e	equivalent duration
t_{gi}	time for char front to reach glue interface
T_n	duration of negative phase
T_p	duration of positive phase
$t_{so,f}$	fictitious duration of the positive phase of static overpressure
T_w	thickness of wood/CLT necessary to prevent perforation; depth penetrated by projectile
u	particle velocity
v	velocity
V, Vol	volume
V_{BL}, V_{50}	ballistic limit
v_f	final velocity
v_i	initial velocity
V_n	actual shear capacity
v_R	residual velocity

v_s	striking velocity
V_u	assumed shear capacity
w	weight
W	work
x	displacement
x_e	displacement of panel
Z	scaled distance parameter
z_i	distance between center point of each layer and neutral axis
β_n	nominal char rate
ϵ_d	densification locking strain
ϑ	angle of obliquity
θ_r	support rotation
μ	ductility ratio
μs	microsecond
ρ	density
σ_{cr}	crushing stress
$\sigma_{plateau}$	plateau stress
τ	shear force

SUMMARY

The design and construction of temporary military structures, built to house personnel in theater, have changed little since World War II. While lightweight, rapidly deployable, and quick to erect, these gage metal or wood frame structures provide minimal ballistic and blast protection for occupants. Cross-laminated timber (CLT) is a new building material gaining attention in the U.S. construction industry for its many unique characteristics. This prefabricated, engineered wood product, composed of three or more plies of 2x lumber with alternating ply directions, is strong, stiff, and has the potential to meet the requirements for temporary military structures. CLT structures can be assembled rapidly as they arrive to the site in large sections, are machined in the factory to fit together and interlock, and are typically fastened with self-tapping screws using cordless tools.

Ballistic and blast resistance are key criteria for temporary military structures. Together, these requirements for military structures are known as force protection. In order to expand its use into temporary military structures, a better understanding of the force protection performance of CLT is needed. In the past, typical wood products such as dimension lumber have not been desirable as a protective material due to overall poor performance. However, the composite nature of CLT coupled with the energy absorbing capacity of the thicker wood panels have warranted further investigation into the viability of CLT for temporary military structures.

The mechanical properties of wood influence the overall response of CLT to impact loads like those experienced in a blast or ballistic event. Mechanical and physical

properties such as hardness, density, and shear strength all aid in determining the expected response of the CLT panel and were evaluated for two types of CLT. Specimens in this research included commercially produced Spruce-Pine-Fir (South) CLT as well as Southern Pine CLT specimens fabricated as part of this research program. Use of CLT in temporary military structures would require a broad market availability of CLT – so the work focused on the two most common species available from Western U.S. forest (Spruce-Pine-Fir South) and Eastern U.S. forests (Southern Pine).

Ballistic testing of both types of CLT indicate that the material's inherent penetration resistance is significantly greater than that of dimension lumber and plywood used in current common temporary military structures. By conducting the first ballistic tests on CLT, the relationship between striking velocity and depth of penetration or residual velocity has been established. The study of penetration mechanics is complex with many influencing variables describing both the projectile and the target. A quantitative analysis of the data collected allowed for the calibration of classical penetration models and the parameter estimation to help predict the thickness of CLT required to prevent penetration. The research examined existing equations found in *UFC 4-023-07, Design to Resist Direct Fire Weapons Effects* and found that these equations dramatically over-predict the thickness of CLT needed for ballistic protection. Updated parameters are therefore proposed that more accurately capture the performance of CLT. To ensure CLT performance in a wide range of site environments, specimens subjected to high moisture environments were tested and exhibited no degradation in ballistic resistance relative to samples at typical kiln-dried moisture contents (8 percent to 12 percent). This initial investigation into the ballistic response of CLT will help shape future testing in this realm

with the aim of meeting performance ratings for the material such as those found in UL 752

The pre-fabricated, laminated nature of CLT allows for modification of the layup through the addition of one or more enhancing layers for improved ballistic resistance, creating enhanced CLT (or ECLT as it is referred to in this thesis). Fourteen panels representing eight different ECLT configurations were produced in the Digital Fabrication Laboratory (DFL) at Georgia Institute of Technology using various hardening materials including thin metal plates and gratings, polymer-based armors, and fiber-reinforced epoxy matrix panels. The enhancing layers were evaluated based on ease of production, ballistic resistance given a small initial test series, and a cost-benefit evaluation. Solid metal plate presented challenges in fabrication but performed well. Perforated metal offered a lighter option with good resistance as well. The fiber-based panels, composed of high-performance armoring materials, performed well, but are costly to procure and difficult to incorporate into the CLT stack. The E-glass-epoxy configurations were the least effective but showed improved resistance to baseline CLT at a relatively low cost.

A qualitative analysis examined the damage to the CLT panels relative to the unique anisotropic and inhomogeneous properties of wood. This analysis focused on local failure modes and the local response of the wood under ballistic impact. The resistance mechanisms of wood were directly observed by dissection of the projectile paths through the CLT panels. The bi-directional layups of the multiple plies of CLT allowed a cross-sectional cut to show the different failure modes based on grain orientation of the wood. Multiple failure modes of the material in a localized damage zone were observed with the ballistic penetration. Unexpected data, such as shallower penetration or faster residual

velocity, was critically examined for a variation in the wood structure to help better understand the variability observed in ballistic testing of CLT.

In addition to ballistic response, blast resistance is a critical attribute of interest for materials to build temporary military structures. Based on data from live blast testing and use of the shear analogy method to account for the strength and stiffness of the CLT panel given the cross-laminations, a single-degree-of-freedom model was used to evaluate the response of a CLT panel under blast loads in the elastic regime. A CLT blast analysis tool was developed to help predict the blast response of different grades of CLT in different dimensional and geometric configurations. The initial version of the tool is limited to response in the elastic regime, due to a lack of available data on CLT panel response in the inelastic regime.

Multiple requirements, constraints, and limitations to consider while meeting mission requirements create a complex decision for military leaders with regard to what material to use in the construction of temporary military structures. The construction industry uses multi-attribute tools to help assess risk and to determine design and construction alternatives. One potential tool to evaluate construction material system and assist in making decisions regarding temporary military structure construction is the analytical hierarchy process (AHP). In this process, materials are evaluated using pairwise comparisons and relative weights for multiple criteria of interest, with the goal of selecting the best material system for the temporary military structures within a given operational environment. A simplified tool based on a radar chart was developed to present a visual representation of the decision for military leaders. Ultimately, the decision is highly dependent on a thorough definition of the evaluation criteria. The research defines a

tailored set of decision criteria for temporary military structures along with proposed methodologies for rating their performance.

CLT presents significant potential for improved performance over traditional lightweight construction materials for use in temporary military structures. Improvements in ballistic resistance and blast response are critical force protection considerations for temporary military structures. While additional research is needed to definitively rate the performance of CLT for ballistic resistance, this research presents the first such tests ever conducted and provides a foundation for future work. The concept of enhanced CLT defined by this research holds much promise and has demonstrated that specialized variants of CLT can be designed to meet military specifications for ballistic resistance. The blast analysis tool shows good agreement with the response of CLT in the elastic regime and can be modified to include the inelastic regime with further blast simulation testing. Lastly, tailored evaluation criteria for comparative assessment of a construction material system, like CLT, for use in temporary military structures was developed and implemented in the context of decision making required of military leaders.

CHAPTER 1
INTRODUCTION

1.1 Problem Statement

As the siren of the mass notification system blares signaling that the base is under attack, sleep-deprived soldiers grab their helmets and body armor and retreat *outside* of their vulnerable living quarters, ducking into cramped, fortified bunkers placed intentionally near the temporary housing structures. A scene like this has played out multiples times a day on the military bases in Iraq and Afghanistan over the last 15 years. The United States Army and other Department of Defense (DoD) agencies operating in expeditionary, forward environments face unique challenges in balancing the many competing requirements for construction of temporary structures used by deployed personnel. While the structures are temporary, their needed lifespan can be highly variable as can the purpose of each structure over that lifespan – today's operational unit headquarters could be tomorrow's combat support hospital. In addition to the evolving purpose of a temporary structure, the location of forces can also rapidly change within a forward geographic area. This change, combined with today's construction materials, results in more structures built in the new location, increasing construction effort and material requirements.

A top priority of DoD decision makers is the safety of personnel in temporary structures. Therefore, force protection and anti-terrorism measures are always incorporated into designs. However, in forward operating environments these considerations typically translate to large standoff requirements enlarging the forward

operating military base footprint. This increases local security requirements and therefore forward deployed troop level requirements. A larger base footprint requires more security forces and provides a larger target for enemies to strike. Even with standoff distances between protected areas and potential threats, leaders take measures to protect personnel and equipment against long-range weapons effects by both hardening the structures or by building small concrete bunker-type shelters in which troops evacuate to during an attack.

Hardening structures for these types of attacks typically involves installing layers of soil-filled sandbags on roofs or along the first few feet of a wall to protect against rockets and shrapnel. In order to remain functional, these methods of hardening require constant maintenance and a sizeable labor force. Additionally, the original structure must handle the additional weight of the hardening efforts. In practice, the structure must be adapted in the field to accommodate these larger loads. These modifications are often undertaken by troops without engineering expertise, posing additional safety concerns.

The most common type of temporary structure used today is the B-hut structure. Built of a light timber frame, it typically takes 24 to 30 total hours to construct using eight trained Soldiers equipped with tools and a power source [72]. The structure, while generally adaptable in functional use, does not provide high levels of protection and cannot be easily disassembled and re-built at an alternative location. Further, B-huts are usually uninsulated and require large amounts of power, in extreme environments to maintain basic quality of life levels. Power requirements increase the demand for fuel, straining logistical systems and further putting Soldiers at risk due to transport requirements.

To improve structures, the construction industry and researchers are developing new construction materials in today's technology-enhanced world. Engineered wood

products and other new materials have unique properties that distinguish them from traditional construction materials like concrete, steel and sawn timber. Because of their unique features, these new materials should be investigated and considered for all potential uses, including for use in temporary military structures.

Temporary military structures require different attributes and metrics compared to typical construction. Characteristics such as adaptability, reuse and repurposing, strength-to-weight ratio, environmental impact, cost, local availability of materials, economic value, inherent force protection, and aesthetics are all considerations when selecting a construction material. A multi-criteria tool, which rates construction materials by different metrics for a given environment or need, would be a useful tool for decision-makers, planners, and designers in the realm of construction. This research evaluates the use of a new material, cross-laminated timber (CLT), using a multi-criteria tool for decision-making. The tool can be adapted to general construction applications or set-up to meet specific project requirements. While the tool is presented in a general sense, the main focus of this research is the use of CLT for force protection. The research examines CLT's ballistic performance and investigates methods to modify the material for enhanced ballistic performance, as well as its performance under blast loads.

1.2 Objectives and Scope: Research Questions

This research seeks to add to the existing CLT body of knowledge by examining a newly proposed use for CLT in temporary military structures and offering a tool for holistically assessing material selection based on specific construction requirements. Temporary military structures have unique requirements compared to conventional construction that can vary substantially based on mission location, threat, and the

operational environment. The urgency of the requirement can vary with the military mission of that temporary structure. These unique requirements include: 1) the level of protection the structure provides without additional hardening; 2) the energy efficiency in which the structure can operate; 3) the ease of construction, including construction time, resource staging, and logistical support requirements; 4) the adaptability of the structure to different uses; and 5) the cost to build.

In deciding on a temporary military construction material, different requirements may be weighed more heavily than others. Nonstandard requirements may be added or removed depending on the environment and intended use of the structure. Much like the triple constraint of project management where cost, scope, and schedule must be balanced while maintaining quality, achieving a finished building of any type that meets or exceeds every requirement is a significant challenge. Existing research on CLT shows it to have potential as an improved material solution for temporary military structures.

1.2.1 Research goals and objectives

In the construction industry at large, the choice of material used for any project is typically based on multiple requirements that best fit a variety of criteria. These include the structure's function, appropriateness for location, and other user-determined attributes or requirements. Material considerations when planning for military base camp construction are much different from typical construction considerations. Attributes of interest in that scenario can include, but are not limited to, the following variables: transportation, availability, ease of construction with minimal engineer effort, experience and tool requirements, energy efficiency from the thermal envelope of the structure, structural strength, blast and ballistic resistance, seismic performance, environmental

concerns with both occupants and in end-of-life disposal, flexibility in terms of size of structure as well as the ability to adapt and expand in phases.

This research concentrates on exploring CLT material for use in temporary military structures, a very specific construction type. The goal of this research is to investigate the performance of CLT, evaluate its use in a specific military application, and understand its inherent force protection capabilities and limitations. This dissertation explores the use of CLT for temporary military structures by investigating the material's ballistic performance and predictive models, the opportunity for enhancing modifications for improved ballistic performance, and blast performance.

Existing multi-criteria tools in the construction trade generally appear to be limited to risk and life cycle assessment. This research aims to introduce a broader tool that allows stakeholders to determine relevant attributes for a proposed structure and then assess various construction materials in terms of those attributes on a polar or radar chart that allows for quick visual comparison. The radar chart allows for the evaluation of aggregate data on the building material, including both quantitative and qualitative data sets. The tool allows for rapid decision making by stakeholders with less technical expertise in each of the attributes assessed. Figure 1-1 shows a hypothetical example of a multi-criteria assessment tool. Each construction material has certain attributes and limitations that can be weighted and prioritized based on specific project constraints and requirements.

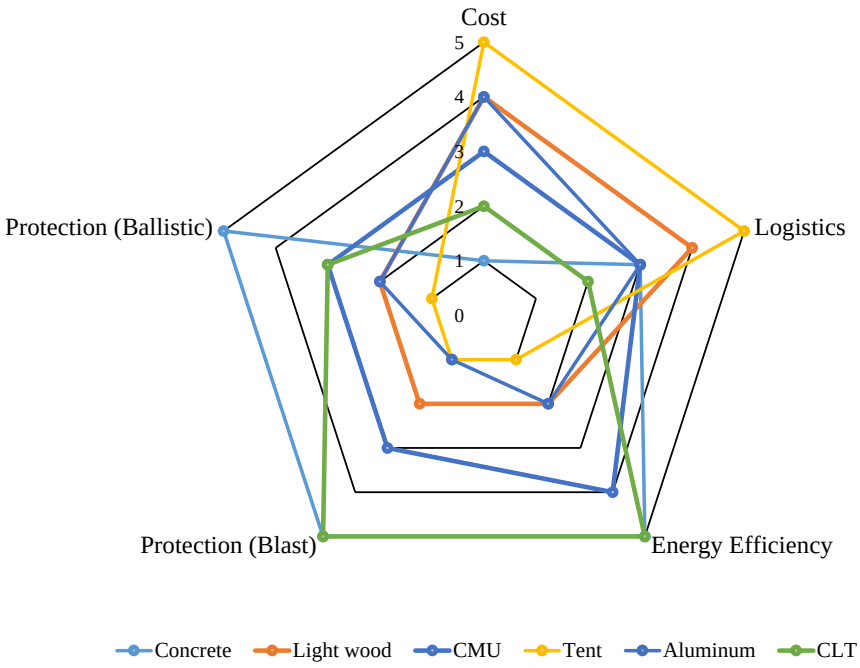

Figure 1-1. Example of a radar chart tool for comparing different building materials for temporary military construction across several criteria.

Currently, the temporary structures used by the United States armed forces in deployed locations offer little to no inherent blast or ballistic protection without hardening. Additionally, most of these temporary structures take weeks to construct and are not energy efficient, causing forward bases to consume large amounts of fuel. The fuel is used to power generators and environmental control units (ECUs) to keep the structures within a minimal standard of temperature comfort and provide a basic quality of life to enable service members to accomplish their missions. New construction materials like cross-laminated timber (CLT) offer an opportunity to rapidly build temporary structures for military forces while improving force protection, providing greater energy efficiency, and being more adaptable to a changing operational environment.

Presently, the military relies on guidance from Unified Facilities Criteria (UFC) to employ standardized designs to meet threat parameters of a given location. The goal of this research is to inform those agencies that produce guides and standards for CLT, on the use of the material in military construction by assessing the level of ballistic protection provided by CLT systems. This is achieved by examining methods to model ballistic performance based on experimental data from CLT and enhanced CLT (ECLT). In addition to informing potential users considering CLT for future construction planning, this research develops hybrid CLT (ECLT) panels consisting of a layer of non-wood material incorporated in the lay-up to significantly increase ballistic resistance.

Blast resistance is another important parameter of force protection performance in temporary military structures. While increased standoff distance is a common tactic to limit the vulnerability of structures, achieving the necessary standoff distances can be extremely difficult especially in urban environments. A material's blast resistance or performance under impulsive blast load conditions, is indicative of the level of protection that the structure can provide to occupants or equipment within it. A single-degree-of-freedom (SDOF) model provides insight into the response of a CLT panel under a blast load in the elastic regime.

The analysis of risk for blast and ballistic impact are similar in that the threats are identified and rated in terms of probability and consequences. The function, value, and vulnerability of the structure or elements within a structure are evaluated so that mitigation measures can be identified. With temporary military structures, critical assets are strategically positioned to provide the best possible protection but there are limitations to measures of mitigation. CLT has the potential to be an additional construction material

option that provides increased levels of protection above current methods while also meeting other beneficial criteria such as rapid assembly and energy efficiency. This research aims to characterize the ballistic and blast resistance of CLT.

1.2.2 Research Questions

Based on the problem statement and motivation presented earlier in this chapter, the research questions (R), hypotheses (H), and specific aims (SA) of the proposed research are:

- **R1. How can a new construction material be assessed for temporary military structures across multiple criteria to meet military mission requirements?**
  - H1. Competing requirements for construction material selection can be adequately included for decision-makers using a multi-criterion tool.
  - SA1. Develop a thorough analysis of requirements for temporary military structures and employ a multi-criterion tool using a radar chart format that graphically illustrates and allows comparison of construction materials for a non-technical audience. Present an example of how to assess a single requirement, ballistic performance.

    Chapter 9 addresses this question.
- **R2. How can the ballistic resistance performance of CLT be characterized and predicted?**
  - H2. The ballistic performance of CLT can be characterized using experimental ballistic testing and residual velocity and depth of penetration data collection. Empirical models, either physics-based or curve-fitting, can be calibrated to test

data. CLT shows the potential to achieve an improved ballistic resistance over the current materials of plywood and 2x4 dimensional lumber.

- SA2. Conduct a rigorous experimental evaluation of the ballistic performance of CLT yielding data on residual velocities and depth of penetration across a range of striking velocities. Examine current wood penetration models in military design guide for appropriateness for mass timber products.

  This question is primarily addressed in Chapter 5 with related work in Chapter 4 and Chapter 6. Chapter 4 investigates the relevant wood properties to ballistic and blast performance. Chapter 6 examines a qualitative analysis of the ballistic test results.

- **R3. Can CLT be altered to enhance its ballistic resistance? What modified layups of enhanced CLT (ECLT) present the greatest cost-benefit ratio?**
- H3. CLT, as a composite material, can be adapted to an enhanced CLT (ECLT) product with improved ballistic resistance for use in high-threat environments for temporary military structures.
- SA3. Explore if a hybrid CLT product, consisting of multiple materials including the standard wood lamina as well as a non-wood layer such as a aramid fabric or a thin layer of steel, can be produced. Determine what level of ballistic protection can be achieved with a modified ECLT compared to standard CLT, without the enhancing non-wood layer. Conduct a cost-benefit analysis and weight analysis comparing the experimental layups.

  This question is covered in Chapter 7.

- **R4. How is the blast resistance of CLT characterized and predicted?**
  - H4. CLT can be characterized through experimental investigations using live blast tests and measurements related to panel response under blast pressures. From this data CLT can be modeled generically for blast performance. CLT shows the potential to achieve an improved blast resistance over the current materials used in temporary military structures.
  - SA4. Using existing live blast test data from full-scale testing conducted by WoodWorks, explore the blast resistance of generic CLT (unspecified grade) by examining the pressure-time history and using the impulses to create a single degree of freedom (SDOF) model and a blast resistance function for the material. Determine a characterization of blast performance of generic CLT.

    This question is addressed in Chapter 8.

1.3 Outline of this dissertation

Chapter 2 of this thesis introduces cross-laminated timber (CLT) as a construction material, provides background on current military temporary structures, and provides background on typical force protection designs used by DoD. Chapter 3 discusses the fundamentals of penetration mechanics as a background for the ballistic testing and analysis. Chapter 4 presents an in-depth investigation of the wood properties and their role in ballistic penetration and blast response. Chapter 5 presents the ballistic performance of cross-laminated timber based on experimental testing and empirical data analyses. Chapter 6 qualitatively examines the resistance mechanisms for ballistic performance based on experimental testing and closely examines the test specimens in the context of the wood properties discussed in Chapter 4. Chapter 7 discusses the potential of enhancing the

ballistic performance of the cross-laminated timber by adding non-wood materials to the wood composite. This includes a cost-benefit and weighted criterion analysis between the different proposed enhancing materials investigated. Chapter 8 discusses the blast performance of the material and presents a generic SDOF model for initial feasibility assessment purposes. This model is intended to guide future work in blast performance evaluation of CLT. Chapter 9 presents a multi-criteria assessment tool with the previous chapters providing relevant information for rating for a portion of the tool. Finally, Chapter 10 presents conclusions of this research and recommendations for future work.

CHAPTER 2
BACKGROUND

2.1 Cross-Laminated Timber (CLT)

2.1.1 The introduction of CLT: a brief history

Cross-laminated timber (CLT) is an engineered wood product that in recent years has been developed and studied as a new structural building material for use in place of, or in conjunction with, concrete, masonry and steel. While builders and designers have used engineered wood products such as plywood and glue-laminated (glulam) products for over a century, CLT is a relative newcomer to the market. First introduced widely in the 1990's in Austria and Germany, the product has gained visibility and interest as more structures make use of it and international building codes and standards allow its use in construction [68].

According to European CLT manufacturer Kreuz Lagen Holz (KLH) Massivholz, the first patent for CLT was issued in 1985 in France [119]. Projects in Austria and Germany incorporating the material combined with a joint research effort involving the timber industry and academia resulted in the development of today's CLT product. Another milestone for the product was the development of press technology in the mid 1990s to increase the bonding of the layers, a critical factor in the material's strength. Following that technological milestone, Europeans built hundreds of structures from CLT, including residential and non-residential mid-rise (three to ten story) buildings.

In the last decade, global interest in CLT expanded into North America, especially in the densely forested areas of Canada and the Pacific Northwest region of the United

States. The interest was motivated by the inherent strengths of wood, a renewable resource. By strategically manufacturing a building product to optimize those strengths in a layered composite, the industry is investing that CLT has the potential to be a revolutionary construction material.

Industry interest in CLT has led to the incorporation of the technology into various guidelines and regulations. In 2011, FPInnovations, a non-profit organization focused on research and technology for the Canadian forestry industry published the Canadian edition of the *CLT Handbook* to aid in design and construction with CLT before the material was incorporated into building codes [68]. The U.S. Forest Products Laboratory, the Binational Softwood Lumber Council, and several forest industry groups like the American Wood Council and the Wood Products Council combined efforts to publish the U.S. version in 2013. The premise of these handbooks is to provide a comprehensive resource on the manufacture, design, and performance of CLT for use in construction as a starting point until the new material can become fully incorporated into standards and building code [68].

In December 2011, the American National Standards Institute (ANSI) and Engineered Wood Association (APA) published *Standard for Performance-Rated Cross Laminated Timber* (PRG 320). Most recently, the 2015 International Building Code (IBC) incorporated CLT in exterior walls and CLT floors. Additionally, the 2015 Edition of the *National Design Specification for Wood Construction (NDS)* includes design provisions for CLT, with a chapter specifically addressing CLT and new sections on connections with CLT [102]. In the United States, the Department of Agriculture (USDA) has worked towards promoting the study and use of CLT for construction through various means,

including the Tall Wood Building Prize Competition held in 2014-2015 and the U.S. Forest Service Wood Innovation grants starting in 2015.

Outside of the U.S., the quest for the tallest CLT building continues. Structures like the nine-story, multi-family residential building of Stadthaus in London, United Kingdom in 2009 staked one of the first claims. It was followed by the ten-story apartment building called Forte in Melbourne, Australia in 2012. More recently, the 18-story, student dormitory building named Brock Commons at the University of British Columbia, Canada, was completed in the spring of 2017. While structures like these have shown the viability of the material for use in high-rise structures, many builders construct low and mid-rise structures with CLT. Mid-rise buildings, with uses from residential to commercial are more common. As more designers, builders and developers learn about the construction material, they become more inclined to test the limits of CLT including use in unique construction projects such as parking decks, hotels and more.

2.1.2 CLT: What is it?

Natural wood is an orthotropic material with a strong and a weak axis. Strength of wood is highly dependent on the grain direction as well as defects such as knots. Being orthotropic, wood has independent properties along three perpendicular axes: longitudinal, radial, and tangential. These axes and their orientation with respect to grain direction are shown in Figure 2-1 [77, 96]. Wood properties with respect to each of the axes include different tensile, compressive and shear properties. These properties depend on orientation – parallel or perpendicular to grain. Radial and tangential are both perpendicular to the grain, with tangential being tangent to the growth rings formed in the wood; longitudinal is parallel to the grain.

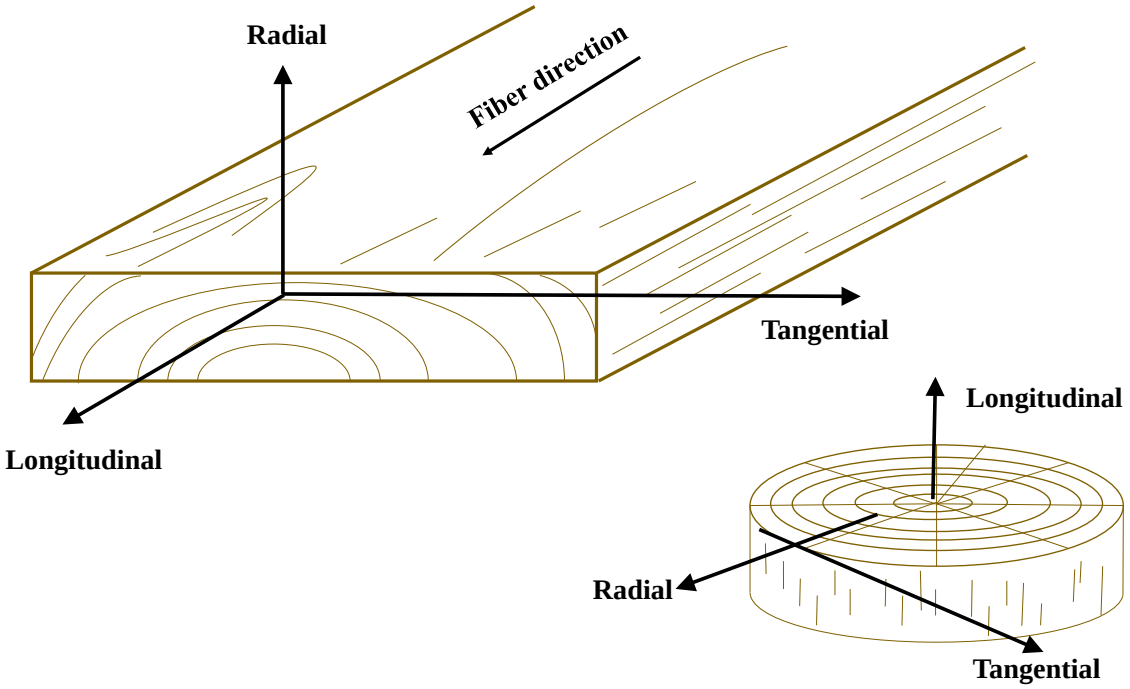

Figure 2-1. The three perpendicular axes of wood shown with respect to grain, or fiber, direction (adapted from [77] and [96]).

Mechanical properties and design values for natural wood can vary significantly between species. Even within samples of the same species, mechanical properties depend on the age of the wood, as well as the quantity size of defects. This variation is the reason for sawn lumber grading through either visual inspection, by machine stress rating, or evaluating density by x-ray. Grades classify the lumber into groups with known mechanical properties for use in structural design [34]. Pieces with more defects receive lower grades as they lack the strength of clear wood, which is homogeneous, straight-grained wood without defects. References typically provide mechanical properties of wood as averages for a given species based on much sampling and testing [96]. With wood

products, variability can be challenging in determining mechanical properties. Within a single species or even within one harvested tree, pieces may have differing properties. Engineered wood products are one method of overcoming the non-homogeneous nature of wood with its high variability [81].

Engineered wood products are composite, wood-derived materials of greater strength and thus increased performance over natural wood or sawn timber. These products can also make use of lower quality wood, which lacks the strength and size to be used independently. Through processing and performance-oriented production, wood-based end-products of increased capability and value can be created. CLT is one of many commercially available engineered wood products and is commonly referred to as *mass timber* or *massive timber*. Other engineered wood product categories include solid timber construction and structural composite lumber (SCL). Oriented strand board (OSB) and glued-laminated timber (glulam) are common solid timber products while laminated strand lumber (LSL) and laminated veneer lumber (LVL) are common SCL products. The 2005 edition of the *National Design Specification for Wood Construction* package included a manual for Engineered Wood Construction, showing industry acknowledgment and acceptance of these products [34]. While, OSB and other products listed previously have been widely used for decades, CLT is a relatively new product in this family of composite materials.

A CLT panel is formed from stacked, solid sawn lumber boards. Panels typically consist of an odd number of layers, varying from three to nine. Figure 2-2 shows a stack of ten 3-ply CLT panels. However, variations can exist as the product is customizable within the constraints of production capabilities. Similar to a sandwich panel, the outer

layers and alternating layers of the inner core are oriented such that the primary strength axis of the wood corresponds to the direction of the design load. Thus, the grain of the wood typically runs parallel to the loading direction in those layers. Manufacturers often call these the longitudinal layers for floor and roof panels and vertical layers for wall panels.

Figure 2-2. Ten 3-ply CLT panels stacked.

For walls, the planks typically run vertically, or parallel to the gravity loads and for floors and roofs, the planks align parallel to the major span direction [68]. Alternating

layers are typically rotated 90-degrees, forming a crosswise laminate. Manufacturers often call these the transverse layers in floor and roof panels and horizontal layers in wall panels. In transverse or horizontal layers, the grain of the wood runs perpendicular to the direction of the loading. Figure 2-3 and Figure 2-4 from the CLT Handbook illustrate the layering and alternating wood grain [68]. This alternating and crosswise orientation gives CLT a high strength and stiffness, which are useful qualities in construction. These properties are achieved by orienting the wood panel sub-components, or lamina, in such a manner as to maximize the wood's inherent strength and minimize its weaknesses.

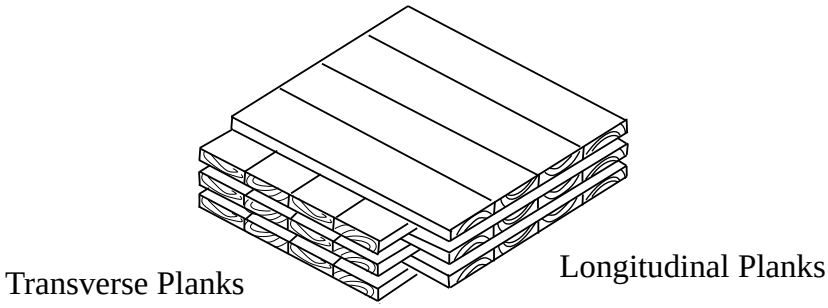

Figure 2-3. CLT nomenclature in panel configuration (adapted from [68]).

The thickness of each layer in the CLT panel varies from 5/8 to 2-inches (16mm to 51mm). The width of the individual pieces varies from approximately 2.4 to 9.5-inches (60mm to 240mm) [68]. The full panel size varies depending on both manufacturer equipment and specific customer need. Typical widths for the panels are 2-ft (0.6m), 4-ft (1.2m), 8-ft (2.4m) and 10-ft (3m). Lengths can reach 60-ft (18m) which facilitates

prefabrication and ease of rapid construction on-site, although lifting and hauling limitations may prevent use of larger dimensions. Additionally, transportation means and haul routes, along with local regulations, can influence the allowable sizes of panels. Lastly, the thickness of the entire panel with all its layers can reach up to 20-in (508mm) by the current standard rating guidance from the Engineered Wood Association (APA). The customizable nature of the material allows for minimizing waste both at the construction site and in manufacturing.

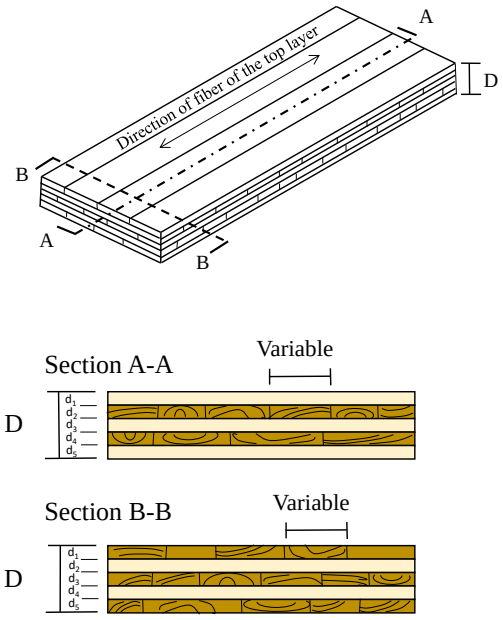

Figure 2-4. CLT panel example showing direction of wood grain in face and alternating layers (adapted from [68]).

Manufacturers make CLT from specific grades of sawn lumber, dependent on design specifications. As a composite product, a panel gets its own classification or rating

of CLT grade. Different tree species have varied mechanical properties and characteristics, and so the species used in the panel as well as the quality of the lamina dictate the grade of CLT. Quality control also checks the grades of both the panel and the lamina to ensure the product meets or exceeds minimum mechanical properties for each grade. Often, the transverse (perpendicular to direction of load) lamina can be of lesser quality because they are sandwiched between two higher quality parallel layers.

Table 2-1 lists the wood types and rating for the various CLT grades. The "E" designation refers to timber based on mechanically rated or machine stress rated (MSR). The "V" designation refers to visually graded timbers. Each grade of CLT is composed of specific grades of specific species in the parallel and perpendicular layers. Some CLT grades use a combination of E-rated and V-rated timbers in different layers.

Table 2-2 defines the symbols used for various strength parameters in PRG 320. The upper and lower case strength parameter symbols correspond to the characteristic and allowable value, respectively. The subscript value denotes the direction for which the parameter applies: 0 for the parallel to the major strength direction and 90 (degrees) for perpendicular. The varying strengths across the CLT grades can be seen in Table 2-3 and Table 2-4, adapted from ANSI/APA PRG 320. It can be observed that the interlaminar shear strength does not vary between major and minor strength directions. Additionally, the number in the grade title does not necessarily correlate to increasing or decreasing strength as can be observed with E4 compared to the other three E-grades. Each grade is independent of the others in terms of material properties shown in Table 2-3 and Table 2-4.

Table 2-1. Wood lamination composition by CLT grade [12].

Grading	
E1	1950f-1.7E Spruce-pine-fir MSR lumber in all parallel layers and No.3 Spruce-pin-fir lumber in all perpendicular layers
E2	1650f-1.5E Douglas fir-Larch MSR lumber in all parallel layers and No. 3 Douglas fir-Larch lumber in all perpendicular layers
E3	1200f-1.2E Eastern Softwoods, Northern Species, or Western Woods MSR lumber in all parallel layers and No. 3 Eastern Softwood, Northern Species, or Western Woods lumber in all perpendicular layers
E4	1950f-1.7E Southern pine MSR lumber in all parallel layers and No. 3 Southern pine in all perpendicular layers
V1	No. 2 Douglas fir-Larch lumber in all parallel layers and No. 3 Douglas fir-Larch lumber in all perpendicular layers
V2	No. 1/No. 2 Spruce-pine-fir lumber in all parallel layers and No.3 Spruce-pine-fir in all perpendicular layers
V3	No. 2 Southern pine lumber in all parallel layers and No. 3 Southern pine lumber in all perpendicular layers
V4	SmartLam CLT manufactured with spruce-pine-fir south lumber in accordance with custom layup combination approved by APA

Table 2-2. Symbols in strength parameters.

Symbols	Meaning
f_b and F_b	Characteristic bending strength and allowable bending stress
E	Modulus of elasticity in bending
f_t and F_t	Characteristic tensile strength and allowable tensile stress
f_c and F_c	Characteristic compressive strength and allowable compressive stress
f_v and F_v	Characteristic shear strength and allowable shear stress
f_s and F_s	Characteristic interlaminar (rolling) shear strength and allowable interlaminar (rolling) shear stress
Subscript 0 (ex. $F_{b,0}$)	Value for parallel to the major strength direction of CLT
Subscript 90 (ex. $F_{b,90}$)	Value for perpendicular to the major strength direction of CLT

Table 2-3. Required Characteristic Test Values for PRG 320 CLT, adapted from [12].

	Major Strength Direction						**Minor Strength Direction**					
CLT Grades	**$f_{b,0}$ (psi)**	**E_0 (10^6 psi)**	**$f_{t,0}$ (psi)**	**$f_{c,0}$ (psi)**	**$f_{v,0}$ (psi)**	**$f_{s,0}$ (psi)**	**$f_{b,90}$ (psi)**	**E_{90} (10^6 psi)**	**$f_{t,90}$ (psi)**	**$f_{c,90}$ (psi)**	**$f_{v,90}$ (psi)**	**$f_{s,0}$ (psi)**
E1	4,095	1.7	2,885	3,420	425	140	1,050	1.2	525	1,235	425	140
E2	3,465	1.5	2,140	3,230	565	190	1,100	1.4	680	1,470	565	190
E3	2,520	1.2	1,260	2,660	345	115	735	0.9	315	900	345	115
E4	4,095	1.7	2,885	3,420	550	180	1,205	1.4	680	1,565	550	180
V1	1,890	1.6	1,205	2,565	565	190	1,100	1.4	680	1,470	565	190
V2	1,835	1.4	945	2,185	425	140	1,050	1.2	525	1,235	425	140
V3	2,045	1.6	1,155	2,755	550	180	1,205	1.4	680	1,565	550	180
SL-V4*	1,628	1.1	735	1,900	425	142	1,628	1.1	735	1,900	425	142

*U.S. manufacturer, SmartLam's customized CLT grade which was used for preliminary research

Table 2-4, adapted from ANSI/APA PRG 320, details the Allowable Design Properties for PRG 320 CLT. APA bases the required characteristic test values on these properties with factors of safety to account for the variation in the natural wood product.

Table 2-4. Allowable Design Properties for PRG 320 CLT, adapted from [12].

	Major Strength Direction						Minor Strength Direction					
CLT Grades	**$F_{b,0}$ (psi)**	**E_0 (10^6 psi)**	**$F_{t,0}$ (psi)**	**$F_{c,0}$ (psi)**	**$F_{v,0}$ (psi)**	**$F_{s,0}$ (psi)**	**$F_{b,90}$ (psi)**	**E_{90} (10^6 psi)**	**$F_{t,90}$ (psi)**	**$F_{c,90}$ (psi)**	**$F_{v,90}$ (psi)**	**$F_{s,90}$ (psi)**
E1	1,950	1.7	1,375	1,800	135	45	500	1.2	250	650	135	45
E2	1,650	1.5	1,020	1,700	180	60	525	1.4	325	775	180	60
E3	1,200	1.2	600	1,400	110	35	350	0.9	150	475	110	35
E4	1,950	1.7	1,375	1,800	175	55	575	1.4	325	825	175	55
V1	900	1.6	575	1,350	180	60	525	1.4	325	775	180	60
V2	975	1.4	450	1,150	135	45	500	1.2	250	650	135	45
V3	975	1.6	550	1,450	175	55	575	1.4	325	825	175	55
SL-V4	775	1.1	350	1,000	135	45	775	1.1	350	1,000	135	45

Currently, two manufacturers produce CLT in the U.S., both located in the Pacific Northwest with the promise of a third manufacturer opening in the southeast in 2018 [39]. One manufacturer, DR Johnson, exclusively produces E1 graded CLT, while the second, SmartLam LLC, produces a variety of grades including, V4, a grade recently approved by the APA. Neither existing manufacturer produces the grade made from Southern Pine, V3. This product is of significant interest to forestry officials in the southeast portion of the U.S. due to the large volumes of the species that could be available for CLT production.

Similar to sawn lumber, designers and builders may elect to use different CLT grades based on availability of wood species for the product in addition to design and strength requirements. For example, if grades of different species have comparable

strength values such as E1 and E4, and are both readily available, it is likely that whichever grade is made from a local wood species would be used due to the financial and environmental transportation costs associated with shipping the heavy panels long distances.

2.1.3. The Manufacturing Process of CLT

In manufacturing, the individual boards used as laminations are finger-jointed together lengthwise at the ends with structural adhesive to obtain greater lengths, as shown in Figure 2-5. The widths and lengths of the boards in the layers can vary. The lumber used to produce CLT is individually graded and kiln dried. Typically, manufacturers use higher quality wood for the face layers and corresponding alternating layers, which align the grain parallel to the primary load direction. In essence, CLT is a much larger scale version of plywood. Lesser quality, or weaker, wood can be used in the transverse direction because of the overall performance of the layered product still achieves the desired specifications [33].

Laminas are laid out alongside similarly graded boards with contact on the narrow edges and pressed together to form layers of laid planks. Unlike some European manufacturers, most North American manufacturers do not add adhesive on the narrow faces. A layer of adhesive then coats the top surface of the laid planks before another layer of planks is stacked on top with the grain direction orthogonally oriented. The number of layers stacked is dependent on the designed layup. Generally, as each layer is stacked on top of the base layer(s), the panel is then pressed, often under heat and with high pressure to form one solid, layered panel of desired specifications. Alternatively, all the plies may

be stacked with adhesive between them and then pressed. The details of production methods may differ slightly depending on manufacturer's methods and equipment.

Figure 2-5. Close up view of a finger joint in a CLT panel.

Other wood products like glulam, have provided the industry with experience in adhesive application. CLT manufacturers use that knowledge to determine the type and quantity of adhesive product to use, as well as required pressures for the best bond between

layers. Dowel-type fasteners such as nails, screws, or wooden dowels can also be used to bond the layers together, although the resulting product may be classified as a different product known as nail-laminated timber (NLT). According to Austrian researcher Dr. Reinhard Brandner, the CLT's dimensions and layup of the cross-section heavily influence the performance of the panel and are therefore critical to designing with the material [33].

Building designers and engineers can specify CLT panels in various customizable sizes that a manufacturer then produces to order, limited typically only by production equipment size or the ability to transport. Manufacturers generally ship large panels of prefabricated wall, floor, or roof panels from the production facility to the construction site. The prefabricated nature of CLT lends itself to rapid construction and significantly decreases material waste, both in manufacturing and on the construction site.

2.1.4 Wood and Moisture Content – how it relates to CLT

Wood is a hygroscopic material, meaning it absorbs water from the atmosphere. Moisture content is an important quality of the timber laminas because the moisture content of the wood affects the mechanical strength properties of the wood. The wood's equilibrium moisture content (EMC) is a value that the wood naturally approaches as it dries from green wood, or recently cut wood. Green wood typically contains more moisture than seasoned wood. Seasoned wood has dried over time or through a kiln drying process. According to the Wood Handbook, EMC is the moisture content where wood is neither gaining nor losing moisture [96]. EMC is a function of environmental conditions such as relative humidity, temperature, and tree species features. EMC can be calculated using Equation 2.1 [96]:

$$EMC\ (\%) = \frac{1800}{W}\left[\frac{Kh}{1-Kh} + \frac{K_1Kh + 2K_1K_2K^2h^2}{1 + K_1Kh + K_1K_2K^2h^2}\right] \quad (2.1)$$

where h = relative humidity in decimal form

W, K, K_1, and K_2 = temperature dependent parameters

Another important property of the wood is its fiber saturation point. The fiber saturation point occurs when wood is dried to the state where only bound water within the wood cells' walls remain and all other water has been removed by drying. Typically between 20 and 35 percent moisture content, this value varies by wood species [52]. When the moisture content is greater than the fiber saturation point, wood is considered dimensionally stable and as the moisture content decreases or increases the dimensions change with shrinkage or swelling respectively [96]. When dried below the fiber saturation point, the decrease in moisture content is matched by an increase in the majority of the strength parameters for wood [52]. For example, at a moisture content of 12 percent, a clear specimen of wood can have twice the strength in bending and compression of green wood. When kiln-dried to 5 percent, the increase in strength can be as much as three times that of the unseasoned wood [52].

Unfortunately, at moisture contents less than the fiber saturation point, wood shrinks which can cause warping, checking, and splitting, degrading the overall performance of the wood [96]. The shrinkage rates differ with respect to orientation. The most shrinkage occurs tangentially followed by radial direction shrinkage. Only minor, if any, shrinkage occurs longitudinally for most species. Longitudinal shrinkage leads to shape distortion in sawn timber sections [96]. To avoid shrinkage issues while also maximizing the strength of the wood, builders typically install wood products at the in-

service moisture content. This results in challenges for construction of exposed wood in locations that experience significant seasonal changes. With glued wood products and laminated members, the practice is to dry the members to a level below the expected in-service moisture content to avoid issues with moisture absorbed from the adhesive [96].

Performance-rated CLT component requirements, outlined in the 2012 standard, call for the low moisture content of the lumber at the time of manufacture – just 12 ± 3 percent [12]. Typical dry solid-sawn lumber has a moisture content of 19 percent or less. Therefore, the lumber used in making CLT is drier and a reduction in moisture content to 15 percent increases most properties of interest in structural design [34]. With such a low moisture content, variations in the size of the pieces due to shrinkage as well as surface cracking can be avoided [68]. Strict quality control is necessary in the manufacturing of CLT to maintain low moisture contents and maximize the wood strength while also minimizing surface cracking. Important characteristics of the process include consistency in lumber quality and control of factors that could negatively influence the adhesive bond between the wood pieces [68].

Adhesive is also an important component of CLT. Requirements on the types of adhesives used are the same as other engineered wood products like glulam. Common adhesive products used in CLT production are polyurethane, melamine, and phenolic-based adhesives. The adhesion process typically involves use of a press, either hydraulic or vacuum, and compressed air. Use of a plane and sander is common after assembly for a smooth, even finish of the panel. If the design specifications call for an opening in the panel such as for fenestrations in a wall or for utility infrastructure and ducting, manufacturers use Computer Numerical Controlled (CNC) routers to make the exact cuts.

Production facilities typically include standard compliance checks as a part of their quality control processes [68].

2.1.5 Mechanical performance of CLT

The performance of CLT is dependent on many factors. One large factor is the wood species used for the lamina and the density of the wood. Even the bonding pressure required for good adhesion can be dependent on the species of base wood [33]. In general, the mechanical properties for CLT are evaluated through two methods: 1) the determination of properties based on models of single boards or layers; or 2) the determination of properties based on the testing of CLT elements [33]. Critical performance metrics for floor and roof elements are in-plane and out-of-plane bending strength, shear strength and stiffness. For wall panels, essential performance characteristics include load-bearing capacity, as well as in-plane and out-of-plane shear and bending strength [68]. CLT is engineered to withstand bearing loads both in- and out-of-plane through the various lay-up compositions [33]. Unlike glulam, in CLT the cross-wise orientation of the wood layers offer high in-plane and out-of-plane strength and stiffness with two-way action much like a reinforced concrete slab [68].

As a natural material, wood is subject to variation in mechanical properties. Wood variability can be a product of tree species, growing environment, and tree age. There is an entire branch of agriculture called silviculture dedicated to the science of producing and maintaining a forest with the goal of achieving consistency in the wood [77]. Variation can even occur within a single piece of wood due to the growth and development of the wood. Earlywood (or springwood) sections exhibit a wider radial diameter and thin-walled cells while latewood (or summerwood) sections exhibit thicker walls, observed as being darker

in color in the annual growth rings observed in wood [77]. Engineers and designers approach such variation by using conservative design values and factors of safety in engineering design. With CLT, a sandwich composite, the variation in the material is seemingly lessened as the composite nature homogenizes the variability.

When constructing with wood, certain strength parameters are commonly used in design and analysis. They include modulus of rupture in bending, maximum stress in compression parallel to grain, compressive stress perpendicular to grain, and shear strength parallel to grain. The modulus of rupture, a measure of strength before rupture, describes the load-carrying capacity and bending stresses the material can handle [96]. The compressive strength parallel to grain is based on the maximum stresses the material can sustain within specific length ratios to the smallest other dimension, commonly length to depth.

Shear strength parallel to grain is an important property for wood and can be described as the ability to resist internal slipping along the grain lines. For wood, average values of shear strength may be documented for radial and tangential planes. With CLT, the alternating layers can mitigate a weakness in the radial or tangential direction because every other layer is the opposite. Rolling shear, or interlaminar stress, is also an important and often limiting property that has been the subject of much recent research. The cross-wise layering means the orthogonal layers reinforce the longitudinal layers, which produce higher elastic modulus values than observed with glulam products [33]. This cross-wise layup also indicates that shear in longitudinal (parallel) layers and rolling shear in transverse (perpendicular) layers require verification to ensure sufficient strength for specific designs.

Studies modeling the influence of factors such as edge-gluing, wood density and span-to-depth ratio on rolling shear capacity of CLT show increased panel capacity gained through edge-gluing, use of denser wood and lower span-to-depth ratios [99]. These critical factors need to be considered in the design of a CLT panel and structure in order to optimize rolling shear capacity. High shear stresses are typically observed in the central layers oriented on a weak axis. In order to counter rolling shear stresses in the layers, it is recommended that the minimum width of a lamina be at least four times the lamina thickness [33]. PRG 320 requires the width to be no less than 3.5 times the thickness [12]. Wood sourced from closer to the pith, or center, of the tree in current CLT products seems to be contributing to the observation of higher rolling shear moduli [33]. This wood tends to be softer with a spongy consistency.

2.1.6. Hardness of wood

When considering impact resistance, an important characteristic for wood design is hardness. Hardness is seen as a measure of durability and structural quality combined in one number. Commonly, hardness is defined as the resistance to indentation and values can be identified through a test called the modified Janka hardness as outlined in *ASTM D1037, Standard Test Methods for Evaluating Properties of Wood-Base Fiber and Particle Panel Materials* and *ASTM D143 Standard Test Methods for Small Clear Specimens of Timber* [5, 11]. An Austrian researcher, Gabriel Janka, who worked for the U.S. Department of Agriculture, Forest Products Laboratory, developed the test in 1906 as a modified Brinell hardness test for wood. It has been the specified standard ASTM test for solid wood since 1927 [56].

The test measures the force required to embed a small (0.444-in) ball into the wood to half of the ball's diameter. An average value of the force from four indentations, two in the tangential face and two on the radial face, determines the side hardness of the wood. End hardness is distinguished from side hardness for wood due to the grain direction. At its initial development there was a shafted test jig and collar; set-ups were later adapted to incorporate more precise measurements using digital equipment. More recently, researchers explored the test for a reduced cross-section to accommodate thinner pieces of wood as well as engineered wood products and concluded the hardness values were equivalent for the nonstandard specimen size [56].

The force values of hardness gained through the testing show relationships with strength parameters like the modulus of rupture, ultimate compressive stress parallel to the grain, and a proportional relationship to density of the wood. Hardness also varies with moisture content. For woods in the range of 6 to 20 percent moisture content, Forest Products Laboratory estimates the hardness as shown in Equation 2.2:

$$H = H_{12}\left[\frac{H_{12}}{H_{green}}\right]^{[(12-M)/(M_p-12)]} \tag{2.2}$$

where H_{12} = hardness at 12% moisture content
H_{green} = hardness of green lumber
M = moisture content
M_p = intersection moisture content

Hardness values vary between 21 and 28 percent with the note to use 25 percent for other unlisted species [56]. Intersection moisture content is defined as the point when the mechanical properties of the wood begin to change due to drying from green wood [96].

Janka hardness ratings are commonly used for wood flooring materials as indications of resistance to indentation and durability. This is not a structural design issue but a characteristic of interest related to impact resistance. Tabulated values are typically reported as an average due to the variability in wood. Hardness values are typically provided as an average of radial and tangential penetrations [96]. Historically, other testing procedures have been used for wood, such as Rockwell, S Scale for thin, relatively soft materials and Brinell scale [41, 80]. There is not an ASTM standard for measuring the Brinell hardness of wood.

2.1.7 Seismic performance

Testing and analysis to date have shown that structures built of CLT perform well under seismic loading conditions. CLT wall systems have shown to effectively handle lateral loading conditions, even under extreme earthquake loads [36, 101]. The layering of timbers in a CLT panel offers more ductile behavior than other mass load bearing construction materials such as reinforced concrete. When considering CLT for use in seismically active areas or where code requires, care must be taken in the design of the connections. CLT walls appear to provide structural redundancy and CLT structures are less susceptible to soft story failures than other platform framed systems [68].

2.1.8 Fire Performance

Fire protection is a common concern in wood construction, in part because of historic urban fires in cities like London in the 17th century and Chicago in the 18th century when timber construction was commonplace. These fires spread quickly and caused vast destruction and economic loss. Wood is commonly accepted as a combustible material that provides fuel for a fire. Today, building codes incorporate fire safety issues to ensure

structural integrity, provide adequate fire resistance, and limit the spread of fire. A fire-resistance rating is "the period of time a building element, component or assembly maintains the ability to withstand fire exposure, continues to perform a given structural function, or both, as determined by the tests" according to 2015 International Building Code [16]. CLT can be manufactured with fire resistances of 30, 60 and 90 minutes because of the thickness of the panels. CLT panels have predictable char rates that allow CLT to maintain its structural integrity for long periods of time, contrary to initial perceptions [68].

Research on the fire resistance of CLT panels was conducted for future building code inclusion using full-scale experiments. CLT has been shown to be capable of meeting fire safety requirements related to flame spread and fire resistance outlined in *ASTM E84-15b, Standard Method of Test for Burning Characteristics of Building Materials* and *ASTM E119-16, Standard Test Methods for Fire Tests of Building Construction and Materials*, respectively [88]. The standards incorporate the following criteria: 1) maintaining adequate strength for test duration which is to allow for building evacuation and first responders; 2) prevent passage of flames or hot gases which could ignite additional elements; and 3) prevent a significant temperature rise (325˚F at any location and an average of 250˚F at a number of locations) above the initial temperature [68]. The time at which the assembly cannot meet all three criteria determine the fire resistance, typically classified in whole hours or parts of hours.

Under fire conditions, the behavior of wood can be predicted. The *National Design Specification for Wood Construction* cites a nominal char rate (β_n) of 1.5 inches per hour for CLT, which is the same as the rate assumed for solid sawn pieces and other engineered

wood products [19]. Table 2-5 shows the effective char depths for various lamination thicknesses at three required fire endurance durations. During a fire, a chard layer is formed on the exterior due to the fire exposure. The wood behind the charred layer is insulated and protected by the charring. When the adhesive between layers withstands the heat, the fire is not able to rapidly burn through the massive wood panel. However, issues with adhesives debonding due to the intense heat have been observed. Further details on this topic can be found in Frangi et al. [51].

Table 2-5. Effective char depths according to the National Design Specification for Wood Construction [19].

Required Fire Endurance (hr.)	Effective Char Depths (inches) (for CLT with β_n = 1-1/2 in./hr.)								
	lamination thicknesses, h_{lam} (inches)								
	5/8	**3/4**	**7/8**	**1**	**1-1/4**	**1-3/8**	**1-1/2**	**1-3/4**	**2**
1-hour	2.2	2.2	2.1	2.0	2.0	1.9	1.8	1.8	1.8
1 1/2-hour	3.4	3.2	3.1	3.0	2.9	2.8	2.8	2.8	2.6
2-hour	4.4	4.3	4.1	4.0	3.9	3.8	3.6	3.6	3.6

The NDS also includes an effective char depth equation, applicable to CLT [102] for use with Table 2-5 and shown as Equation 2.3:

$$a_{char} = 1.2\left[n_{lam}h_{lam} + \beta_n\left(t - \left(n_{lam}t_{gi}\right)\right)^{0.813}\right] \tag{2.3}$$

where $t_{gi} = \left(\frac{h_{lam}}{\beta_n}\right)^{1.23}$ = the time for the char front to reach glued interface (hours)

h_{lam} = lamination thickness (inches)

β_n = nominal char rate (inches per hour), based on 1-hour exposure

$n_{lam} = \frac{t}{t_{gi}}$ = number of laminations charred (rounded to the lowest integer)

t = exposure time (hours)

Some CLT manufacturers are working to have their products fire-rated by Underwriters Laboratory (UL) Standards for fire rated performance in building construction. In fire performance research, the behavior of CLT is highly influenced by the specific adhesive used to manufacture the CLT, which explains the additional standard for the adhesives used in CLT to meet the structural plywood heat-rating standards. Some undesirable adhesives fail under extreme heat conditions causing the burning layer to detach thereby eliminating that protective charcoaled layer of charred wood, and exposing the next layer of the composite product to the fire [51]. When adhesives that can tolerate high heats are used, the performance of the CLT is similar to that of a solid timber panel.

Additionally, CLT, as a panelized construction system, reduces the ability of the fire to spread either through concealed spaces such as ventilation ducts or utility corridors or between panels due to the inherent tightness of the system. Recent long duration fire testing using exposed CLT showed the ability of CLT to self-extinguish after the furnishings and room contents were consumed [71]. With proper engineering design, CLT buildings can limit fire spread and damage even though wood is inherently flammable. The 2015 International Building Code permits CLT in exterior wall assemblies with a 2-hour fire rating or less under the conditions that the CLT is protected by fire-retardant-treated wood sheathing not less than 15/32-inch thick, gypsum board not less than ½-inch thick, or a non-combustible material [16]. Loadbearing interior walls of CLT require one-hour fire-resistance rating and a minimum thickness of 4-inches [68].

2.1.9 Connections with CLT

As with any structural system, the design of connection to transfer load from one structural element to another is critical, and CLT is no exception. Widespread research

and study continues on all types of connections for CLT structures including panel to panel, wall panel to foundation, and wall to floor or roof. The cross-layered composition of CLT offers an advantage in that it reinforces itself and resists splitting at the connection for species where that failure is problematic in sawn timber elements [68]. Metal brackets, hold-downs and plates are used with massive timber to transfer loads between connected panels. Connection design is an area of ongoing innovation in terms of structural design and construction assembly practices. Given the high stiffness and strength of CLT panels, connections between them can be the limiting factor in terms of loading capacity [33].

2.2 Advantages of CLT as a building material

Decades of successful use of CLT in Europe have shown several significant advantages of the material. A product of a joint effort from academia and industry, CLT has benefitted from the increased emphasis on sustainable construction practices [68]. As a wood product, CLT is made from a renewable resource and studies examining the sustainability of managing forests in order to manufacture CLT have shown positive results [48]. The high degree of prefabrication and relative ease of assembly make on-site construction times significantly shorter with less waste. Additionally, the panels are lighter than steel, masonry, and concrete construction and therefore allow a smaller and less expensive foundation to support the structure [68]. Smaller foundations use less concrete, a major carbon dioxide producer.

In addition to the environmental benefits gained from using a renewable resource, CLT exhibits the potential for significant energy savings during the use phase of the building. The tight tolerances achieved through the precise cuts and customization lead to low infiltration rates, and the interior tends to maintain thermal and humidity levels at

comfortable levels. Therefore, CLT structures require less heating, ventilation, and air conditioning (HVAC) system demands. With the inherent insulating properties of timber, CLT combined with supplemental insulation can achieve a performance rating equivalent to that of concrete but with a much reduced weight [63]. The panel itself acts as a thermal mass with its solid and thick nature in contrast to lightweight wood framing or steel framed structures, which require much more insulating material. The thermal mass of CLT aids in reducing the heating and cooling requirements of the building as well as shifts the peak demand time [81]. This has the added benefit of reducing energy consumption during the most costly times of the day.

As a building material, CLT offers the ability to cover long-spans without intermediate supports or bracing and can feature unique architectural elements because it can be precision crafted using CNC machines for exact cuts [33, 45]. The capability to customize the material is also a beneficial feature as the panels can be designed to a specific layup to meet structural requirements. For example, panels could be constructed with double layers of boards oriented in the same direction or other variations.

In terms of on-site construction, the prefabricated nature of the large panels translates to a reduction in the size of construction crews with faster completion times. This results in a lower likelihood of accidents and significantly less disruption to the area surrounding the construction site [45, 81]. These features add up to cost savings in construction and assist in making engineered timber a financially competitive building material [46]. Additionally, cost savings can be gained in the design and construction of the foundation. As a lighter building material than steel, reinforced concrete, and masonry, CLT structures can require a less robust foundation and reduce costs related to load transfer

designs for buildings constructed over pre-existing rail, roads, and utility corridors or on less than ideal soil conditions [63].

2.3 Challenges of CLT as a building material

Challenges of CLT are: 1) durability; 2) logistics; 3) creep; 4) sound transmission; and 5) pests. A major concern with the durability of any wood product is moisture exposure. Mitigation measures to avoid exposure for CLT, include the proper design of coverings and interior plumbing lines to ensure sufficient moisture protection and the use of vapor barriers. For areas where the CLT would potentially be in contact with the ground and its associated moisture, designers should consider either a concrete layer or treatment of the panel to mitigate water and insects from the ground [63]. While structurally suitable for exterior walls, CLT panels should be covered or coated with a waterproof membrane to ensure long-term durability of the wood. A common construction practice is to construct the CLT structure on a concrete pedestal foundation although this is not required.

While not unique to the material, other disadvantages of CLT include transportation requirements of the large prefabricated pieces, the absence of wood in some areas, the current limited knowledge with respect to the design and construction of the product, perceived concerns with creep due to long-duration loading, fire resistance, and sound insulation. The transportation issue can be mitigated through the design of smaller pieces. In the decision-making process, the transportation costs of using larger panels should be balanced with the benefit of rapid construction and fewer connections. The absence of local wood product can hinder the use of any wood product including CLT and there may be areas where wood of any variety is not an ideal construction material due to limited availability or poor quality.

Load duration and creep behavior are critical considerations in the structural design when using CLT as a building material. The cross-wise nature of the layers makes CLT more likely to experience issues in terms of creep than in other engineered wood products [68]. The 2015 *National Design Specification for Wood Construction* (NDS) included design provisions specifically for CLT. In the standard, a time dependent deformation (creep) factor of 2.0 is specified for design of CLT in dry-service conditions [19]. Other sections of the standard include CLT connections and fire design provisions.

Sound transmission or the acoustics of buildings is a large area of research on its own. The main concern with the introduction of a new construction material with respect to sound transmission ties to the IBC's minimum requirements for sound insulation between adjacent areas. These areas include adjacent living and work areas, or living and work areas adjacent to public spaces like halls and stairwells. Despite some challenges in terms of achieving required sound ratings on its own, CLT does offer some advantages. Due to its customizable nature, CLT structures typically have the tight tolerances that are important to limiting sound transmission. Cracks at wall and floor junctions, utility connections, and insets are where flanking noise — sound that transmits indirectly through spaces — leaks through even when the main separating system has good acoustic insulation [68]. Building assemblies can be rated with a single number for airborne sound insulation, the Sound Transmission Class (STC). A higher STC indicates less noise passage and greater acoustic insulation. Similarly, the Impact Insulation Class (IIC) is a single number rating for wall and floor assemblies with respect to impact sound insulation. The IIC indicates how well a floor assembly reduces the footstep sounds from the floor above. CLT characteristics like weight per unit area, stiffness, and porosity all

contribute to its performance as a sound insulator. Table 2-6 shows sound ratings for several common interior wall and floor assemblies compared to CLT panels of 3- and 5-ply thicknesses.

Table 2-6. Sound ratings of common wall and floor assemblies compared to CLT [9].

Assembly Composition	STC	IIC
Interior wall examples		
3-ply CLT	**32-34**	**n/a**
1/2" gypsum & 3/16" plywood	28	n/a
2x4" studs, 16" on center (o.c.) & 5/8" gypsum board screwed to studs	28-35	n/a
1/2" gypsum board, no studs & 2-1/2" air space	30	n/a
1-5/8" metal studs, 24" o.c. & 1/2" vinyl-faced gypsum boards screwed to studs	27	n/a
2-1/1" metal studs, 24" o.c. & 5/8" gypsum board screwed to studs	37	n/a
Floor assembly examples		
5-ply CLT	**39**	**24**
4" thick concrete slab	44	25
6" thick concrete slab	55	34
3" thick reinforced concrete slab, 35 psf, ceiling bare, flooring: carpet over soft padding, at least 1/4" thick	44	70

The IBC minimum requirement for walls and floors is STC 50 and for floors an IIC 50 is required. To meet IBC minimum requirements, most wall and floor assemblies, to include CLT, require additional measures beyond their inherent sound transmission insulation. Several solutions have been proposed and tested for CLT walls including the addition of gypsum board, use of two panels of 3-ply, use of mineral wood insulation material, and wood studs attached to gypsum board, as well as combinations of these

additions to achieve STCs in the range of 50-60 depending on the thickness of the CLT layers [68].

CLT is more deficient with impact sounds. This shortfall can also be overcome by additional supplemental layers on top of the CLT to cushion the footfalls of the floor above, or adding sound absorption material, such as fiberglass insulation, sound isolation chips, or suspended gypsum board below the CLT floor panel. These CLT assemblies achieve IIC rates in a range of 59-72 depending on the exact composition [68].

Typical concerns with wood durability and performance as a construction material in the long-term include decay, and pests like termites and marine borers [34]. Decay requires significant moisture exposure where the moisture content is typically greater than 20 percent. Used properly, wood can outlast the design life of a structure and current design practices include protection from weathering effects and moisture leaching from ground contact [34]. Treatment and protection from pests would be similar to other wood products. The advantage of CLT is that there is significantly more mass than in lightweight wood structures, and so the damage would have to be unobserved for a long duration to lead to structural damage.

2.4 Military temporary structures

The military uses a variety of temporary structures ranging from canvas tents to modular soft-walled structures to vehicle-based extensions, much like the pop-out on modern day campers. By military doctrine, there are different levels of construction defined by their life expectancy. Temporary construction is expected to last five years and semi-permanent facilities have a life expectancy of less than 10 years, which can be extended to 25 years with maintenance and upkeep [14]. The structures discussed below

and for the remainder of this research would, by military doctrine, be defined as semi-permanent construction but for the purpose of simplicity and clarity to readers outside of the military, will be referred to more generally as temporary military structures.

Generally, temporary military structures must be set-up or built quickly. Tents can be erected in a less than an hour, but offer little protection from the enemy and only nominal protection from the weather. For locations that Soldiers operate out of for months to years, often a deliberate engineer effort is brought in to build temporary structures out of lightweight wood timbers or seamed thin-walled metal hanger-like structures such as the proprietary K-spans shown in Figure 2-6. More commonly, B-huts are constructed to provide temporary Soldier housing.

Figure 2-6. Thin-walled metal hangers called K-spans erected by military engineers as temporary structures (photo by LTC Ken Frey, used with permission).

2.4.1 The Barracks Hut or B-hut

For decades the United States military has used a simple standard design for temporary shelter at the more enduring base camps set up in contingency or overseas operations from Bosnia to Afghanistan. The structure has been called a South-East Asia (SEA) hut, a South-West Asia (SWA) hut, and most generically a Barracks hut (B-hut). Typically, Army, Air Force and Navy Engineer forces build these structures from standard dimension lumber forming a wood frame with plywood sheathing. Often they are built in clusters to facilitate power by generator as well as consolidation of living areas by unit. They have been built as part of a larger base camp in support of combat operations in places like Iraq and Afghanistan but also have been used in Africa in response to the Ebola outbreak and other locations for humanitarian missions. Figure 2-7 shows a B-hut under construction.

Figure 2-7. U.S. Army Soldiers construct B-huts in Afghanistan (photo by LTC Ken Frey, used with permission).

Historically, the Army traces the use of the B-hut or similar design back to World War II with use in locations like Vietnam and the Philippines as well. While best known for use as living quarters, the rectangular standard design of the B-hut has also served as administrative space for offices, planning rooms, and conference rooms.

The simplicity of the design makes the structure multi-functional in use but, also rudimentary in functional building operation. There is typically no plumbing as other solutions are developed for bathroom and shower use, but the design does allow for basic electric wiring for both lighting and outlets for occupant use. The structure relies on heating and cooling from an exterior HVAC unit called an Environmental Control Unit (ECU) powered by generators that run on diesel fuel. While the B-huts are an improvement in energy efficiency over a canvas tent, the lack of insulation provided by the standard lumber makes these structures inefficient for climate control.

A standard B-hut is a single-story rectangular shaped structure of approximately 32-feet long by 16-feet wide (512 square feet) although variations exist. Figure 2-8 shows elevation, plan and isometric views of the generic B-hut structure [1]. Two common variations include an “extended B-hut” 18-feet by 52-feet design (936 square feet) and a “super B-hut” with 32-feet by 88-feet dimension (2,816 square feet) as seen in Figure 2-9. The largest size is usually built for use as a command headquarters, a dining facility, combat hospital, or other administrative purposes. The structure is typically built on a foundation of pier-type footers to accommodate sites that are not perfectly level. Since the B-huts are frequently built in clusters, the first step of construction often includes earthwork at the desired site to clear and level the site.

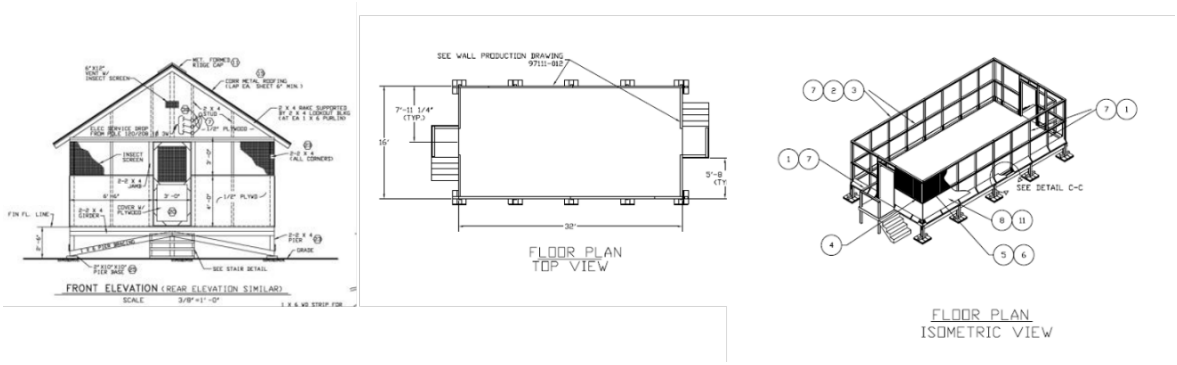

Figure 2-8. Front elevation, plan and isometric views of a generic B-hut design.

Figure 2-9. A large B-hut variation nears completion in Afghanistan (photo by LTC Ken Frey, used with permission).

In each individual B-hut, there is a set of steps and a door at each end, which lead into a center corridor running the length of the building. In the B-huts built for living

quarters, on either side of this corridor are sets of small individual living quarters with plywood walls separating the individual rooms. These interior walls do not extend up to the ceiling to allow for the central running of both lighting and ventilation from the ECU. Additionally, it is a simpler construction method as the roofs typically have a pitch and the interior roof is left unfinished with the roof trusses exposed.

Depending on intended use, the interior configuration of walls can vary. Some B-huts are built without any interior partitions, even for living quarters. The roofs of the B-huts have a slight pitch to allow for rain and snow runoff with less leakage into the interior of the structure. Frequently, the structure is windowless to offer increased protection and privacy to the occupants, although there is the potential to have windows if desired. Often, seams between the floor structure and walls as well as the walls and roof are lined with caulk to help with thermal conditioning and prevent insect intrusion.

Since B-huts are built as temporary shelters rather than permanent structures, they are finished relatively primitively. Typically, there is no façade layer to protect the wood from the elements and repeated exposure to rain, snow and sun other than sand bags placed to harden the structure. An exception may be found with the roof where, depending on location and materials available, the roof may be corrugated metal or wood with an asphalt paper at the exposed surface as seen in Figure 2-10.

Despite their intended temporary use, B-huts have been used for over a decade in places like Afghanistan, Iraq, Bosnia, Kosovo, as well as countries in Africa, Central and South America. At the end of their useful life, the structures are often demolished with heavy equipment, leaving behind wood scrap for disposal. Sometimes the buildings are turned over to the host country or non-governmental organization (NGO) for future use.

In areas where wood construction is not customary this can become problematic for the future occupants to upkeep.

Figure 2-10. Army engineers construction a cluster of B-huts to house soldiers on a Forward Operating Base in Afghanistan in 2007 (photo by CPT Ashley Dellavalle, used with permission).

2.4.2 Logistics and B-hut supply chain

The wood that the structures are built from usually ships from the United States, which is a large logistical burden. Engineer units may deploy with containers, typically ranging in size from 20-ft by 8-ft to 40-ft by 8-ft. The shipping containers are packed with U.S. grade lumber and plywood for the construction of B-huts. Additional construction materials may be re-supplied through the military logistics system for continued construction and repair as well as any in-theater stocks should expansion of current base camps become necessary. The military spends significant manpower, effort and dollars to

ensure an uninterrupted supply chain for all required resources, including materials to build B-huts.

Within the military logistics support system, construction and barrier material, such as the lumber and plywood for B-huts, is known as military supply classification IV (Class IV). Class IV encompasses all construction materials including plywood, lumber, plumbing supplies, heating, ventilation, and air-conditioning equipment as well as barrier materials such as barbed wire, sandbags, and other force protection materials. As its own class of supply, construction materials have their own distinct supply chain, which begins with contracted producers or manufacturers of the specific materials.

These suppliers provide the DoD with a finished product such as a box of nails or bundles of 3/4-inch plywood. Each item has its own supply chain, often with numerous suppliers and contracts as well as production lead-times and delivery availability dates. The contract specifies the transition point from supplier to military distribution system, which is normally a warehouse or depot. There are many people involved in the supply chain, both civilian and military personnel, many of whom work for critical agencies in the supply chain such as the Defense Logistics Agency (DLA), which provides nearly all of the construction material, and U.S. Transportation Command (TRANSCOM), which coordinates the movement of the supplies.

From the warehouse or depot, the supplies move to forward storage points for distribution down through the military supply chain to the user in need, such as the Army engineer soldiers building the base camp or the unit for whom the camp is being built. The Army estimates requirements for construction materials based on tables and computer programs built from historic data and a level of intensity projected for the given operation,

the geography, climate, and number of troops supported [114]. Operations like a surge of troop deployments in Iraq or Afghanistan or a deployment of troops to assist with an Ebola outbreak in Africa each require tons of materials and thousands of stocked shipping containers.

Military logisticians coordinate to find available stock in depots and warehouses and may contract for additional amounts beyond what is available at those locations. Contracts with lumber providers in the United States exist but DLA can also purchase materials from Europe and other locations in an effort to decrease the distance of moving the materials, thus allowing shorter lead-times and reduced transportation costs. Given the weight of most lumber and other construction materials, it is generally transported overseas by ship through commercial sea vessels. However, shipments may also move by rail, if available. Air and other modes of transport may be used in an emergency or high-priority situation.

2.4.3 Sustainability and the next generation of B-huts

In the last five years, interest in building more sustainable B-huts has grown and the Engineer Research and Development Center (ERDC), and Construction Engineering Research Laboratory (CERL), U.S. Army Corps of Engineers, as well as the U.S. Military Academy (USMA) faculty and cadets have worked towards a potential solution for the next generation of B-huts. The research has focused on the use of an innovative building material called Structural Insulated Panels (SIP), which would allow for improved thermal efficiency and faster construction time due to the prefabrication options available. The panel is made from oriented strand board (OSB) faces with polystyrene or similar foam insulation as a 4- to 12-inch interior between the OSB pieces.

Sustainability for the construction of B-huts in austere environments differs from green building methodologies in the United States. A major component of sustainability from the military perspective is the concept of using fewer resources. This could be using less labor for construction of the B-huts but also increasing the energy efficiency throughout the life of that B-hut. Lower energy usage in B-huts translates to a reduction in the transportation of fuel and other required resources on high-risk supply routes. This results in lower costs and reduced risk to military personnel and civilian contractors. As technology develops for alternative power sources, military planners will continue to look to build base camps that require less fuel, a major consumable at base camps in the past 15 years in Iraq and Afghanistan. In addition to the alternate power sources, an energy efficient building can greatly reduce the fuel requirements.

Air-conditioning the troop shelters is blamed for up to 80% of energy consumption by an ECU, the largest power draw on the base camp [53]. Attempts to alleviate the lack of shelter efficiency have included spray-on foam, which raised issues with fire safety as well as ventilation concerns. Technologies like foam-insulated tents were attempted, however once coated in the polyurethane spray foam insulation, the tent could no longer be taken down, moved and reused. It was also difficult to dispose of due to the insulation.

2.4.2. Survivability and force protection of B-huts

From a force protection perspective, the traditional lightweight wood frame construction of B-huts offers little protection to those inside it. Structures can be easily damaged, as shown in Figure 2-11. As indirect (rocket, artillery) or direct fire impact the structure, the wood itself can do further damage as it splinters into more fragments within the B-hut. Since the B-huts themselves offer little protection, military leadership addresses

the protection of its personnel by constructing nearby bunkers made of concrete c-channels, sandbags, or earth-filled barriers as shown in Figure 2-12. The challenge for occupants is that there is little to no early warning to send them into the more fortified bunkers until the shells are already falling. Soldiers have to get to those bunkers in order for them to be effective and that often means running from their bunks in their underwear, helmets and body armor thrown on hastily in the middle of the night.

Figure 2-11. A damaged pole barn roof and damaged living quarters in Orgun-E, Afghanistan (author photos).

Figure 2-12. Concrete bunker structure sits outside K-span in Orgun-E, Afghanistan (author photo).

2.5 Other uses of temporary structures

The military is not the only organization that uses temporary structures. There are many other uses for temporary structures and future research could explore the use of CLT for other purposes. In the United States, agencies like FEMA, local response teams, and law enforcement often rely on temporary structures to live and work. Internationally, aid groups like USAID, Red Cross, and UNICEF all operate in transient locations dictated by immediate need. A temporary structure package could provide a solution for improved working and living conditions for volunteers, evacuees, refugees and others. Each scenario would have its own set of requirements related to the structure and the material used to build it. Examples of other temporary structures include post-disaster housing, which would require quick construction, potentially enhanced protection from the conditions such as earthquake aftershocks or continued extreme weather events, and reusability. Other uses

could include seasonal structure need or simply relocatable structures that need to move as those inhabiting them move, such as scientists on expedition or foresters harvesting a timber crop.

2.6 Force protection of military facilities

A unique parameter in the construction of all military facilities, regardless of life expectancy, is the need to meet specifications related to the building's force protection, which is the structure's inherent ability to provide safety and security to the occupants and equipment inside. Force protection is an active, dynamic process in that it is constantly assessed for changes based on the potential threat, hazard, and risk. From a macro view of the military base's footprint down to individual structures on it, the Force Protection Condition (FPCON) dictates the current level of threat.

Different levels of FPCON describe the measures needed to be taken in response to terrorist threats against these facilities. As such, all structures must meet specific guidelines for varied threat levels as outlined in Unified Facilities Criteria (UFC) publications. DoD Instruction 2000.12 instructs each military service to ensure that antiterrorism (AT) protective features be integrated into planning, design and execution of facility construction to lessen AT weaknesses and threats to the force [15]. Title 10, U.S. Code, which governs the Armed Forces, necessitates the Secretary of Defense to develop common guidance and criteria for the development of construction standards which mitigate vulnerabilities to attack and improve security.

Historically, attacks on military facilities have taken place overseas in locations not even considered combat zones, such as the 1996 bombing of Khobar Towers in Saudi

Arabia, and the Marine barracks in Beirut, Lebanon in 1983. Within the United States, military recruiting centers are a frequent target as demonstrated by attacks in New York City in 2008, Little Rock, Arkansas in 2009, and Chattanooga, Tennessee in 2015. Military bases at large such as the Fort Hood shooting massacre in 2009 and the Washington Navy Yard shootings in 2013 have also been targeted. Nationwide, military facilities are seen as a common target for terrorist attacks and thus, design and construction methods to prevent attacks, mitigate damages, and enhance protection of personnel and equipment are a priority.

2.6.1. How buildings are built for force protection – Unified Facilities Criteria and threat levels

Unified Facilities Criteria (UFC) documents provide planning, design, construction, sustainment, restoration, and modernization standards that apply to the military services, Defense agencies and DoD field activities. Some UFC publications, like those shown in Table 2-7, outline different antiterrorism, security, and force protection tactics and procedures. Planning for force protection measures is a deliberate process specified within the DoD Security Engineering Facilities Planning Manual. After the planning team is formed, critical assets are identified and valued. The threat to those assets is then determined by examining aggressor likelihood, probable tactics, and threat severity levels.

Table 2-7. Unified Facilities Criteria titles that relate to force protection.

UFC Number	Title	Distribution	Release
4-010-01	DoD Minimum Antiterrorism Standards for Buildings	Public release	Distribution A
4-010-02	DoD Minimum Antiterrorism Standoff Distance for Buildings	For Official Use Only	Distribution C
4-010-03	Security Engineering: Physical Security Measures for High-Risk Personnel	Public release	Distribution A
4-020-01	DoD Security Engineering Facilities Planning Manual	Public release	Distribution A
4-020-02FA	Security Engineering Concept Design	For Official Use Only	Distribution C
4-020-03FA	Security Engineering Final Design	For Official Use Only	Distribution C
4-023-07	Design to Resist Direct Fire Weapons Effects	Public release	Distribution A
4-022-01	Security Engineering: Entry Control Facilities Access Control Points	Public release	Distribution A
3-340-01	Design and Analysis of Hardened Structures to Conventional Weapons Effects	For Official Use Only	Distribution C
3-340-02	Structures to Resist the Effect of Accidental Explosions	Public release	Distribution A
Distribution A: Approved for public release, unlimited distribution authorized. Distribution C: Distribution authorized to U.S. Government Agencies and their contractors.			

The threat severity levels indicate the tools, weapons, and explosives associated with the likely tactics to be used based on a host of intelligence information. Designations for threat severity level include very low, low, medium, high or very high. Protective systems are designed for the threat severity level, or the design basis threat. Threat parameters combine the aggressor's likely tactic and threat level to identify possible weapons types, tools or delivery methods which the facility needs to designed to handle, as shown in Table 2-8.

Table 2-8. Examples of Threat Parameters as outlined in the security planning UFC[8].

Aggressor Tactic	Design Basis Threat	Weapons	Tools or Delivery Method
Moving and Stationary Vehicle Devices	Very High	2000 kg (4400 lb) TNT, Fuel	7000kg/~15,000 lb truck
	High	500 kg (100 lb) TNT, Fuel	2500 kg/ ~5500 lb truck
	Medium	250 kg (550 lb) TNT, Fuel	1800 kg / ~ 4000 lb car
	Low	100 kg (220 lb) TNT	1800 kg /~ 4000 lb car
	Very Low	25 kg (55 lb) TNT	1800 kg / ~ 4000 lb car
Hand Delivered Devices	High	IID, IED (up to 25 kg/55 lb TNT) &hand grenades (Mail bomb limited to 1 kg/2.2 lb TNT)	None
	Medium	IID, IED (up to 1 kg/2.2 lb TNT) & hand grenades	
	Low	IID	
Indirect Fire Weapons Attack	Very High	Improvised mortar (up to 20 kg/44 lb TNT)	None
	High	122 mm rocket	
	Medium	82 mm mortar	
	Low	Incendiary devices	
Direct Fire Weapons Attack	Very High	Light antitank weapons, and UL 752 Level 10 (12.7mm (0.50 caliber), 1 shot)	None
	High	UL 752 Level 9 (7.62mm NATO AP, 1 shot)	
	Medium	UL 752 Level 5 (7.62mm NATO ball)	
	Low	UL 752 Level 3 (.44 magnum)	

Based on the threat tactics shown in Table 2-8, an initial level of protection is determined. Level of protection refers to the amount of damage a facility could sustain given a specific threat. Different weapons and explosive threats require different mitigation methods. In general, standoff distance, building hardening, barriers, and manned guard forces as well as procedures comprise the design strategy for most threats [8]. Standoff distances allow the pressures created in an explosive blast to be less

impactful on the structure through the quick dissipation of those pressures. It should be noted that expeditionary and temporary construction should apply the same design strategies as permanent structures unless otherwise differentiated.

2.6.2 Ballistic and fragment penetration

One guideline for military facility design in response to security threats is *UFC 4-023-07, Design to Resist Direct Fire Weapons Effects*. The purpose of this document is to provide engineering guidance for protection against direct fire weapons, including small arms and shoulder-fired antitank weapons systems [7]. Small arms are defined as handguns, rifles, shotguns, and automatic weapons systems capable of firing munitions up to 0.50-caliber in size. Anti-tank weapons include rocket propelled grenade (RPG) launchers. Many direct fire weapons require a direct view or line-of-sight to the intended target but the relatively long-range capability of these weapons can make these threats difficult to defend against as the aggressor can be outside the limits of the base perimeter. For this reason, facilities that are more vulnerable are typically situated at the most interior and insulated section of a base.

The threat parameters and four threat severity levels associated with direct fire weapons are shown on Table 2-9. Standards listed refer to the Underwriters Laboratories (UL) level accompanying with the specific weapon or munition type. UL 752 and the National Institute of Justice (NIJ) 0108.01 are the most common commercial standards in the U.S. for ballistic standards. The resistance of the building components to ballistic threats must be tested and evaluated for each material or system. Test standards like those listed define the caliber, weight, composition, muzzle velocity, and number of impacts.

Outside of the military, these standards are used in the design of facilities such as banks, and government buildings.

Table 2-9. Threat parameters for Direct Fire weapons.

Design Basis Threat	Weapons / Standards	Effective Range
Very High	Anti-tank weapons ANSI/UL 752 Level 10 (12.7 mm/0.50 caliber)	AT Weapon: 300 meters 0.50-caliber: 2000 meters
High	ANSI/UL 752 Level 9 (0.30 caliber Armor Piercing)	800 meters
Medium	ANSI/UL 752 Level 5 (7.62mm/0.308 caliber)	1000 meters
Low	ANSI/UL 752 Level 3 (0.44 caliber Magnum)	100 meters

Fragments from indirect weapons, such a ground-fired rockets and mortars, can cause extensive damage even without a direct hit by an explosive device on a structure. Fragments can penetrate, perforate, and ricochet from a structure leading to damage to structural elements from the fragments themselves as well as spall damage from the shock wave of the explosion. Important characteristics in the evaluation of fragment penetration are similar to those of ballistic penetration: mass, velocity, shape, and dimensions. Such characteristics are used to design in defense of these threats.

Methods to defeat low-level threats can include techniques such as denial of an unobstructed line-of-sight for targeting through site layout, landscaping, fences and walls. Pre-detonation screens may be used to intercept the threat before the intended target. The function of this screen is to reduce the energy of the incoming projectile as an energy

absorption layer. Use of these screens can be beneficial to protect areas needing additional security without having to harden the entire facility and can also be a cost effective technique for construction.

Wood is a common material used or considered for use for these screens and the required thickness varies depending on the species of wood as well as the design basis threat level (Table 2-9). Currently, wood is not assessed for the design of a protective structure beyond use as a pre-detonation screen because of its low strength compared to steel and concrete. Technical manuals cite that wood is often used in expedient field construction and some protective shelters thanks to its high strength to weight ratio. Mass timber products, such as CLT, which can achieve strengths comparable to steel and concrete construction methods, change the viability of wood use for protective design.

Thanks to its use as a protective screen, wood penetration has been examined and experimental testing for traditional sawn timber and plywood has yielded empirical equations relating wood penetration to fragments and projectiles. The UFC for direct fire threats provides an equation, shown in Equation 2.4, to determine the thickness of wood required to resist perforation [7]. *Penetration* is defined at the entrance of the projectile into the target without complete passage while *perforation* is defined as complete passage through the target by the projectile [67].

Common wood density and hardness parameters are provided in the UFC for a variety of wood species at both dry and wet states. This research shows that Equation 2.2 does not apply to CLT or that the equation may need factoring or adjustment for the significantly thicker wood products available in engineered wood products.

$$T_w = 9837\left[\frac{v^{0.4113}w^{1.4897}}{\left(\rho(\frac{\pi D^2}{4})^{1.3596}H^{0.5414}\right)}\right] \quad (2.4)$$

where T_w = thickness of wood necessary to prevent perforation (in)
v = projectile impact velocity (ft/sec)
w = projectile weight (lb)
D = projectile diameter (in^2)
ρ = wood density (lb/ft^3)
H = wood hardness (lb)

2.7 Summary

While CLT has been the topic of much research in the last decade, most of the focus has been on introducing the material in the United States for use across all construction sectors and building taller structures or wooden skyscrapers. The material is just starting to gain widespread use across building divisions but remains most heavily used in locations closely tied to the forest industry and primarily as a novelty structure – such as the first CLT parking garage in Oregon or the first hotel constructed out of CLT at Redstone Arsenal, Alabama.

Architects, engineers and developers are interested in CLT as a building material because it provides a highly customizable, environmentally sustainable product with the strength of commonly used materials like concrete and steel. Builders who have worked with the material, such as LendLease, advocate for use of the material due to the rapid construction speed and the reduced number of laborers required while maintaining a cleaner, less wasteful, and safer construction site [109]. Barriers to the expansion of CLT use include fears about fire safety, concerns about moisture exposure and wood, and limited experience with the material.

Initial research on the blast performance of CLT has begun through a partnership with WoodWorks, a Wood Products Council initiative providing technical expertise, North American manufacturers, who are motivated to expand the market, and the Protective Design Center, U.S. Army Corps of Engineers. Simultaneously, the Army strives to find better ways to build temporary military structures while protecting the soldiers living and operating out of them.

CHAPTER 3
FUNDAMENTALS OF PENETRATION MECHANICS

3.1 The importance of studying penetration mechanics and terminal ballistics

For over 200-years, scientists and engineers have exhibited interest and exerted effort in understanding the science at work with an impulsive loading event such as a bullet shot from a gun or a cannon ball impact on the ground. Today, understanding the behavior of materials and structures under intense impulsive loading like ballistic penetration is significant to a wide variety of areas from demolition of structures, especially pre-stressed concrete structures, to safe transportation of hazardous materials, to nuclear reactor safety, especially in natural disasters. Other areas that make penetration mechanics a topic of interest include vehicle crashworthiness, development of lightweight body armor used by law enforcement and military forces, the vulnerability of vehicles, aircraft and structures as well as spacecraft and satellite survivability to meteors [125, 126]. While the study of penetration mechanics is often attributed to military scenarios, the field extends well beyond those applications to any high mass or high velocity debris event brought on by an accident, or other high rate energy release like the examples given above [126].

3.2 Fundamental governing equations

Study of the science behind penetration mechanics depends fundamentally on the classical physics laws of conservation. Specifically, conservation of mass, conservation of momentum and conservation energy. Conservation of energy is the most apparent with ballistics. With an impulsive loading event such as a bullet shot from a gun and hitting a target, the conservation of energy aids in understanding what it takes to stop that projectile,

or the work required to transition the kinetic energy of that projectile moving to a stationary state within the target. Equation 3.1 shows a generic version of the conservation of energy equation where the sum of the initial internal energy and kinetic energy must be equal to the sum of the final internal energy, kinetic energy, and work done within the system.

$$\sum E_i + \sum \frac{1}{2} m_i v_i^2 = \sum E_f + \sum \frac{1}{2} m_f v_f^2 + W \tag{3.1}$$

Where E represents internal energy, m is the mass, v is velocity and W is work, and subscripts i and f represent initial and final states, respectively. In the case of a ballistic event, the work done by the bullet is typically the plastic deformation of the target and any kinetic energy remaining after that work is done either movement of the whole system, target and bullet, or a perforation with the bullet retaining kinetic energy as it moves at a residual velocity after exiting the target.

In penetration mechanics, it may be difficult to account for various mechanisms that dissipate the energy of the system. Some systems see energy transfer mechanisms change with striking velocity magnitude. For example, higher velocities see energy at least partially dissipated by plastic work or permanent deformation of the target. Energy may also be dissipated in the form of heat during penetration. This change in temperature can be difficult to quantify in terms of measurement methods and due to the temperature sensitivity of some materials.

Conservation of momentum is demonstrated as an impulse, I, felt on a body changes the momentum from an initial value, mv_i to a final value, mv_f, where m is mass and v is velocity as shown in Equation 3.2.

$$I = \int F\, dt = \int m\, dv = mv_f - mv_i \tag{3.2}$$

Conservation of mass states that in a closed system the mass, *m*, must remain constant over time, *t*, hence the quantity of mass is conserved over time, as shown in Equation 3.3:

$$m_1 = m_2 = (\rho Vol)_1 = (\rho Vol)_2 = (\rho tvA)_1 = (\rho tvA)_2 = constant \tag{3.3}$$

where ρ represents density, *Vol* is the volume, *v* is velocity, and A is the area; all variables are with respect to the mass of the closed system.

The conservation laws and continuum mechanics assist in an increased understanding of penetration mechanics. Continuum mechanics is the analysis of the kinematic and mechanical behavior of solids and fluids modeled as a continuous mass. Penetration mechanics, with a large number of influencing variables can require involved calculations such as wave equations, Bernoulli's equation, and equations defining impact-induced stress and strain. All these may be derived from the fundamental conservation laws as well as both solid and fluid mechanics, illustrating how these physics-based methods serve as the foundation for the field of penetration mechanics. Bernoulli's equation is important because at high velocity impacts with correspondingly high pressures, common target materials like metal are shown to behave like fluids.

3.3 Early science of penetration mechanics

3.3.1 Poncelet Equation

Mathematician Leonard Euler and engineer Benjamin Robins analyzed information about the penetration of steel cannonballs in soils based on impact velocity in the mid-1700's as the first documented researchers to examine the science behind terminal ballistics. Shortly after their experiments, the French mathematician and engineer, Jean-

Victor Poncelet, who served as an engineer under Napoleon, began extensive work in the area and proposed an equation, shown in Equation 3.4. Today, the equation is known as the Poncelet equation, founding the field of penetration mechanics.

$$\frac{d}{dt}(mv) = -A_{cs}c_0 - A_{cs}c_1v^2 \tag{3.4}$$

Poncelet's equation states that the instantaneous time rate of change, *d/dt*, of a bullet's momentum, *mv*, is equal to the sum of two retarding forces: 1) a general form of drag that is proportional to the cross-sectional area of the penetrator, A_{cs}; and 2) a dynamic drag term proportional to the cross-sectional area of the penetrator multiplied by the square of the penetrator velocity, *v*, a kinetic energy term. The constants, represented by c_0 and c_1, dependent on the target material being penetrated. The Poncelet equation describes rigid body penetration and assumed the cross-sectional area of the penetrator remained constant and no significant mass loss during the projectile's movement through the target. This assumption is not always accurate as penetrators may experience expansion, mushrooming, fragmentation and erosion during an impact event.

Poncelet effectively took the ballistic impact phenomena of a rigid penetrator, known to be governed by deceleration of the penetrator, and applied mathematics to transform the equation so that a solution could be obtained from measureable data. Accurate measurement of deceleration during penetration is difficult to capture with most materials. Instead, penetrator depth measurements from experiments across a range of velocities can be captured and used to determine material dependent constants in the empirical relationship.

3.3.2. Classic penetration equations

Often it was assumed, as Poncelet assumed, that the penetrator is rigid with an unchanging mass. The penetration depth of a projectile thus was recognized to be dependent on the deceleration of the projectile in the target and the velocity of the projectile as shown in Equation 3.5:

$$P = \int_{v_0}^{0} \frac{v}{a(v)} dv \tag{3.5}$$

where P represents the final penetration depth, v is the velocity and v_0 is the striking velocity, and a is the deceleration. The relationship between the deceleration and the velocity was unknown and various theories were proposed early in the investigation of penetration mechanics. Equation 3.6 shows a general expression for the deceleration term.

$$a(v) = C + Av + Bv^2 \tag{3.6}$$

where v represents velocity, $a(v)$ is deceleration relative to velocity and A, B, and C are constants that must be determined empirically. The terms on the right side of the equation are commonly associated with the cohesive resistance of the target, C; a frictional effect, Av; and acceleration of target material in the impact area, Bv^2.

Classic penetration equations based on these fundamental relationships and assumptions were developed by Euler and Robins, Poncelet, and the French engineer, Resal. Through integration, the expression for deceleration relative to velocity can transform into an expression for the final penetration depth, P, in terms of striking velocity, v_s. Table 3-1 shows the equations credited to each scientist.

Table 3-1. Classic penetration equations.

Scientist/Engineer	Deceleration Expression	Penetration Depth Expression
Euler-Robins	$a = C = constant$	$P = \frac{v_s^2}{2C}$
Poncelet	$a = C + Bv^2$	$P = \frac{1}{2B}\ln\left(1 + \frac{Bv_s^2}{C}\right)$
Resal	$a = Av + Bv$	$P = \frac{1}{B}\ln\left(1 + \frac{Bv_s}{C}\right)$

3.3.3 Shaped-charge jet penetration

For two centuries, scientific understanding of terminal ballistics depended on empirically derived relationships, primarily between impact velocity and penetration depth, for various projectile and target combinations. During World War II, American and British scientists independently researched shaped-charge jet penetration, which considered a jet with constant velocity, length and density. A jet referred to the force of the explosive charge such as those observed in projectiles with lined hollow noses, like bazookas used by the Americans and Germans. In this style of projectile, the impact event caused the charge detonation which created a high speed jet, or long, small-diameter stream of steel from the steel cone liner of the projectile and effectively perforated the target with a slower velocities than previously developed antitank projectiles [30]. Penetration by jets later became known as long rod penetration and an extensive body of work exists in examining long rod penetration impacts. Long rod penetration is outside the scope of this research.

3.4 Impulsive loading

Solid materials deform under the stresses they experience during loading. In a ballistic event, there is an impulsive load that result in large applied pressures over a very short duration. Structural and material response to impulsive loading can be a very complex phenomenon. Conceptually, impulsive loading can be characterized into three regimes: 1) stresses below the elastic limit; 2) increased stresses resulting in plastic behavior; and 3) very high stresses where hydrodynamic behavior is observed.

Geometry and the material properties, both target and projectile, all play significant roles in the resulting effects of the many contributing factors in an impulsive loading event. Materials may behave elastically if loading conditions apply stresses below their material yield point. As loading increases and surpasses the yield and ultimate strengths of the material, deformations become plastic with large deformations. If the deformations are large enough, fracture and rupture of the target, and possibly the projectile, will result. In the third regime, with stresses of even higher intensity, pressures may exceed the material strength by multiple orders of magnitude and the material behavior is viewed to act hydrodynamically, or as a fluid.

Studies in impact dynamics examine deformable bodies that experience a dynamic loading at rates that make it necessary to consider inertia effects. In classical mechanics inertia is neglected and stress states are assumed to be uniform throughout the body [61]. Material characteristics such as bulk stiffness and shear modulus are typically considered constant. However, for high-pressure impacts such as a ballistic penetration, they may vary. The inclusion of inertia effects and stress wave propagation are key to impact

dynamics. The high strain rates have been shown to produce an increased material strength for dynamic conditions compared to static loading.

The applied pressure of a penetration event leads to compressive stresses on the face of the target. The pressure causes an acceleration of the surface layer particles, which move towards the second layer behind it, and compressive stresses build and accelerate the second layer at an increasing rate. This continues at each successive layer [126]. Stress waves develop when the compressive stresses between the layers equal the applied pressure and these waves propagate through the material. In accordance with the conservation laws, this changes particle velocities as well as the states of strain and stress. At low impact velocities, stresses may be below the material yield strength and thus only develop elastic stress waves. With elastic waves, particles move but return to their original positions. Inelastic stress waves can develop where stresses exceed the yield stress.

3.5 Shock Waves

With an explosion or a high-velocity impact, a discontinuity in pressure and particle velocity is created which propagates through the material and is known as a shock wave [115]. Shock waves result in a scenario where matter is moving faster than the speed that surrounding matter can displace [25]. With a dynamic impact, a shock wave is a moving discontinuity of compressed matter into undisturbed matter. It is a scenario of intense, short-duration loading distinct because of the fast rate of loading compared to a static loading.

The shock wave initiates at the impact face when the projectile strikes the target and moves into the target by sweeping through the material at a constant velocity. Material behind the shock front is compressed to a high pressure state and density dependent on the

impact velocity and material characteristics. The shock wave decays through relief and residual waves reflecting from free surfaces. Tensile stresses are induced with the relief waves as they reflect the initial compressive force of the shock wave and this can cause spall in materials with relatively low tensile strengths like concrete [49].

A wave travels in the material with an almost instantaneous rise in pressure detectable by high density behind the shock front. The presence of this wave visually can often only be detected by high-speed cameras. Graphically, this travel is depicted as shown in Figure 3-1 with a wave front in terms of pressure and time.

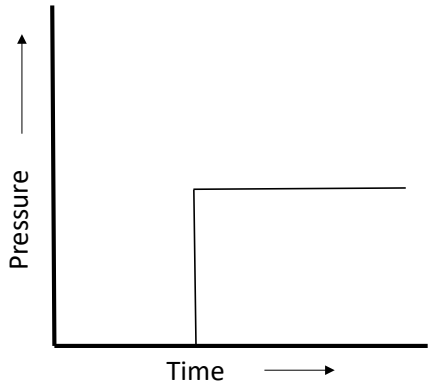

Figure 3-1. Graphical depiction of a shock front at steady-state in terms of pressure and time.

A shock wave creates discontinuity in the system in that it induces large pressures, mass particle speed, and internal energy changes. To maintain equilibrium, the stress of the shock wave must be reduced and this is done through relief waves, which brings the pressure back down to the initial state, often zero pressure. Relief waves are not steady

like the shock wave but rather can be thought of as a number of small stepped waves with a range of velocities determined by functions of pressure governed by the material and its equation of state [49]. These relief waves propagate in the opposite direction of the shock wave when the shock wave contacts a free surface, where the pressure remains at zero, releasing the pressure or stress of the shock wave. Relief waves can also occur when the shock front hits a boundary between two different solids due to different material response, or shock impedance, where only a portion of the shock conditions continue transmitting and the remaining energy is conserved through a relief wave at that material boundary. The transmitted and reflected waves are conceptually how the split-Hopkinson pressure bar (SHPB) works to determine the dynamic characterization of materials under high strain rates. The SHPB test, or Kolsky bar test set-up, is useful in determining dynamic stress-strain curves of solids under uniaxial stress conditions.

3.5.1 Applying shock wave theory

Different theories, such as plastic wave theory and rate-dependent theory, have been developed to assist in determining expected material behavior. Plastic wave theory assumes behavior is represented by the same stress-strain curve as a static test of the material. By this theory, solutions can be found mathematically with the wave equation and correctly identified initial boundary conditions. Rate-dependent theory recognizes that strain rate is dependent on plastic flow and, as the name suggests, dependent on the loading rate [126].

Shock loading can be studied using rod geometry, with uniaxial stress, where the stress intensity is limited by plasticity or plate geometry, with uniaxial strain, where the stress intensity is dictated by bulk properties and material failure decides the pressure limit

[124]. Historically, work with shock waves used plate geometries which examined a state of uniaxial strain and three-dimensional stresses. Uniaxial strain is appropriate for a ballistic impact or other high-rate phenomena where the material does not have time to deform laterally, at least initially.

3.5.2 Shock Hugoniot curve

With a shock wave, the relationship between the states on both sides of the shock wave can be described with Rankine-Hugoniot relations, which express the relationship between variables on either side. These conditions effectively set the conservation equations for mass, momentum, and energy in the conditions of the shock wave speed. Based on the conservation equations, the mass density on either side of the wave, the particle velocity, the pressures and specific internal energies both behind and in front of the shock wave can be determined [20]. Assumptions made for the Hugoniot relationship include inviscid fluid, no heat transfer through conduction or radiation and neglect of gravitational acceleration. The Hugoniot relationship of a material is unique to it and can be found experimentally with embedded stress gauges or using interferometric techniques.

The conservation laws apply and assist with equations regarding the behavior of shock waves. A Hugoniot curve for a material can be developed based on the combination of the laws of conservation of mass, momentum and energy and knowledge of material characteristics such as density, stress, modulus of elasticity at initial and final states of shock. Equation 3.7 shows the conservation of energy Rankine-Hugoniot equation for a steady plane one-dimensional shock wave:

$$E_1 - E_0 = \frac{(P_1 + P_0)\left(\frac{1}{\rho_0} - \frac{1}{\rho_1}\right)}{2} = \frac{1}{2}(u_1 - u_0)^2 \tag{3.7}$$

where E_i is the internal energy, ρ is density, u is particle velocity, P is shock pressure and the subscripts *0* and *1* are the state in front of and behind the shock front, respectively. The curve, which is typically a graphic depiction of the pressure-specific volume relationship, or P-V curve as it is sometimes identified in the literature, can be determined by a series of plate impact experiments with a flyer plate of varied velocities forming the curve. Each shock wave experiment of a set velocity yields a single P, V point, or Hugoniot end state. A straight line connecting two of those points is called a Rayleigh line, or compression path, and can be drawn to connect an initial state and a final state. The slope of the Rayleigh line determines the shock speed [49]. A generic Hugoniot curve is depicted in Figure 3-2.

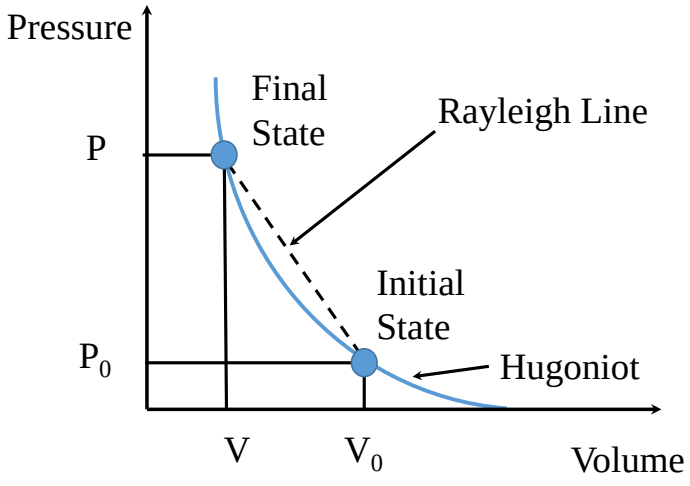

Figure 3-2. Relationship of the P-V Hugoniot and Rayleigh line.

The Hugoniot elastic limit (HEL) is the position on the curve where the material transitions from purely elastic state to an elastic-plastic state, or where plastic deformation or material yielding is initiated. It should be noted that above this point the material loses the majority of its shear strength and thus can be represented as behaving like a fluid, or hydrodynamically.

Dynamic compression in elastic-plastic solids is complex but anisotropic solid materials like wood make the problem even more difficult. Hydrocodes and iterative calculations help find solutions. However, these codes cannot operate alone and require input on the material equation of state, constitutive relations, and response to dynamic loading.

3.6 Hydrodynamic Theory of Penetration

The study of penetration by jets lead to the development of the hydrodynamic theory of penetration. This theory is useful in understanding and predicting results of many penetration experiments but it does neglect the strength of target materials because it was observed that the high velocities of the shaped-charge jets produced pressures well beyond the material yield strength. It was determined with such large pressure values, the materials involved could be treated as fluids, hence the hydrodynamic term. The foundation of the theory centered on the conservation of momentum and Bernoulli's equation, a conservation of energy principle for flowing fluids. The theory is based on additional assumptions beyond representing the materials as fluid, such as the incompressibility of both the jet material and target material and that, a steady state of constant velocity is reached instantaneously allowing the shock phase to be ignored. It was also applied to semi-infinite

targets. These assumptions allow the depth of penetration for continuous jets to be calculated using Equation 3.8:

$$\frac{P}{L} = \sqrt{\frac{\rho_p}{\rho_t}} \tag{3.8}$$

where P is the depth of penetration, L is the original jet length, ρ_p is the density of the projectile and ρ_t is the density of the target. However, this applied only to hydrodynamic materials where the projectile and target have no strength because the strength of the materials is neglected. It is believed these strength can be ignored because the pressures inflicted by the jet are orders of magnitude larger than the strength of the materials. In reality, penetration depth is known to depend on material strengths, even at high velocities [30]. Later research in the 1960's worked to include a dynamic yield strength of the target material [23]. This work was based on a modified Bernoulli equation with an additional term accounting for material strength. However, it also relied on restrictive assumptions such as those valid for very high velocity impacts and that the projectile is consumed entirely, making it applicable to mostly weak projectiles.

3.7 Phases of penetration

A phases of penetration model was developed by Christman and Gehring in 1966 for high-velocity projectile penetration [38]. Their study examined dynamic behavior during penetration by rod projectiles and characteristics of the target post-penetration for semi-infinite targets. The first phase, also called the transient phase, is extremely short and is on the order of microseconds. It is when the projectile first comes in contact with the target face. There is a high-pressure spike as the shock wave moves from the interface

between the projectile and target into the target. This phase is annotated with the marking I in Figure 3-3.

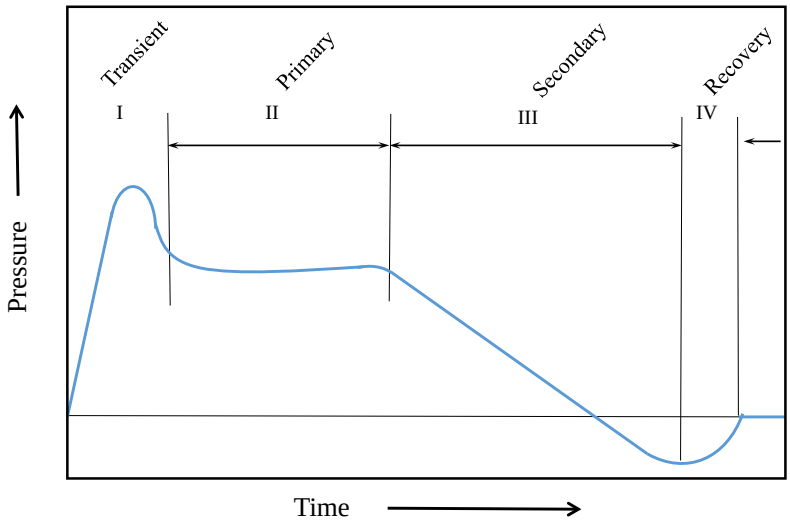

Figure 3-3. Phases of penetration with respect to time and pressure, adapted from [38].

The next phase, marked as II on Figure 3-3, is the primary penetration phase. During this phase, the kinetic energy of the projectile is transitioned to the target material in a hydrodynamic process. The pressure field at this stage is a product of the densities and compressibility of both the target and projectile materials, as well as the velocity and dimensions of the projectile. The pressure level is shown as a horizontal line as it is modeled as steady-state, where the pressure behind the shock front is constant. The duration of this phase is influenced by the aspect ratio of the projectile with a low ratio causing it to have a short duration and high ratio leading to a relatively long period where the crater develops [38].

The secondary penetration phase, or cavitation, follows and is marked on Figure 3-3 with III. Christman and Gehring describe this phase as the projectile being deformed and removed as an energy source from the system where radial expansion occurs from the crater. As the pressure field decreases, the material strength and strain-rate response come into play and can no longer be neglected as they are when assumed as hydrodynamic. Primary and secondary penetration phases may occur simultaneously where shear deformation occurs parallel to the crater and the projectile and target material are ejected from the crater. This phase ends when the energy density behind the shock wave can no longer out-match the material resistance to deformation [38].

The final phase, the recovery phase, annotated with IV on Figure 3-3, sees a contraction of the crater. Depending on the brittleness of the target material, fractured and spalled material may congest the crater, making it smaller than its maximum diameter in previous phases. Some material recovery may also take place as the material rebounds from the compressing pressures of the impact event [38].

One significant aspect of this model is the similarities between a ballistic projectile induced impact and a blast induced impact. Both have the hallmarks of a very short duration, high pressure front at the beginning, followed by shock wave sweeping at a constant pressure and then ending with a recovery period with a slightly negative pressure period. While the area impacted by a ballistic projectile may be limited to two to three diameters of the projectile, the impact phenomena is not dissimilar from a blast where dynamic loading under high strain rates effects the material.

3.8 Ballistics

3.8.1 Breakdown of the science of ballistics

Ballistics breaks down into three distinct areas of science, as follows:

1. Internal ballistics, with a focus on the inner workings of the gun and the interaction of the gun, projectile and propellant charge
2. External ballistics, with a focus on the projectile in flight from the end of the gun barrel to the target-projectile interface
3. Terminal ballistics, which is generically, the science and engineering of impacts

Terminal ballistics, now more commonly called penetration mechanics, is specifically the science behind what happens when a projectile strikes a target, including the behavior and effects of the projectile when it makes contact with the target and transfers energy to the target. The penetration effectiveness is typically determined by the projectile design in terms of shape, size, and striking velocity. There are two perspectives to the field of terminal ballistics. One view is in terms of protection and research from this vantage point in terminal ballistics is for armor design or force protection assessment of structures. In essence, it involves design of a target with minimal areal density to defeat, or resist the penetration of a projectile. On the other hand, there is the lethality viewpoint used in weapons design to maximize the desired effect and design projectiles capable of defeating or penetrating a given target with minimal energy. Due to challenges in gathering data related to terminal ballistics, the science of penetration mechanics has lagged behind the other two areas of ballistics, although recent developments in computer simulation, radiography and high-speed photography have all helped in the recent past.

3.8.2 Basic ballistic terms defined

Common ballistics terminology must be defined for clarity. Penetration is the entry of a penetrator, or projectile, into any portion of a target; this includes perforation, embedment and ricochet. Ricochet is the scenario where the penetrator deflects from the target without being stopped or perforated. Embedment is where the penetrator is stopped during contact with the target and there is the formation of a crater in the target. Perforation is when the penetrator passes through the target and may also be called a complete or full penetration. Cratering describes the localized deformations in target [27].

Ballistic limit (V_{BL} or V_{50}) is a commonly referenced velocity threshold for perforation and is defined as the average of two striking velocities where one is the highest velocity giving a partial penetration and the second is the lowest velocity giving a complete penetration or perforation. This value is determined experimentally with at least six shots where half perforate the target and half experience embedment, or stop the penetrator. The typical difference between the highest and lowest velocities in the test set is less than 60 m/s (200 fps). There are several measures used in rating the penetration performance of armor or other materials of interest. Three of the most extensively used criteria are the Army Ballistic Limit, the Protection Ballistic Limit and the Navy Ballistic Limit [27]. Figure 3-4 shows the differences between the three criteria for partial and complete penetrations.

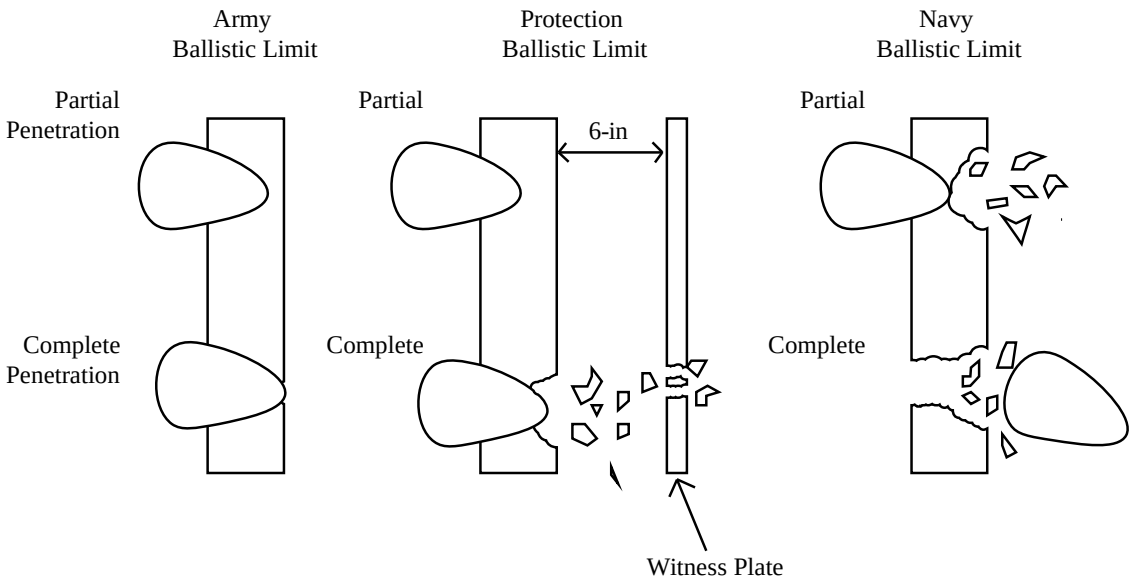

Figure 3-4. Illustration of three main penetration criteria, adapted from [27].

The main distinction between the three criterion is the definition of a perforation or complete penetration. While the Navy definition involves the total projectile emergence from the target, the Army limit requires the projectile to be visible on the back face such that light could pass through the hole or crack formed. The protection limit defines complete penetration as the instance where a witness plate located 6-inches behind the back face of the target is perforated, either by fragments of the target created by the impact or by the projectile itself. For the protection limit partial penetration, the witness plate may be dented but not perforated.

3.8.3 Regimes of velocity

For the purposes of penetration mechanics, the striking velocity is generally broken down into regimes of velocities. One rationale for these regimes is different mathematical models seem to apply to impact phenomena at different velocities. It should be noted

however that the quantities associated with the different regimes are just guidelines, not rigid rules for application due to the influence of numerous other variables beyond the striking velocity.

The low velocity regime generally applies to projectiles with a striking velocity of less than 250 m/s (approximately 820 fps). In this regime, structural analysis mythologies of taking an equivalent load distribution over the impact area fit, making it a regime where problems fall into the realm of structural dynamics. The loading and response times in the low velocity regime are milliseconds (ms), which is much longer than the following regimes.

Intermediate velocity, refers to a striking velocity in the range of 500 to 2,000 m/s (approximately 1,600 to 6,500 fps). In this range, the material behavior governs the response and places the response of the structure as secondary. However, the impact area where material response is observed is typically limited to just two to three times the diameter of the impacting projectile. The impact phenomenon in this range is described with a shock wave influenced by the velocity, geometry, and material characteristics of both the target and projectile to include density and strength. Loading and reaction times are now microseconds (μs). This regime coincides with the velocity range for typical ordnance of conventional weapons systems. The velocity ranges in this research fall within this regime.

The high velocity regime is a velocity range of 2,000 to 3,000 m/s (approximately 6,500 to 10,000 fps). At these rates, the localized pressures exceed the strength of the material by an order of magnitude. Under those circumstances, the collision of the target and projectile as solids can be treated as fluids and the problem can be examined with the

principles of hydrodynamics. The realm of hypervelocity starts in this regime. The impact velocity of shaped charge jets are typically in the range of 2,000 to 8,000 m/s (6,500 to 26,000 fps) and their study is often in the interest of armor and anti-armor design [95].

The fastest velocity regime is called ultra-high velocity with rates greater than 12,000 m/s (approximately 40,000 fps). With an explosive impact in this regime, colliding materials result in vaporization. Projectiles moving in this regime tend to be involved in studies in space and aeronautical areas.

3.8.4 Hypervelocity impact

The 1950s and 1960s saw an era of great interest in hypervelocity impact due to the race to space. Concern with spacecraft impact with meteoroids led to significant work exploring this ultra-high velocity range. Ultimately, scientists and engineers determined the larger stresses allowed for the neglect of rigidity and compressibility and the impact was viewed as a fluid flow scenario. The National Aeronautics and Space Administration (NASA) extensively studies hypervelocity impact even today in the interest of designing spacecraft and satellites capable of withstanding impact from debris and small meteoroids.

3.8.5 Dynamic Properties

In a high velocity impact, such as those in a ballistic event, high pressures and temperatures exist in the projectile and the target for very short (μs) periods of time through fast moving shock waves. The impulsive nature of the event is characterized by high strain rates in excess of 10^2 s^{-1} and pressures over 10 GPa. The high temperatures are of note because for temperature sensitive materials, like many metals, an elevated temperature can cause material softening and lead to adiabatic shearing and greatly contribute to material failure. Some dynamic properties affect the material's equation of state, or thermodynamic

equation relating state variables like pressure, volume, temperature or internal energy. Other properties determine constitutive relations, which account for strength and failure characteristics under high loading rates. Strength and failure are important properties for terminal ballistics, which vary with loading rate, pressures and temperature.

3.9 Process of penetration

The process of penetration is complex in terms of all of the variables changing and being influenced by the impact event. The projectile hits the target and strong compressive shock waves propagate through both bodies as visually represented in Figure 3-5. Shock waves compress materials in fractions of microseconds traveling faster than the speed of sound and changing internal energies [49].

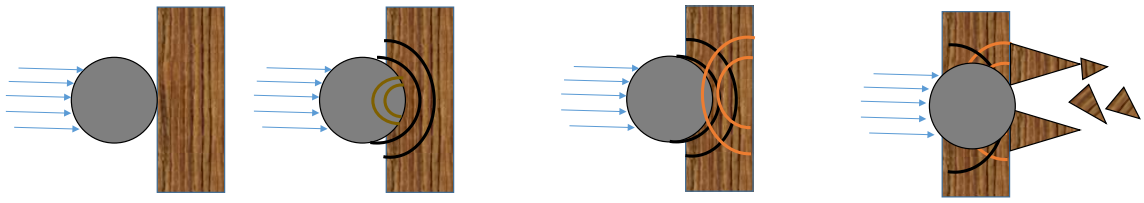

Figure 3-5. Projectile penetration into target creating compression waves (black) and relief waves (orange).

An almost instantaneous rise in pressure moves into and through the target with the shock wave. If the striking velocity is high enough, relief waves propagate and develop high tensile stresses in the projectile material. When the original compressive wave reaches a free boundary, such as the rear surface of the target, additional relief waves are generated to reduce the stresses and bring the pressure back down to the initial pressure. If

the load intensity and duration exceeds a critical value for the target material, a material failure initiates [125]. For impact situations, two types of material failure exist: 1) exceeding the elastic limit and plastic flow occurrence with permanent deformation and cratering; 2) exceeding the cohesive strength of the target material leading to fracture occurrence and perforation. When the kinetic energy of a projectile is greater than the shear strength and material resistance of the target, perforation results.

3.10 Response of materials

Upon an impact, the material of the target responds through multiple mechanisms. Part of the mechanical energy may be transformed into heat, which can change the strength properties of the material if thermally sensitive. As mentioned, the material response to a dynamic impact loading such as a ballistic projectile is distinctly different from static loading because inertia effects should be included with the stress wave propagation.

An accurate understanding of what occurs during a penetration event requires material characterization of both the target and the projectile. Material properties are needed for analysis, prediction and interpretation of penetration phenomena. Three physical properties of importance due to their influence on ballistic performance include hardness, toughness and soundness. Hardness is the material's resistance to indentation. Toughness is the ability of the material to absorb energy before fracture. Soundness is the presence or absence of localized flaws or weaknesses within the material. Generally, a deformation occurs in a material when applied stresses reach a critical value or yield limit. Rupture or fracture occurs in a material when the stresses exceed an ultimate strength. These stresses can be compressive, tensile, or a combination such as in flexure.

For some materials, the constitutive relations are not well developed or frequently applied, and this is the case with wood, a highly anisotropic material. Dynamic material behavior for wood has not been extensively investigated. The extreme range of stresses applied in dynamic impacts such as a bullet penetration require knowledge on the material response under that type of loading. Existing models for materials under that type of loading are based on extrapolations from experimental information. Metals and plastics, which are generally homogeneous and isotropic, have well-known constitutive relations. These materials are frequently used as targets in penetration mechanics research because of both their homogeneity and isotropy, and their history of use in armor and penetration resisting materials.

3.11 Target classification

The material composition is not the only influence of the target on the impact phenomenon. The ratio of target thickness to diameter of the projectile is also an important influencer. The thickness, or depth, of the target is a large factor because of the transmittance of shock waves and the distance those waves need to travel to reach a free boundary. For convenience, targets are classified by thickness into the following categories [27]:

1. Semi-infinite, where the distal boundary, or rear surface of the target does not influence the penetration process,
2. Thick, where the influence of the distal boundary on the penetration process is only after substantial travel by the projectile into the target,
3. Intermediate, where the rear surface influences the deformation process considerably during most of the penetration process,

4. Thin, where stress and deformation gradients do not exist throughout the thickness.

Table 3-2 aligns a target classification with a ratio of target thickness to diameter of the projectile.

Table 3-2. Classification of target by thickness, adapted from [90].

Target Classification	**Ratio of target thickness to projectile diameter**
Thin	<1
Intermediate	1-8
Thick	8-12
Semi-infinite	>12

Experiments with semi-infinite targets are typically designed with a focus on the penetration process and the physics of the process whereas thinner targets are typically used to simulate design options in armor or weapons design.

3.11.1. Target modeling assumptions

Based on years of studies involving a range of projectile type, it can be assumed that localized influence with the cratering deformation of a projectile only extends two to three projectile diameters. In thin plate targets and striking velocities near the ballistic limit, this assumption gets more uncertain. Additionally, the target should be fixed in its position to avoid complications with the motion of the target upon impact. It is effectively a rigid body from the perspective of the penetrator. Often, the thermal effects are neglected due to the relatively small dissipation of heat and limited number of materials significantly influenced by the temperature change. It is also extremely challenging to measure in

experimental testing as the rise in temperature is internal to the target which would require a thermal image detecting camera and which may or may not be sensitive enough to measure the relatively short temperature surge.

A breakdown of material characteristics is integral to penetration mechanics research. These characteristics include bulk and shear moduli, strengths, density, and thickness. Thorough documentation on the geometry, density, and other observable characteristics of the target should be captured. Target thickness is a key parameter, even for the simplest of models.

3.12 Failure mechanisms

Generally, failure modes can be summarized by the target thickness and striking velocity of the projectile. While other factors such as material characteristics and target support methods also influence the situation, the target thickness and speed of the striking object are the most influential. Failure can occur in both the target and the projectile. Target material failure is in the form of severe deformation and presence of a crater from the projectile's path. Projectile failure is more likely to occur in brittle materials due to the reflected tensile relief waves initiated by contact with the target.

In the case of ballistic penetration, elastic deformation is typically limited to very low striking velocities, well below the normal ordnance range of conventional weapons. A limiting velocity for elastic deformation has been calculated based on the applied stresses of the projectile and the material characteristics such as stiffness, Poisson's ratio, and density of the target and project [27]. Permanent deformations are more commonly seen and those can stem from a variety or combination of failure mechanisms. The mechanism of failure experienced with a ballistic impact event is influenced by material properties, the

striking velocity, projectile shape, method of target support and relative dimensions of the target and projectile. Frequently, more than one failure mode occurs with the same impact. Common modes of failure include scabbing, spalling, fracture, plugging, petaling, and ductile failure. Figure 3-6 provides a visual depiction of the difference failure modes.

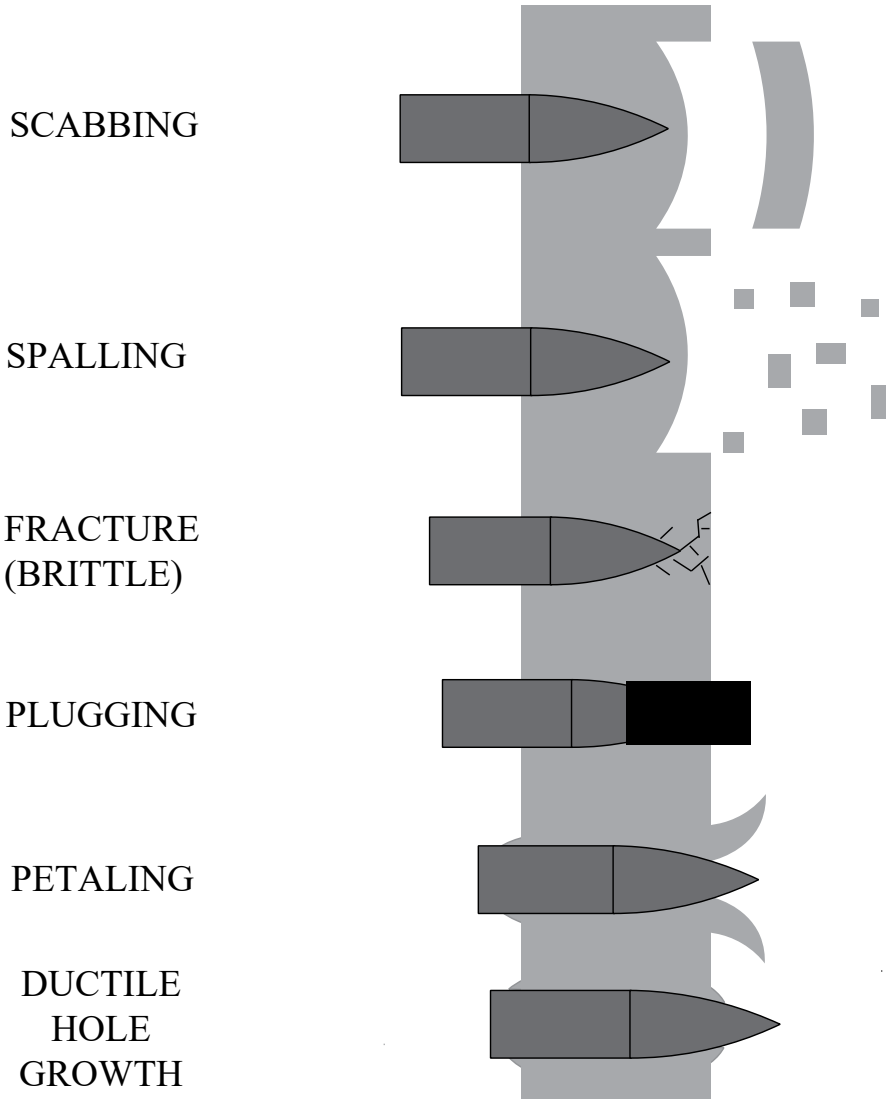

Figure 3-6. Examples of failure modes induced by projectiles.

Scabbing is caused by large deformations, which are influenced by local inhomogeneity and anisotropy of the material. Fracture can occur when the stress wave exceeds the material's yield strength. Spalling appears similar to scabbing but is caused by tensile failure, typically on the back face of the target, and is induced by the reflection of the initial compressive shockwave in relief waves. It is a common failure mode for materials stronger in compression than tension, such as concrete. Radial cracking is also common in the same materials.

Brittle fracture typically involves sudden, very rapid crack formation and there are no signs of ductility. The cracks can lead to fragmentation into smaller pieces. There is little or no plastic deformation and low energy absorption before fracture. The fracture surface is distinct and often relatively smooth.

Plugging is a failure mechanism that has been the topic of many studies. This failure mode typically occurs with a blunt or hemispherical nose-shaped projectile where a process termed adiabatic shearing results in the development of a cylindrical slug. This slug, with a size approximately the same diameter or slightly larger than the striking projectile, is ejected from the target or at least completely perforated from the original target. This failure type is frequently seen with temperature sensitive materials because the plastic deformations of the projectile can convert to heat as the energy dissipates. This increased temperature influences the shear strength of some materials, hence the adiabatic shearing or formation of adiabatic shear bands. Striking velocities near the ballistic limit are often credited with this failure mode as higher velocities tend to cause fragmentation of the material instead of formation of an intact plug [125].

Petalling of the target material takes place when high radial and circumferential tensile stresses arise after the initial stress wave. This failure mode is common in thin targets and ogival or conical nosed projectiles. High stress gradients develop in the area of the tip of the projectile, or the leading edge, resulting in plastic flow and permanent flexure in the material. Upon exceedance of the material's strength, star-shaped cracks develop and target material is pushed back further by the projectile's continued motion forming protruding petals of target material still attached to the original target but with large deformations [125].

Ductile failure combined with spalling is common for thick targets with low or medium hardness [125]. In this failure mode, stresses exceeding the material strength induce plastic deformations and eventually fracture is induced as the material pulls apart. Due to the complexity of the penetration mechanics and the number of influencing factors, it can be challenging to correlate the performance of target and projectiles with the different failure mechanics responsible for the final state.

The thickness of the target and the length of the projectile can change the failure occurring during penetration. One example is a theory called entrance phase effect, which is credited for relatively higher penetrations of rigid penetrators in lower velocity ranges, due to lower decelerations by the target. Early in the target deformation, when the projectile is just deforming on the front face, the target has a lower retarding force as the target material can displace around the projectile and be pushed out the front face. Whereas in deeper penetrations, the target material has nowhere to escape so the projectile must push that material forward to sideways as it advances or compress that material until the

projectile has passed. With shorter projectiles, it may be easier for that deformed target material to displace behind the projectile [95].

3.13 Projectile characteristics and influence

In terms of ballistics and munitions design, there are multiple types of projectiles. Kinetic energy projectiles are where the energy of the projectile motion results in penetration or the projectile pushing into and possibly through a barrier or target [126]. Other projectiles may be designed with different desired terminal effects, such as a warhead which can contain explosive or chemical charge designed to initiate upon contact with the target. An example of a specialized warhead is a munition known as a bunker buster which is designed to penetrate, either into the earth or through reinforced concrete, and then explode in order to reach underground or hardened targets. These warhead munitions are often dropped from aircraft above the target so they are not without an element of kinetic energy. Unlike the small arms kinetic energy penetrators, these munitions often have delayed or advanced technology fuses and explosive packed into the nose which can inflict the desired terminal effect on the target when employed.

Small arms projectiles like those fired from handguns and rifles also have various designs. Terms like full metal jacket, hollow point, semi-wad cutter all apply to conventional small arms munitions. The main differences with this type of munition is the shape and structure of the nose of the projectile, which vary depending on the desired terminal effects of the individual shooting the projectile. Some rounds, like the hollow point variety are designed to expand upon impact, creating a larger diameter crater or projectile path than a full metal jacket. With the exception of tracer ammunition, which have a small charge in the base that burns to illuminate the path of the projectiles, the

explosive portion of the small arms projectiles takes place within the weapon. Powder in the cartridge ignites and the burning propellant rapidly generates a large amount of hot gas. The pressure of this gas expels the projectile from the end of the cartridge and sends it down the gun barrel at high speeds towards the target. These are kinetic energy projectiles and the standard kinetic energy equations as shown in Equation 3.9 applies.

$$KE = \frac{1}{2}mv^2 \tag{3.9}$$

where *KE* represents kinetic energy, *m* is mass and *v* is velocity.

Basic parameters for ballistic penetration calculations include the following information about the projectile: mass, length, diameter, nose shape, nose length, density and striking velocity. In experimental research, deformation and fragmentation of the penetrator data are also collected to help understand the event. Damage to the projectile can be as telling as target damage in regards to how the energy was dissipated.

3.13.1 Nose shape

Shape of the projectile is significant to the mode of perforation and the ability of the target to resist penetration. Pointed penetrators allow for a piercing perforation where the target fails about the projectile axis and high stress gradients are experienced at the pointed tip. In contrast, blunt projectiles often lead to a plugging penetration where the target fails over a larger cylindrical or conical surface. While the thickness of the target still plays a large role in determining the post-impact end state, the efficiency of a sharp versus a blunt nosed projectile also influence the effects felt. Once the target is penetrated, the least deceleration is experienced by ogive-nose projectiles making them efficient in penetration and the most deceleration occurs with flat-ended projectiles such a fragment

simulating projectiles (FSP). Examples of different nose shapes are demonstrated in Figure 3-7.

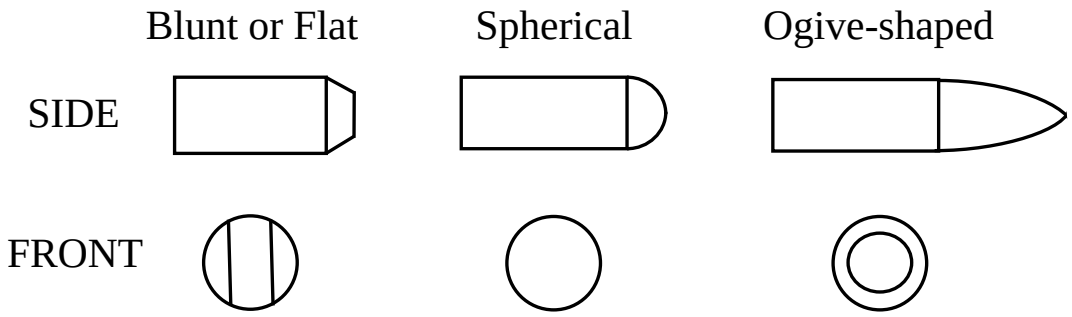

Figure 3-7. Projectile nose shape examples.

3.13.2 Obliquity of projectile

Besides nose shape, flight orientation, or how straight the projectile flies through the air, and angle of obliquity are other separate projectile parameters. For normal impacts, where the projectile's path is perpendicular to the plane of the target face, the stress state is two-dimensional [125]. When the target strikes the face at an angle other than normal there is an angle of obliquity, as shown in Figure 3-8. This situation increases the level of complexity by introducing bending stresses with the asymmetrical loading condition. As preliminary investigative ballistic testing on CLT, the scope of this research is limited to normal impacts.

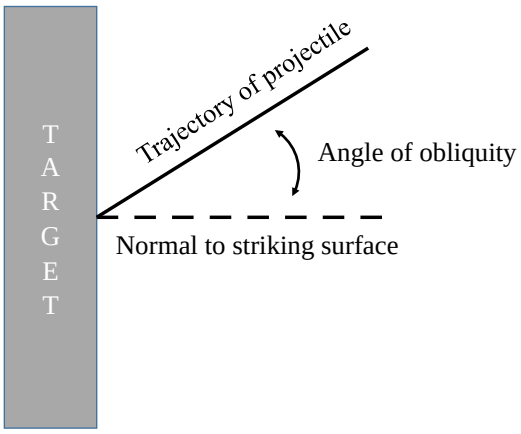

Figure 3-8. Angle of obliquity.

3.13.3 Rigid sphere impact

While studied less than long rods, the impact of rigid spheres into semi-infinite targets has been studied. Complexities arise with the sphere due to the entrance phase effect in that the small length to diameter ratio (L/D) of the projectile potentially allows more material to fill in behind it as the projectile moves through the target. Numerical simulations have shown that with sphere projectiles, target density may have an increased importance relative to penetration depth compared to long rod projectiles. Empirical relations of the penetration depth developed from simulations of a rigid sphere impacting an aluminum target indicate dependence on the strength of the target and the density ratio expressing the density of the projectile divided by the density of the target [95].

3.13.4 Cavity Expansion

High velocity impact with its cratering deformations through a target also introduces the concept of cavitation. Borrowed from fluid mechanics and hydrodynamics,

cavitation refers to the crater or channel diameter created during penetration which has a diameter larger than the penetrator itself and illustrated in Figure 3-9. This cavity expansion is believed to be one aspect of the penetration event where energy is dissipated. Typically, low velocity impacts do not develop cavitation or any expansion of the crater channel. Studies have shown cavitation occurs for all projectile nose shapes at high velocities. Multiple researchers have concluded that penetration without cavitation is associated with a constant resisting stress by the target material [61, 94, 95].

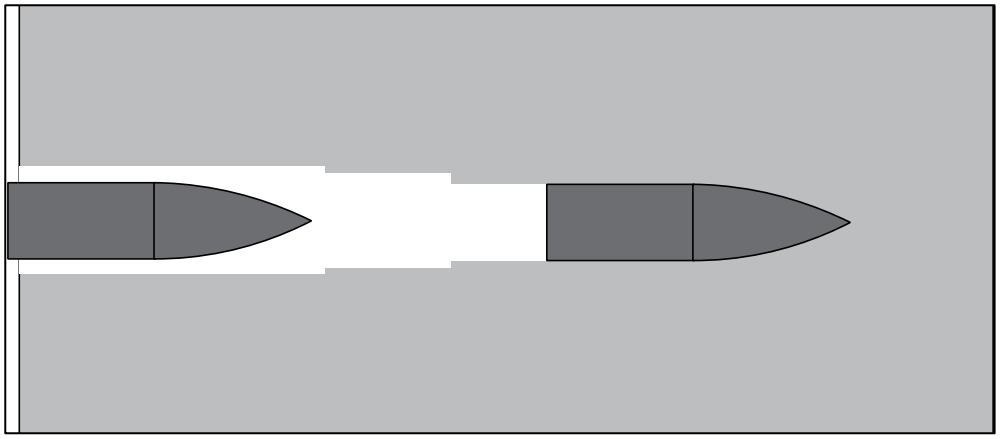

Figure 3-9. Cavitation is demonstrated by the projectile on the left.

Like most phenomena of impacts, the velocity of the projectile and the strength of the target are key factors in the presence of cavitation. Many past studies of aluminum for velocities in the range of 1,000 to 2,000 m/s (3,250 to 6,500 fps) did not witness cavitation [50]. This work lead to further simulations showing the presence of an expanded channel depends on both the target material strength and density, as well as the projectile nose

shape. Additionally, the work further showed that the deceleration of the projectile is not constant, as often assumed in analytical models. In essence, with cavitation the projectile must expend a portion of its kinetic energy on the initial penetration of the target and this creates lateral deformation in addition to the crater hole. The lateral deformations result in the crater expanding past the diameter of the projectile.

The concept of cavitation expansion is an example of how complex penetration events can be. The material response may change multiple times within the short duration of penetration due to changes in velocity and interaction between the projectile and the target. With a change in nose shape or material density, very different penetration results can be seen.

3.14 Approaches to understanding ballistic impacts

3.14.1 Empirical approaches to studying impact dynamics

Historically, empirical approaches are the most common type of analysis because of the challenges and complexity associated with ballistic testing and results. While an impact event has many variables, an empirical relation describing penetration mechanics is most useful when a small number of variables are correlated [27].

Ballistic testing is typically very resource intensive in terms of both cost and time. This makes obtaining large data sets difficult. Using the experimental data, algebraic equations are developed in terms of material properties, dimensions, and velocity, through curve fitting equations and constants. These equations may be used for predicting future iterations of experiments with the same test parameters. The constants do not provide a great understanding of the material behavior or the mechanisms at work in the impact event. Due to this, it is considered difficult and even dangerous to extrapolate beyond the

materials or test parameters used for the data set the relationship is based on. Independently, ballistic test results and empirical relationships do not provide significant insight into the penetration processes at work. That is not to say that empirical approaches are without value. Much of the seminal research on penetration mechanics was based on experimental testing and empirical relationships. Future experiments can be guided by the results and relationships observed in empirical equations fit to the data.

Models developed from experimental data often have many variables, which create so many parameters in developing a mathematical relationship that the value of such analysis may be limited. A large number of variables usually results in a complex equation and less statistical meaning than a small number of variables would allow [27]. For this reason, the design of experiments and careful attention to controllable parameters are both important.

An example of an empirical approach is found with the THOR equations. In the 1960s the Ballistic Analysis Laboratory and Ballistic Research Laboratory studied penetration for metallic and non-metallic materials and published reports with empirical equations developed from testing. The projectile in the experiments was designed to simulate fragments. Two base equations were developed with five experimental variables and five adjustable constants. These equations calculating residual velocity and residual mass can be seen in Equation 3.10 and 3.11, respectively.

$$v_r = v_s - 10^{c1}(hA)^{c2} m_s^{c3} (\sec\theta)^{c4} v_s^{c5} \tag{3.10}$$

$$m_r = m_s - 10^{d1}(hA)^{d2} m_s^{d3} (\sec\theta)^{d4} v_s^{d5} \tag{3.11}$$

Where v_r represents fragment residual velocity, v_s fragment striking velocity (fps), h target thickness, A average impact area of fragment, θ angle of obliquity, m_s weight of the original fragment (grains), and m_r weight of residual fragment, or largest piece to perforate.

The THOR equations were fit to a data set for blunt-nosed steel cylinder projectiles impacting different relatively thin target plate materials and the constants were determined by a least squares type of best fit. Each material tested yielded a separate set of constants for the equation. The form of the equation was set to be simple and practical while including all the important parameters. An additional benefit of the exponential form was the ability to convert it into logarithmic form. This was seen as an advantage because of the linearity achieved in this form [2].

3.14.2 Analytical approaches to studying impact dynamics

Analytical approaches started to develop during World War II based on physical considerations with identifying the force of the projectile during penetration and using that value in the equation of motion [95]. Analytical models aimed to simplify the complicated problem without sacrificing the laws of physics and could be compared to systematically conducted experiments designed with limited parameters [95]. Analytical models provide correlations like empirical models but the models are based on a foundation of physical science and not adding correlating variables and parameters to best fit the data of a specific experiment. Often analytical approaches require restrictive assumptions such as rigidity of the projectile, ideal plastic behavior of the target, and specific modes of target deformation in order to keep the problem as simple as possible. Analytical models typically experience the same limitations as empirical equations in that recalibration is required if the variable of the penetration problems are different.

An example of an analytic approach in terms of Newton's law for deep penetration of rigid long rods is outlined in Rosenberg and Dekel's Terminal Ballistics text [95]. A retarding force, *F*, is defined as the force the target creates on the projectile. This force is assumed to be constant in the process, as is the deceleration rate of the projectile. The resistive force equation is shown in Equation 3.12 and the normalized penetration depth, P/L_{eff} based on the transformation of that initial force equation in Equation 3.13:

$$F = ma = \rho_p L_{eff} \pi r^2 a = const = \pi R_t \tag{3.12}$$

$$\frac{P}{L_{eff}} = \frac{\rho_p V_0^2}{2R_t} \tag{3.13}$$

Where *F* is the resistive force required by the target material to prevent penetration, *m* is the mass of the long rod penetrator, *r* is the radius of the penetrator used to calculate the cross-sectional area, L_{eff} is the effective length of the penetrator, *a* is the acceleration or deceleration in this case, v_0 is striking velocity, and R_t is the resisting stress of the target. In this model, the penetration depth is not dependent on the target density, just the strength of the target in terms of a resisting stress value. The shape of the projectile's nose is also not a factor in this model. The assumptions made and exclusions of known factors involved in the penetration process show that while science-based, an analytical model has its limitations due to its simplifications.

Some analytical models are based on energy balance and conservation of momentum equations but they also require assumptions and limitations to simplify the circumstances and make the model solvable. Recht and Ipson developed analytical equations based on the work required by the projectile to eject a material plug from the target [91]. Analytical models tend to ignore entrance phase effects and cavitation effects,

and require a target's resistive strength or other material characteristics, which are specific to the target-penetrator combination of the test scenario. Like empirical models, the analytical models are only applicable to a narrow set of defined parameters without recalibration.

3.14.3 Numerical approaches to studying impact dynamics

Numerical models are becoming more common in the field as computers and finite element techniques develop. The challenge with numerical models lies in the necessity for accurate material models to feed into the simulation. Without robust material characteristic data, including elastic, plastic and hydrodynamic regimes of behavior, such as dynamic characteristics and strengths over a wide range of high strain rates, the numerical outputs will be flawed or inapplicable.

Computer codes called hydrocodes can perform numerical simulations of high velocity impact events. These computer models can run rapid simulations, changing only one variable at a time while maintaining all other variables, which helps determine the influence and dependence of the problem on that variable. However, the hydrocodes depend on the input of equations of state and constitutive relations for the materials involved. Errors in the material characterization are more common in numerical approaches than an error in the numerical method [95].

3.15 Summary

Penetration mechanics is a complex field with many factors influencing the scenario, often factors unable to be controlled in experimentation. Experimental testing and empirical equations best fit to that data are prevalent due to challenges with associating unlimited analytical models, and requirements for dynamic strength characteristic required

with numerical solutions. With each velocity regime, projectile nose shape, target material and target thickness, different variables and equations influence the solution.

This research is limited to small-arms projectiles and a 1/2-inch sphere penetrator with the intent of investigating the material response and penetration resistance of CLT. As a composite material with multiple plies adhered together and alternating the strong axes direction, its response to a ballistic event is of interest. The propagation of the shock waves of such an impulsive load may be interrupted, or at least influenced, by the anisotropy and inhomogeneity of the material as has been seen in composites [85].

CHAPTER 4
WOOD PROPERTIES AND THEIR LIKELY ROLES IN BALLISTIC PENETRATION AND BLAST PERFORMANCE

The purpose of this chapter is to discuss specific wood properties within the context of how the material's performance with respect to ballistic penetration and blast loading response is influenced in a composite panel. This chapter presents a background on wood properties; the historic use of wood against impact threats; development, fabrication, and testing of Southern Yellow Pine CLT; wood hardness testing of CLT panels; shear behavior in wood, CLT panels, and the shear analogy method for composite panels; and the behavior of wood at high strain rates.

4.1 Background on wood properties

Wood is a natural material with higher variability and a more complex microstructure than most man-made structural materials. One highly relevant property of wood is its anisotropic nature. The material has different properties in different directions relative to the direction of tree growth. The highest structural properties are aligned with the longitudinal axis of the tree. At the micro-scale, sawn wood timber is described as having longitudinal, radial and tangential properties, coinciding with the growth direction of the tree. For sawn timber, it is generally too difficult to assess the difference between properties in the radial and tangential directions. Instead, these properties are homogenized in the test data and the properties of the wood are given in the longitudinal and transverse directions. The wood is therefore treated as transversely isotropic, where the first principle stress direction corresponds to the material properties of the growth direction of the tree and the second and third principle stress directions are considered to have equal material

properties but different than that of the first principal stress. The directional properties of wood are exploited in CLT because the orthogonal orientation of the alternating layers changes the overall strength and stiffness of the panel.

In addition, wood exhibits high variability between species and between wood lots of the same species. The variations in wood are even greater due to the presence of defects like knots or checking, as well as dimensional instabilities like cupping or warping. These variations are important to note in the context of experimental characterization of the material and its structural properties. The nature of wood and its flaws provide a partial explanation for variability in test results and tend to raise the number of required tests to achieve reliable characteristic values of engineering properties. Average coefficients of variation for wood products are shown in Table 4-1.

Comparatively, coefficients of variation for the in-place strength of concrete due to batch variation are estimated as 10 percent for cast-in-place construction and 6 percent for precast construction [28]. Typical coefficients of variation for the yield strength of steel range from 3 to 11 percent, and 6 to 10 percent for high strength steel, while the average coefficient of variation for the modulus of elasticity of steel is under 2 percent [60].

At the microscopic level, wood is comprised of wood cells that are elongated and oriented in the longitudinal direction. At this scale, the wood material itself is basically a laminate composition of the individual wood cells. Differences in the proportion and nature of the cellulose, lignin, and hemicelluloses contained within the cellular structure of wood determine the properties of the wood. Hardwoods, which may be softer than some softwoods, have vessel elements or a wood cell with open ends forming a tube for the

transport of water or sap within the tree. In contrast, softwoods have a simpler cell structure and do not have vessels. As a result, they are considered nonporous. [96]. The key physical and mechanical properties, such as density, hardness, flexural modulus, and strength, for a given wood species are directly related to the cells that make up the wood.

Table 4-1. Average coefficients of variation for some mechanical properties of clear wood, adapted from [96].

Property	**Coefficient of Variation* (%)**
Static bending	
Modulus of rupture	16
Modulus of elasticity	22
Work to maximum load	34
Impact bending	25
Compression parallel to grain	18
Compression perpendicular to grain	28
Shear parallel to grain, maximum shearing strength	14
Tension parallel to grain	25
Side Hardness	20
Toughness	34
Specific gravity	10

*Values based on results of tests of green wood from approximately 50 species. Values for wood adjusted to 12% moisture content may be assumed to be approximately of the same magnitude.

The cellular structure of wood enables the material to absorb the energy of an impact and deform locally without brittle failure. For instance, a nail can be driven into a piece of wood whereas most plastics, glass and even some concrete would crack or experience damage under such an impact. The following key properties are thought to influence the ballistic performance of wood: compressive strength; shear strength; density; bulk shear modulus; and the modulus of elasticity [69, 111, 121]. Additionally, the Hugoniot elastic limit – the yield stress under uniaxial dynamic loading – is of interest to the material's ballistic performance [69, 93]. For many wood species, these properties are well known and therefore have been drawn from the literature. A number of key properties were investigated in the context of the production and behavior of CLT and are discussed in the following sections. Discussion of hardness and shear strength is based on experimental testing while other properties are presented as unique aspects of CLT which warrant further investigation and research.

Wood is one of the oldest construction materials. In current practice, wood is viewed as limited in strength and stiffness compared to steel and concrete, as evidenced by code restrictions on multi-story wood construction. However, engineered wood products and in particular mass timber products like CLT are challenging this view and encouraging a re-evaluation of wood products for use where design specifications would previously have eliminated wood as a potential material. As a renewable material with a high strength-to-weight ratio, wood holds many attractive qualities. Compared to other lightweight materials, wood has shown interesting capacity in terms of energy absorption [123]. Despite historical use of timber in protective structures, research on the capacity of CLT for energy absorption is just beginning.

4.2 Historic use of wood against impact threats

Throughout history, there are examples of wood used to counter high impact threats. One example is the USS Constitution shown in Figure 4-1. The ship is a wooden-hulled, three mast frigate built for the U.S. Navy and commissioned into service in 1797. The ship was used for 58 years of active Navy service that included battle engagements with the French in the Barbary Wars and with Britain in the War of 1812. It is credited with 33 battle victories and no losses. While the armament and skill of the ship's captains and crew were huge contributors to the ship's winning record, historic records document stories of British iron cannonballs bouncing off the 25-inch oak hull, earning the nickname Old Ironsides despite (or maybe because of) its wooden hull [65].

Figure 4-1. USS Constitution docked in Boston Harbor, May 2014 (author photo).

Almost 150 years after the wooden hull of the USS Constitution defeated iron cannonballs, wood was again being used in warfare. The Japanese forces employed wood to construct their fighting positions and defenses in the Pacific theater during World War II. Readily available on most islands, coconut logs were found to be extremely resilient to projectile impacts thanks to their soft and fibrous interior, which also reduced splintering. Some native hardwood species, such as ironwood, were also used for the construction of bunkers.

Roofs for fighting positions designed to protect from artillery and bombs were often made from logs laid in solid layers with perpendicular alternating layers. This layered wooden roof was commonly two to three layers of 4- to 18-inch diameter logs but as many as six layers have been documented in some bunkers [97]. The Japanese even added enhancing layers such as rocks to deform or deflect projectiles and promote early detonation of explosive charges. In some cases, U.S. artillery were unable to completely penetrate such structures [97].

More current applications of wood against impact loads include composite panels being developed by researchers at the University of Maine's Advanced Wood Engineering Composites Center for the U.S. Army Corps of Engineers. Based around a wood core, a lightweight composite panel with fibers and resin has been developed to fit inside tents and provide increased protection from projectiles and blast. By employing techniques such as use of fiberglass reinforced plastic (FRP) materials, and blast-resistance coatings, researchers work to capitalize on the high strength-to-weight ratio of wood by combining it with other materials known for tensile reinforcement and impact resistance [24]. One Dutch manufacturer, Lignostone, makes a composite for the military using compressed

beechwood and aramid, glass epoxy or carbon [24]. Other researchers, like those at the University of Maryland have focused on increasing the strength of wood by compressing and heating the wood lignin, which then exhibits improved ballistic resistance to natural wood [59].

4.3 Southern Yellow Pine CLT: Small-scale production

In the interest of examining multiple wood types and their properties with respect to ballistic and blast performance, a small-scale production process was developed for this research. This allowed for investigation of two different classifications of CLT with different physical properties. A portion of the work focused on the production of Southern Yellow Pine CLT because in order to be considered as a viable material for use in temporary military structures, it needs to be more widely produced beyond Canada and the Pacific Northwest region. Using local and different sources of timber increases the availability of CLT for employment. Additionally, a greater understanding of the composite panels was gained through the production process, and this contributed to the concept of developing the enhanced CLT prototypes discussed in Chapter 7.

4.3.1 Current CLT manufacturing

Current North American manufacturers produce CLT made from softwood species native to their location. A common wood species used in the manufacture of CLT is Spruce-Pine-Fir (SPF), which grows abundantly in the northern U.S. as well as Canada. Specific tree types that fall within that species classification include Balsam Fir, Red Pine, Red Spruce, Black Spruce and Lodgepole Pine. SPF wood is commonly used for dimensionally sawn lumber. Located in Montana, SmartLam manufactures CLT from both SPF harvested in Canada and Spruce-Pine-Fir (South) (SPF-S) harvested locally in

Montana. SPF-S is a species of softwood very similar to SPF but with minor differences in the specific types of trees included or excluded. SPF is distinct from SPF-S in that the wood source is exclusively Canadian in origin. Nordic Structures, a Canadian manufacturer, also uses Spruce-Pine-Fir species for their E1 graded CLT product, X-Lam.

Another category of wood species used extensively in lightweight wood frame construction is Southern Yellow Pine. To date, there is not a manufacturer who produces and sells a CLT product made from Southern Yellow Pine. Researchers and manufacturers alike have expressed interest in the wood species because it is widely available in the Southeastern U.S [58, 62, 79]. It is commonly used as sawn timber but is also used to manufacture the engineered wood product of glulam. The species is known for strength, fastener-holding ability and long, clear spans. It is also easy to treat for weather and insect resistance, making it a good option for outdoor applications such as decks.

By using wood species grown locally for construction, transportation costs and associated transportation related environmental impacts are reduced. This applies to both sawn timber as well as engineered wood products. To implement CLT construction in the southern and eastern United States, manufacturers must ship the heavy CLT panels across the country from the Pacific Northwest or import them via ship from Europe. Due to the variability in parameters and characteristics between wood species further research and testing are required establish the manufacturing parameters for producing Southern Pine CLT. However, a CLT grade classification already exists in the Standard for Performance-Rated CLT (PRG 320) for a Southern Pine lumber.

4.3.2 Small-scale CLT production

As part of this research, small-scale specimens of CLT made from Southern Yellow Pine were produced in the Digital Fabrication Laboratory (DFL) at the Georgia Institute of Technology using commercially available 2x8 sawn lumber (actual size 1.5-inches by 7.25-inches). The classification of the sawn lumber was No. 2 Prime, which is a higher classification than required for the performance-rated V3 CLT specified by PRG 320. Grading rules for V3 CLT allow for No. 3 Southern Pine lumber in all transverse layers. However, No. 2 Prime was used for all layers as No. 3 was not readily available. Though the intent was to produce Southern Pine CLT according to the standard, it should be noted that there is potential for use and further investigation with lower grades of Southern Pine sawn lumber.

By PRG 320, the requirement for CLT adhesives is to meet *American Institute of Timber Construction (AITC) 405, Standard for Adhesives for Use in Structural Glued Laminated Timber* with small modifications [4]. The modifications include the adhesives be evaluated for heat performance based on the standard for structural plywood which focuses on delamination of the bonded layers after exposure to extreme heat from a flame. Additionally, PRG 320 excludes the requirement for exterior wet use wood adhesives since CLT is not designed for exterior exposure under typical conditions.

CLT can be made with the same adhesives used in other engineered wood products. These adhesives typically consist of polyurethane, melamine, or phenolic-based adhesives that meet the AITC 405 requirements. For this research, a single-part, moisture cure, polyurethane adhesive was used to fabricate Southern Pine test specimens. The availability and applicability of the polyurethane glue for adhering wood together made it the first

choice for initial experimentation and is consistent with current manufacturing processes. SmartLam used a polyurethane adhesive product for their manufactured CLT panels [110].

CLT manufacturing, according to the CLT Handbook, consists of the following steps:

1. Lumber Selection
2. Lumber Grouping
3. Lumber Planing
4. Cut to length
5. Apply adhesive
6. Panel lay-up
7. Assembly pressing
8. On-line quality control, machining and cutting
9. Product marking, packaging and shipping

For selection and grouping, the moisture content was checked with a pin resistance moisture meter and each lamination piece was weighed in order to minimize variation in moisture content and density within layers. Pieces with similar density were more likely to have the same engineering properties, which is required of major and minor strength directions [68] and recommended by the adhesive manufacturer. Prior to gluing and pressing, the 2-inch by 8-inch lumber was planed to 7-in. wide and trimmed to 14-in. long to fit the size limitations of the small hydraulic press. These dimensions remained within the recommended maximum lamination thickness to width ratio of 3.5. Planing the lumber activates the wood surface to improve gluing effectiveness. As recommended, the wood was planed within two hours of adhesive application. This allows for a reduction in surface oxidation, surface ageing, and dimensional instability, preparing the wood for a more effective bond [68]. By running the lumber through the planer, any superficial defects from the handling and transport of the lumber were removed as well. It should be noted that

early experiments with Southern Pine timber showed that wood laminations made with lumber planed the day before pressing were not as consistent as those that were made from wood that was planed and pressed on the same day. The pieces of cut lumber were then set in the desired lay-up with the orthogonally oriented layers as shown in Figure 4-2.

Based on the technical specifications of the adhesive, existing guidance from the CLT Handbook, and existing literature on CLT, the initial specimens were face glued, but not intentionally edge glued. The process did allow some glue to migrate between the individual pieces' narrow faces. This was unavoidable and is likely to happen to some extent in large scale production as well. Currently, North American produced CLT does not require edge gluing. Concerns related to interlaminar stresses (rolling shear) are instead addressed in PRG 320 by dimensional guidelines related to individual timber widths and thicknesses. The polyurethane adhesive was moisture activated, and so the individual pieces were dampened with a wet cloth before the glue was applied.

The adhesive was applied in thin ribbons parallel to the grain direction and spread evenly across the surface with a scraper and each successive layer was stacked as soon as the glue was spread. An average of 29.3 grams of adhesive per square foot of lumber was used. The 14-inch by 14-inch (36 cm by 36 cm) specimen block was held in place laterally by two plastic corner braces and ratchet strips as the expanding adhesive caused the pieces to push out and create undesirable gaps between the pieces in a single layer. The braces and straps were not intended to apply a specific clamping pressure but to hold the small pieces in place horizontally.

Figure 4-2. Cut lumber pieces laid out for CLT specimen production.

Layers, or plies, were added to reach the desired number and then the specimen was pressed using a small hydraulic press, applying up to 100 psi for a period of two hours. Figure 4-3 shows the press and lateral bracing techniques used to fabricate the CLT. In most cases two or three CLT specimens were produced at one time by using a bond breaker between the non-glued plies. Common pressures for CLT manufacturing ranged from 85 to 115 psi in the literature [32, 33, 103]. The adhesive specifications call for a clamping pressure in the range of 14 to 100 psi for a duration of one to two hours. For the test specimens the clamping pressure remained constant for two hours before the specimen was removed. After removal from the press, excess adhesive was cleaned off the edges and the specimen were trimmed to a standard 12-inch by 12-inch (30.5 cm by 30.5 cm) size.

Figure 4-3. Two specimens, one 3-ply and one 5-ply, of Southern Yellow Pine CLT in the hydraulic press set-up at the Georgia Institute of Technology's Digital Fabrication Lab.

4.3.3. Shear block testing for bond line adhesion

In order to verify adequate bond line adhesion, shear block samples were cut from the blocks of Southern Yellow Pine CLT. Additional shear blocks were also extracted from pieces of SmartLam V4, 3-ply CLT. The blocks were tested by the process outlined in *ASTM D905, Standard Test Method for Strength Properties of Adhesive Bonds in Shear by Compression Loading*, in the apparatus shown in Figure 4-4 [18]. The test provides an estimate of bond line adhesion for CLT, however, the test cannot be assumed to measure the true shear strength of the bond for many reasons. The factors include the strength of wood tested, the non-standard shearing tool, and the rate of loading used. Additionally, the specimen could not be sized exactly as outlined in the ASTM D905 standard due to the

size limitations of the CLT being tested. However, the test method is deemed suitable for product research and development per the standard [18]. The primary interest here was to identify if the shear block specimens failed due to adhesive failure or wood failure and thus determine if the Southern Yellow Pine CLT manufacturing process achieved satisfactory bond lines.

Figure 4-4. Shearing tool for bond line testing per ASTM D905.

ASTM 905-08, Standard Test Method for Strength Properties of Adhesive Bonds in Shear by Compression Loading calls for the loading on the blocks to occur parallel to the grain, however, with cross-laminated specimens of CLT, there is typically one lamella parallel and one lamella perpendicular [18]. Because of this, the shear block specimens were tested with both orientations in the set-up. In some specimens the shorter side of the

block was oriented parallel to the compressive load and in other cases, the shorter side consisted of a wood section with the grain direction oriented perpendicular to the compressive loading. Figure 4-5 shows an example of both perpendicular and parallel classified specimens for the shear tests. The configuration shown in Figure 4-6 is described as the *perpendicular* direction in the discussion that follows.

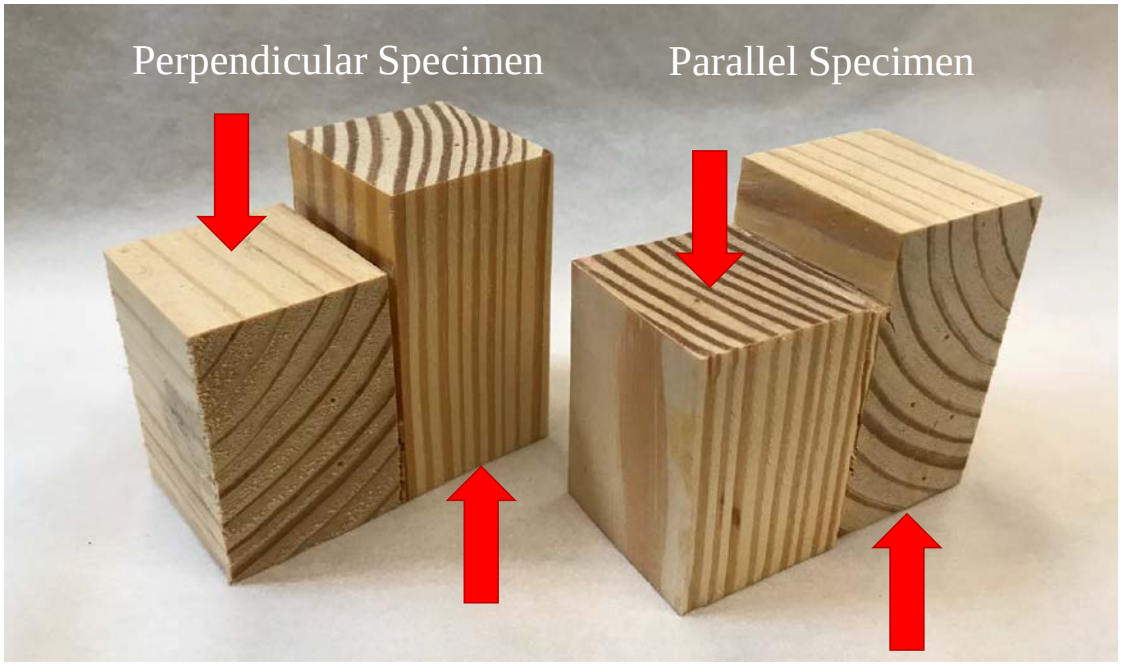

Figure 4-5. The two types of shear block specimens with respect to grain orientation of the shorter side relative to the applied load represented by the red arrows.

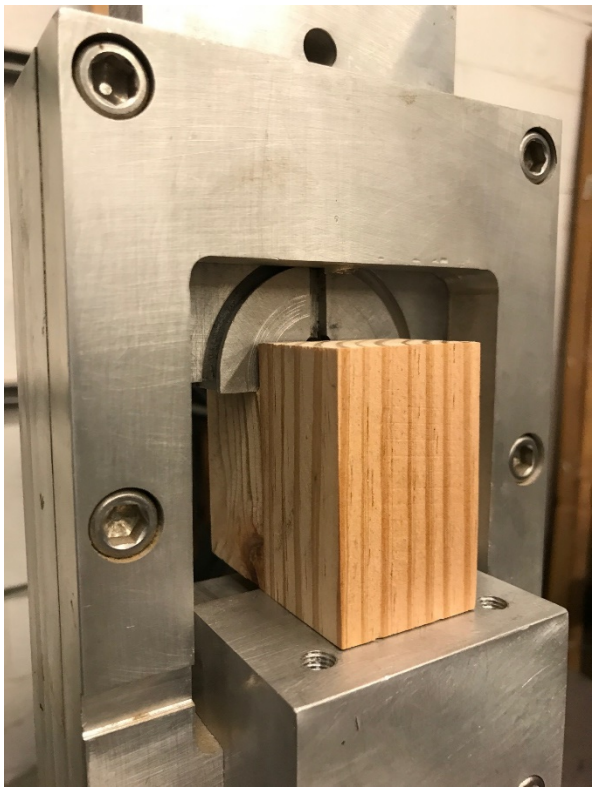

Figure 4-6. Shearing tool loaded with a bonded block of wood. The short section is oriented with the grain direction perpendicular to the compressive force in this specimen.

The specimens were carefully loaded to ensure that the bond line aligned with the shearing sections of the tool. The specimens were loaded using displacement control with a loading rate of 0.20-inches per minute. The shear tool was loaded in compression with a servo-controlled hydraulic pump and an actuator controlled by an MTS Flextest SE controller. Once the measured load on the specimen dropped and the specimen was no longer supporting an increasing compressive load, the test was concluded. Occasionally, the load would drop only slightly or stay almost constant while still showing an increasing measurement of displacement. These loads were closely observed but the test was not stopped until a drop of 50-lbf compressive force from the peak was detected.

Upon conclusion of the test, each specimen was examined to determine the percentage of wood failure versus adhesive failure along the bond line. Some specimens exhibited a combination of wood and adhesive failure. Figure 4-7 shows an example of such a failure in shear block test specimen, T11. In this test, the wood failure was assessed as 75 percent. T11 is a *parallel* specimen by the classification type used in Table 4-2. Since the majority of the failure in the fabricated Southern Pine specimens greater wood failure, it was determined that the small-scale manufacturing process was sufficient to achieve good CLT bond lines.

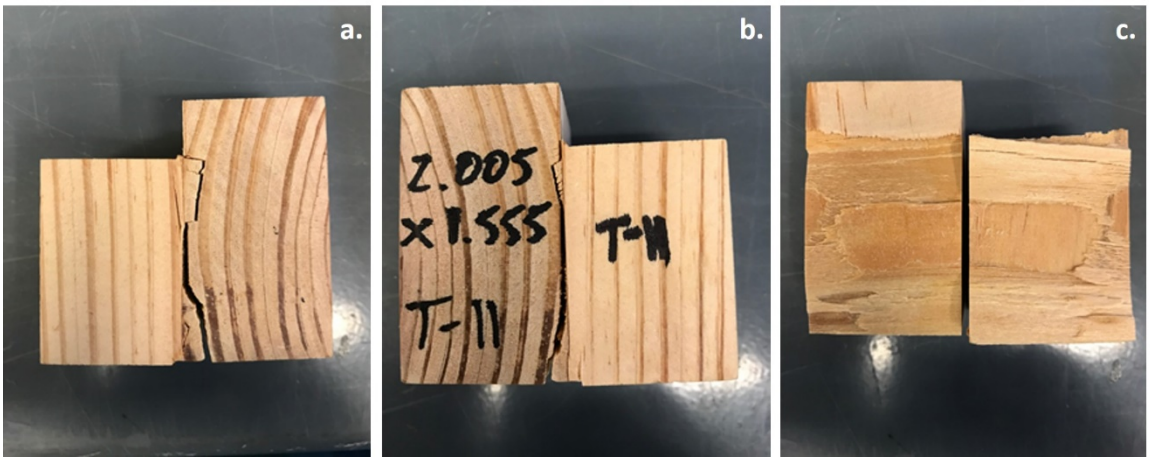

Figure 4-7. A representative shear block test specimen post-test (a.) wood failure shown across the growth ring beyond the adhesive bond line from one side perspective, (b.) wood failure occurring along the growth ring from the opposite side, (c.) a combination of wood and adhesive failure shown from interface of two pieces, assessed as 75 percent wood failure.

The results of the shear block testing are shown in Table 4-2. Table 4-2 shows the average shear stress calculated from the shear block testing by specimen type: SYP CLT is from locally fabricated Southern Yellow Pine CLT and SPF-S CLT is the

SmartLam commercially manufactured CLT. Although the test standard cautions against assuming it measures the true shear strength of the bond, the standard states it may be informative for research and development purposes. According to ASTM D905, the coefficient of variation of shear strength parallel to the grain is 14% for a given species.

Table 4-2. Comparison of average shear stress achieved through shear block testing and coefficients of variations for two types of CLT.

Specimen type	Average Shear stress (psi)	Coefficient of Variation (CoV)	N (# of samples)
SYP CLT (all)	**729.7**	**30%**	**14**
perpendicular	579.9	26%	7
parallel	879.6	19%	7
SPF-S CLT (all)	**341.7**	**29%**	**11**
perpendicular	294.5	9%	6
parallel	398.4	32%	5

The shear block testing showed that the lab-produced Southern Yellow Pine CLT achieved an average shear stress almost twice that of the SPF-S manufactured products with similar coefficients of variation. For the Southern Pine CLT, there also appeared to be a difference in shear strength depending on the orientation of the grain in the shorter block of the specimen. This difference was not as obvious for the SPF-S specimen.

4.3.4 Shear block testing with non-wood layers

Shear block testing was also conducted with wood specimens fabricated with layers of E-glass fabric and with a 0.25-in. thick steel plate in preparation for production of

enhanced CLT specimens (see Chapter 7). The steel was sandblasted in preparation for adhering to the wood. Two weights of E-glass fabric and a woven roving were selected, to assess the efficacy of bonding as a function of fiber thickness. Trialed fabrics included: (1) a light weight (10 ounces per square yard) plain weave E-glass fabric; (2) a heavy weight (26 ounces per square yard unidirectional fabric); and (3) an 18 ounces per square yard woven roving fiberglass fabric. Samples of each of these fabrics are shown in Figure 4-8. The woven roving layup used four plies of the fiberglass fabric. The light and heavy weight e-glass fabrics layups used one ply of fabric, which had been saturated in the epoxy resin-hardener mixture and then sandwiched between the cross-oriented wood. The epoxy used for all four specimens was a West System resin and hardening system. It served as the saturating resin for the dry fiber fabrics and as the adhesive. The clamping pressure was greatly reduced from the traditional CLT production methods using polyurethane adhesive based on the recommendations of the epoxy manufacturer. Additionally, baseline traditional CLT specimens were fabricated with epoxy in lieu of polyurethane for comparison purposes.

The intent behind this series of tests was to compare the bond strengths of an epoxy adhesive to the polyurethane adhesive as well as the relative bond strength between the wood and non-wood layers. It should be noted that the polyurethane adhesive used for bonding wood to wood is not suitable for bonding wood to fiberglass fabric or wood to steel. The test results from these specimens are tabulated in Table 4-3. Similar to the first test of bonded shear block tests, several of the specimens were set-up with the loaded side of the specimen aligned with the wood grain perpendicular to the compressive load. This particular set-up appears to yield smaller values of shear stress and likely indicates a bias

in the test set-up. Based on this testing, it is recommended that a so-called “parallel” specimen be used for all future testing.

10 oz/sq yd Plain Weave fabric | 26 oz/sq yd Unidirectional fabric | 18 oz/sq yd Woven Roving

Figure 4-8. Fabrics materials trialed in shear block tests to verify adhesive bond strength between components.

The shear stresses observed in these tests are generally lower than the average SYP CLT test results from the all-wood specimens. The fabric-based specimens exhibited predominantly wood failure over adhesive failure while the steel specimens exhibited adhesive failures. Figure 4-9 shows examples of the four types of shear specimens. A high value of shear stress was achieved with the SYP-woven roving specimen type. The other fabric specimen trials may have lower shear strengths due to a smaller volume of epoxy used; these pieces were trial iterations to refine production techniques. The steel also yielded lower bond stresses, which may demonstrate the challenge of bonding these materials with this method.

Table 4-3. Average shear stresses achieved through shear block testing for epoxy and non-wood layers.

Specimen type	Average shear stress (psi)	Coefficient of Variation (COV)	N (# of samples)
SYP - epoxy	**423.0**	**42%**	**8**
perpendicular	277.2	42%	4
parallel	568.8	8%	4
SYP- heavy fabric	**688.7**	**50%**	**7**
perpendicular	440.8	22%	4
parallel	1019.2	22%	3
SYP- light fabric	**532.5**	**32%**	**7**
perpendicular	380.3	22%	3
parallel	646.6	16%	4
SYP - stainless steel	**500.5**	**44%**	**6**
perpendicular	148.4	-	1
parallel	571.0	27%	5
SYP- woven roving (all parallel)	**1329.7**	**18%**	**10**

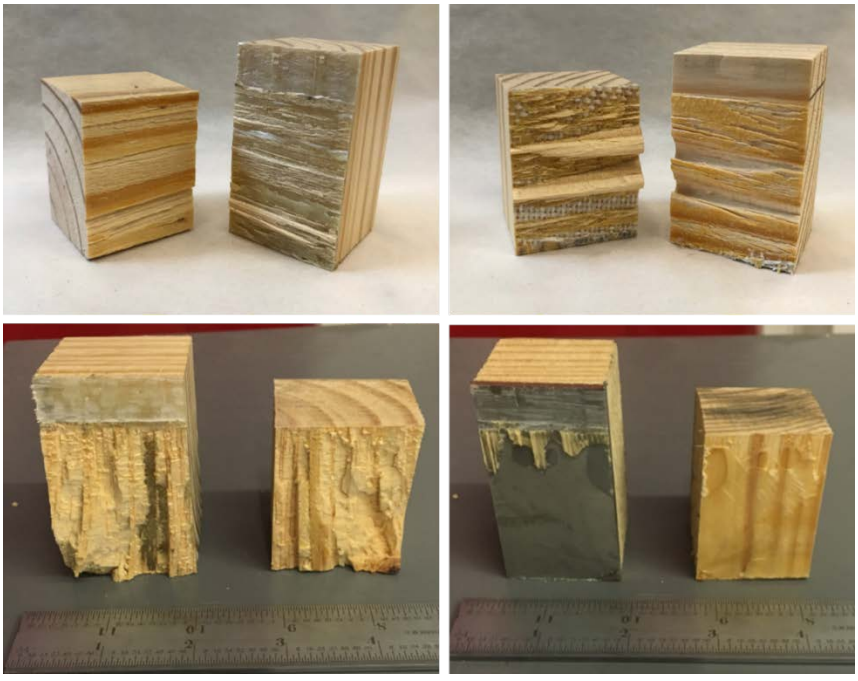

Figure 4-9. Shear block testing of enhanced specimens, (upper left) Unidirectional fabric, (upper right) Plain Weave fabric, (lower left) Woven Roving, (lower right) steel.

4.4 Wood Hardness

Wood hardness is an important material property in predicting the ballistic response of CLT. The variable is used in the existing UFC guidelines for calculating the thickness of wood required to prevent perforation during a ballistic impact, discussed more in Chapter 5. The design guide provides a handful of reference values for general use in the equation. These given values do not correspond with commonly accepted wood hardness values from the U.S. Forest Service Wood Handbook, indicating that the UFC may use a different hardness scale, although the actual scale used is not specified. The inclusion of the characteristic in the calculation indicates that the ballistic penetration of wood is, at a minimum, empirically related to hardness.

4.4.1 Hardness, the material property

In this context, wood hardness is not a reference to the classification of a hardwood or softwood tree. Rather, hardness is a physical property indicative of a material's resistance to local deformation or penetration, typically measured by indentation, that is caused by the application of loading over a relatively small area. Wood hardness can be defined as the resistance to indentation by a harder material. Hardness is commonly associated with wood flooring as it is an important property for consideration as durable and resilient wood products are desirable characteristics for flooring.

Metals, plastics, and rubbers are often also rated in terms of hardness, and so several different scales of hardness exist. A few common scales and test methods for hardness include Rockwell, Vickers, Brinell and Knoop. The general process for testing uses a small indenter, sometimes spherical in shape, which is pressed into the specimen to a specified load or indentation. The hardness value is often based on the measured applied load, or it

may include calculations that take into account other variables such as indenter and indentation geometry. Hardness may also be reported as an empirical measure, without units, accompanied by nomenclature representing the test method. Examples include HB for Brinell hardness numbers, HV for Vickers hardness values, and HRA for Rockwell Scale A.

For wood, a common test for hardness is the Janka hardness test [6]. Like other hardness test procedures, the Janka hardness test measures the force required to embed a 0.444-inch (11.28-mm) diameter steel ball halfway into the wood. Janka hardness values are reported in force units and are based on an average for the wood species. The test is destructive in the sense that it leaves deformations in the tested surface, typically undesirable for finished wood products. Brinell testing has also been used to measure wood hardness, and like the Janka hardness test is based on a steel ball indenting the wood specimen surface. Whereas the Janka test measures the applied load required to indent the wood to a specified depth (half the diameter of the steel ball), the Brinell test measures the depth of the indentation for a specified force. Measuring the depth of indentation can be difficult to accurately ascertain. In the Janka test, a ball diameter of 0.444 in. was selected so that the area loaded at full indentation is exactly 100 mm^2. Janka has been the ASTM accepted standard for solid wood since 1922 [56].

Dynamic hardness test methods are less commonly used for wood, although a 2011 study explored the use of a drop weight test with wood specimens [84]. Much like the static tests, the dynamic methodology found that dynamic hardness increased with density. Furthermore, the radial and tangential hardness did not differ significantly in dynamic tests. Longitudinal hardness was found to be approximately 1.5 times higher than transverse

hardness, which is a smaller difference than observed in static testing. Therefore, researchers have concluded that the dynamic hardness test method was less sensitive to the direction of wood orientation than in comparable static tests [84].

According to *ASTM D143-14, Standard Test Methods for Small Clear Specimens of Timber*, the specimen size for hardness testing should be 2-inches by 2-inches by 6-inches [5]. The hardness value recorded is the applied load when the sphere has penetrated half of its diameter. The load application rate should be 0.25-inches per minute (6 mm/min). *ASTM D1037-12, Standard Test Methods for Evaluating Properties of Wood-Base Fiber and Particle Panel Material*, also covers the procedures for determining hardness, but it uses a modified Janka test method [11]. The modification is to account for the less than 2-inch thickness of most manufactured fiber and particle panels. For these panels, the test specimen is composed of several layers bonded together to achieve the required thickness. For clear specimens, the standard calls for two penetrations on a tangential surface, two on a radial surface and one on each end. For the wood-based panel materials two penetrations are required on each of the two faces of the panel.

The Forest Products Laboratory published a report in 2006 on non-standard specimens, which examined thinner specimens such as 1.5-inch by 3.5-inch sawn lumber (2x4s) [56]. In testing 1-inch, 1.5-inch and 3-inch specimens, the study found no difference in Janka hardness values. Additionally, an historical analysis conducted in conjunction with the study found no significant difference between radial and tangential direction hardness values [56]. End hardness values, taken at the longitudinal direction, were distinctly different, however. Through experimental testing over the years, empirical relationships between hardness and other properties such as compression strength

perpendicular to grain, modulus of rupture, and ultimate compressive stress have been developed. An approximate relationship also exists between hardness and specific gravity, as shown in Equation 4.1, with coefficients listed in Table 4-4. Around the time that the Janka hardness test became the ASTM standard method for testing wood hardness, distinctive coefficients between hardwood and softwood were added.

$$H = A(Gr)^n \tag{4.1}$$

where H = Janka hardness (pounds)
Gr = specific gravity
A and n = separate coefficients for green and dry wood

Table 4-4. Coefficients for relationship between Janka hardness and specific gravity for domestic species, adapted from [56].

Species group	Moisture Content	*A*	*n*
Hardwood	Green	3,720	2.31
	12%	3,400	2.09
Softwood	Green	1,400	1.41
	12%	1,930	1.50

The thickness requirement for the test specimen was based on the theory that in thinner specimens, the hardness of the supporting surface could potentially influence the hardness measurement. This concept was explored in this research through experimental

testing of single ply SPF-S and SYP sawn lumber pieces, as well as a series of tests on both 2- and 3-ply specimens. As recommended by the Forest Products Laboratory report, the multiple ply specimens were bonded together and not just stacked.

4.4.2 Experimental hardness testing

Ten specimens per wood type were randomly selected from stock used to produce Southern Pine CLT and from parent stock of SPF-S provided by SmartLam. All specimens had been planed to approximately 1.375-inches thickness in preparation for CLT production. The SPF-S specimens were approximately 15-in. long by 5-in. wide, with three columns and seven rows of hardness measurements taken for each specimen, as shown in Figure 4-10a. The Southern Pine specimens were approximately 10-in. long and 7-in. wide with four columns and five rows of measurements per specimen as shown in Figure 4-10b. Defects, such as knots and cracks, and finger joints were not excluded from the test samples, as they would doubtless be present in a CLT produced from these materials. There were a total of 209 hardness values recorded for SPF-S, and 197 hardness values recorded for Southern Pine.

The test apparatus used to conduct the Janka hardness testing used a servo-controlled hydraulic pump and actuator controlled by an MTS Flextest SE controller and load cell. The specified 0.444-inch (11.28-mm) steel sphere was magnetically attached to the fixture and the platen raised the test specimen and aluminum block base up at the designated rate of 0.25-inches/minute. The machine program was set to apply load from the starting position to a displacement of 0.222-inches, half of the diameter of the test sphere. The test specimens had to be carefully aligned with the surface of the wood in contact with the surface of the sphere prior to starting the test. This was completed

manually by observing contact as well as monitoring the load cell reading. Figure 4-11 shows a test in progress with the sphere slightly embedded in the SPF-S wood specimen.

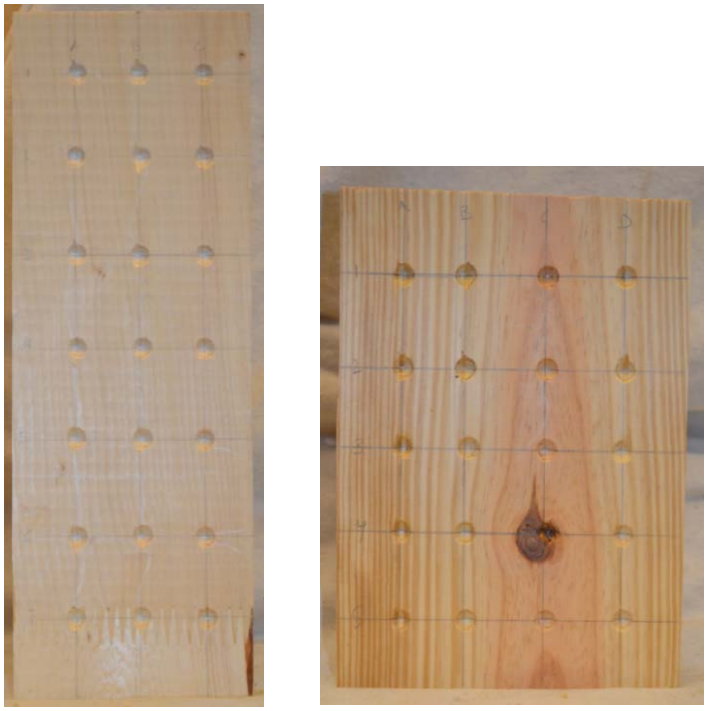

Figure 4-10. a. (left) SPF-S hardness test specimen; b. (right) SYP hardness test specimen.

In addition to the single-ply test specimens, 2-ply and 3-ply sections cut from CLT layups were also tested. The goal of the testing was to determine hardness values for each of the species used in CLT ballistic testing (see Chapter 5). Additionally, while the Forest Products Lab report indicated that thicknesses of less than 2-inches would not be skewed by the hardness of the supporting plate, there was interest in verifying if the adhesive and additional plies in a multiple-ply specimen produced a difference in measured hardness [56].

The 2-ply specimen measured approximately 3-in. thick by 12-in. long by 12-in. wide. The size of the specimen allowed for seven rows of seven columns on each side of the specimen, for a total of 98 hardness test values recorded. Both faces were tested per *ASTM D1037-12, Standard Test Methods for Evaluating Properties of Wood-Base Fiber and Particle Panel Material.* The 3-ply specimen measured 4.25-in. thick by 12-in. long and 12-in. wide. The same test layout was adopted, allowing for 98 tests on the 3-ply specimen, bringing the total number of multi-ply tests to 196. Moisture contents were recorded for all hardness test specimens.

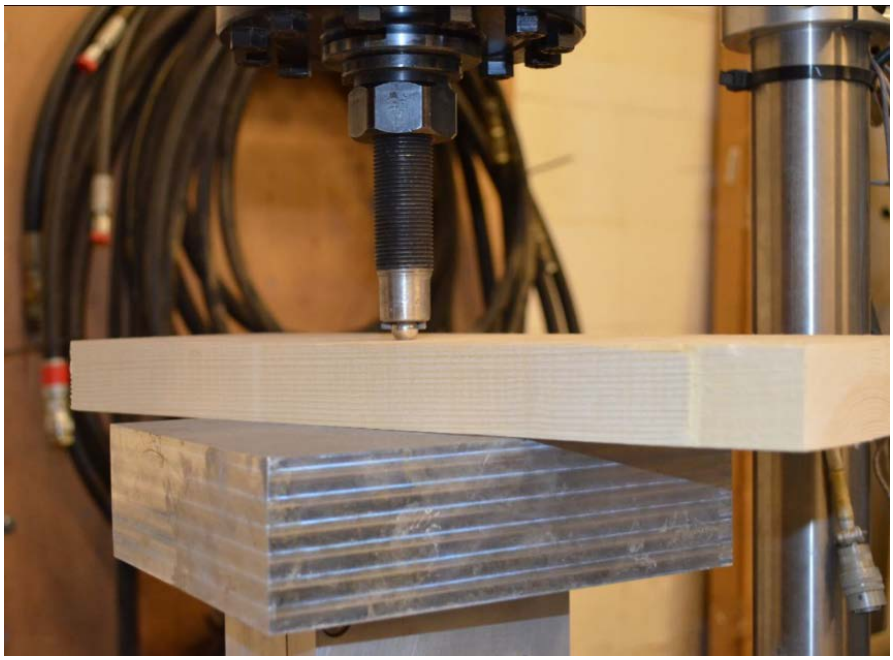

Figure 4-11. Janka hardness testing set-up with in progress test.

The average Janka hardness for the SPF-S single-ply specimens was 606.3 pounds, which was higher than expected based on the reference value [96]. The average Janka hardness for the Southern Pine single-ply specimens was 652.3 pounds, which was slightly lower than expected; Figure 4-12 shows the histogram of Southern Pine and SPF-S lumber,

normalized by the total number of specimens, with a bin size of 50 pounds. High hardness values tend to represent the presence of knots in the wood in that location or close proximity.

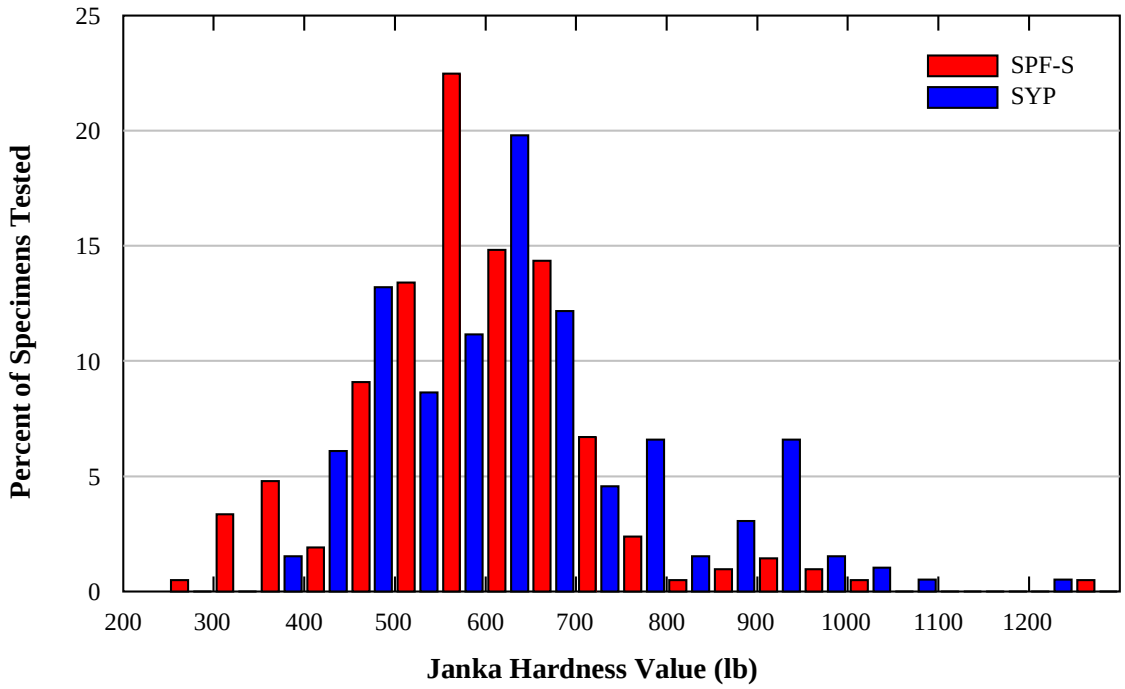

Figure 4-12. SPF-S and SYP hardness value distributions.

Table 4-5 summarizes the results of the hardness testing. The 2-ply Southern Pine specimen provided a lower mean Janka hardness value, 533.8, compared to 652.3 for the single ply. This particular 2-ply specimen also had a lower average density than that of the single ply specimen, however. The 3-ply SYP, which happened to have the lowest average density of any of the hardness specimens, produced a Janka hardness value of 612.7 pounds, which is still lower than the single ply of the same wood type but higher than that

of the 2-ply specimen. The average density values must be compared with caution as they represent the mean density of four to six boards. Individually tested boards could be more or less dense than the average. A comparison of the normal probability distribution functions for single and multiple ply SYP hardness test values is shown in Figure 4-13.

A histogram comparing the single and multiple ply Janka hardness values and their bin frequency, with a bin size of 50, is shown in Figure 4-14. The histogram and resulting probability distribution function indicate that there may be some difference between the single ply and multiple ply test specimens, with the single ply specimens showing an apparent Janka hardness greater than the 2-ply and 3-ply specimens. However, an insufficient number of tests were conducted to reach a conclusion that contradicts the findings of the Forest Product Laboratory report. Additional testing, outside the scope of this research, is needed to further examine the influence of thicker, adhesively connected specimens compared to thin single ply specimens. Nevertheless, based on these test results and the prior Forest Products Laboratory work, the hardness values for the single ply testing are acceptable for obtaining Janka hardness values.

Table 4-5. Results of Janka hardness testing.

Species	# of plies	# of tests	Mean density (pcf)	Mean Janka Hardness (lb)	Standard Deviation	Coefficient of Variation (%)
SPF-S	1	209	31.7	606.3	175.3	28.9
SYP	1	197	32.8	652.3	195.6	30.0
SYP	2	98	32.4	533.8	169.7	31.8
SYP	3	98	29.7	612.7	109.5	17.9
SYP	Multi	196	31.1	573.3	148.2	25.8

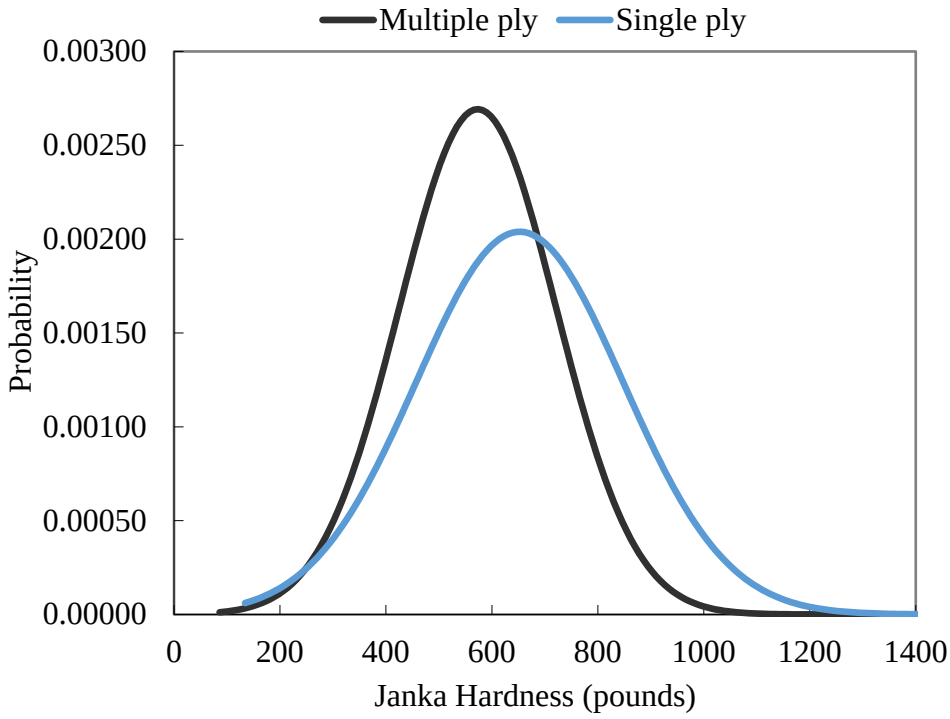

Figure 4-13. Normal probability distribution functions for single and multiple ply hardness testing of SYP.

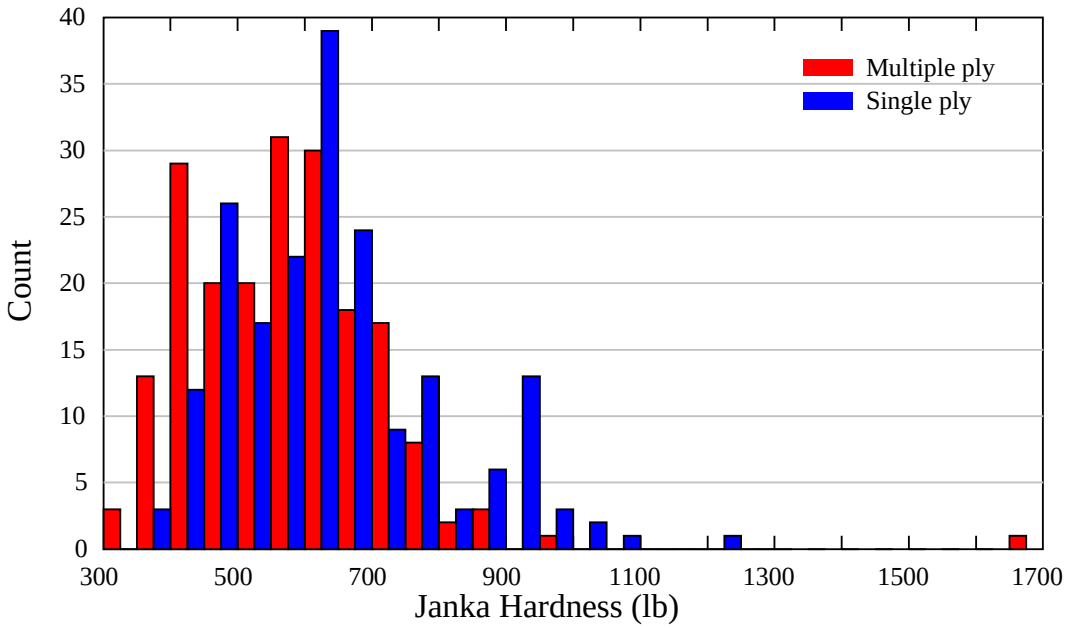

Figure 4-14. Janka hardness values for multiple and single ply SYP specimens.

4.5 Shear behavior of wood

It is important to know the shear strength of wood in order to create wood to wood and wood to other material bonds that are as strong or stronger than the underlying shear strength of wood. Strong bonds are imperative to high performance from CLT and ECLT. Furthermore, research has suggested that material ballistic performance is related to the shear strength, in addition to hardness [69, 93]. The anisotropic nature of wood makes shear strength an interesting characteristic. With the longitudinal, radial and tangential axes, there are effectively three different shear strengths for the wood. Due to the complexities associated with the three directions, wood is often assumed to be transversely isotropic, meaning that in the radial and tangential directions, or those perpendicular to the grain, the properties may be considered the same. Wood is known to have relatively low shear strengths parallel to the grain, compared to its tensile and compressive strengths

parallel to the wood grain. It is almost impossible to propagate shear failures perpendicular to the grain due to the fibrous nature of wood causing other failure modes before shear perpendicular to the grain can be achieved.

In examining ballistic resistance, shear strength is known to indicate the material's ability to decelerate the projectile [121]. The localized high velocity impact causes shear failure as the projectile moves through the target material [121]. Therefore, in addition to the bond line shear push-off testing discussed in Section 4.3.3., an additional set of shear tests was conducted to examine the shear strength of the two wood types serving as the basis of the CLT test specimens. The testing apparatus and specimens were the same as the shear bond line testing described previously. While the previous focus was on the shear strength of the bond between the two pieces, for this series of testing the shear strength of the wood itself was of interest. The material used to make the shear test specimens was the same wood types and grades used to make the CLT specimens. As a result, the specimen dimensions were slightly smaller than the *ASTM, D143 Standard Test Methods for Small Clear Specimens of Timber* specification of 2-inch by 2-inch cross-section for shear parallel to grain tests. However, the specimens were representative of the timber size in the composite product.

For these tests, the load was applied at a rate of 0.20-inch/min (5 mm/min) on the end-grain surfaces. This is the rate specified by *ASTM D905, Strength Properties of Adhesive Bonds in Shear by Compression Loading,* and was used to compare the bonded sample shear strength to the parent stock wood shear strength. The maximum load until shear failure was recorded and the specimens were examined after the test for types of failure. Table 4-6 provides the test result details. Figure 4-15 demonstrates how the

specimens looked post-test with the top images showing two SPF-S specimens and the bottom images presenting two SYP specimens.

Table 4-6. Shear stress test results.

Species	Average Shear stress (psi)	Coefficient of Variation (CoV)	N (# of samples)
SYP	1,597	13%	19
SPF-S	1,302	27%	14

Figure 4-15a and b both show alternating ridges along the growth ring lines as the shear fracture occurred in the radial axis of the wood. The specimen shown in Figure 4-15c had a relatively large knot, which caused the jagged fracture line shown in the photo. Figure 4-15d shows how a specimen with the annual rings aligned differently experienced a shear fracture on the tangential axis, which creates a nearly smooth surface at the fracture as the growth rings split apart. In softwoods, wood shear failures often follow the growth ring line or transition of early and latewood.

Figure 4-15. Examples of shear test specimens post-test, (a, b) SPF-S specimens, (c,d) SYP specimens.

4.6 Rolling Shear

A material characteristic of particular interest in CLT is rolling shear. Rolling shear occurs in the radial-tangential plane (G_R) and thus represents the weakest plane for shear stiffness and strength. Rolling shear is defined as shear stress causing shear strains perpendicular to the grain direction of wood [47]. CLT, with its individual lamella in the transverse direction, may be limited in some situations by its rolling shear capacity or by excessive deformation due to rolling shear. As Figure 4-16 demonstrates with a schematic

representation of the radial-tangential plane of a wood timber, the wood fibers in this sensitive plane may roll over one another when a high enough shear force, τ, is applied.

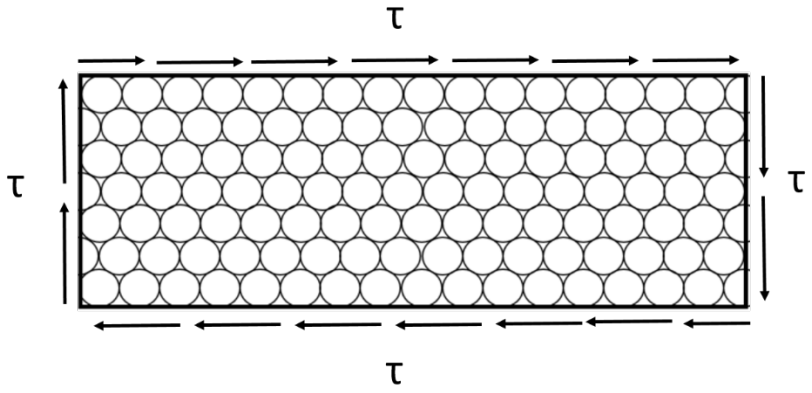

Figure 4-16. Stress due to rolling shear, adapted from [47]. The longitudinal axis of the wood fiber is out of the plane.

The rolling shear strength of concern is not just a property of the wood timber itself but also a panel characteristic based on the stiffness of the lamella, as well as their geometry. It is in essence a macroscale shear value for the structural element. With out-of-plane loading which causes the CLT panel to bend, the transverse layers are subjected to rolling shear which can have a significant impact on the panel overall strength. A rolling shear failure effectively disconnects the layers from each other and thus reduces both stiffness and strength of the composite panel. It is theorized that the cut of the wood with respect to the grain direction for the timbers in the even layers may influence the rolling shear modulus as the stiffness in the radial and tangential directions may vary [21].

Location of the pith, the softer wood located at the center of the tree, and eccentric location and asymmetric annual ring growth likely all influence the sawn timber rolling shear modulus [21, 47]. Manufacturers use wide boards for the plies in the transverse layers to limit the influence of rolling shear on the design.

PRG 320 requires that the width of cross-layer lamella layers be at least 3.5 times the thickness, if not edge bonded, unless additional rolling shear strength testing is conducted. The standard assumes the rolling shear modulus, $G_{R,}$ to be one-tenth of the shear modulus parallel to the wood grain, G_0. In addition, PRG 320 assumes that G_0 is 0.0625 of the material's modulus of elasticity, E, based on testing and previous literature [68]. The reduced rolling shear modulus caused by the cross-lamination of the layer in CLT can lead to large shear deformations depending on the loads, span-to-depth ratios and boundary conditions of the panels.

4.7 Shear analogy method

The shear analogy method is an analytical model developed and currently used for the calculation of basic mechanical properties of CLT elements, taking into account the composite nature of the panels. It is included in this discussion of wood properties because it is important for evaluation of the CLT panels in modeling the blast response to accurately account for the increased strength and stiffness from the cross-laminations. The cross layers combined with the anisotropy of the wood affect the load bearing behavior of the composite panel. When loaded perpendicular to the plane, longitudinal layers transmit shear and deform proportionally to G_0 while the cross layers experience rolling shear and deform proportionally to G_R. This behavior is shown in Figure 4-17.

Several other models and theories have been applied to CLT to determine the stress and deformation behavior in a panel. These include classical plate theory, first-order shear deformation plate theory, and more advanced plate theories. However, most of these methodologies fall short in modeling behavior for various reasons, including inability to account for shear deformation [83, 106]. PRG 320, the NDS, and the German design standard for timber structures (DIN 1052) have adopted the shear analogy method [68, 106] for CLT. This analytical method was popularized by the German researcher Kreuzinger and allows for the inclusion of different moduli of elasticity and shear moduli from the different layers and has no restrictions on the number of included layers. As a result, it is considered to be the most accurate design method for CLT as shear deformations are not neglected. It should be noted that this method is only applicable for CLT products that are face-glued and is not applicable for nailed or doweled CLT.

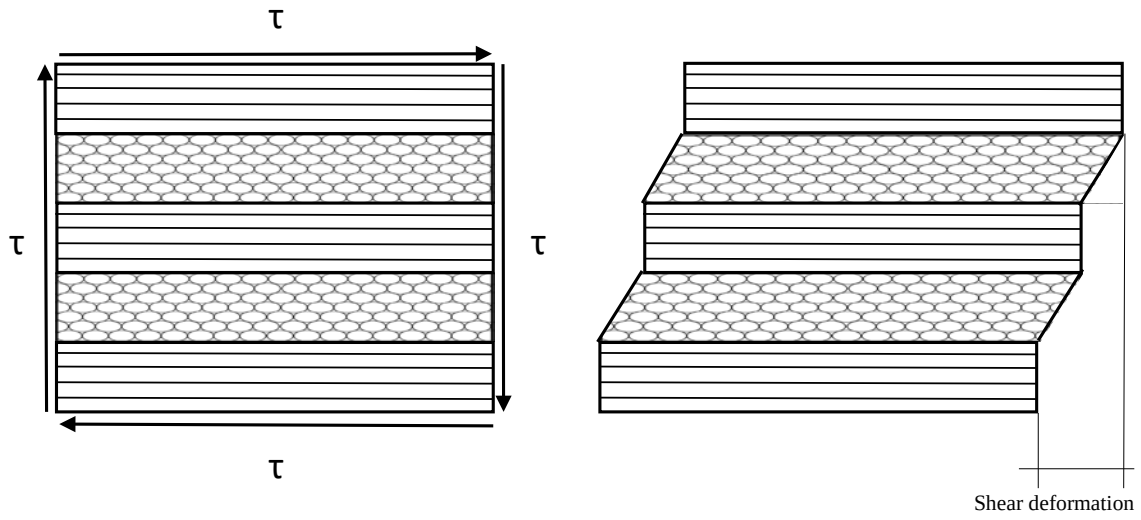

Figure 4-17. Shear deformation in a CLT cross-section view, adapted from [83].

The shear analogy method is particularly useful in the design of CLT bending members that resist loads perpendicular to the face of the CLT panel. With the shear analogy method, an effective bending stiffness, defined as the product of the modulus of elasticity and area moment of inertia, is used to describe the bending resistance of the composite panel. The effective bending stiffness accounts for the stiffness contribution of each layer. The method allows for each layer to have a differing stiffness to account for the orientation of the layer. The span of the panel plays a significant role and shear influence on capacity can be seen for span to depth ratios less than 20 for bending perpendicular to the grain direction of the outermost plies [47]. Smaller span to depth ratios experience higher shear deformation due to the low rolling shear modulus.

The procedure for the shear analogy method starts with the multiple layered panel is divided into two virtual beams as shown in Figure 4-18. One beam, Beam A, uses the flexural and shear stiffness values of the individual plies along their own centers. The second beam, Beam B, has an increased moment of inertia because of the distance from the neutral axis. The two beams are connected with rigid web members in the model to enable equal deflection between the beams.

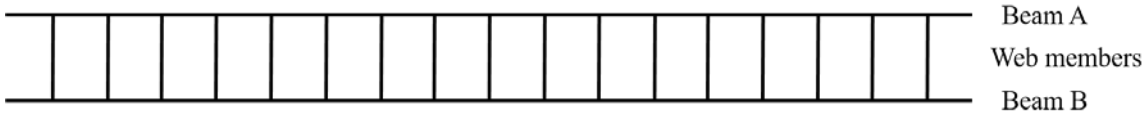

Figure 4-18. Virtual beams for use in the shear analogy method.

Beam A has a bending stiffness, B_A, equal to the sum of the bending stiffness of all the individual layers or cross-sections, as shown in Equation 4.2.

$$B_A = \sum_{i=1}^{n} E_i I_i = \sum_{i=1}^{n} E_i \, b_i \frac{h_i^3}{12} \tag{4.2}$$

where B_A = $(EI)_A$, bending stiffness of Beam A
E_i = modulus of elasticity
I_i = second moment of area
b_i = width of individual layer, usually taken as 1-ft for CLT panel
h_i = thickness of each individual layer

For Beam B, the bending stiffness, B_B, is determined using the parallel axis theorem, as demonstrated in Equation 4.3.

$$B_B = \sum_{i=1}^{n} E_i A_i z_i^2 \tag{4.3}$$

where B_B = $(EI)_B$, bending stiffness of Beam B
E_i = modulus of elasticity
A_i = cross-sectional area
z_i = the distance between the center point of each layer and the neutral axis

The modulus of elasticity value for the longitudinal layers is the material property, E_0, while the cross laminations' modulus of elasticity value, E_{90}, should be calculated as 1/30 of that longitudinal value. The effective bending stiffness, EI_{eff}, for the composite CLT panel may then be calculated using Equation 4.4, which simply added the two bending stiffness values found for Beam A and Beam B.

$$EI_{eff} = \sum_{i=1}^{n} E_i b_i \frac{h_i^3}{12} + \sum_{i=1}^{n} E_i A_i z_i^2 \tag{4.4}$$

For the effective shear stiffness, the longitudinal lamella should be assumed to be the shear modulus parallel to the grain, G_0, and the cross laminations shear modulus should be the rolling shear modulus, G_R, which is calculated as 0.10 G_0. Based on guidance from PRG 320, the shear modulus parallel to the grain can be calculated as 0.0625 of the modulus of elasticity, E. Given these parameters, an effective shear stiffness of the composite section, GA_{eff}, can be found using Equation 4.5.

$$GA_{eff} = \frac{{a_{shear}}^2}{\left[\left(\frac{h_1}{2G_1 b}\right) + \left(\sum_{i=2}^{n-1} \frac{h_i}{G_i b_i}\right) + \left(\frac{h_n}{2G_n b}\right)\right]} \tag{4.5}$$

where a_{shear} = effective shear thickness = h(n-1)
h = thickness of each individual layer
b = width of individual layer for CLT panel
G = shear modulus = G_0=E/16 or G_R=E/(16*10)

According to the CLT Handbook and PRG 320, the design of bending members in flexure can use a simplified method to determine panel capacity using the extreme fiber approach of the effective section modulus, S_{eff}. With this method, the effective bending stiffness from Equation 4.4. is divided by the modulus of elasticity of the outer layer and half the thickness of the panel, as shown in Equation 4.6.

$$S_{eff} = \frac{2EI_{eff}}{E_1 h_{panel}} \tag{4.6}$$

where EI_{eff} = effective bending stiffness (see Eqn 4.4)
E_1 = modulus of elasticity of outermost layer
h_{panel} = entire thickness of panel

The moment capacity of the panel can then be determined by multiplying the effective section modulus by the allowable bending stress of the outermost layer. PRG 320 further reduces the moment capacity with a factor of 0.85 for conservatism in CLT design.

To determine the corresponding shear capacity of the CLT panel, a simplified method can again be used to find the effective shear parameters. Equation 4.7 demonstrates this method and calculation of the $(Ib/Q)_{eff}$ term. The shear capacity of the designed panel can then be calculated by multiplying that value of $(Ib/Q)_{eff}$ by the shear strength of the panel, F_v, and any required adjustment factors.

$$\left(Ib/Q\right)_{eff} = \frac{EI_{eff}}{\sum_{i=1}^{n/2} E_i h_i z_i} \tag{4.7}$$

where EI_{eff} = effective bending stiffness (see Eqn 4.4)
E_i = modulus of elasticity of an individual layer
h_i = thickness of an individual layer, except the middle layer, which is half its thickness
z_i = distance from the centroid of the layer to the neutral axis, except for the middle layer, where it is to the centroid of the top half of that layer

An apparent stiffness value, EI_{app}, is a reduced effective bending stiffness value modified to account for the shear deformation. Equation 4.8 shows the method to determine the apparent stiffness. The K_S value in the equation is a constant related to the influence of the shear deformation based on load and end conditions, as shown in Table 4-7.

$$EI_{app} = \frac{EI_{eff}}{1 + \frac{K_S EI_{eff}}{GA_{eff} {L_p}^2}} \tag{4.8}$$

where EI_{eff} = effective bending stiffness (See Eqn 4.4)
K_S = constant based on load conditions
GA_{eff} = effective shear stiffness (See Eqn 4.5)
L_p = panel height

Table 4-7. K_S values for various loading conditions, adapted from [68].

Loading	End Fixity	K_S
Uniformly distributed	Pinned	11.5
	Fixed	57.6
Concentrated at mid-span	Pinned	14.4
	Fixed	57.6
Concentrated at quarter points	Pinned	10.5
Constant moment	Pinned	11.8
Uniformly distributed	Cantilevered	4.8
Concentrated at free-end	Cantilevered	3.6

4.8 High strain rate strengths in wood

Physical experiments have shown wood demonstrates an increased strength under high strain rates, as has been observed with other materials such as structural steel and reinforced concrete [54, 113, 120]. Wouts et al. have shown that wood mechanical properties are sensitive to strain rate and that loading direction relative to grain direction influences this sensitivity [123]. Much of the literature on wood under high strain rates has been limited to balsa wood used in the cores of sandwich panels. A few key references report on wood properties of typical softwood lumber, examined at higher strain rates [66, 113, 123].

Wouts et al. used a Split Hopkinson Pressure Bar (SHPB) to evaluate beech and spruce wood sensitivity to high strain rates. The wood species studied were selected due to their differences as a hardwood (beech) and softwood (spruce) with dissimilar microstructure composition and varied specific density, which relates to many mechanical properties. It was determined that the initial longitudinal crushing strength is strain rate

sensitive with a significant increase in the range of 60 to 110 percent from quasi-static (0.001 s^{-1}) to high strain rates (600 s^{-1}). This increase is most apparent in the longitudinal direction but still observable in the transverse directions [123].

Based on wood specimen responses to high strain rates, the compressive behavioral response is defined in terms of three parameters: an initial crushing stress, σ_{cr}; a plateau stress, $\sigma_{plateau}$; and densification locking strain, ϵ_d. The three values are commonly values of interest in the study of cellular materials and impact energy absorption. The parameters can be extracted from an engineering stress versus strain curve, like the generic curve shown in Figure 4-19. The initial crushing stress relates to the yield stress depending on load direction and specimen orientation and has an accompanying initial crushing strain value. This value is sensitive to strain rate with higher strength values occurring with high strain rates. The plateau stress represents a relatively constant level of stress across a range of strains, which aids in determining absorbed energy. At extremely high strain rates such as those higher than 600 s^{-1}, the failure mechanisms make it difficult to determine to the plateau stress. The densification locking strain value occurs before a large increase in stress and signifies the upper limit with respect to energy absorption capacity [123]. It is important to note that the deformation capacity and subsequent hardening depicted in Figure 4-19 applies only to the compression loading of wood and it is unlikely that wood loaded in tension, shear, or flexure would demonstrate this behavior.

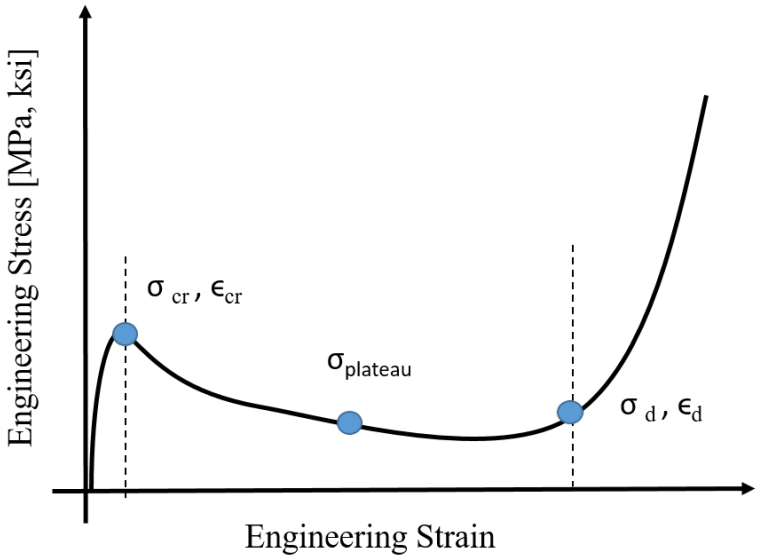

Figure 4-19. Typical compressive response of wood in the longitudinal direction, adapted from [123].

Gilbertson and Bulleit also completed SHPB testing of wood and concluded that the maximum stress and strain of the wood specimens were significantly different over a range of strain rates. They found that with increased strain rates, such as those felt with an impact loading scenario, the modulus of elasticity, compressive strength and maximum strain all increased while the time to reach ultimate stress decreased [54]. Generally, a limited quantity of research has been conducted on wood materials under high loading rates – and both of these studies focused on compression loading. There is no standard test procedure or testing apparatus to date which makes comparing the limited data available difficult [107].

4.9 Summary

The unique characteristic of wood and wood products make it a construction material unlike many others in terms of design for blast and ballistic resistance. Parameters such as the species type and composite layup can significantly change the performance of CLT. In addition to species, the mechanical properties of the wood the panel is comprised of, including density, hardness and shear strength all heavily influence the overall response to impact loading conditions like those experienced in a blast or ballistic event. Additionally, the cross-layering of the sawn timbers that gives CLT its strength and stiffness also increases concerns with rolling shear capacity. Design methodologies, such as the shear analogy method, have been developed in the past two decades to accurately determine the flexural and shear strength design values for the CLT panels. However, the need for improved data and procedures with respect to high rate loadings is significant. There is little available literature on the dynamic properties for wood and even less data for engineered wood products like CLT.

CHAPTER 5
BALLISTIC PERFORMANCE OF CLT

5.1 Background on ballistic performance

Current design guidance for DoD planning and design of ballistic penetration is detailed in *Unified Facilities Criteria (UFC) 4-023-07, Design to Resist Direct Fire Weapons Effects* [7]. This standard provides guidance for facility design with the intent of protection from direct fire weapon effects, which includes small arms ballistic weapons such as pistols, rifles, shotguns and submarine guns up to 0.50-caliber (12.7 mm), and shoulder fired antitank weapons. The UFC uses the Underwriters Laboratories (UL) ballistic standards for testing and characterizing building elements' or assemblies' resistance to ballistic effects. The UFC provides an equation for the thickness of wood necessary to resist perforation (see Equation 5.1), referred to as the "UFC equation" for the remainder of this document.

$$T_w = 9837\left(\frac{v^{0.4113}w^{1.4897}}{\rho\left(\frac{\pi D^2}{2}\right)^{1.3596}H^{0.5414}}\right) \tag{5.1}$$

Where:

Tw = thickness of wood necessary to prevent perforation (in)
v = projectile impact velocity (fps)
w = projectile weight (lb.)
D = projectile diameter (in^2)
ρ = wood density ($lb./ft^3$)
H = wood hardness (lb.)

Wood density and wood hardness values are given in a "Wood Properties" table included in the UFC. These are replicated in Table 5-1.

Table 5-1. Wood properties table from UFC for use in wood equation.

Species		Density (lb/ft^3)	Hardness (pounds)
Pine	Dry	23.5	38.7
	Wet	30	51.1
Maple	Dry	35	76.9
	Wet	40	72
Green Oak	Dry	55	88.1
	Wet	55	72.1
Marine plywood	Dry	37	68.7
	Wet	37	58.8
Balsa	Dry	6	21
	Wet	6	61.5
Fir plywood	Dry	30	75
	Wet	30	68.9
Hickory	Dry	50	74.3
	Wet	55	63.5

Other than the wood properties listed in Table 5-1, there is limited information given about the wood or the projectiles that determined the UFC equation. Furthermore, the method for determining hardness values is not specified and these values differ significantly from today's accepted reference values for hardness. The projectile variables in the equation include the velocity of the projectile, with the recommendation of conservatively using the muzzle velocity for the weapons that the wood would be designed to defeat, as well as the projectile weight and diameter. For the wood species of interest,

the material variables included are the density and hardness. From a physics-based perspective, the equation makes sense with the velocity and weight of the projectile in the numerator. As the two values become larger, the thickness of the wood needs to be proportionally thicker. In the denominator of the equation are the wood density and hardness as well as the cross-sectional area based on the diameter of the projectile. As these terms increase, less wood thickness is required to stop the perforation because harder and denser wood resists the penetration to a higher degree. The relation between a larger diameter of the projectile and the requirement of less wood thickness is a bit less intuitive. From an energy dissipation perspective, it requires more energy for a larger diameter projectile to penetrate compared to a smaller diameter projectile because more target material must be overmatched in order to penetrate.

The UFC equation ties to a series of studies conducted by the Department of Defense's Ballistic Analysis Laboratory in the 1960s known as the THOR reports. The report consists of empirical equations and these equations were based on testing of metallic, nonmetallic, and wood targets with projectiles intended to simulate primary fragments [42]. Specifically, Equation 5.1 may originate from THOR Report Number 62, *The Resistance of Various Woods to Perforation by Steel Fragments and Small Caliber Projectiles*, a document categorized as unclassified, distribution C, "For Official Use Only" by DoD employees and contractors [80]. This is likely due to the inclusion of data on specific small arms caliber ammunitions, which highlights the sensitivity of data for military munitions.

5.2 Ballistic Resistance Standards

As mentioned in the *UFC 4-023-07, Design to Resist Direct Fire Weapons Effects,* the design standards are based on the UL ballistic standard. Common references for bullet

resistance include the UL Standard 752, *Standard for Safety, Bullet-Resisting Equipment* (UL752) and the National Institute of Justice Standard 0108.01, *Ballistic Resistant Protective Materials* (NIJ 0108.01). UL752 includes materials, devices, and fixtures used in forming a bullet-resisting barrier with the intent of protecting against robbery, holdup, or armed attack. According to the reference, it may also be used to determine the bullet resistance of building components such as windows, walls, and other barrier components.

Test specifications for UL752 standards are very specific in terms of test samples and test equipment. The rating levels classified by UL752 can be found in Table 5-2 [13]. Without a laboratory designed specifically for the tests, it is difficult to achieve the exact standards, which include temperatures and shot patterns. The experimental testing in this research was not intended to meet all the specifications for UL-level testing. Rather, as the first experimental tests examining the ballistic performance of CLT, the intent was to characterize material performance in terms of failure modes and mechanisms (discussed in Chapter 6) for the development of initial empirical models for CLT ballistic penetration performance.

NIJ 0108.01 is a standard for the performance requirements and testing methods for characterizing ballistic resistant protective materials or armor intended to protect against gunfire. This excludes police body armor and ballistic helmets, which have separate specified performance standards. Protective materials include portable ballistic shields, ballistic protection in fixed structures, or vehicles fabricated from metals, ceramics, transparent glazing, fabric, and fabric-reinforced plastics. The standards for levels of performance according to NIJ 0108.01 can be found in Table 5-3 [3].

Table 5-2. From UL 752, Table 3.1, the rating levels by ammunition specifications.

Rating	Ammunition	Protection from	Grains	Grams	Minimum velocity		Number of shots
					fps	m/s	
Level 1	9-mm full metal jacket with lead core	Med power hand guns	124	8.00	1,175	358	3
Level 2	0.357 Magnum jacketed lead soft point	High power hand guns	158	10.20	1,250	381	3
Level 3	0.44 Magnum lead semi-wadcutter gas checked	Super power hand guns	240	15.60	1,350	411	3
Level 4	0.30 caliber rifle lead core soft point	High-power hunting rifle	180	11.70	2,540	774	1
Level 5	7.62-mm rifle lead core full metal copper jacket, military ball	Military ball from hunting or military rifle	150	9.70	2,750	838	1
Level 6	9-mm full metal jacket with lead core	Multiple shots of submachine gun	124	8.00	1,400	427	5
Level 7	5.56-mm rifle full metal copper jacket with lead core	Multiple shots of military assault rifle	55	3.56	3,080	939	5
Level 8	7.62-mm rifle lead core full metal copper jacket, military ball	Multiple shots of military assault rifle	150	9.70	2,750	838	5
Level 9	Armor Piercing (AP) 0.30-caliber rifle steel core lead point filler full metal jacket	Armor piercing rounds; high power hunting rifle	166	10.80	2,715	828	1
Level 10	0.50-caliber rifle lead core full metal copper jacket, military ball	One shot from military sniper rifle; 0.50-caliber round	709.5	45.90	2,810	856	1
Supple-mentary shotgun	12-Gauge rifled lead slug and 12-Gauge 00 lead buckshot (12 pellets)	Rifled lead slug 00 lead buckshot	437 650	28.30 42.00	1,585 1,200	483 366	3
Note: Maximum velocity is 110 percent of the minimum velocity.							

Table 5-3. The level of performance standards based on NIJ 0108.01.

Level of Performance	Test Ammunition	Nominal Bullet Mass		Suggested Barrel Length		Required Bullet Velocity		Required Hits Per Armor Specimen	Permitted Penetrations
		(grams)	(grains)	(cm)	(inches)	(m/s)	(ft/s)		
	22 LRHV Lead	2.6	40	15-16.5	6-6.5	320+/- 12	1050+/- 40	5	0
Type I	38 Special RN Lead	10.2	158	15-16.5	6-6.5	259+/- 15	850+/- 50	5	0
	357 Magnum JSP	10.2	158	10-12	4-4.75	381+/-15	1250+/- 50	5	0
Type II-A	9mm FMJ	8	124	10-12	4-4.75	332+/-12	1090+/-40	5	0
	357 Magnum JSP	10.2	158	15-16.5	6-6.5	425+/- 15	1395+/- 50	5	0
Type II	9mm FMJ	8	124	10-12	4-4.75	358+/- 12	1175+/- 40	5	0
	44 Magnum Lead SWC Gas Checked	15.55	240	14-16	5.5-6.25	426+/- 15	1400+/- 50	5	0
Type III-A	9mm FMJ	8	124	24-26	9.5-10.25	426+/- 15	1400+/- 50	5	0
Type III	7.62 mm 308 Winchester FMJ	9.7	150	56	22	838+/- 15	2750+/- 50	5	0
Type IV	30-06 AP	10.8	166	56	22	868+/- 15	2850+/- 50	1	0

Abbreviations:
AP - Armor Piercing
FMJ - Full Metal Jacket
JSP - Jacketed Soft Point
LRHV - Long Rifle High Velocity
RN - Round Nose
SWC – semi-wadcutter

5.3 Design of Experiment

A material's response to a ballistic threat is dependent on many characteristics of the projectile, including its composition, shape, caliber, mass, and impact velocity. Although many variables are credited with having an effect on the response, the initial ballistic testing of CLT was simplified to a limited set of variables. For example, the majority of the testing was conducted with 0.50-in. steel sphere test rounds and a small number of tests were conducted with a 0.50-caliber fragment simulating projectile (FSP). These two experimental projectiles have the benefit of being the same caliber (the measurement of the inner diameter or bore of the gun barrel) and thus the same cross-sectional striking area while also having different masses and distinctly different nose shapes. Both rounds are frequently used in ballistic testing of armors as baseline data for comparison to the performance of other materials.

Nose shape is an important and relatively complex parameter in penetration mechanics. There is a significant amount of research that has compared different nose shapes and their penetration behavior into materials like metals and concrete. Since this research is focused on isolating variables to best understand the behavior of CLT, for simplicity the parameter of nose shape was not included in this research. Future work in the ballistic performance of CLT and mass timber products could build off this initial work and include experiments with varying nose shape. Empirical models could then be calibrated to include a nose shape factor much like any other variable in the model.

5.3.1 Set-up and testing methodology

The majority of the ballistic experiments took place at the U.S. Army Corps of Engineers' Engineer Research and Development Center (ERDC) in the Survivability Engineering Branch fragment simulating facility. The experimental test set-up consisted of an indoor, conditioned, ballistic range with a smooth bore powder gun with a 50-caliber barrel. Figure 5-1 shows the firing apparatus. While the firing system can be adapted for multiple barrels, only a 50-caliber barrel was used. This barrel is the same type as those used with a military M2 weapons systems.

Figure 5-1. ERDC's fragment simulating facility firing apparatus shown with one 50-caliber barrel mounted.

The firing apparatus was mounted and secured to a table to prevent movement with test shots. Four infrared photoelectric velocity screens were connected to two chronographs in

order to capture two different velocity measurements as the projectile moved down range in the direction of the target. The screens are shown in Figure 5-2.

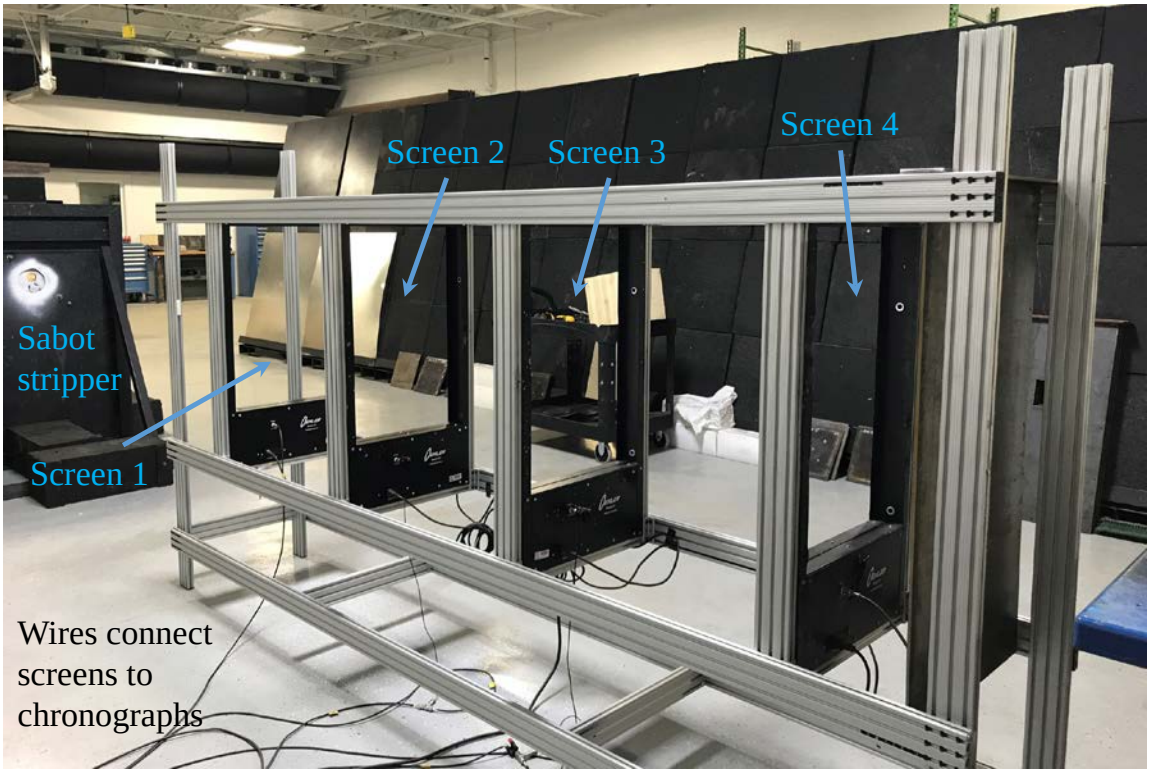

Figure 5-2. Infrared photoelectric strike velocity screens connected to two chronographs determine the impact velocity at the target face.

The screens determine the impact velocity, v_s, using Equation 5.2, based on the measured velocities and known distances between the screens and the fourth screen and target:

$$v_S = v_2 + \left(\frac{L_2}{L_1}\right)(v_2 - v_1) \tag{5.2}$$

where v_1 is the velocity as determined by screens one and three (first and third screen the projectile passes), and v_2 is the velocity as determined by screens two and four. L_1 is the distance from which v_1 and v_2 were measured (known from test set-up), and L_2 is the distance between where v_2 was measured and the impact side of the test specimen (front face of the target).

The CLT test specimen was mounted to a steel frame using ratchet straps, as shown in Figure 5-3. The frame also had a small shelf to rest the specimen, which helped ensure it was level and at the same location placement for each test. The steel frame was clamped with c-clamps to a small hydraulic lift on rails affixed to the facility floor. This lift enabled the repositioning of the target both horizontally and vertically.

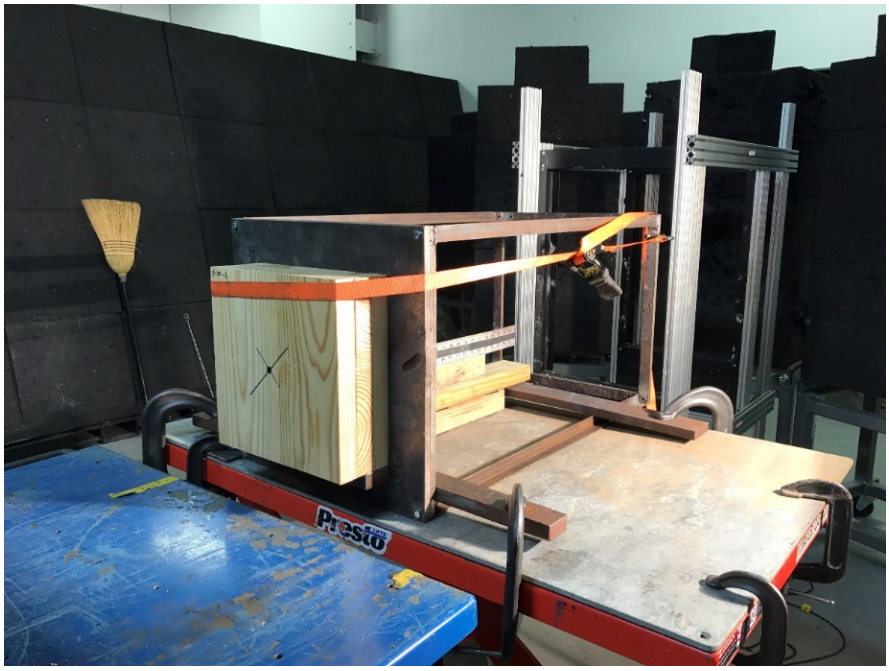

Figure 5-3. A CLT specimen mounted on the steel frame-lift base in preparation for a test shot.

Behind the target, a measuring device was placed to assist in tracking the residual velocities using high-speed video, as shown in Figure 5-4. An additional set of two infrared photoelectric velocity screens connected to a chronograph were also used; however, wood debris occasionally caused a misreading and thus analyzed high-speed video was the primary source of residual velocity data. With the video, the researcher could identify the projectile from the debris and ensure the right residual velocity was captured.

Figure 5-4. Back of mount set-up is equipped with a ruler to help with acquiring residual velocity from high-speed video.

One Phantom V710 and one Phantom V711 high-speed cameras were mounted on tripods to capture the ballistic event from two perspectives. One was focused on the front target face and the second was positioned to capture the back face and behind the target to acquire the residual velocity. The cameras were set to an acoustic trigger and captured the event in 512 x 384 pixel resolution at 14,035 frames per second.

The projectile for the majority of testing was a 0.5-inch (12.7 mm) rigid steel sphere constructed of hardened impact-resistant S-2 tool steel. This projectile was selected as a benchmark for CLT due to the vast ERDC database for ballistic tests with other target materials. Additionally, use of the sphere projectile eliminated any security concerns with collecting data as they are purely used in experimental testing and not a munition for military use outside of research. From a ballistic modeling perspective, the hardened steel sphere may be a starting point for more in-depth ballistic testing as nose effects like fragmentation and mushrooming of the round are atypical.

The projectiles were mounted by hand in a .50-caliber cartridge with a plastic sabot. The sabot holds the projectile in the cartridge without letting air or moisture into the cartridge interior where the powder burns and initiates the ballistic event. The sabot falls away from the projectile as it moves down range due to a pre-cut perforation and is removed from the experiment by a sabot-stripper in the set-up, which is shown in the far left of Figure 5-2 before the infrared screens. This device blocks the plastic sabot pieces from continuing in the direction of the velocity screens and the target. Figure 5-5 shows a schematic of the ballistic test set-up from the sabot stripper forward. The projectile moves from right to left in the schematic as indicated by the red arrow.

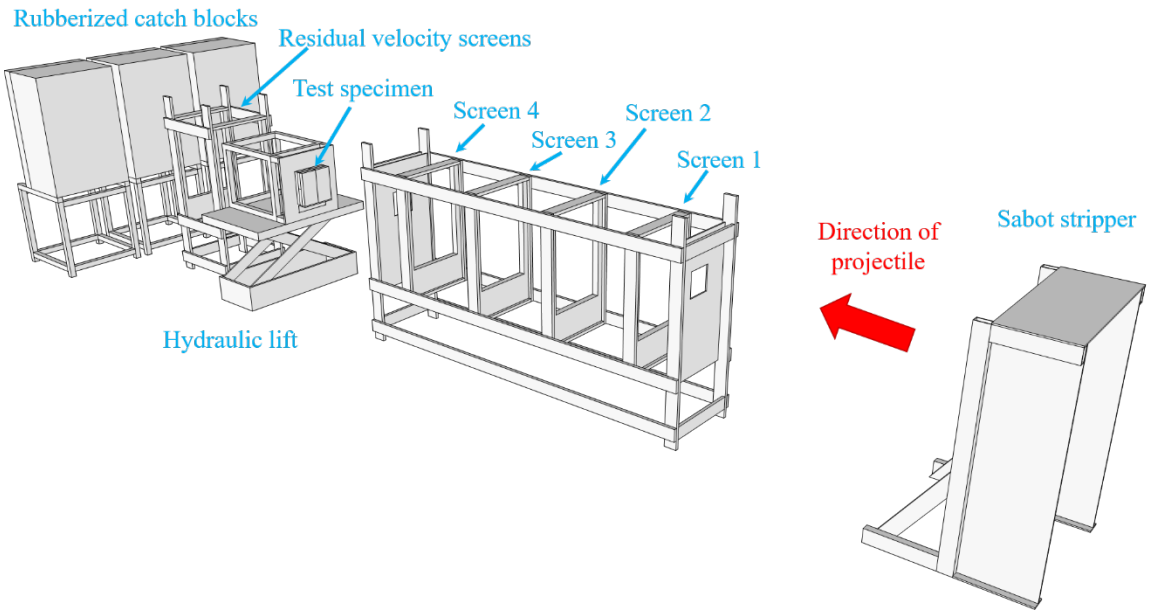

Figure 5-5. . Schematic of the ballistic test set-up.

5.4 Ballistic testing series

The test specimens were comprised of two different types of softwood: Spruce Pine Fir – South (SPF-S) and Southern Yellow Pine (SYP). These two softwood species were used for testing due to availability and interest in the incorporation of a local forest product, widely available in Georgia and the rest of the southeastern U.S. While both softwoods, the two species have different densities and hardness values as discussed in Chapter 4.

The SPF-S was manufactured into a V4 grade CLT by the manufacturer SmartLam to the APA standard specifications and came with a material product report outlining allowable design properties for both major and minor strength directions, including strengths and stiffness. The SYP specimens were manufactured at the Georgia Institute of Technology's Digital Fabrication Laboratory. They were made in accordance with the

guidelines and standards presented in the *CLT Handbook: US Edition* and *Standard for Performance-Rated Cross-Laminated Timber ANSI/APA PRG 320-2012* (PRG 320), as outlined in Chapter 4.

The SYP test specimens were not large enough for significant static strength and stiffness testing but based on the lumber used for construction, would be expected to roughly perform as well as the V3 CLT grade specifications in PRG 320 with layups on No. 2 Southern pine lumber in all parallel layers and No. 3 Southern pine in all perpendicular layers. The specimen size was limited by press capability, as the largest size without bigger equipment that could be made was approximately 14-inches by 14-inches in size.

Two types of ballistic data were gathered depending on the effect of the shot. If the projectile perforated the CLT specimen, then a residual velocity (v_r) was recorded based on the high-speed video capturing the round exiting the back face of the specimen. If the shot was a partial penetration and the projectile remained embedded in the specimen then the depth of penetration (T_w) was recorded. The breakdown of number of shots by species type, munition, and type of data gathered is shown in Table 5-4. The specifications and results for each test including, dimensions, weight, moisture content, and striking velocity are documented in Appendix A. Analysis of the data is presented in the following sections.

Table 5-4. Breakdown of number of ballistic tests by munition, species and data gathered.

Species of Wood	0.50-cal FSP			1/2" sphere			Overall Total by Species
	Depth of Penetration (T_w)	Residual Velocity (v_r)	Total (n)	Depth of Penetration (T_w)	Residual Velocity (v_r)	Total (n)	
Southern Yellow Pine	4	12	16	35	19	54	70
Spruce Pine Fir - South	4	29	33	27	35	62	95
Total by Munition	8	41	49	62	54	116	165

5.5 Depth of penetration data analysis

5.5.1 Linear and quadratic regression

Data from 70 tests were analyzed to explore the relation between depth of penetration and striking velocity for both types of wood species. Two regression types were considered: linear and quadratic. For the SPF-S specimens the depth of penetration based on the striking velocity yielded a linear relationship with good correlation of determination ($R^2 = 0.971$). A polynomial regression yielded similar results to the linear regression and had similar goodness of fit ($R^2 = 0.972$). Figure 5-6 shows the data and lines of best fit for linear and quadratic regressions.

Linear Regression: $T_w = -2.871 + 0.005189 v_s$

Quadratic Regression: $T_w = 3 * 10^{-7} v_s^2 + 0.0042 v_s - 2.1348$

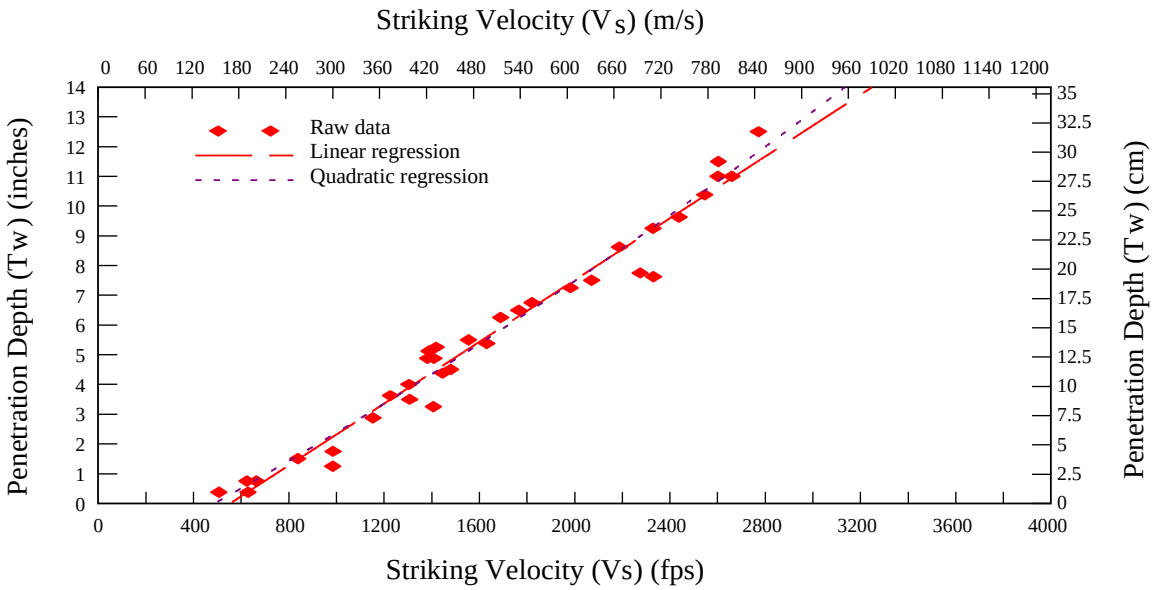

Figure 5-6. Spruce Pine Fir-South data shown with linear and quadratic regression lines.

Similarly, Figure 5-7 shows the data and linear and quadratic regression lines for the SYP specimen tests. The R^2 values for both the linear regression and quadratic regression were 0.929.

The values for both the linear and quadratic regression of the data were both high suggesting good correlation for linear and quadratic models. While striking velocity is a key component of the penetration event, past penetration research has shown it is not the only variable in determining how far the round penetrates into the test specimens so further analysis is warranted.

$$\text{Linear Regression:} \quad T_w = -3.307 + 0.004445 v_s$$
$$\text{Quadratic Regression:} \quad T_w = 9 * 10^{-8} v_s^2 + 0.0048 v_s - 3.6456$$

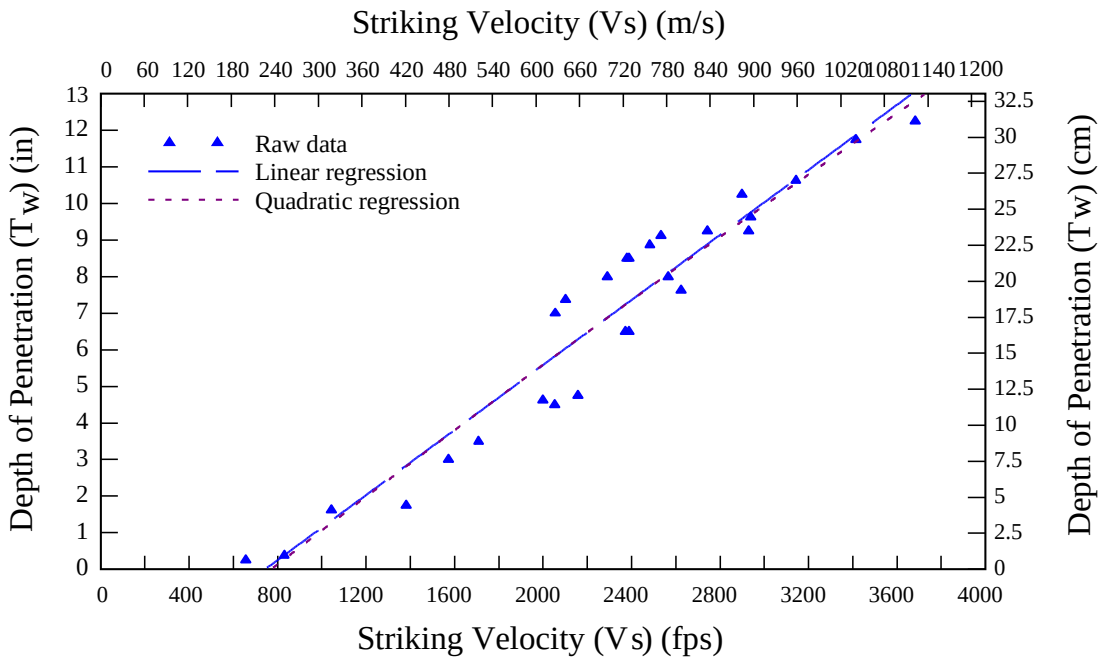

Figure 5-7. Southern Yellow Pine data shown with linear and quadratic regression lines.

5.5.2 UFC equation for required wood thickness

Most UFC design manuals that focus on protection and hardening of structures against ballistic or blast threats classify wood as a material with relatively little penetration resistance. As such, wood is not typically used in protective design with the noteworthy exception of rapid construction of field fortifications in overseas military construction. This low penetration resistance conclusion is based on plywood and sawn dimensional lumber used in lightweight wood frame construction and not inclusive of newer mass timber products like CLT.

The current design guidance issued by *UFC 4-023-07*, offers Equation 5.1, the UFC equation for the calculation of required wood thickness in terms of striking velocity. Using the variables of the CLT ballistic test set-up, as outlined in Table 5-5, the equation was

plotted and compared to the CLT ballistic test data for the ½-inch sphere projectile. This comparison is shown in Figure 5-8.

Table 5-5. Values used in UFC equation for calculation of required wood thickness.

Variable	Value used	
v	varied	striking velocities (x-axis) (fps)
w	0.018371	projectile weight (lb.)
$\pi D^2/4$	0.19625	cross-sectional striking area based on diameter of projectile (in^2)
ρ_1	28.4	Spruce Pine Fir-South density ($lb./ft^3$)
ρ_2	34.2	Southern Yellow Pine density ($lb./ft^3$)
H	38.7	wood hardness based on UFC table (lb.)

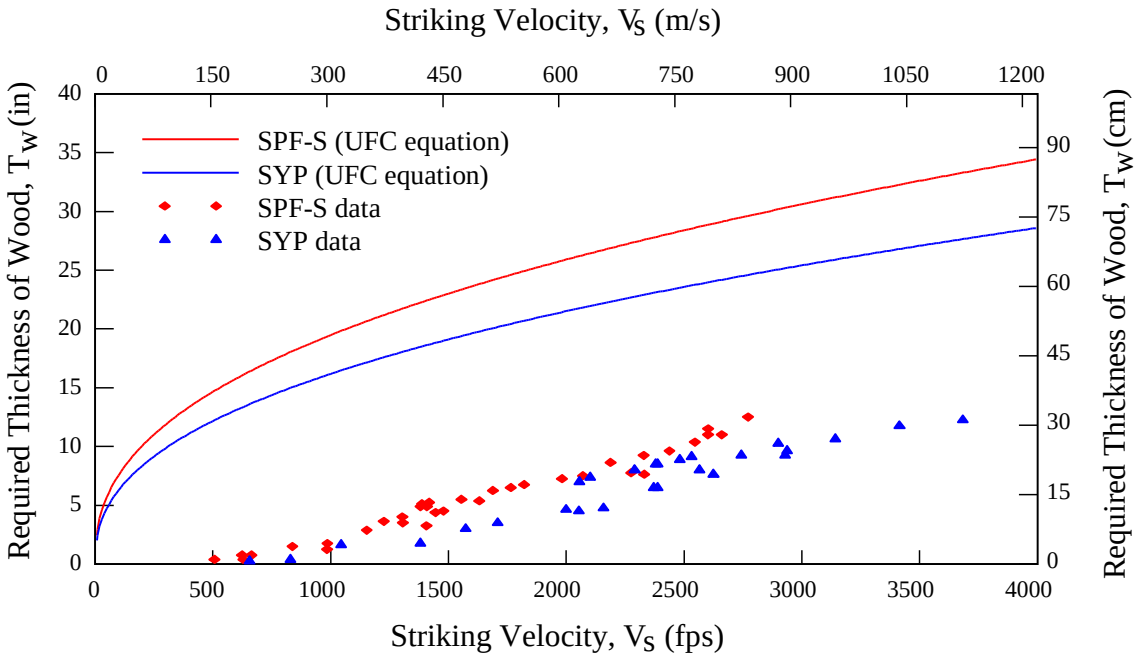

Figure 5-8. UFC equation for required wood thickness compared to CLT test data.

Clearly, the data from the CLT testing does not align well with the projected thickness of wood required based on the UFC equation. It is important to note that empirical models developed from ballistic studies can often predict response accurately within some specified range, but that those models should often not be extrapolated for use in conditions other than those from the test scenario used to develop the model without recalibration. The stark difference between the UFC equation and the CLT data is a perfect example of this. The differences are likely caused by a lack of calibration in addition to the difference between CLT and sawn wood without laminated layers. Like all empirical models for ballistic penetration, this equation should be presented to users with the caveat of what the test conditions were that produced the equation. This would allow for an easier factoring or recalibration of the model. The lack of a good fit between the existing UFC equation and the data from the CLT ballistic testing initiated an exploration into other potential empirical models, which could better predict the thickness of CLT required based on striking velocity of the projectile. A summary of the models considered in the following sections is provided in Table 5-6.

Table 5-6. Summary of models.

Model	Section	Data	Type
Revised UFC model	5.5.3	All SPF-S SYP	Curve-fit
Euler-Robbins	5.5.4.1	All	Classical
Poncelet (base)	5.5.4.2	All	Classical
Poncelet (Variant 1)	5.5.4.2	All	Classical
Poncelet (Variant 2)	5.5.4.2	All	Classical
Resal	5.5.4.3	All	Classical
Force Law model	5.5.5	All SPF-S SYP	Physics-based
General THOR model	5.5.6	All	Curve-fit
CLT THOR model	5.5.7	All SPF-S SYP	Curve-fit

5.5.3 Recalibration of the UFC equation: a curve fitting model

While the UFC equation did not fit the experimental data well, it did incorporate variables both measurable and relevant to a ballistic penetration event. Using multivariate analysis and the test data, the UFC equation was recalibrated to determine the constants and exponential parameters for a better fitting curve. Variables were set to logical units such as grains for the projectile weight, a commonly used measure of weight for projectiles. A generic version of the UFC equation with unsolved parameters is shown in Equation 5.3. To construct this curve fit to the data, the computer software Mathcad was used to determine a nonlinear least squares curve fit. Using the experimental data and initial guess values for the equation parameters, which were based on the original UFC equation, the program was solved for the residuals between the input data and the curve fitting function, as shown in Equation 5.3.

$$T_w = C_1 \left[\frac{(v^a w^b)}{\rho \left(\frac{\pi D^2}{4} \right)^c H^d} \right] \tag{5.3}$$

where
T_w = thickness of wood necessary to prevent perforation (in.)
v = projectile striking velocity (fps)
w = projectile weight (grains)
D = projectile (in.)
ρ = wood density (lb./ft^3)
H = wood hardness (lb.)
and C_1, a, b, c, d = parameters fit to data

Within Mathcad, the function ‘minerr’ used the Levenberg-Marquardt method to sum and square the residuals, solving for the parameters that minimized the residual values.

The Levenberg-Marquardt method is a common algorithm used for solving least squares of nonlinear functions and works well for curving fitting. The Levenberg-Marquardt method enables interpolation between the Gauss-Newton algorithm and the method of gradient descent for solving systems of nonlinear equations [82]. It effectively takes the empirical data, in this case the thickness of wood penetrated (T_w) and all the independent variables including the striking velocity, wood density, wood hardness, projectile weight and diameter, and then solves for the parameters in the proposed equation, in this case, C_1, a, b, c, and d. It does this through an iterative process to minimize the difference between the equation and the actual data. The newly solved for parameters were the optimal fit for the nonlinear model function. The Mathcad code for this procedure can be seen in the screenshot captured in Figure 5-9.

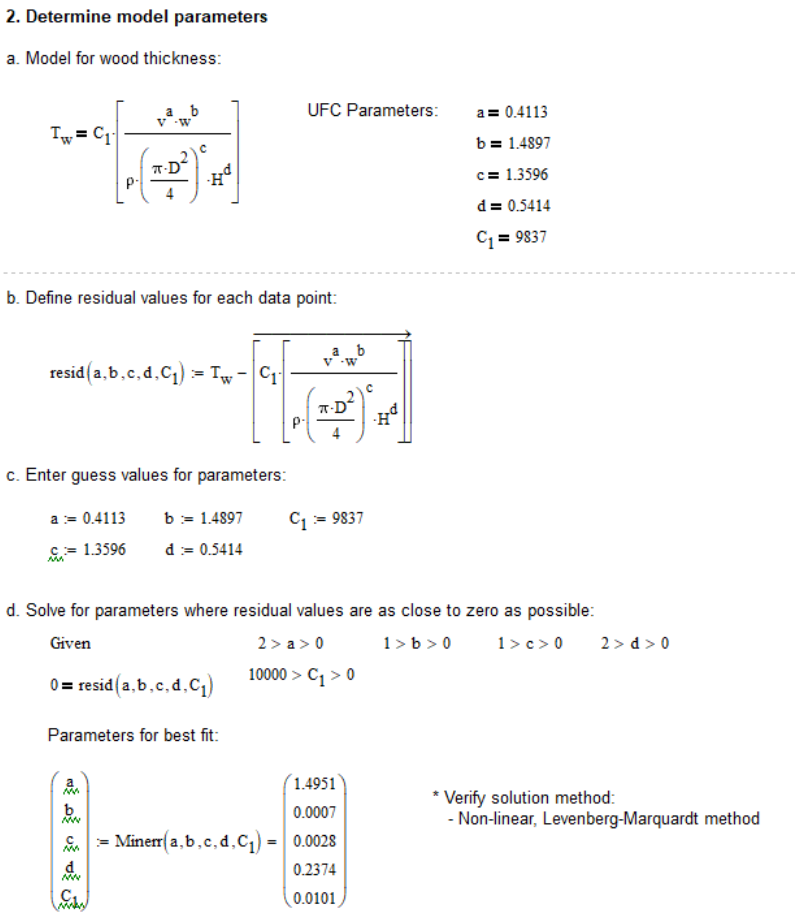

Figure 5-9. Mathcad software aids in use of Levenberg-Marquardt algorithm to solve for parameters.

The goodness of fit of the new parameters can be assessed by the mean squared error (MSE), calculated as shown in Equation 5.4. The MSE examines how close the modeled function with the optimized parameters fits to the set of data points. It takes the distance between the function and the data points, or the errors, and squares them. The squaring step removes any negative signs and gives more weight to larger errors. Then the mean is found to provide the average of the set of errors. The smaller the mean squared error, the closer the function is to fitting the data. A perfect fitting model would have a mean squared error of zero. With some data sets, obtaining a small value for the mean

squared error may be difficult as the data may be widely scattered about the fitting function. In this case, models could be compared for best fit by finding the smallest mean squared error.

$$MSE = \frac{1}{n}\sum_{i=1}^{n}\left(T_{w\_fit} - T_w\right)^2 \tag{5.4}$$

where $\sum\left(T_{w\_fit} - T_w\right)^2$ is the sum of squares minimized by the method (Sum Squared Error)
and *n* is the length of the data set

With a large number of parameters, multiple combinations of parameter values yield equations that fit the data relatively well. In this case, there are five parameters: one constant and four exponential parameters for four of the five variables. Each combination of parameters creates nearly the same curve. Some conditions were set with the initial guess based on the physical representation of the equation and desire to find values close to the UFC parameters as much as possible. For example, negative exponential parameters would have changed how an independent variable affects the dependent variable such as a negative parameter for the weight of the projectile. With a positive parameter, the projectile weight variable stays in the numerator and logically fits with a heavier projectile requiring a larger thickness, whereas a negative parameter would flip that relationship.

Through the recalibration of the UFC equation, a new equation with the same variables was developed from both SPF-S and SYP test data as shown in Figure 5-10. For this empirical model, the parameters where calibrated using the actual density of each tested specimen. For the hardness values in the input data, a reference value was used for each of the two species based on recognized hardness values from the Forest Product

Laboratory's *Wood handbook: Wood as an engineering material [96]*. Hardness values of 475-lb and 750-lb were used for SPF-S and SYP, respectively.

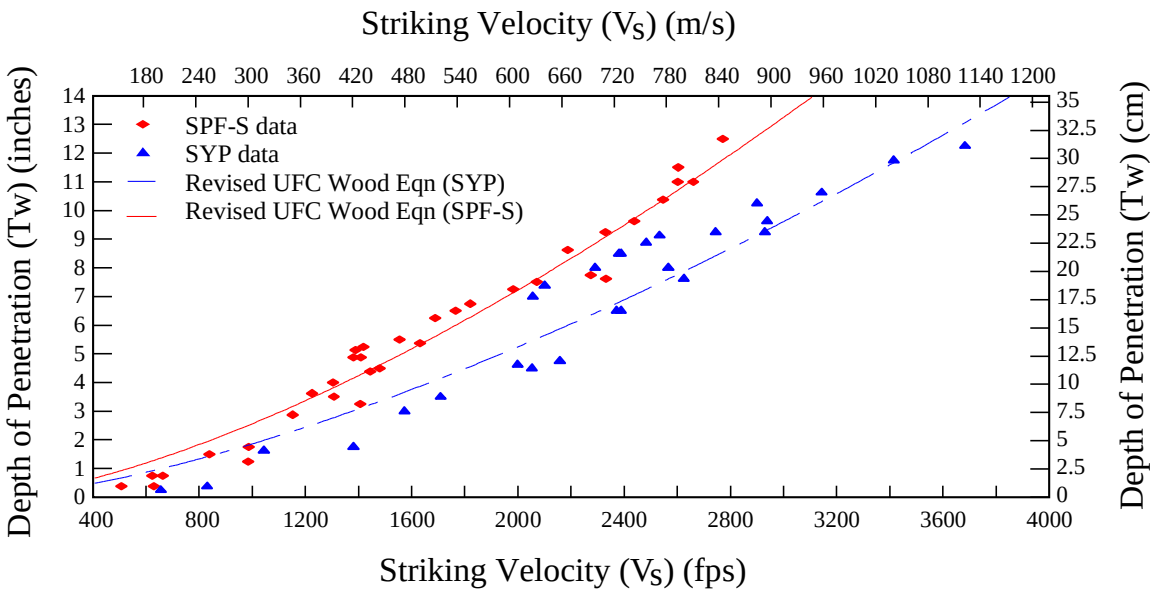

Figure 5-10. Revised UFC Equation recalibrated for CLT data.

Representative densities were used for each species as varying the densities is not possible to represent in the two-dimensional curve. Mean densities of 28.003 pcf and 34.621 pcf were used for SPF-S and SYP, respectively. The MSE for the curve fit model based on the UFC equation was 0.330.

The same procedure for finding the best fitting model parameters using the Levenberg-Marquardt method for finding nonlinear least squares, was used in investigating a recalibrated version of the UFC equation examining one species data at a time. The same hardness values were used as the two species revised UFC model and the model was calibrated with actual density data but plotted using the average density. Figure 5-11 shows

the plot of the SPF-S only revised UFC equation, and Figure 5-12 shows the plot of the SYP only revised UFC equation. Table 5-7 shows the difference in the calibrated model parameters and the MSE for each version of the model.

Table 5-7. Calibrated model parameters and MSE for different revisions of the UFC model.

	Model parameters					
Data set	C_1	a	b	c	d	MSE
SPF-S and SYP	6.91E-06	1.4951	1.4339	0.2009	0.2374	0.330
SPF-S only	417.5111	1.5262	-0.0001	-4.2606E-06	2.0001	0.403
SYP only	1.90E-05	1.4473	1.4873	0.7713	0.5138	0.250

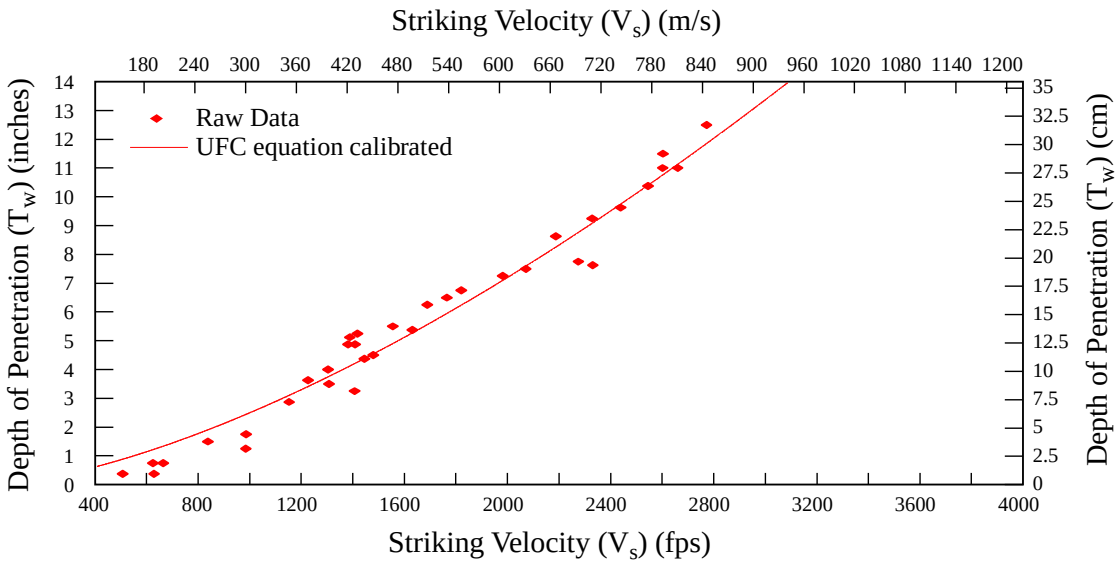

Figure 5-11. SPF-S only revised UFC equation model shown with SPF-S data.

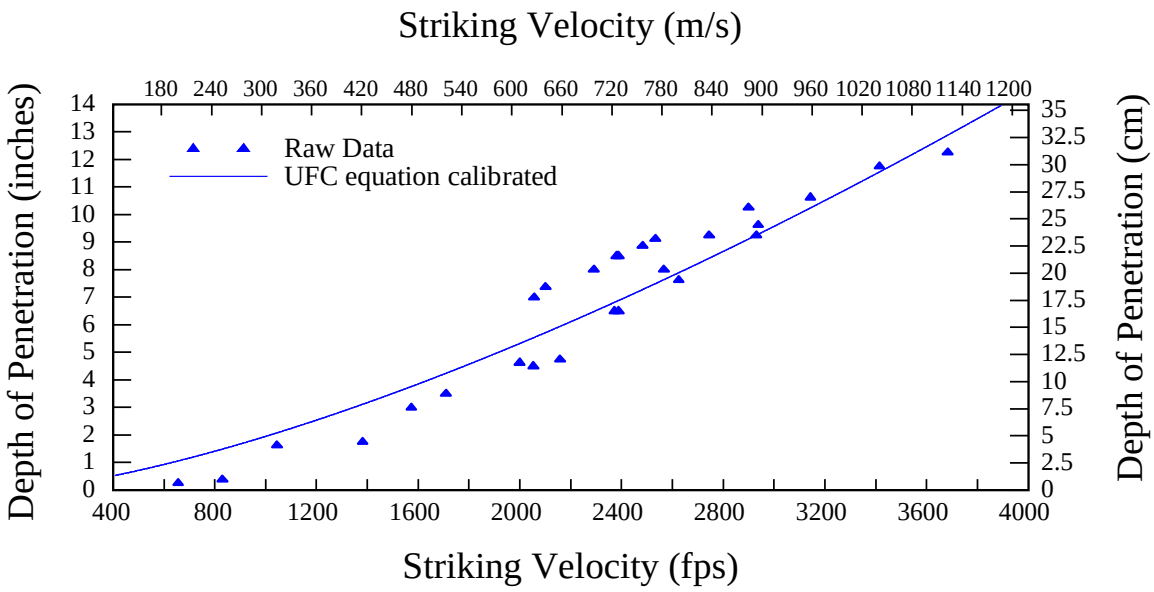

Figure 5-12. SYP only revised UFC equation model shown with SYP data.

It is interesting to note that the MSE is better for the SYP data only model and slightly worse for the SPF-S data only model compared to the original revised UFC model with both data sets. The model parameters vary significantly. Again, it is possible to vary the values of the parameters with different initial guesses or get limitations for the parameters while maintaining the same MSE and curve. The one parameter that does not change is the one associated with the striking velocity, *a*, and this is likely because the striking velocity data varies across a range of values.

The other parameters are associated with the projectile weight, projectile diameter and wood hardness, as well as the constant. These values do not change in the set of experiments and thus they are all acting as constants in the model. With the two species data set, the hardness value varies in addition to the velocity and the parameters for both hardness and velocity, *a* and *d*, do not change like the other variables do with varied

guesses. In order for the model to calibrate a single value to the parameter, the variable needs to vary in the data set, otherwise the variable is simply a part of the constant in the model.

5.5.4 Classical penetration models: physics-based curve fitting models

This research effort also explored the use of several physics-based models that are based on classical penetration equations. These models are applied to the CLT penetration data and examined for goodness of fit. Each of the classical models assessed included striking velocity and constants calibrated to the particular experimental set-up. The classic models explored in this research include the Euler-Robbins model, the Poncelet model with three total variations, and the Resal model.

The equations for these models were developed with the assumptions of a rigid penetrating projectile and a process governed by deceleration. The mass of the projectile was assumed to not change during the penetration event so the acceleration was simply the change in velocity with respect to the change in time, which can be transformed as demonstrated in Equation 5.5.

$$a = \frac{dV}{dt} = v\frac{dv}{dx} \rightarrow dx = \frac{v}{a(v)}dv \tag{5.5}$$

where a = acceleration
v = velocity
x = displacement

The depth of penetration, *P*, can then be obtained by integrating between boundaries as shown in Equation 5.6. The general expression for the deceleration in terms of velocity can be expressed as Equation 5.7, where the constants, *A*, *B*, and *C* are determined

empirically from experimentally testing. The classical penetration models all involved variations of the general expression for deceleration in terms of penetration velocity.

$$P = \int_{V_s}^{0} \frac{v}{a(v)} dv \tag{5.6}$$

where P = depth of penetration, known as T_w in the UFC equation
v = velocity
v_s = striking velocity
a = deceleration

$$-m\frac{dv}{dt} = a(v) = Av^2 + Bv + C \tag{5.7}$$

where m = mass
v = velocity
t = time
a = deceleration
A, B, C = constants

5.5.4.1 Euler-Robbins model

The Euler-Robbins model assumes that deceleration is constant with respect to time [95]. As was used with the UFC equation, the Levenberg-Marquardt method for finding nonlinear least squares was used for determining the model parameters in the Euler-Robbins model for the CLT experimental data. In the Euler-Robbins model, there was only one constant to calibrate. Figure 5-13 shows the curve of the calibrated Euler-Robbins model with the CLT data of both species tested. This model included no material factors or projectile factors other than striking velocity. The MSE was 3.111.

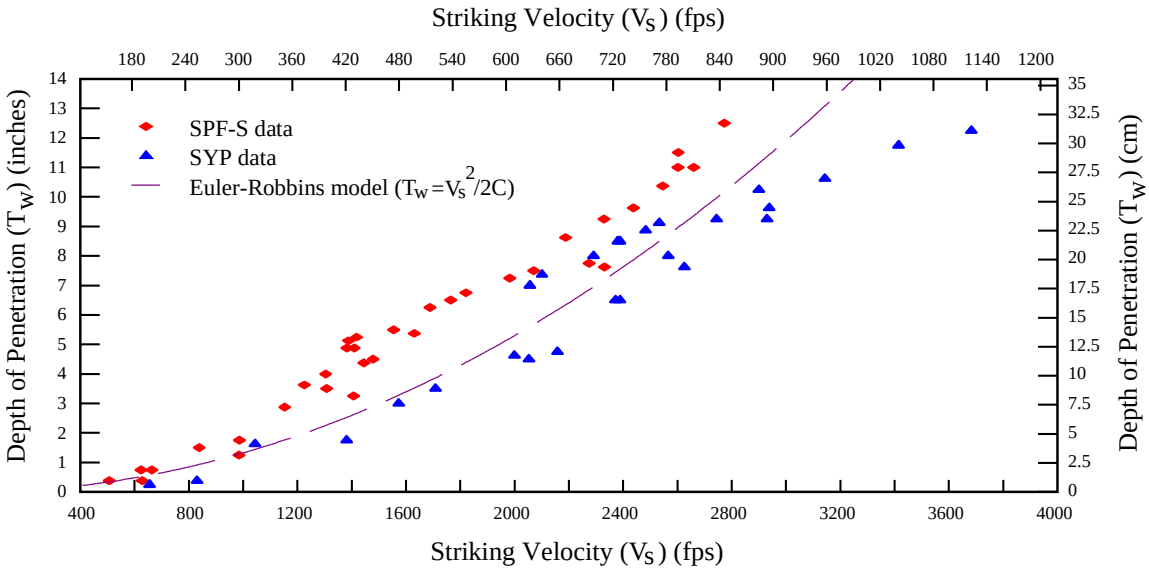

Figure 5-13. Euler-Robbins model calibrated with CLT data.

5.5.4.2 Poncelet models

Poncelet completed notable work in projectile geometry and penetration mechanics [95]. He incorporated kinetic energy and drag terms into the deceleration of a rigid projectile. The base version of the Poncelet equation was also examined with two adjustments, called variant 1 and variant 2 for comparison in this research. In variant 1, the projectile mass and area were incorporated based on variations of the original Poncelet equation. With this version, two constants were calibrated to the data. A second variation, labeled variant 2, is a hybrid of the original Poncelet equation and the variant 1 incorporating the projectile factors, while also keeping just one calibrating constant. Table 5-8 shows the equations, constants, factors included, and the MSE for each of the three Poncelet models calibrated. The base model fit better than the Euler-Robbins model with an MSE of 1.345 but the two variations both had higher MSE values closer to the fit of the Euler-Robbins model with 3.356 for variant 1 and 3.000 for variant 2.

Table 5-8. Variations of Poncelet equations calibrated to CLT data.

Model	Equation	Constants	Factors Included	MSE
Poncelet (base)	$T_w = \left[\frac{1}{2B}\ln\left(1+\frac{Bv_s^2}{C}\right)\right]$	B, C	Striking Velocity, 2 constants	1.345
Poncelet variant 1	$T_w = \left[\frac{1}{2c_1B}\ln\left[\frac{c_0+c_1v_s^2}{c_0}\right]\right]$ where $B = \frac{A_{cs}}{m}$	c_0, c_1	Striking Velocity, projectile area and projectile weight, 2 constants	3.356
Poncelet variant 2	$T_w = \left[\frac{1}{2B}\ln\left(1+\frac{Bv_s^2}{C_1}\right)\right]$ where $B = \frac{A_{cs}}{m}$	C_1	Striking Velocity, projectile area, projectile weight, 1 constant	3.000

Figure 5-14 shows the plotted equation of the Poncelet model with the experimental data. Since the data that the model was calibrated to include both SPF-S and SYP, the equation plots as a line between the two data sets. This model does not include the different density or hardness values, or any target material factors. Variant 1 and variant 2 include the projectile cross-sectional striking area, A_{cs}, and projectile mass, m, through the term B. Figure 5-15 and Figure 5-16 show the two variants and Figure 5-17 shows a graphical comparison of all three versions of the Poncelet equation model.

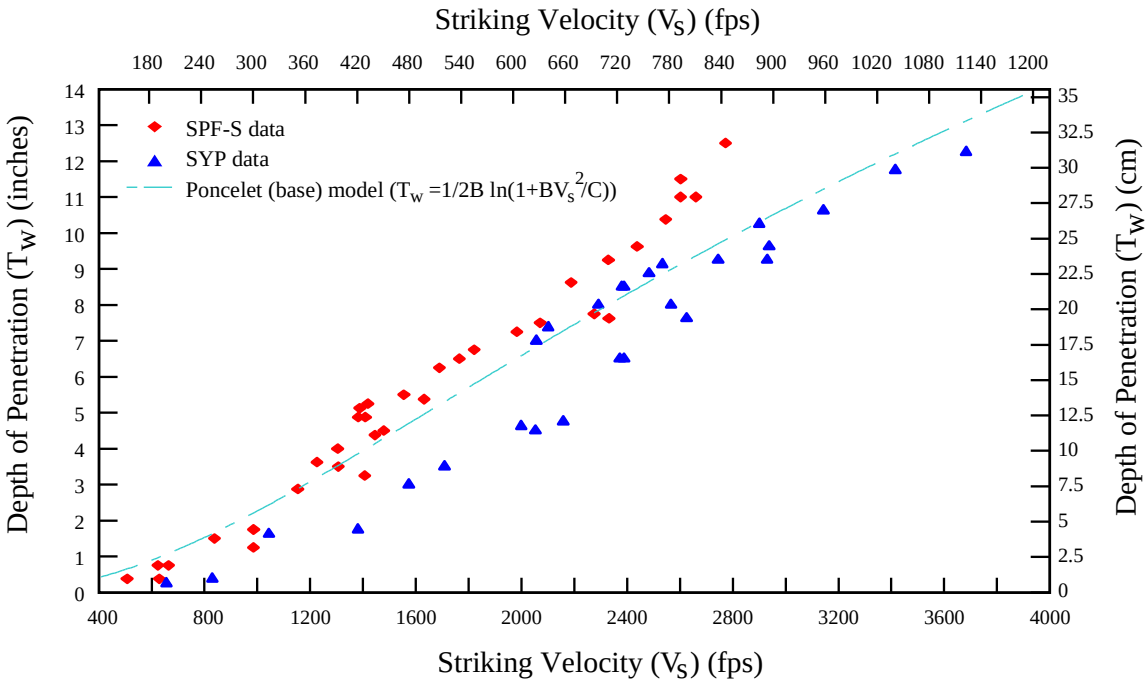

Figure 5-14. Poncelet equation calibrated to CLT data.

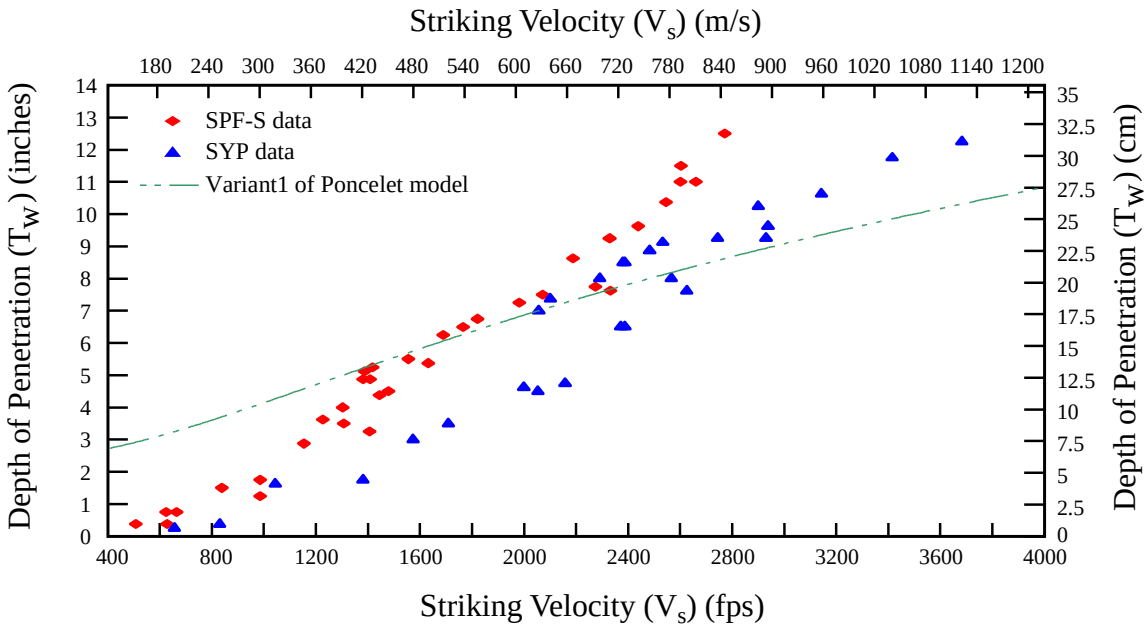

Figure 5-15. Variant 1 of the Poncelet equation calibrated to CLT data.

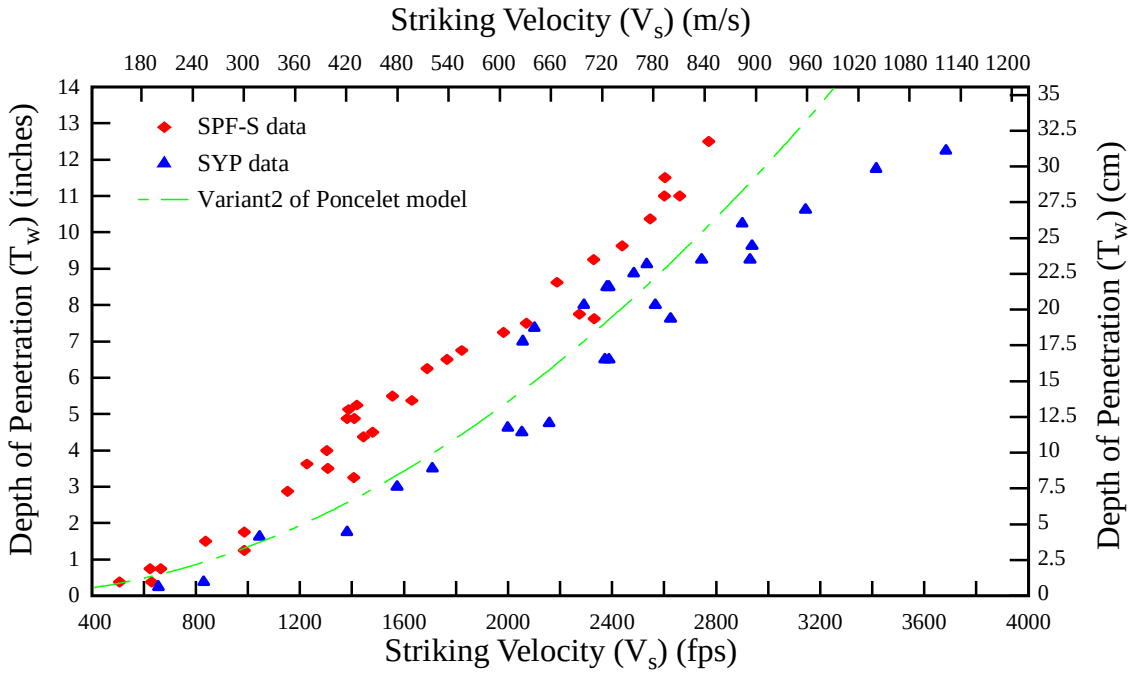

Figure 5-16. Variant 2 of the Poncelet equation calibrated to CLT data.

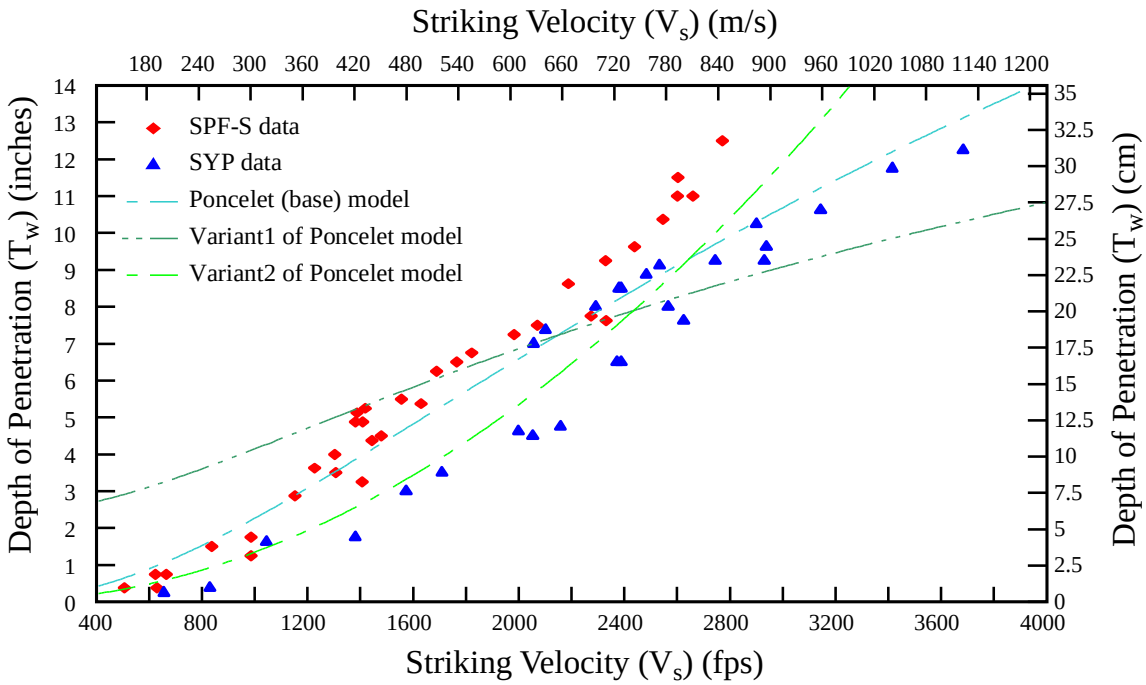

Figure 5-17. A comparison of the variations of Poncelet equation models calibrated to the CLT data.

The comparison of the three variations of the Poncelet equation show how relatively small changes to the calibrated equation can vary the shape and fit of the model significantly.

5.5.4.3 Resal model

The last classical model investigated for this work was based on the work of Resal. His equation was similar to Poncelet's except that the two engineers differed in their beliefs on which coefficients were zero in the deceleration calculation. Equation 5.7 previously showed the general version of the deceleration. Resal believed the value for C in the equation was zero but that A and B both had values while Poncelet believed B to be zero.

The Resal model incorporated two constants but no material variables about the target material or the projectile besides the striking velocity. Figure 5-18 shows the curve of the Resal model calibrated to the CLT data. The MSE of this model was 1.345, the same as the value for the base Poncelet model.

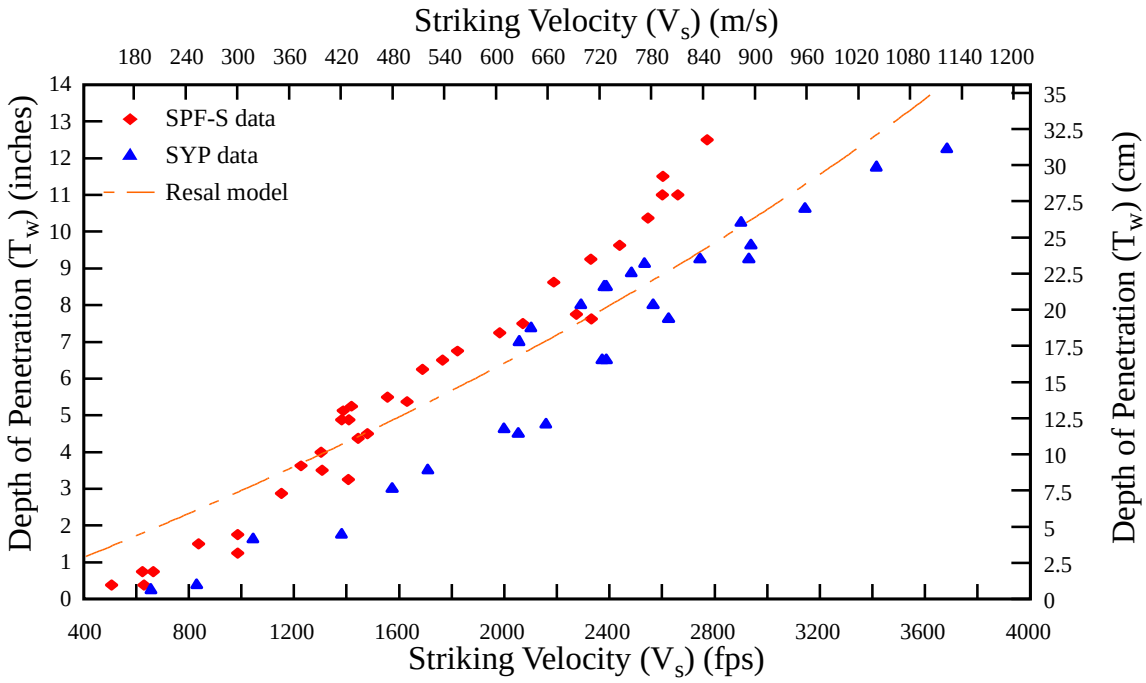

Figure 5-18. Resal equation calibrated to the CLT data.

5.5.4.4 Classical model comparison

All three classic penetration models take the physics of the deceleration into account when solving for the depth of penetration. Table 5-9 shows the different equations, constants, included factors, and the MSE for each of the classic models calibrated to the CLT data. While the shape of the curves varied, there were similarities such as a concave upward shape. Figure 5-19 presents a graphical comparison of the three classical physics-based curves.

Table 5-9. A comparison of three classic penetration models.

Model	Equation	Constants	Factors Included	MSE
Euler-Robbins	$T_w = \left[\frac{v_s^2}{2C_1}\right]$	C_1	Striking Velocity, 1 constant	3.111
Poncelet (base)	$T_w = \left[\frac{1}{2B}\ln\left(1+\frac{Bv_s^2}{C}\right)\right]$	B, C	Striking Velocity, 2 constants	1.345
Resal	$T_w = \frac{1}{B}\ln\left(1+\frac{Bv_s}{C}\right)$	B, C	Striking Velocity, 2 constants	1.345

It is interesting to note that the Poncelet and Resal models trend along the same values for required depth of penetration for the striking velocity range of 1,600 to 3,200 fps (480 to 960 m/s). Additionally, within this range, at approximately 2,600 fps (780 m/s) the Euler-Robbins model predicts the same value for depth of penetration as the other two models.

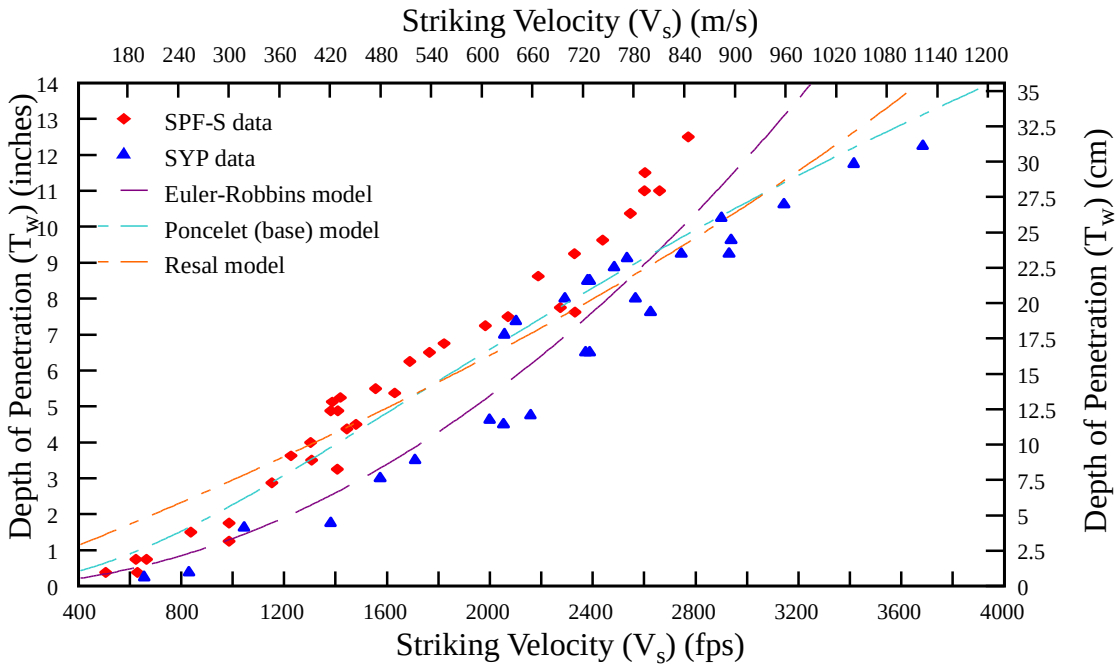

Figure 5-19. A comparison of the three classic penetration models calibrated to CLT data.

5.5.5 Force Law Model

Based on the classical equations with variations on the deceleration equation, an additional physics-based model was developed and calibrated to the CLT data. This model was based on the concept of a resisting force of the target specimen reducing the velocity of the projectile. This resisting force acts as an external force on the projectile compelling it to reduce its velocity or even stop completely. The resisting force is included as a general quadratic form and the residual velocity (v_r) can be calculated as shown in Equation 5.8.

$$v_r = v_s - ax^2 - bx - c \tag{5.8}$$

where
v_r = residual velocity (fps)
v_s = striking velocity (fps)
x = distance traveled in target (in)
a,b,c = model constants

When the CLT specimen stopped the projectile and the residual velocity was zero the equation can be rewritten and solved for the distance, *x*, as shown in Equation 5.9.

$$x = \frac{\frac{\sqrt{b^2 + 4v_s a - 4ac}}{2} - \frac{b}{2}}{a} \tag{5.9}$$

where v_s = striking velocity
x = distance traveled in target
a, b, c = constants

If the depth of penetration is considered *x* is the distance traveled in the target.

Equation 5.9 was calibrated to the CLT ballistic data, creating an empirical, physics-based model. Using the Levenberg-Marquardt method, the parameters were found for the force law model. This model considered no material factors for the target or the projectile other than striking velocity. Figure 5-20 shows the curve of the model fit to the CLT data.

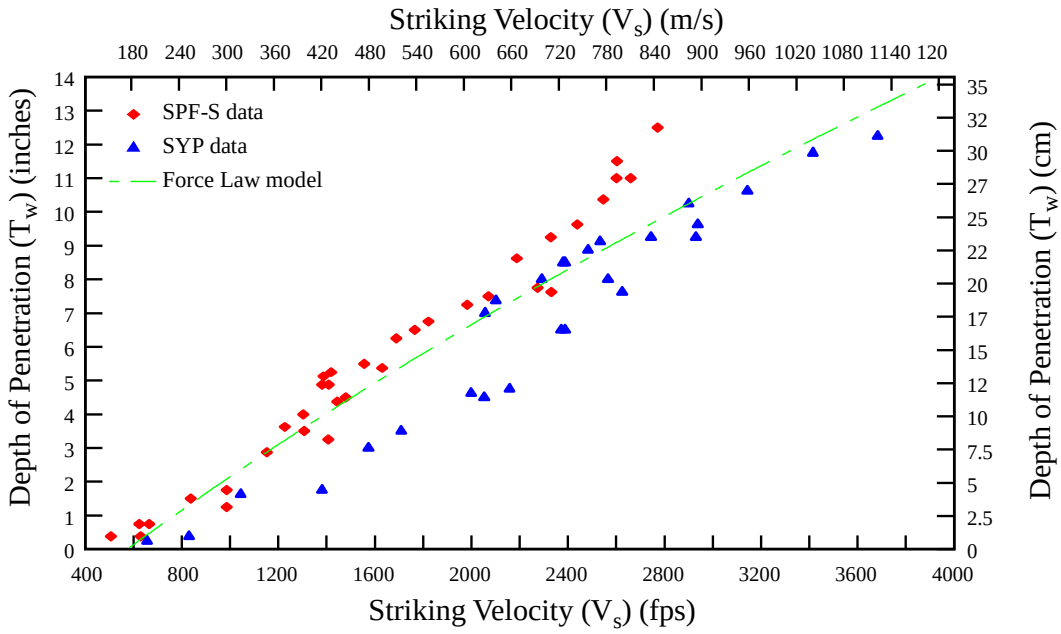

Figure 5-20. The force law model shown calibrated to the CLT data.

It is interesting that the shape of the curve is concave downward, the opposite of the other model curve shapes. However, the fit of this model to the data is generally good with an MSE value of 1.322. Since the model was fit to the data of both species, the curve generally lies between the two sets of data points. This model was further investigated with the data of each species independently, similar to the revised UFC equation. Figure 5-21 shows the force law model fitted to the SPF-S data. The shape of the curve is again concave upward. Figure 5-22 shows the model fitted to the SYP data.

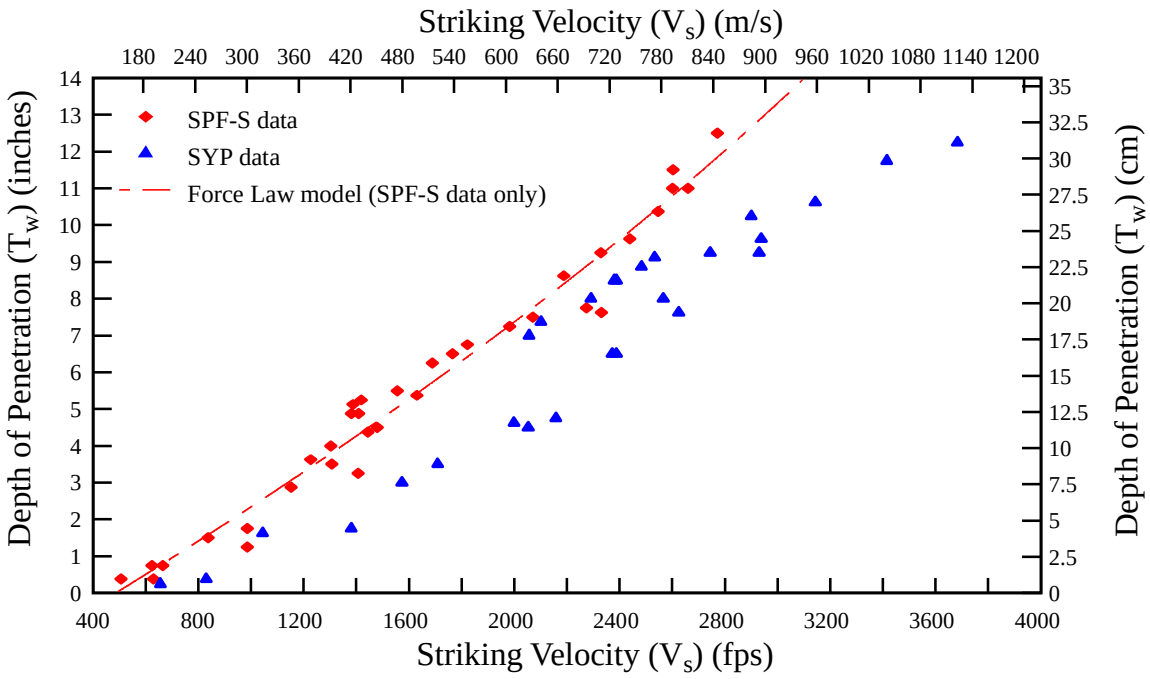

Figure 5-21. The force law model calibrated to the SPF-S data only.

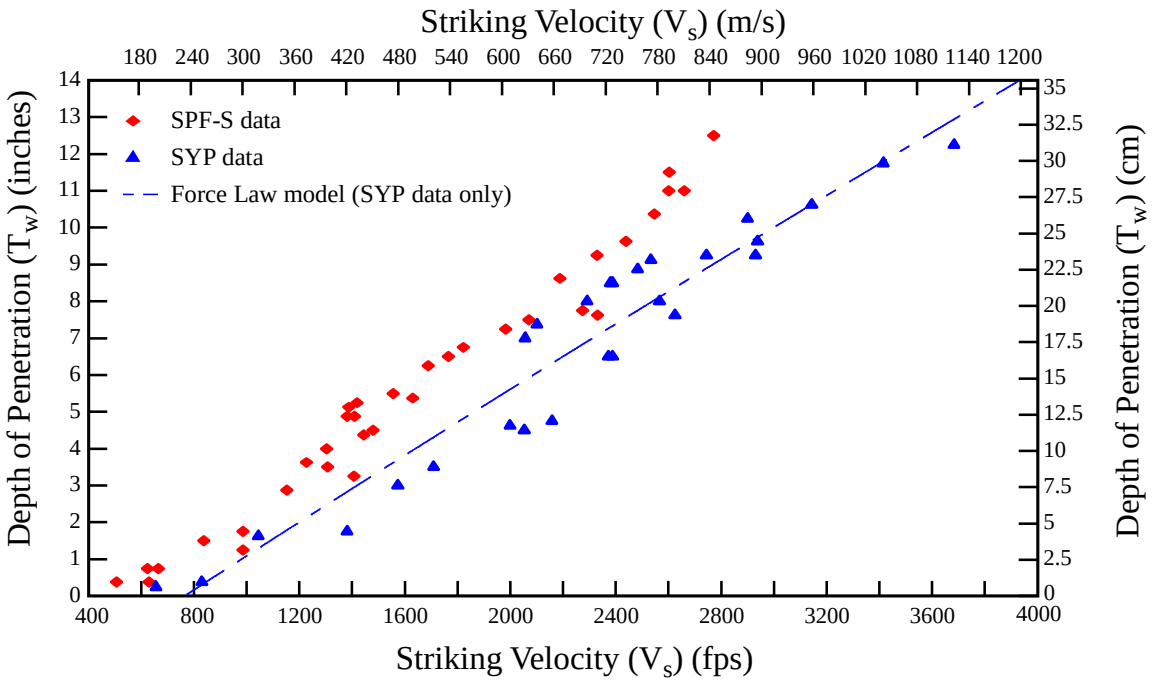

Figure 5-22. The force law model calibrated to the SYP data only.

The models fit to the independent species data sets have lower values of MSE. Table 5-10 shows the model parameters of best fit and MSE for all three data sets calibrated to the force law model. The negative value for the *a* parameter in the SPF-S only model is the reason for the curve direction. Figure 5-23 shows all three versions of the force law model curve and the data.

Table 5-10. Calibrated model parameters and MSE for different calibrations of the force law model.

Data set	Model parameters			MSE
	a	b	c	
SPF-S and SYP	3.5586	190.4839	574.7253	1.322
SPF-S only	-2.7972	226.0455	485.5625	0.333
SYP only	0.7293	216.1392	762.7897	0.839

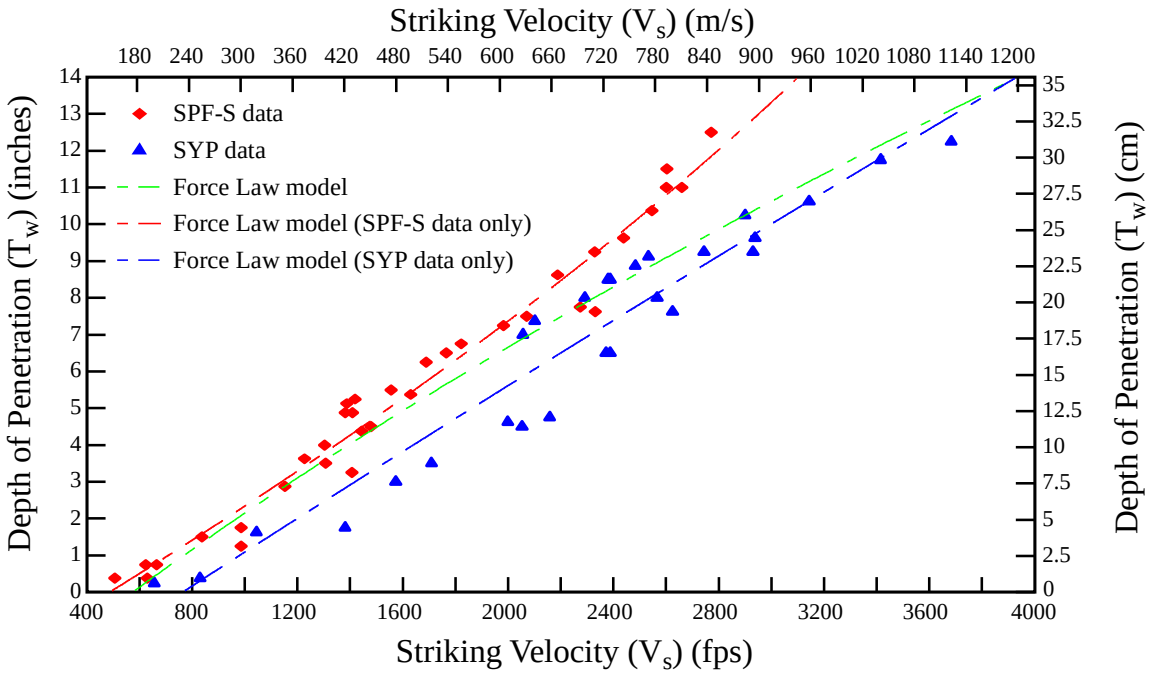

Figure 5-23. The force law model calibrated to different data sets.

5.5.6 General THOR model

The previously discussed, the THOR reports define a general THOR equation for penetration calculations of empirical models based on testing [2]. The general THOR equation is shown in Equation 5.10.

$$v_r = v_s - 10^c (eA)^\alpha m_s^\beta (\sec\theta)^\gamma v_s^\lambda \tag{5.10}$$

where
v_r = residual velocity (fps)
v_s = striking velocity (fps)
e = target thickness (in), T_w in this research
A = average impact area (in^2)
m_s = weight of original projectile (grains)
θ = angle of obliquity
$c, \alpha, \beta, \gamma, \lambda$ = constants

The projectiles used in the THOR research were steel fragments and experimental data was characterized by fragment size, striking velocity and angle of obliquities. The intent of the

empirical formulas was to fit them to the data for each target material, which allowed for a comparison of resistance of materials to perforation and a calibration of material resistance and thickness a projectile could penetrate.

The general THOR equation shown in Equation 5.10 can be rewritten for conditions when the residual velocity is zero as there is no perforation. The scope of this research is limited to normal impacts, an angle of obliquity of zero, which simplifies the formula and allows for exclusion of that variable, θ, and its associated parameter, γ. Next, the equation can be rearranged to solve for the thickness at which the residual velocity is zero, as shown in Equation 5.11. By using the same nonlinear least square fitting method as the previous models and the experimental data from the CLT tests, the equation parameters can be calibrated for the material.

$$T_w = \frac{1}{A}\left(\frac{v_s^f}{10^g w^h}\right) \tag{5.11}$$

where T_w = thickness required
A = projectile impact area
v_s = striking velocity
w = projectile weight
f,g,h = constants

Figure 5-24 shows the general THOR model calibrated to the CLT data. This model, using both species data sets, had a MSE value of 1.532.

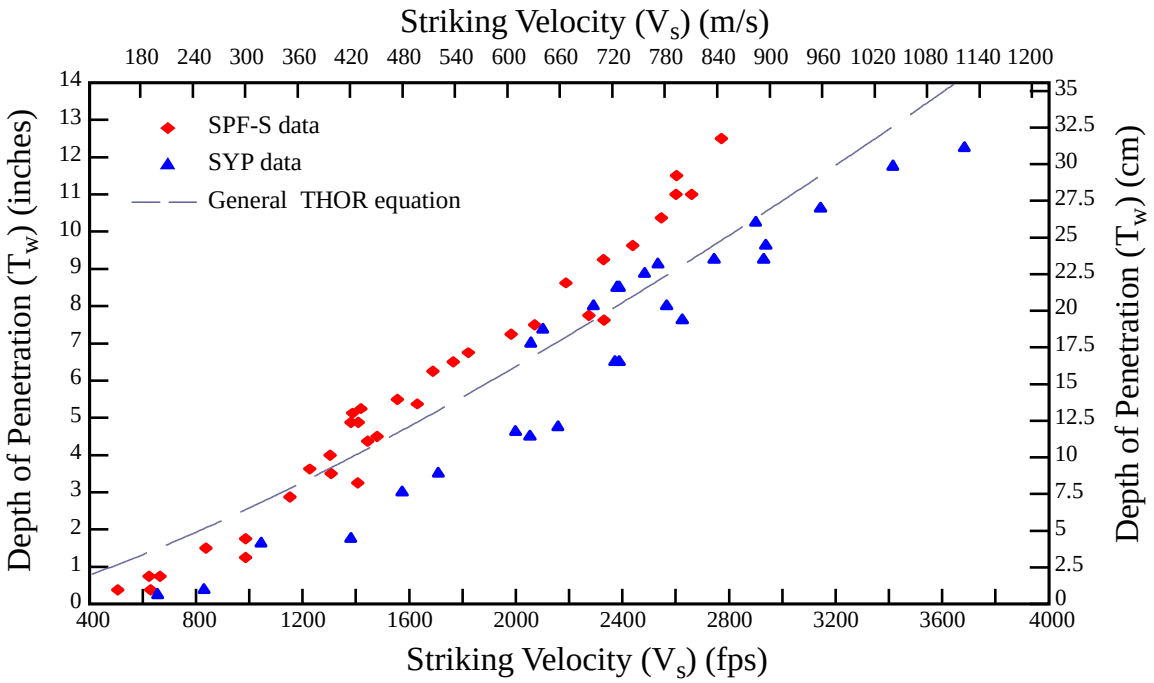

Figure 5-24. The general THOR equation calibrated to the CLT data.

The THOR reports explained how for fragments of a given shape the formula could be simplified with the removal of the impact area term, *A*. This can be done for the THOR model calibrated to the CLT data as well. The curve and MSE for the simplified THOR model are the same as the values for the general THOR model. This is because the projectile area is a constant for the given data set. As discussed previously with the revised UFC models, the calibrated parameters adjust based on the data. Since the weight of the projectile, *w*, is constant, the *g* and *h* parameters in the model equation simply adjust to keep the plotted curve fitting the data with the absence of the additional constant of *A*. A comparison of the general THOR model to the classical penetration models and force law model is shown in Figure 5-25. The yellow lines on the plot mark a range of striking velocities, approximately 1,400 fps to 3,100 fps (420 to 950 m/s) where all of the models except the Euler-Robbins models generally track along the same values.

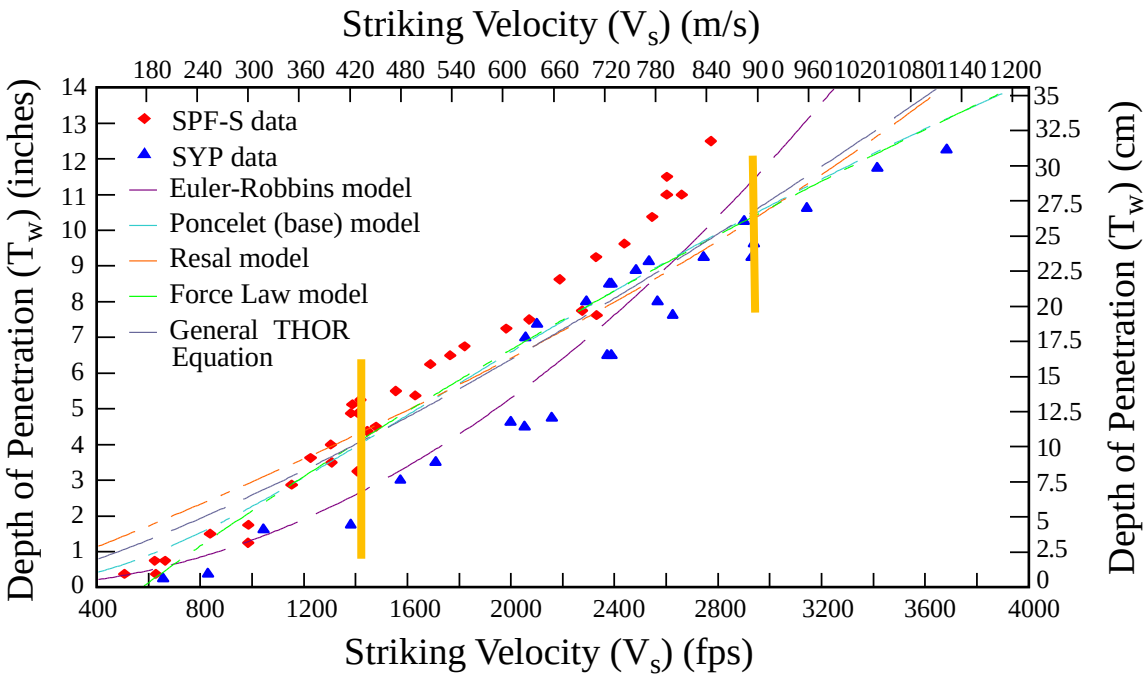

Figure 5-25. The general THOR model compared to previous models.

5.5.7 CLT THOR-based Model

Since the general THOR equation is an empirical formula that is curve fit to data, it is possible to include additional variables of interest with little difficulty. This led to the development of a new CLT model based on the general THOR equation but with the addition of the target density and a strength parameter, wood hardness. Using the same procedure as the previously examined model, the revised THOR equation was fit to the data. Since it was observed in previous models and documented in the THOR reports that unchanging variables could effectively be excluded from the curve-fitting model for simplification, the variable for projectile weight was removed. Removal of the projectile weight from the equation simply adjusted the equation's resulting constant. Because the same projectile weight was used in all tests, inclusion in the model simply acts as an additional constant instead of a calibrating parameter.

Equation 5.12 is the CLT THOR-based equation developed for the CLT experiments. The equation includes the striking velocity of the projectile but no other projectile variables since the same projectile was used for the entire data set. It also includes the density and hardness values of the CLT specimens. Similar to the UFC recalibration, the hardness values are reference hardness values and the densities are the actual density of each individual specimen.

$$T_w = C_1 \left(\frac{{v_s}^a}{10^c \rho^d H^f} \right) \tag{5.12}$$

where
T_w = thickness required to stop perforation
v_s = striking velocity
ρ = density of wood
H = hardness of wood
C_1, a, c, d, f = constants

The curve shown in Figure 5-26 is based on an average wood density for each species. Figure 5-26 shows the general THOR curve in addition to a curve for each species of CLT specimens included in the experiments. For the THOR-based CLT model fit to the CLT data the MSE is 0.303.

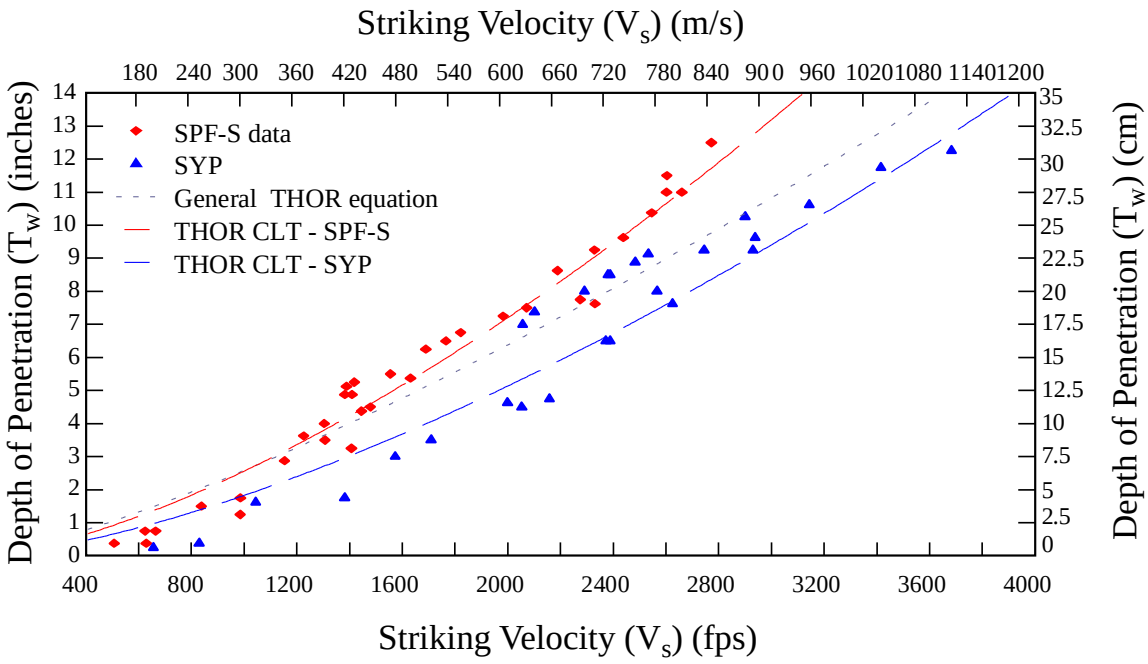

Figure 5-26. A new THOR-based model for CLT calibrated to the CLT data.

As examined with the revised UFC equation and the force law model, the THOR wood model was also investigated with single species data sets. Figure 5-27 shows the SPF-S only THOR wood model. The MSE for this calibration was 0.402, slightly worse than the model incorporating both data sets. Figure 5-28 shows the SYP only THOR wood model. The MSE for this calibration was 0.190, slightly better than the models for both species data. It should be noted that the THOR-based wood model looks very similar to the UFC wood equation. This makes sense since the equation was based on the THOR reports and methodology.

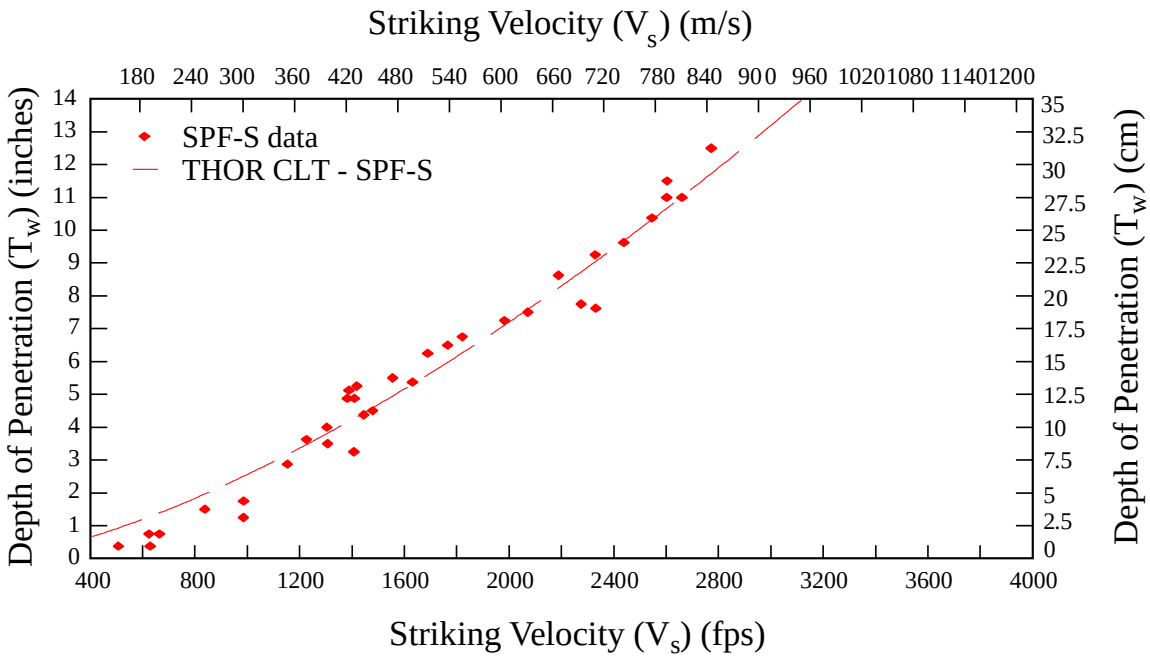

Figure 5-27. The THOR-based CLT model recalibrated to the SPF-S data only.

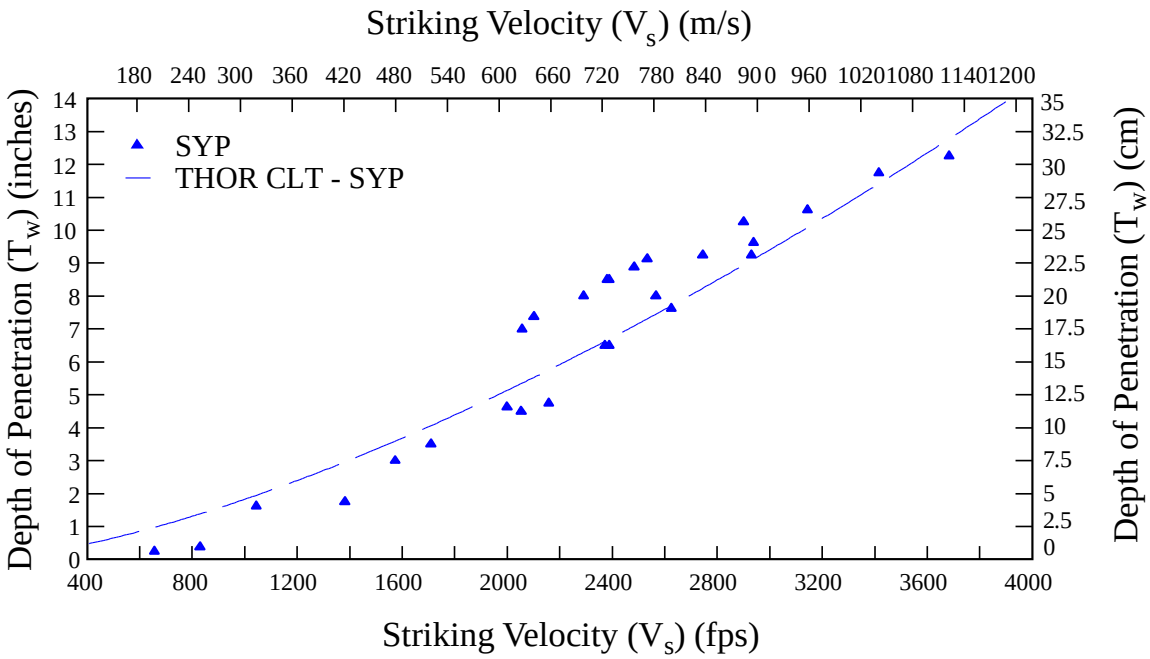

Figure 5-28. The THOR-based CLT model recalibrated to the SYP data only.

5.5.8 Empirical model comparison and recommendations

When investigating a new material for ballistic penetration resistance, such as CLT, experimental testing is a critical first step. Testing helps build a database of parameters and responses, which can be used to develop empirical models either through curve-fitting or applying physics-based methods. These models can in turn guide additional useful testing to help create addition models, eventually ideally leading to analytical models [126]. The classical penetration mechanics models of Euler-Robbins, Poncelet and Resal, along with the force law model are all physics-based empirical models. The force law model demonstrated the best fitting model both with the combined species data set and the individual species fit independently. The THOR models and the UFC model are curve-fitting empirical models. The THOR-based CLT model had a slightly better fit than the revised UFC equation, and both of those wood-specific models fit better than the more general THOR model as they both incorporate specific wood characteristic variables.

Based on this dataset, it is recommended that the THOR CLT model be used for velocity ranges of 400 to 3,000 fps (120 to 910 m/s) given CLT of a thickness of 4-in. or thicker and a 0.50-in. sphere projectile. Different weight, diameter, or nose shape projectiles could use a similar model but it would require recalibration of the model parameters. Additionally, for design purposes, a factor of safety should be implemented when determining how thick a CLT panel should be used against a specific munition as there is variability in both the velocity of ballistic projectiles and in the wood material. Table 5-11 lists the equation, constants, factors and MSE for the models investigated and calibrated in this research.

The classical penetration mechanics models of Euler-Robbins, Poncelet and Resal, along with the force law model are all physics-based empirical models. The force law model demonstrated the best fitting model both with the combined species data set and the individual species fit independently. The THOR models and the UFC model are curve-fitting empirical models. The THOR-based CLT model had a slightly better fit than the revised UFC equation, and both of those wood-specific models fit better than the more general THOR model as they both incorporate specific wood characteristic variables.

Based on this dataset, it is recommended that the THOR CLT model be used for velocity ranges of 400 to 3,000 fps (120 to 910 m/s) given CLT of a thickness of 4-in. or thicker and a 0.50-in. sphere projectile. Different weight, diameter, or nose shape projectiles could use a similar model but it would require recalibration of the model parameters. Additionally, for design purposes, a factor of safety should be implemented when determining how thick a CLT panel should be used against a specific munition, as there is variability in both the velocity of ballistic projectiles and in the wood material.

Table 5-11. Comparison of all models calibrated to CLT data.

Model	Equation	Constants	Factors Included	MSE
Euler-Robbins	$T_w = \left[\frac{v_s^2}{2C_1}\right]$	C1	striking velocity, 1 constant	3.111
Poncelet (base)	$T_w = \left[\frac{1}{2B}\ln\left(1+\frac{Bv_0^2}{C}\right)\right]$	B, C	striking velocity, 2 constants	1.345
Resal	$T_w = \frac{1}{B}\ln\left(1+\frac{Bv_0}{C}\right)$	B, C	striking velocity, 2 constants	1.345
Force Law model	$T_w = \frac{\frac{\sqrt{b^2+4v_s a-4ac}}{2}-\frac{b}{2}}{a}$	a,b,c	striking velocity, 3 constants	All: 1.322 SPF-S: 0.333 SYP: 0.839
General THOR model	$T_w = \frac{1}{A}\left(\frac{v}{10^g w^h}\right)$	f,g,h	striking velocity, projectile area, projectile weight, 3 constants	1.532
CLT THOR model (revised)	$T_w = C_1\left(\frac{{v_s}^a}{10^c \rho^d H^f}\right)$	C_1,a,c,d,f	striking velocity, projectile weight, target density, target hardness, 5 constants	All: 0.303 SPF-S: 0.402 SYP: 0.190
Revised UFC model	$T_w = C_1\left[\frac{\left(v^a w^b\right)}{\rho\left(\frac{\pi D^2}{4}\right)^c H^d}\right]$	a,b,c,d,C_1	striking velocity, projectile weight, projectile area, target density, target hardness, 5 constants	All: 0.330 SPF-S: 0.403 SYP: 0.250

It is important to note that while the curves developed with these models appear to continue on to predict more wood thickness required at high velocities, these models likely do not apply in the hypervelocity range. For this research, the velocity ranges evaluated are limited to the intermediate velocity range, such as those seen with munitions projected from conventional weapons systems. Further evaluation would be needed for hypervelocity ranges and it is likely that an upper bound exists for these models.

Additionally, none of these models incorporate factors for the nose shape of the projectile. This is a known impacting factor in the ability of the projectile to penetrate for munitions and weapons design. Subsequently ballistic testing with rounds of different nose shape, such as ogive and spherical and blunt, would provide more insight on ballistic resistance capability.

5.6 Residual velocity data analysis

5.6.1 Striking velocity range

Ninety-five tests were conducted that resulted in complete penetrations and a corresponding residual velocity. The majority of the tests yielding residual velocity data also fell within a smaller band of striking velocities, as shown in Figure 5-29. Ballistics testing is inherently variable as even factory-produced munitions shoot at a range of velocities. The goal with these experiments was to shoot multiple shots and multiple specimens at the same approximate striking velocity for comparison. A small range in striking velocity allowed for examining the variability of residual velocity occurring with the non-homogenous wood target. In this case, the target striking velocity was 2,500 fps (762 m/s).

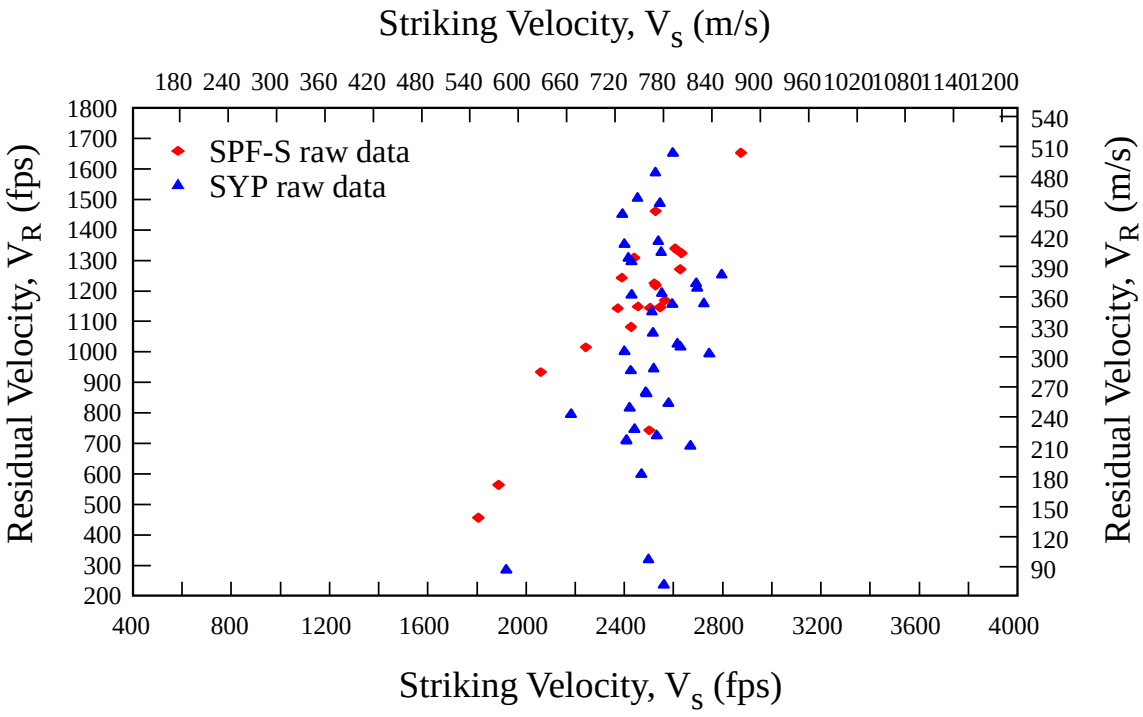

Figure 5-29. Residual velocity based on striking velocity for CLT specimen tests.

Residual velocity data was collected from both the SPF-S and SYP CLT types. Additionally, there were both 3-ply and 5-ply thick specimens for the SYP and 5-ply specimens for the SPF-S. Since most of the specimens were the same thickness and with a small range of striking velocities, attempts to calibrate a model to the residual data set resulted in nonsensical curves and high MSE values in the range of 5000. Ideally, for model calibration as completed with the depth of penetration data more specimens of different thickness, or ply numbers with residual velocity data are needed to fill out more of the curve in terms of different thicknesses of CLT reducing the velocity by different amounts.

5.6.2 Residual data and expected velocity curves from force law model

While the collected residual velocity would not allow for development or calibration of its own fitted model, the previously developed models could be used in combination with the residual data. Figure 5-30 shows a series of curves with each line corresponding to a different striking velocity, which is the velocity at a depth of zero, or the face of the target. As the projectile travels through the CLT specimen, the velocity decreases until it is stopped or exits the back of the target at some residual velocity.

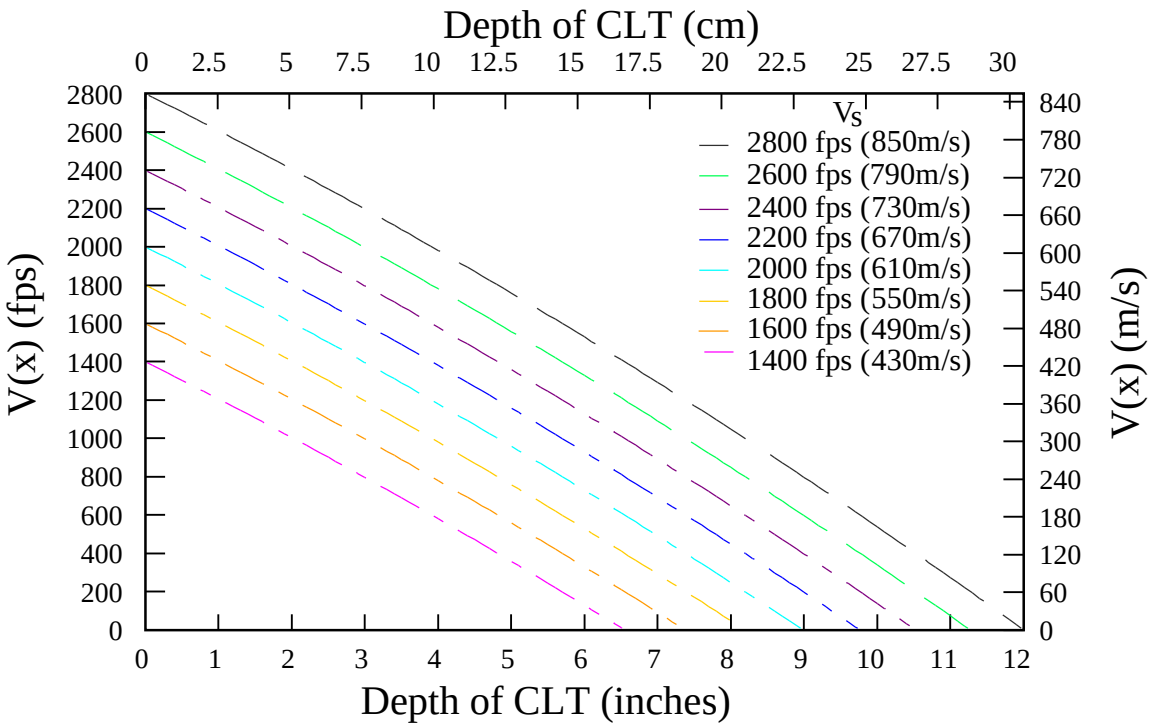

Figure 5-30. Projectile velocity in terms of depth traveled into CLT target.

The shape of the curves in Figure 5-30 is based on the force law model parameters, which were calibrated with both SPF-S and SYP data. Since the force law model was also calibrated for each individual species, the same plot can be made for made for both SPF-S and SYP. The residual data can then be added to these plots with two points for each test shot: the striking velocity at a depth of zero and the residual velocity that was measured at a depth equal to the thickness of the specimen. Figure 5-31 shows the expected velocity curves with several residual data points plotted for SPF-S. The x-axis is adjusted to better show the data at zero or the target striking face.

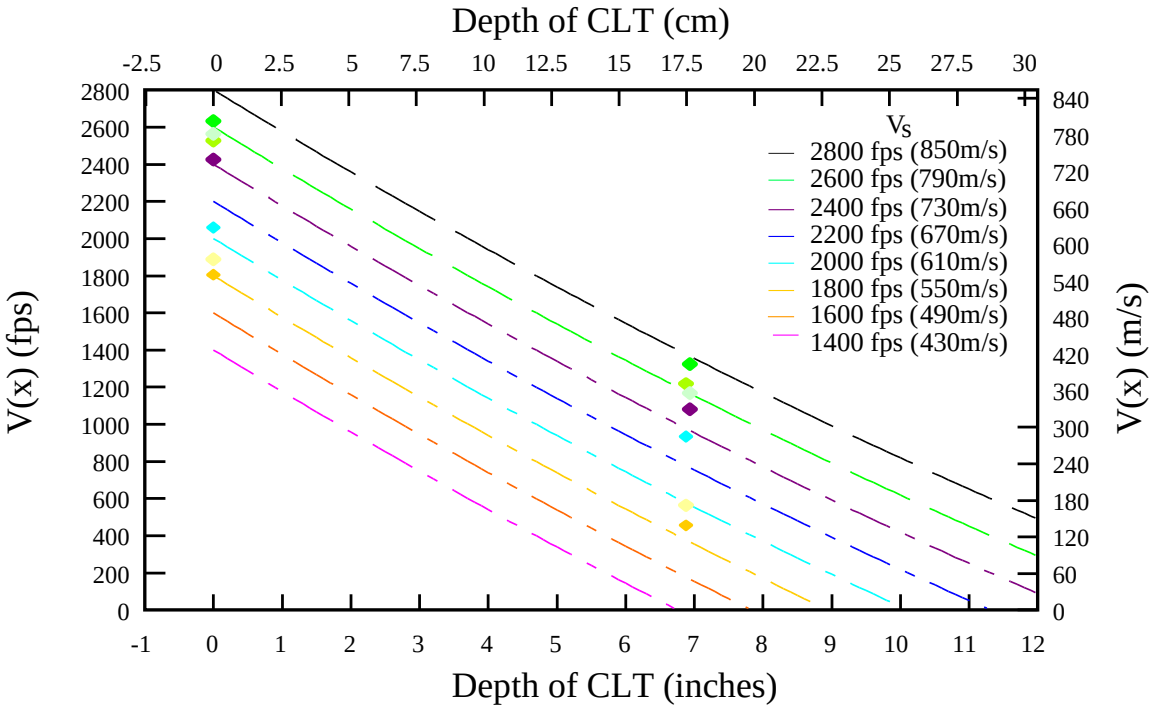

Figure 5-31. Expected velocity by depth curves for SPF-S with residual data plotted.

The color of the data point corresponds to the approximate striking velocity. Thus, the data points should align to the matching colored line. If the striking velocity was in between two striking velocity curves the residual velocity data was colored in a different shade of the color to the closest velocity curve line. For the SPF-S curves, the residual data consistently plotted above its corresponding curve, which indicates that the residual velocity was faster than the modeled curve.

Figure 5-32 shows the expected velocity curves and plotted residual data for SYP. For the SYP curves, five of the residual data points plot below or on the expected velocity curves and two plot above. This indicates that the model performs better for the SYP species than the SPF-S species in terms of predicting residual velocity.

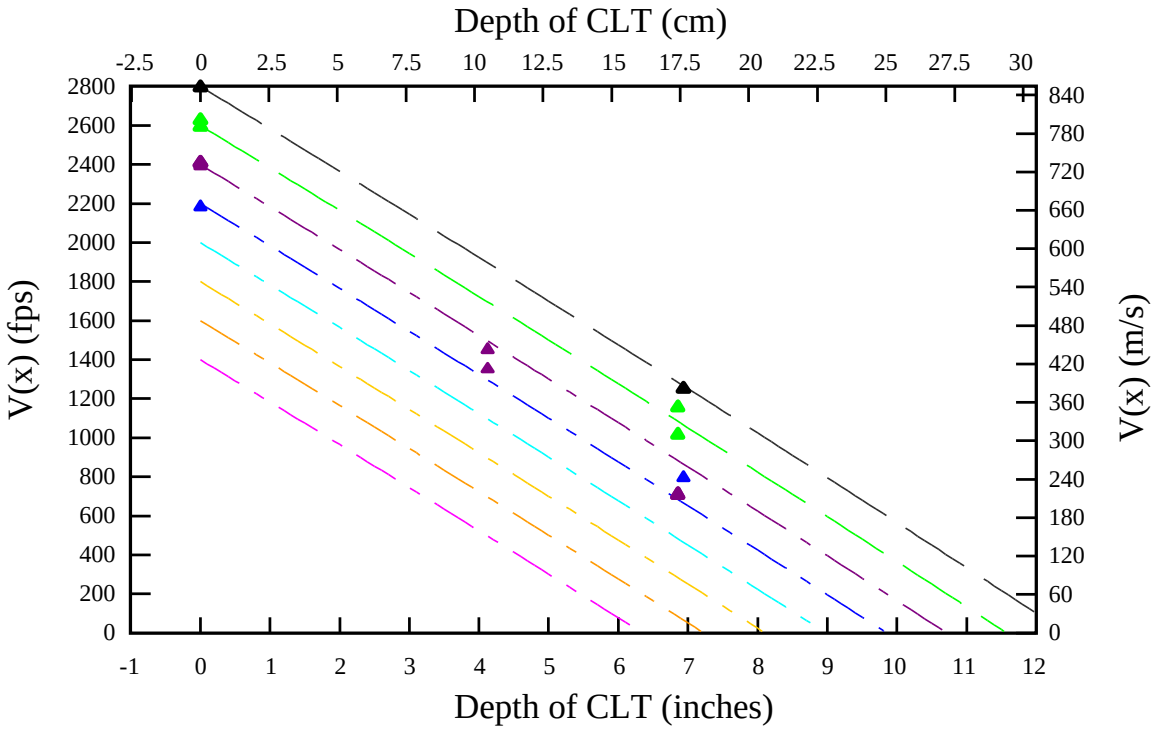

Figure 5-32. Expected velocity by depth curves for SYP with residual data plotted.

5.7 Weathered Specimens

Since the use of CLT panels for temporary military structures would mean the panels would potentially be exposed to the environment, there was interest in whether the ballistic resistance of the CLT would be impacted by specimens of an increased moisture content. Elevated moisture contents of the specimens represented panels that were minimally treated or untreated and therefore exposed to rain, snow and humidity. This is significant because the typical use of CLT is as superstructure elements within the interior of the building envelope with no exterior exposure.

One 5-ply test block of each wood type was placed in a fog room for three days and a second 5-ply test block was submerged in a bucket of water for thirteen days. The purpose of these treatments was to elevate the moisture content of the specimens. The original moisture contents of the four blocks prior to the weathering treatments were in the range of 11 to 13 percent. The fog room was 70 degrees Fahrenheit and 100 percent humidity. Since there was no mechanism to measure the interior moisture content within the specimens, the weight of the blocks were measured periodically and the increase in density required to achieve the desired moisture content in the test specimens was calculated. These values corresponded to moisture contents of 18 percent from the fog room treatment and 28 percent from the water submersion treatment.

When the test specimens were removed from the fog room and water bath they were weighed and a moisture content reading was taken with a pin-type moisture meter on the exterior surface at each ply. All four test specimens were then subjected to the ½-inch sphere projectile at an average striking velocity of 2,500 fps (762 m/s). Post test, the blocks were cut open to the center shot and an interior moisture content was measured at each ply.

Table 5-12 shows the average exterior and interior moisture contents, as a measurement was taken at each ply, 1 through 5.

Table 5-12. Weathered CLT specimens exterior and interior moisture contents.

Species	Treatment	Average exterior moisture content	Average interior moisture content
SPF-S	Fog Room	32%	13%
SYP	Fog Room	28%	15%
SPF-S	Submerged	38%	22%
SYP	Submerged	38%	33%

The dry specimens striking and residual velocity data was plotted along with both types of weathered specimens. Figure 5-33 shows the SPF-S data and Figure 5-34 shows the SYP data comparing the dry and wet specimens. The residual velocities measured for the weathered specimens of both species aligned well with the residual velocities observed for the dry specimens in the same striking velocity range. Additional testing of more specimens should be conducted to confirm this finding, especially for other wood types.

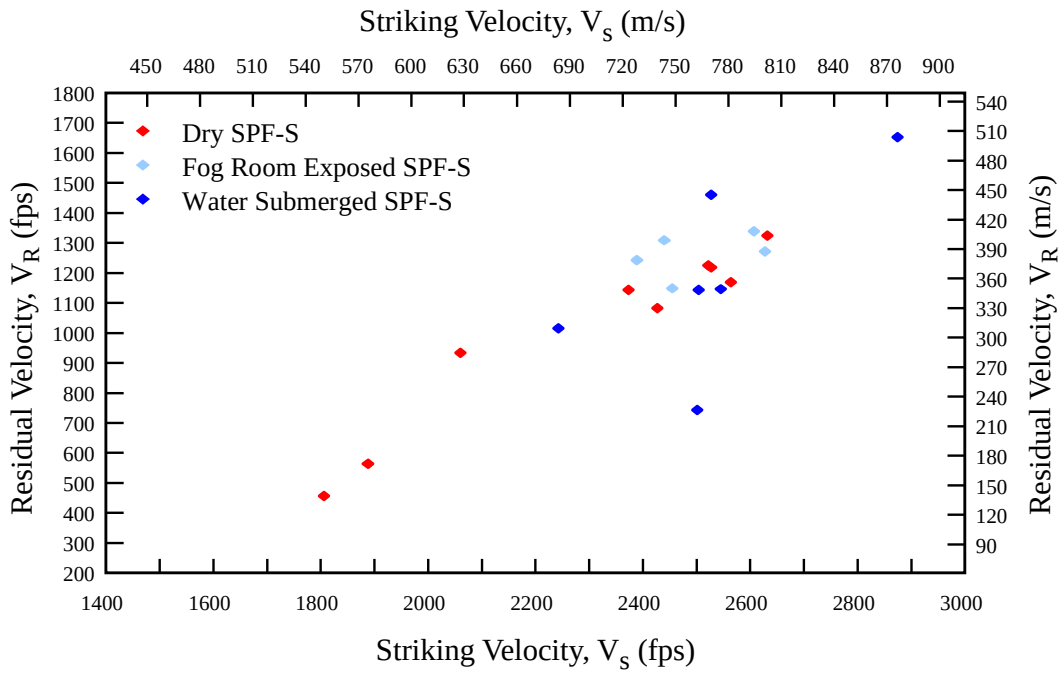

Figure 5-33. Residual velocity based on striking velocity for dry and weathered SPF-S specimens.

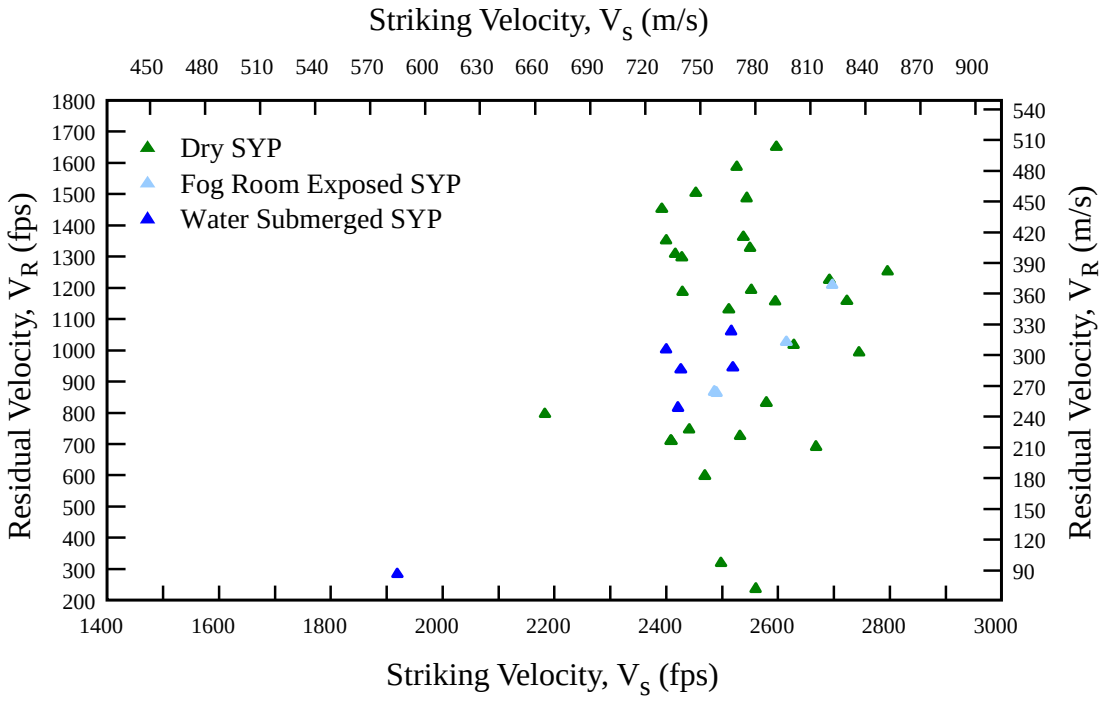

Figure 5-34. Residual velocity based on striking velocity for dry and weathered SYP specimens.

The value of this conclusion for this research is that this preliminary data suggested that there is no decrease in ballistic resistance of the CLT panels with elevated moisture contents. This is important because panels used in B-hut or other temporary military structure construction will likely be without any exterior cover or treatment and exposed to various weather conditions.

5.8 Inclusion of fragment simulating projectile (FSP) data

A small number of tests with the fragment simulating projectile (FSP) resulted in partial perforations. The majority of the data for this heavier projectile resulted in full perforation, thus gathering a residual velocity data point. Four of the eight shots of the FSP which resulted in an embedded projectile were SPF-S and the other four were SYP. Based on the low MSE of the revised UFC model and THOR CLT models using the 0.50-in. sphere projectile, both models were re-run with those additional FSP data points for calibration and inclusion of the projectile weight variable. Table 5-13 shows the MSE values comparing the models based on the sphere-only data versus the combination of the sphere and FPS projectile data. Both MSE values with inclusion of the FSP data were slightly improved.

Table 5-13. MSE of THOR CLT and Revised UFC models for different projectile data sets.

Model	Sphere only (d= 0.50-in)	Sphere and FPS (d=0.50-in. both)
Revised UFC	0.330	0.320
THOR CLT	0.303	0.299

Figure 5-35 shows just the FSP data and its associated UFC CLT model curves. The two different CLT types were plotted as two separate lines. Figure 5-36 shows the UFC model curves and data for both the FSP and sphere projectile. The FSP curves plot slightly above the sphere-only projectile curves with the difference between the two curves increasing as the striking velocity increases. The MSE for the recalibrated model including the FSP data is 0.320.

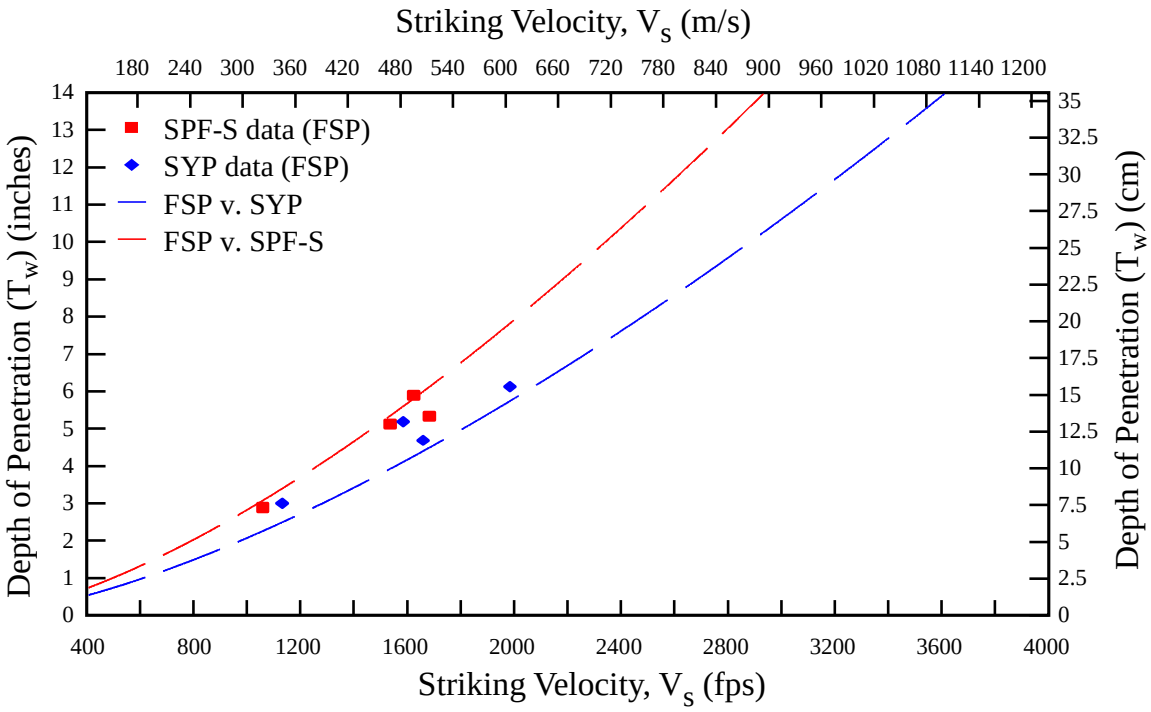

Figure 5-35. FSP data and the recalibrated UFC wood model.

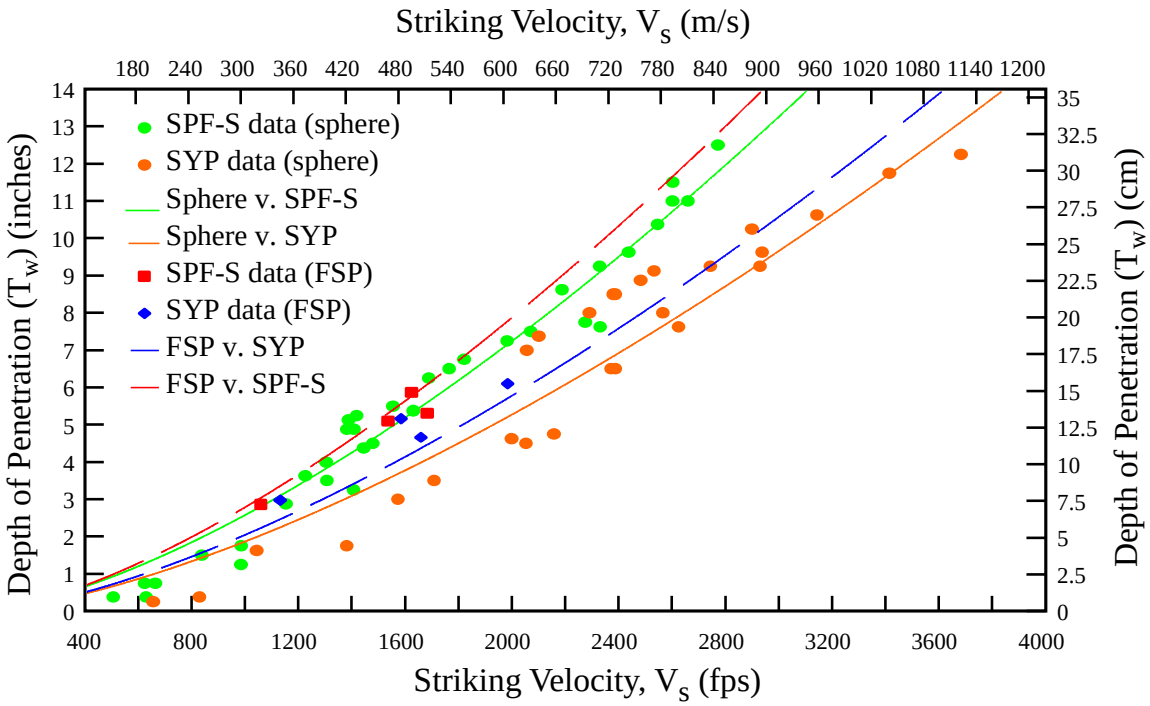

Figure 5-36. FSP and sphere data and curve for the recalibrated UFC wood model.

.

Figure 5-37 shows the THOR wood model with the FSP projectile curves and data only. The additional FSP data gave this model a MSE value of 0.299. Figure 5-38 shows the sphere and FPS data and all four curves for the THOR wood model.

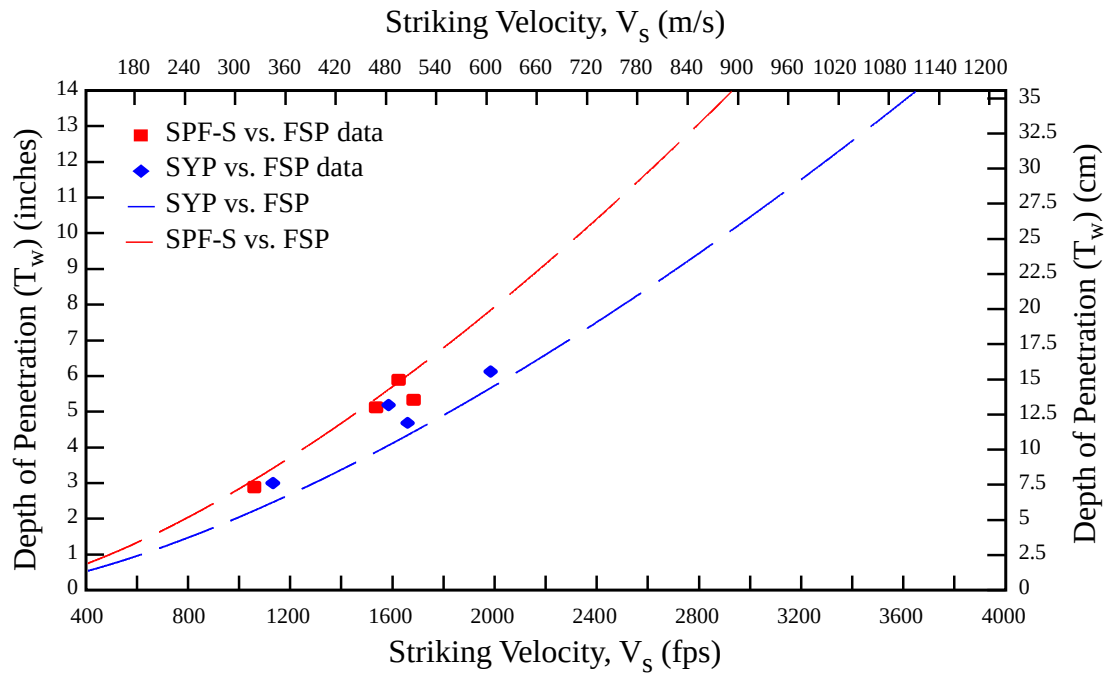

Figure 5-37. FSP data and the recalibrated THOR wood model.

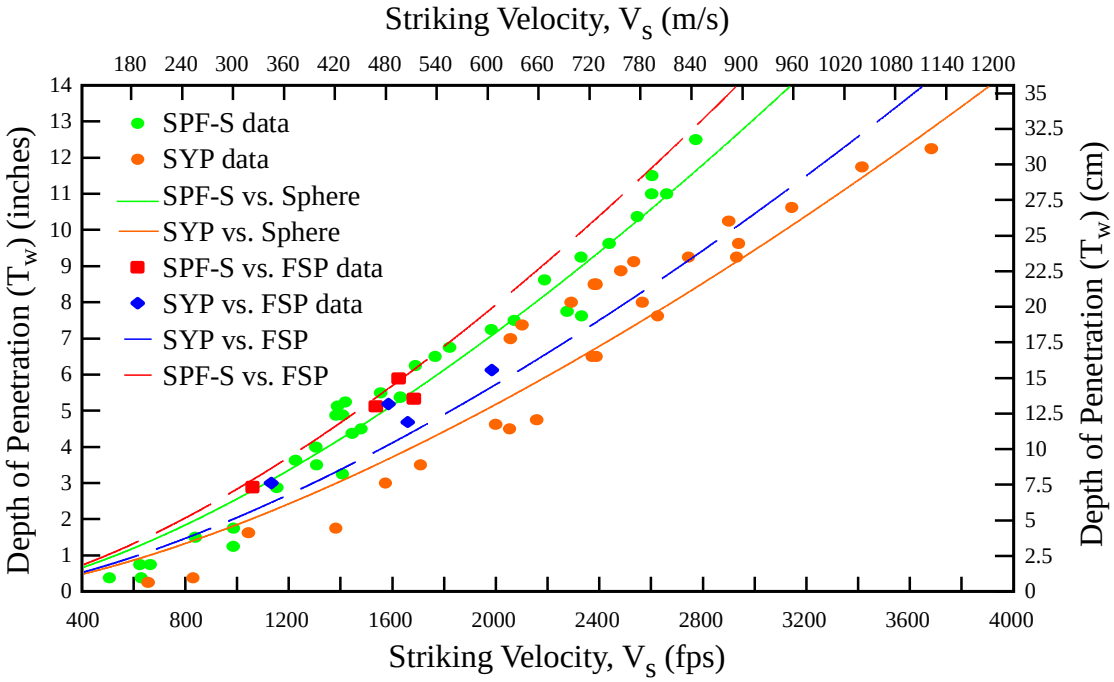

Figure 5-38. THOR wood model with both sphere and FSP data and curves.

While the data is limited for the FSP, it is notable that for the SYP targets, the FSP projectile data points consistently fall above the modeled curve. More testing with the FSP and potentially additional different projectiles would be useful. It should be noted that the plotted curves use an average density and reference hardness. Calculating the value for required thickness using the actual target density and a reference hardness was completed for both the THOR and UFC models for the FPS data set. These values are shown in Table 5-14 and demonstrate that for the SPF-S specimens the curves over predicted the depth required compared to the actual depth of penetration for three of the four data points. For SYP specimens, both models under predicted the depth.

Table 5-14. Actual FSP depth of penetration compared to UFC and THOR wood model predicted depths.

Species	V_s (fps)	Actual depth (in)	THOR predicted depth (in)	THOR % difference	UFC predicted depth (in)	UFC % difference
SPF-S	1536	5.1250	5.6177	9.17%	5.3675	4.62%
SPF-S	1060	2.8878	3.1139	7.53%	3.0079	4.07%
SPF-S	1624	5.8937	6.1273	3.89%	5.8478	-0.78%
SPF-S	1683	5.3346	6.5003	19.70%	6.1936	14.90%
SYP	1132	3.0000	2.9417	-1.96%	2.7616	-8.28%
SYP	1984	6.1250	6.0681	-0.93%	5.8544	-4.52%
SYP	1585	5.1875	4.3739	-17.02%	4.2152	-20.68%
SYP	1659	4.6875	4.6798	-0.16%	4.5095	-3.87%

5.9 Summary

As the first series of ballistic testing on CLT, this research aimed to examine the ballistic resistance of the material. Through experimental testing conducted on two

types of CLT specimens with two types of projectiles, 165 tests yielded data in terms of depth of penetration or residual velocity based on a striking velocity. The existing UFC standard for determining required wood thickness was shown to not fit CLT well, further suggesting that the mass timber product outperforms conventional wood used in lightweight wood construction. Data from the experimental testing allowed for the calibration of classical penetration models, adaptation of an existing curve-fitting model and development of a new curve-fitting model, which predicted the thickness of CLT required to stop a projectile based on striking velocity.

While this initial investigation does not provide enough data to recommend a performance rating of the material by the UL standards, it provides an initial model which can be expanded upon to include additional factors such as projectile nose shape and should be tested with more wood types and a greater variety of ply numbers, or specimen thickness.

Additionally, the effects of weathering were considered in a small number of experiments. This initial dataset suggested that exposed CLT with a higher moisture content appeared to be unaffected in terms of ballistic resistance. This is a promising characteristic for use in temporary military structures.

CHAPTER 6
RESISTANCE MECHANISMS FOR BALLISTIC PENETRATION OF CLT

6.1 Introduction

The natural structure of wood makes it a unique material for impact resistance as described in Chapter 4. On the microscale, the composite-like structure of the wood cells provide characteristics not unlike manmade composites, which are often manufactured specifically for their increased strength and impact resistance while maintaining a relatively light weight. CLT, with its bi-directional layups of multiple plies of wood, adds another dimension to the composite nature of the product.

In a dynamic impact two bodies moving at some relative velocity collide with one another. In the case of ballistic testing, the projectile and the target are the two bodies. The target is typically at rest, and has a much larger mass relative to the projectile. The reaction to the impact is dependent on the forces and stresses created. High speed projectile impact loads typically cause failure in wood targets. As energy from the projectile is dissipated and the impact load is absorbed, the wood's elastic properties are exceeded. However, wood does have significant energy absorption capacity. Wood is commonly used for tool handles, baseball bats, guardrail posts, railroad ties, packaging materials, and gun stocks, all of which experience impact and vibration loads [31].

A unique characteristic of a wood product like CLT is the ability to dissect it after ballistic testing, allowing for visual examination and assessment of the failure modes, and qualitative contrast between test specimens beyond the measured data points of residual

velocity and depth of penetration. This chapter reports on the examination of CLT specimens post ballistic impact testing. The analysis of penetration depths and residual velocities is covered in Chapter 5. The goal of this chapter is to develop an intuitive understanding of the resistance mechanisms of wood penetration and tie these observations to the properties of wood introduced in Chapter 4.

Using a band saw, the CLT test specimens were cut along the projectile path to expose the cross-sectional cut of the cavity created by the projectile. This allowed for the examination of wood failure mechanisms. The observations are used to help explain variability in the penetration data presented in Chapter 5. The ability to examine the specimens helps identify the resistance mechanisms inherent in the CLT and how their potential variability due to wood composition may influence the ballistic resistance.

6.2 Toughness

Aside from the static wood properties discussed in Chapter 4, another characteristic of wood related to resistance is toughness, the ability of the material to absorb energy before fracture. Graphically, the toughness of a material is the total area under the elastic and plastic region of the material's stress-strain curve, or the integral of stress-strain curve. Toughness is not a commonly measured property for wood, but can be measured with a pendulum style impact tester in accordance with *ASTM D3499 Standard Test Method for Toughness of Wood-Based Structural Panels* [10]. Toughness values from the test describe the energy required to experience rapid fracture of the wood specimen. Like other properties discussed in Chapter 4, toughness depends on the wood grain structure and orientation of the specimen relative to the striking direction. Reference radial and tangential toughness values for different softwood species, including those used to make

CLT are shown in Table 6-1. Softwoods generally have a slightly higher toughness in the tangential direction. Additionally, most species have increased toughness in green wood as compared to wood with an approximate moisture content of 12 percent in kiln dried lumber.

Table 6-1. Softwood species radial and tangential toughness values from the Wood Handbook, adapted from [96]

Species Type	Moisture Content (%)	Toughness	
		Radial (J)	Tangential (J)
Douglas-fir	Green	2,900	4,400
	12-14%	2,825	4,600
Fir	Green	2,270	3,525
	12-13%	2,300	3,475
Pine	Green	3,725	5,210
	11-13%	2,500	3,830
Spruce	Green	2,400	3,100
	12%	1,800	2,900

A wood's values for toughness and strength combine to describe the work to maximum load, a reported strength property under static bending. The work to maximum load in bending is the material's ability to absorb shock with the allowance of permanent deformation [96]. Fracture toughness is another related property defined as the ability of the wood to tolerate flaws that initiate failure, or the resistance to propagation of a crack or defect [96].

Toughness data have limitations in scaling, making it a challenging property to use for comparisons due to restrictions in cross-sectional dimensions of fracture specimens [31]. Additionally, toughness values are highly variable. Typical coefficients of variation for toughness and work to maximum load properties for clear wood specimens range between 30 and 40 percent [96].

6.3 Previous work with dynamic loading of wood and wood products

Other researchers have examined the static versus dynamic loading on a panel of light frame wood construction and its associated failure modes. The panels were constructed of dimension lumber studs with one side sheathed by either plywood or oriented strand board. Under static loads, flexural failure was observed with uneven failure in individual wood pieces due to the variability of the wood. Under dynamic loading, the same light frame wood panels also experienced flexural failure. However, the documented observation of the dynamically loaded specimens was described as a cut through the wood fibers in contrast to a more splintering failure that appeared like finger joints disconnecting in the statically loaded panels. The distinct failure modes were attributed to the difference in the duration of loading. Static loads allowed for the initial fracture in the material to find the lowest strength load path, resulting in splintering failure. Under dynamic loads, however, the short duration of the load resulted in a brash tension failure effectively snapping or cutting the fibers more uniformly [74].

A study examining the behavior of Parallel Strand Lumber (PSL), subjected to both static and impact loading found the primary failure response of a typical PSL beam to be a combination of flexural failure, shear failure, and debonding of the wood strands [107]. The difference between the impact loading fracture and the static load was observed to be

the rapid speed of failure but with similar material response. Failure was characterized by initial elastic behavior followed by an inelastic phase with shearing, delamination between strand layers, and then a loss of load carrying capacity. The researchers noted that in order to cause failure in the PSL beam, the loading force had to exceed the flexural, shearing, and bond strengths of the wood product as well as the crushing strength of the wood. This was observed by localized damage at the location of impact.

Vural and Ravichandran examined the dynamic response of balsa wood at the strain rate of 3 $x10^3$ s^{-1}. They also completed detailed examinations of the microstructure of the wood. At the microstructure scale, both static and dynamic compressive loads caused buckling or kink band formation with higher strengths observed under higher strain rates [113]. Figure 6-3 depicts buckling and kink band formation in a wood specimen. In kink bands, the strands in the wood grain are rotated and crushed as the material responds at the cellular level. Reid and Peng had previously investigated dynamic uniaxial crushing of wood noting the inelastic deformation as a localized phenomenon [92] often occurring in bands.

6.4 Observable characteristics in wood and CLT

Wood typically has three orthogonal axes: longitudinal (*L*) in line with the grain and running in the direction of tree growth, radial (*R*) across the grain and transverse to the growth rings, and tangential (*T*) across the grain and lateral to growth rings (see Chapter 4). The orientation of the plies in the CLT test specimen are such that the projectile in the ballistic testing, entering perpendicular to the surface of a wall or floor panel, always move through the target perpendicular to the longitudinal grain direction. This means the projectile is moving in a transverse direction, either radially, tangentially or in some mode

that includes both radial and transverse movement across the wood growth rings. Figure 6-1 shows a CLT panel with timbers of various potential transverse grain orientation.

In the radial direction, Wouts et al. have observed compressive forces that compact the wood layer by layer, independent of strain rate [123]. In the tangential direction, the earlywood is uniformly compacted with the increase in strain until a point where local damage is observed along with the formation of wood fragments. This is commonly caused by annual ring decohesion [123]. It is important to note that the projectile path is not limited to a purely radial or tangential trajectory through the wood. In most cases, the cut of the timber will cause the path to be an offset angle from either of these "pure" orientations.

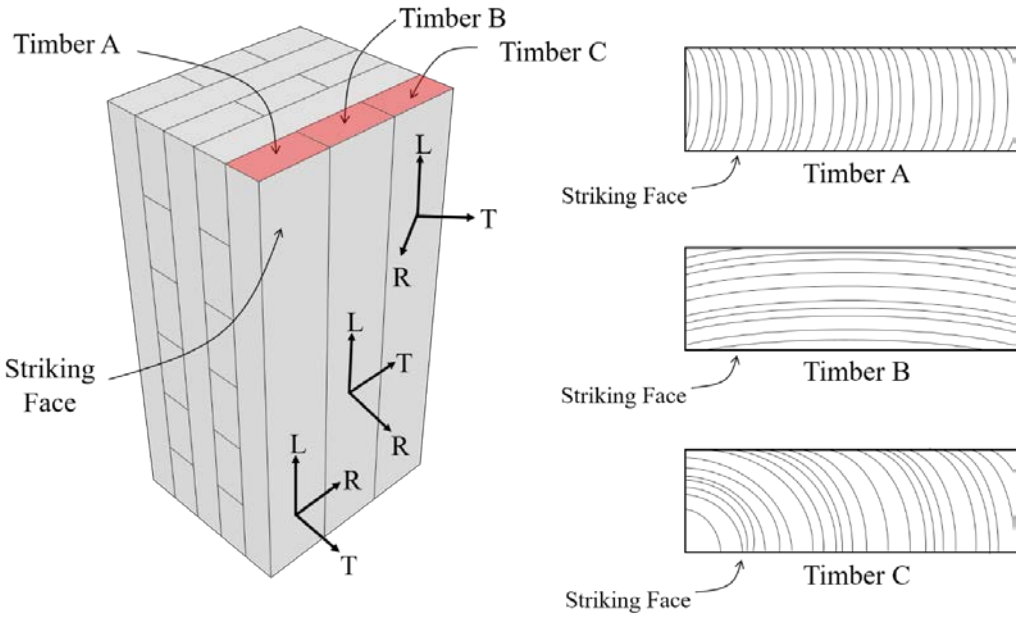

Figure 6-1. A graphical depiction of the potential transverse grain orientations in a CLT panel.

Visual examination of the cross-section cutaway allows for observation of the orientation of the wood grain direction for the plies in the projectile path, as shown in Figure 6-2. The axes are superimposed on the photograph in Figure 6-2 to indicate both the alternating directions with the plies but also to show the longitudinal (*L*), radial (*R*), and tangential (*T*) orientation. In addition to the grain orientation with respect to the projectile's path, the density in terms of thickness of the annual growth rings, the distribution of earlywood and latewood, the presence of heartwood, the existence of pith, and the occurrence of any defects such a knots or sloped grain can all be observed. It should be noted that it is not possible to differentiate what damage may have been caused by the band saw cutting open the cross-section compared to damage attributable to the projectile. Although not without limits, one technique to rule out saw damage is to inspect for saw-incurred damage in specimens not tested with the ballistic set-up.

The cross-sectional cuts, like shown in Figure 6-2, also show the difference in failure based on the grain orientation. It is recognized that if the cut were rotated 90 degrees, the perspective on the damage modes would be different. The bending and shearing of grain in the radial direction in the transverse plies in Figure 6-2 would look different, as the cut would expose an altered perspective with respect to the wood grain. However, the perspective of the cross-cut gives a view of how the wood responds and ultimately fails under the stresses induced by the projectile. In clear wood sections, the lamella with its grain oriented horizontal to the cut appear as thin splintered wood sections, whereas the vertically oriented grain pieces appear as abruptly fractured chunks. Some of the difference in wood response is also attributable to the density of the growth rings.

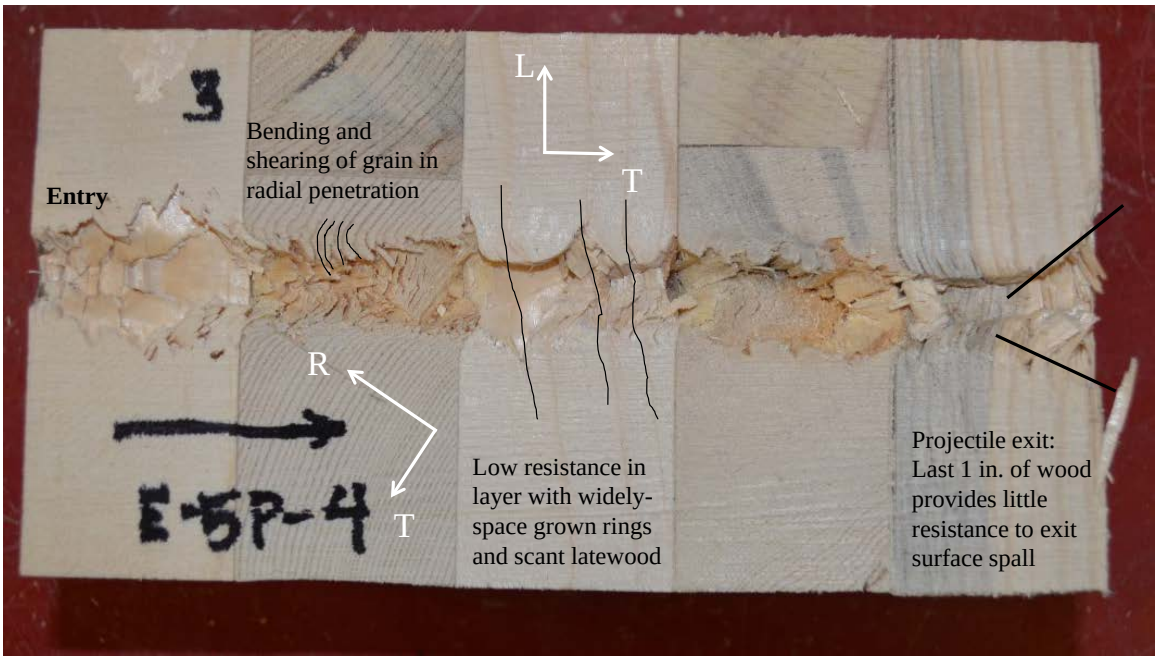

Figure 6-2. A cross-sectional cut along the projectile path exposes the wood damage as well as the orientation of the wood in each ply with respect to longitudinal (L), radial (R), and tangential (T) axes of the wood.

6.5 Wood failure modes

6.5.1 Wood failure under various loading conditions

The failure mechanisms in wood, like other materials, corresponds to the strengths and to some degree the stiffness of the material. However, as an anisotropic material, wood experiences a range of failures depending on the orientation of the wood in relation to the direction of the applied load. In clear wood specimens, a compressive force perpendicular to the grain typically results in three basic failure modes: 1) crushing; 2) shearing; and 3) buckling. These failure modes are shown in Figure 6-3. Buckling in this case represents the instability of the hard and stiff latewood rings as they move transversely and crush the relatively softer surrounding earlywood. The wood grain direction influences the observed

failure mechanism. A loading in the radial direction is likely to cause crushing (Figure 6-3a) while a tangentially aligned loading results in buckling of the growth rings (Figure 6-3c). A load applied at an angular orientation to the growth rings where the load is not purely radial or tangential often yields a shear failure (Figure 6-3b) [31].

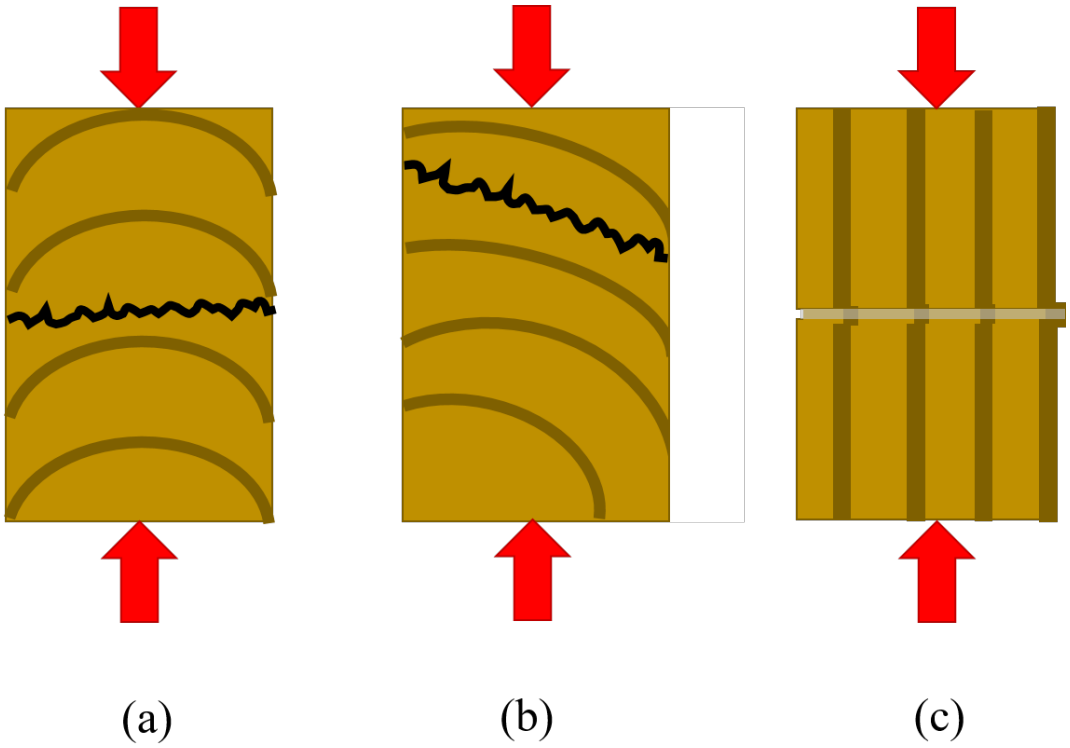

Figure 6-3. Failure types in wood loaded in compression perpendicular to grain: (a) crushing an earlywood zone, (b) shearing along a growth ring, (c) buckling of growth rings, adapted from [31].

For tensile loads perpendicular to the grain, the common failure modes are tension failure and shearing as shown in Figure 6-4. Instead of crushing, the tensile force induces fracture as the wood cells pull apart from each other. In the radial direction, this failure occurs in the earlywood. Shearing along the growth ring, similar to annual ring decohesion,

remains a failure mode. For tangential tensile loads, the wood often fractures in the wood rays (wood rays are a radial-oriented ribbon or sheet, which serves to transport the sap of the tree).

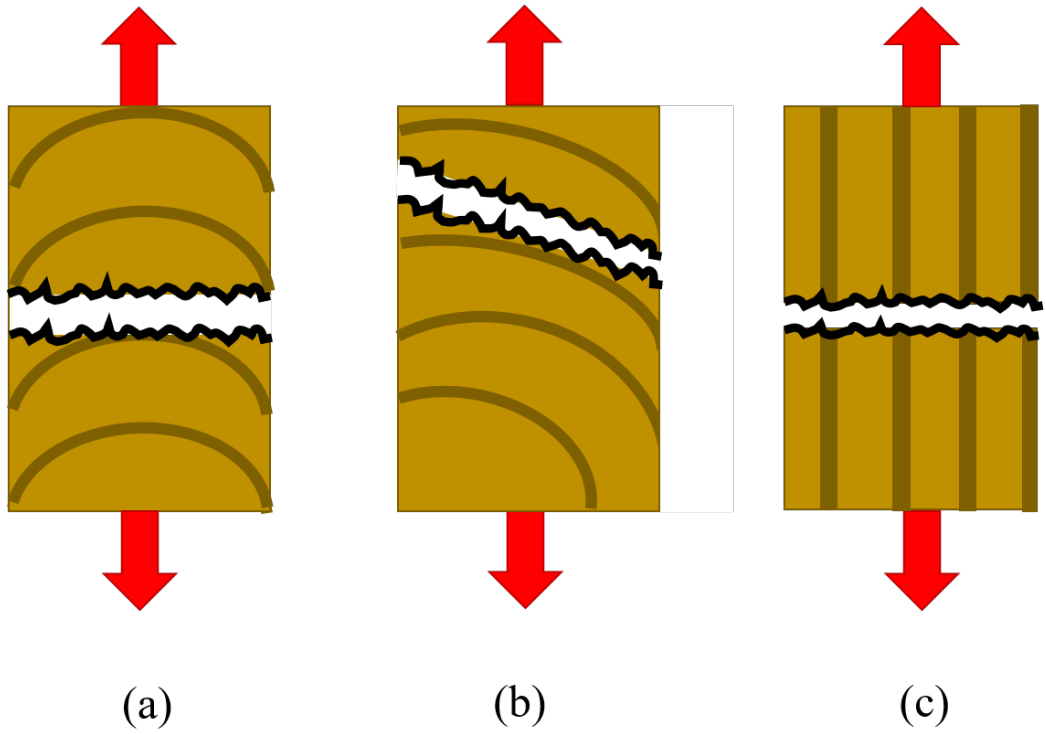

Figure 6-4. Failure types in wood under tensile load perpendicular to grain: (a) tension failure in earlywood, (b) shearing along growth ring, (c) tension failure of wood rays, adapted from [31].

Failure types for wood in bending with the span parallel to the grain can include both tension and compression failures. Figure 6-5 shows six flexural failure modes for clear wood. Simple tension is not common but may be observed in dense wood. Cross-grain tension is seen frequently, where splintering tension is observed in wood with a low moisture content. Brash tension is associated with abnormal molecular structure or

compression wood formed on the underside of branches or a leaning trunk. Compression failure is often observed in low density wood and horizontal shear is common in species more prone to defects with planes of weakness [31]. The aforementioned explanations for the different failure types are based on common observances and are not the only situations for those specific failure modes.

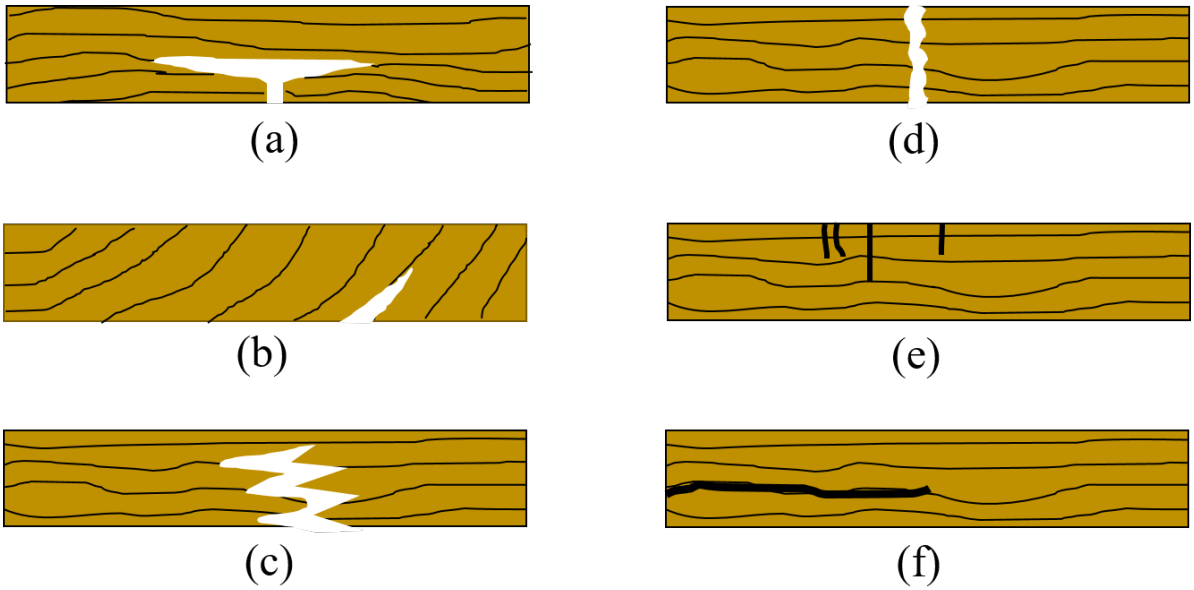

Figure 6-5. Failure types in wood in bending with span parallel to the grain: (a) simple tension, (b) cross-grain tension, (c) splintering tension, (d) brash tension, (e) compression, (f) horizontal shear, adapted from [31].

6.5.2 Wood failure modes in CLT with ballistic impact

In prior studies, the most common failure modes caused by ballistic impact of wood, as outlined by Zukas and discussed in Chapter 3, are typically for thin targets. However, the failure modes are still applicable with the CLT (thick) targets. The projectile creates a combination of failure types as it impacts the wood, creating complex damage

states in the panel. In the cases where the projectile is moving in a primarily radial direction through the wood, the damage to the wood appears most like petaling. In this instance, the growth rings at the edges of the cavity are bent in the direction of the projectile's motion. Petaling in ductile metals is associated with large plastic flow and permanent flexure [27].

Similar transport of material due to projectile passage is visible in those plies with the wood oriented such that the radial-tangential plane is exposed with the cut. The sawn timbers with high contrast in the earlywood and latewood growth rings show a distinct altered curvature to the ring direction caused by the projectile, as shown in Figure 6-6. The natural curve of the darker colored latewood's growth ring deviates from its natural path with the forces applied by the passing projectile. These sections of the wood appear like angular petals bending out of the way, leaving a jagged debris filled cavity in its wake with splits developing between the growth rings, as shown in Figure 6-6.

Unlike a thin-plated target with a single set of petals, possibly on the back face or the front face of the impacted surface, in CLT the petaling appears in layers throughout the projectile path. Additionally, instead of triangular shaped petals, the fractured wood is boxier in shape, which may be caused by the spherical or blunt nosed projectiles, characteristics of the wood, or a combination of both. The damage is localized, within one diameter of the projectile, on either side of the projectile's path. With the 0.50-in. sphere, the zone had a total width of approximately 1.50-in, for entire projectile path, as shown in Figure 6-7. Outside of this damage zone, the wood appears unaffected by the passage of the projectile, although in some locations cracks are propagated beyond this localized region. Within the zone, the area around the petal is no longer continuous wood as there

are frequently gaps between the distinct petals. These spaces likely developed as the force of the projectile and its shock waves split the growth rings in their transition zones.

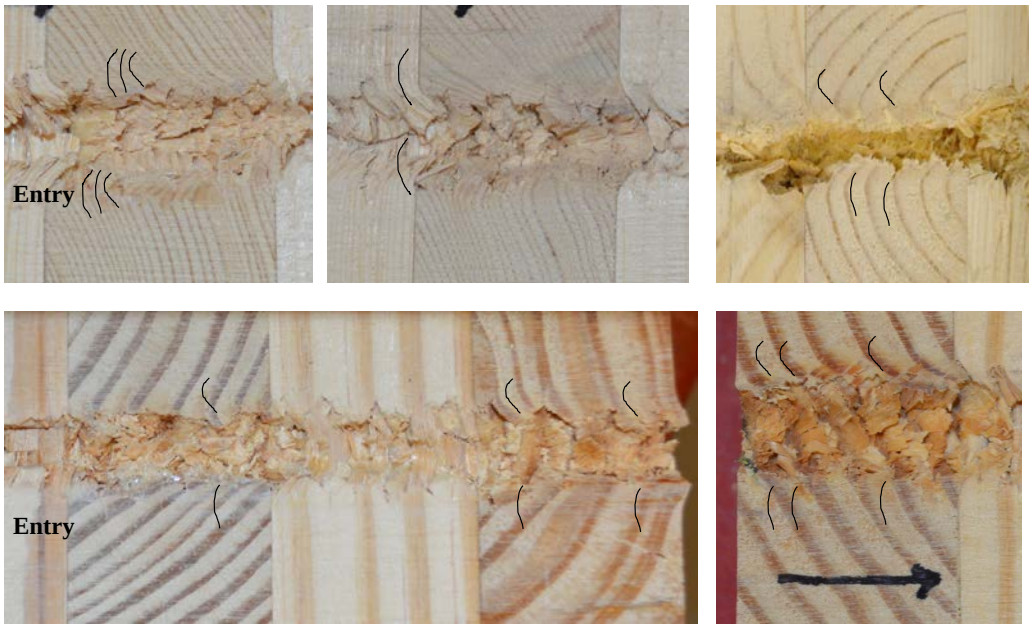

Figure 6-6. Examples of the altered curvature in the latewood (darker colored sections) caused by the moving projectile, (top) SPF-S specimens, (bottom) SYP specimens.

The highly localized nature of the damage to the CLT means it is likely the panel could withstand numerous concentrated impacts of small arms munitions and still preserve its load bearing capacity. However, more testing with multiple impacts and residual capacity strength tests are necessary to draw that conclusion. Within this work, 12-in. square specimens of CLT were subjected to multiple shots and exhibited no evidence of reduction in the panel's structural integrity.

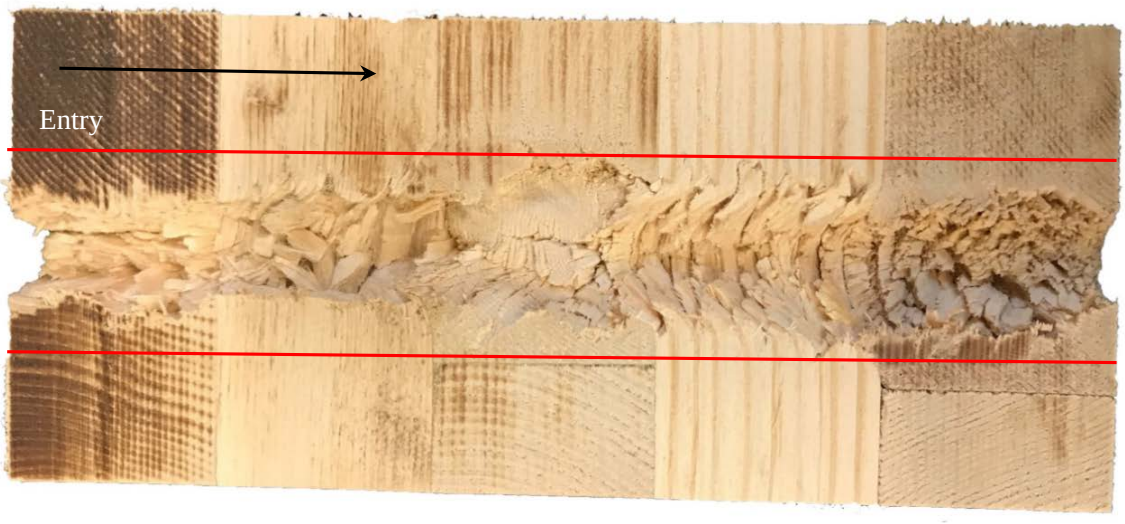

Figure 6-7. A cross-sectional cut of the projectile path exposes angular petals and the newly formed space between growth rings.

Wood fracture occurring at the transition between growth rings in the tangential orientation was observed in some of the examined specimens. With this type of failure, the exposed wood left behind is very smooth, and sometimes shiny in appearance. The smooth surface may maintain the natural curve of the transition between earlywood and latewood in the timber or be evidence of horizontal fracture lines. This cleaving point may likely be attributed to the transitional area where the wood's density abruptly changes [43]. This is most visible in the longitudinal numbers plies, with the longitudinal-tangential plane exposed as shown in Figure 6-8. The yellow ovals in the image highlight the exposed smooth sections where the growth rings have effectively debonded from each other.

Radial cracking was frequently detected close to the damage zone but beyond the initial cavity damage. While this could be caused by the saw, or even just shrinkage of the timber after the lamella were pressed together, the proximity of the cracking with respect

to the projectile path indicates a likely relationship. It may be caused by the initial shock waves induced by the projectile or the force of the projectile as it breaks through the wood. Figure 6-9 shows examples of the observed radial cracking in both the SPF-S and SYP specimens; the yellow ovals highlight the location of the cracks. The cracking appears to initiate close to the cavity and then radiate at a diagonal at a 45 degree angle away from the projectile path regardless of the curve direction of the growth rings. The cracking may be indications of shear failure in the wood. Liu and Floeter observed a shear strength decrease when the angle between the shear force and grain on the longitudinal-tangential plane increased [78].

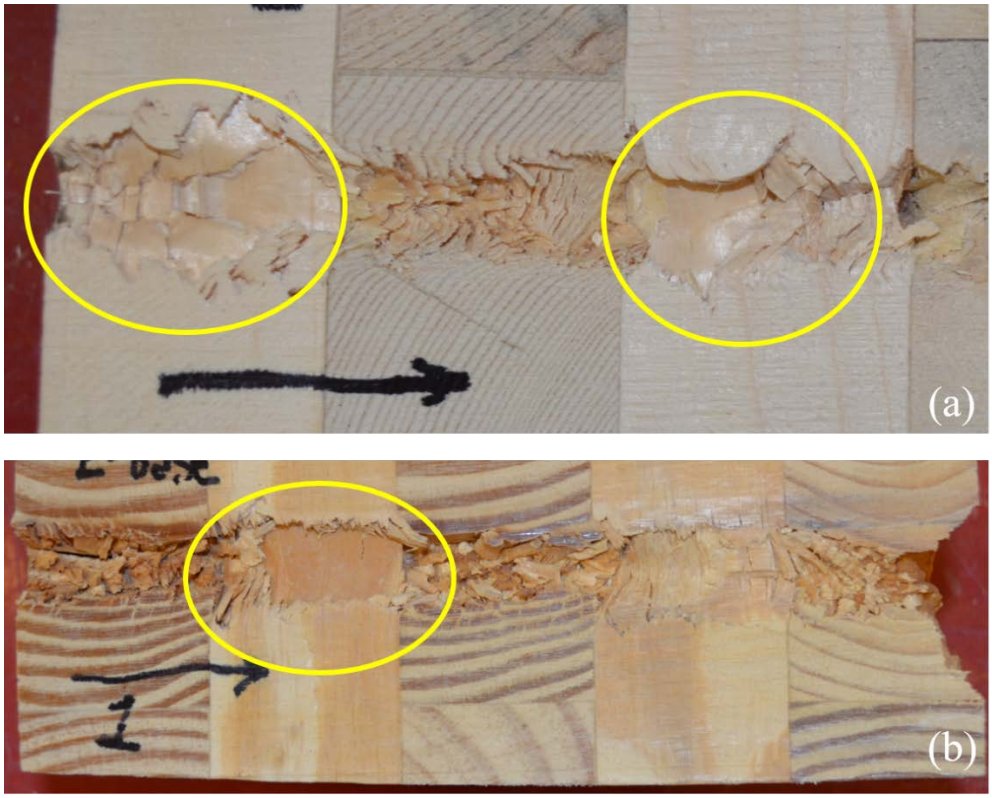

Figure 6-8. Sections of fracture in the wood along the growth ring curvature are highlighted in the projectile path cross-sections, (a) SPF-S specimen, (b) SYP specimen.

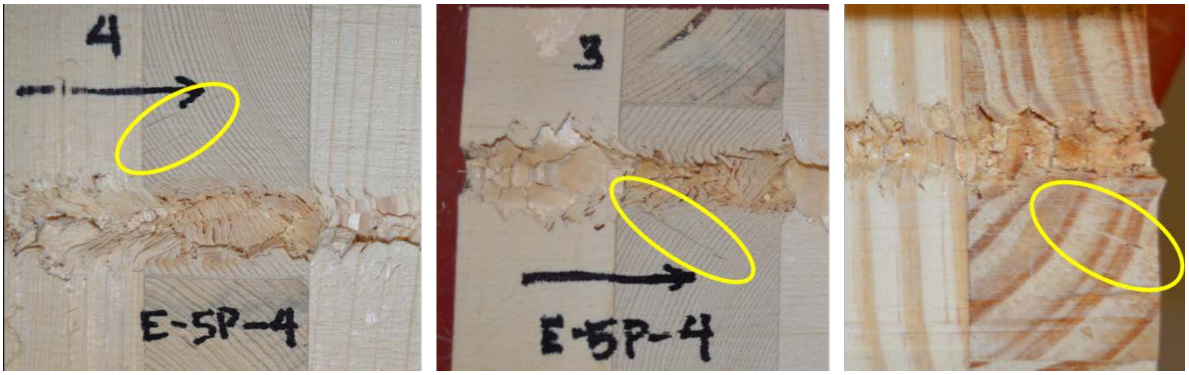

Figure 6-9. Radial cracking in the timbers observed near the projectile cavity.

Another ballistic failure mode is scabbing (see Chapter 3). In this instance, sections of the back face fracture off the back face due to deformation of the fracture and local anisotropy. Figure 6-10 shows two 3-ply test shots where the residual velocity as the projectile neared the rear face of the specimen would still have been relatively high compared to a 5-ply or thicker specimen. This phenomenon was observed in the thicker 5-ply specimens with higher striking velocities.

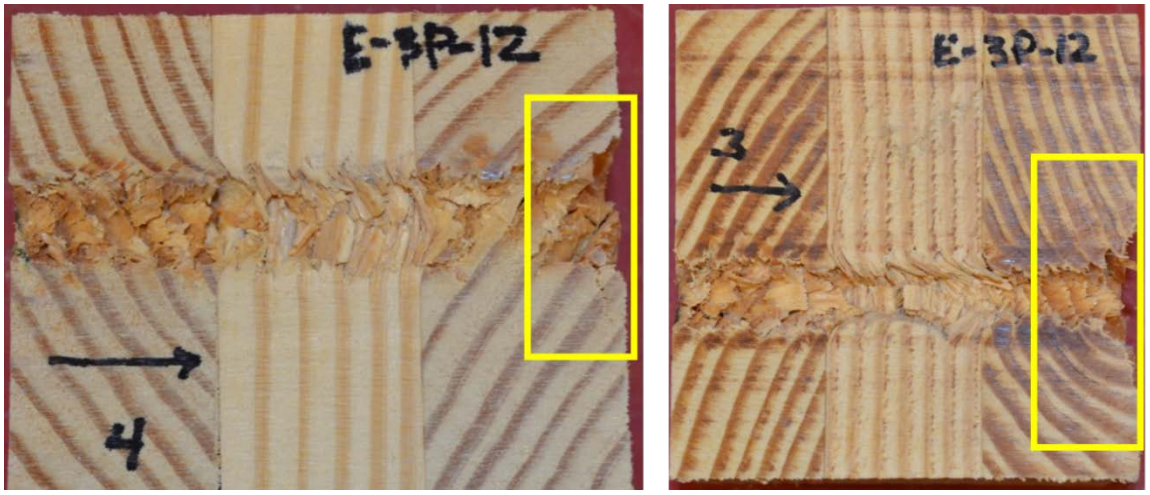

Figure 6-10. The exit holes of the projectile in this 3-ply specimen appears to be larger than the projectile path, potentially due to scabbing, where sections fracture off as debris.

Permanent deformation of the rear face of the specimen does not require perforation. Bulging and dishing are observable plastic deformations that occur without complete penetrations. Figure 6-11 shows the projectile still embedded within the CLT with the wood bending and forming a bulge on the back face. This particular specimen was a 10-ply specimen formed by joining two 5-ply specimens together. The section shown in Figure 6-11 is the last plies of the front 5-ply so the bulging wood observed may be attributed to the second 5-ply immediately behind it continuing to resist the penetration of the projectile. Fracture lines are also visible as lighter colored lines oriented mostly perpendicular to the projectile path in the dark latewood of the last ply; they indicate the plastic deformation of the flexural bending.

Figure 6-11. The embedded projectile causes the wood to bulge on the back face of this section of the target.

Embedded rounds can also show the displacement of fractured wood, as seen in Figure 6-12. The bending in the growth rings is visible in multiple plies. The fractured wood and some debris and sawdust can also be seen in the cavity created by the projectile, in this case a fragment simulating projectile. Splintered sections of the previously penetrated ply are found in the subsequent ply. While loose debris was mostly removed from the cavity prior to the photograph, the projectile path still appears to be more congested with debris closer to the embedded projectile than the channel near the initial entry into the CLT test specimen.

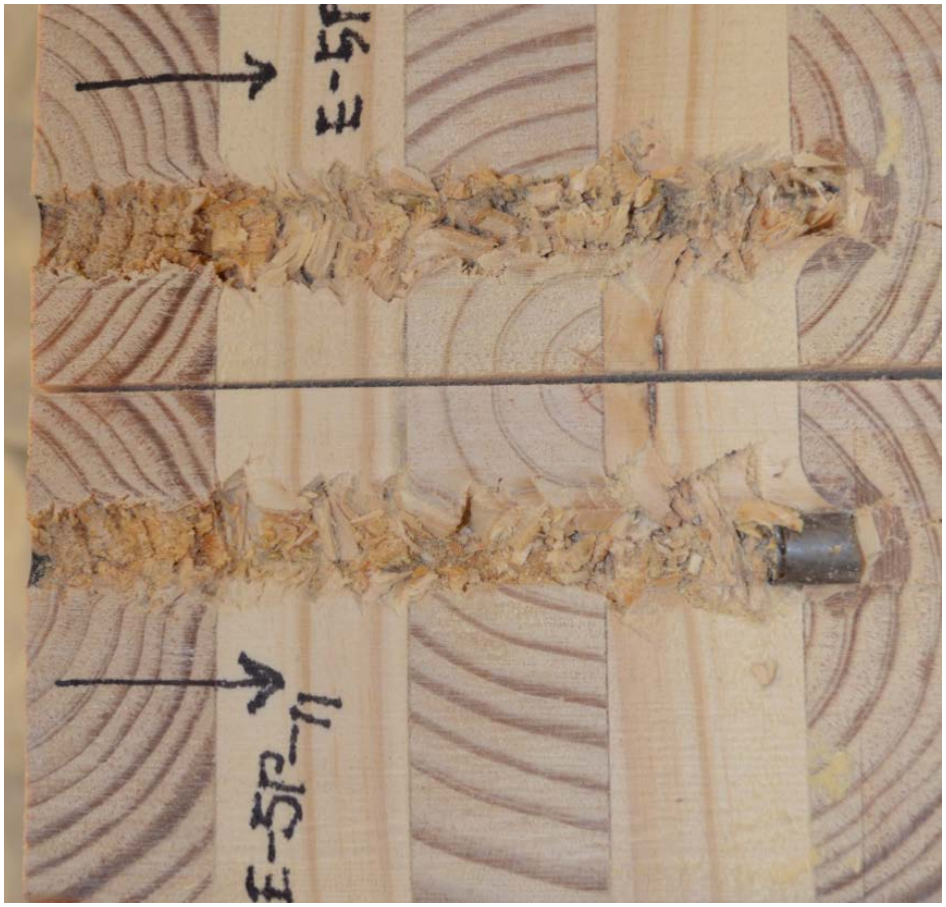

Figure 6-12. The splintered path of the fragment simulating projectile.

Figure 6-13 provides a close-up view of the embedded FSP in the specimen. The projectile was stopped in the CLT with the front edge just beyond a ply bond line. In front of the projectile, radial cracks are visible in the fifth ply, the last ply in the specimen. The compression of the growth rings is apparent with the enlarged area of the darker latewood, which may also indicate the presence of a knot. A small fractured piece immediately in front of the projectile that was originally part of the preceding ply (ply 4) based on the orientation of the wood is evidence of the material plugging. Both above and below the round, the lighter colored wood of the fourth ply can be observed. The bond line between ply 4 and 5 curves forward with the FSP on the top and appears to be a fractured curve below the FSP. The straight horizontal line visible in front of and at the bottom of the round was caused by cutting carefully around the projectile; dissection of specimens with embedded rounds requires extra caution to not damage the saw blade, and in turn the specimen.

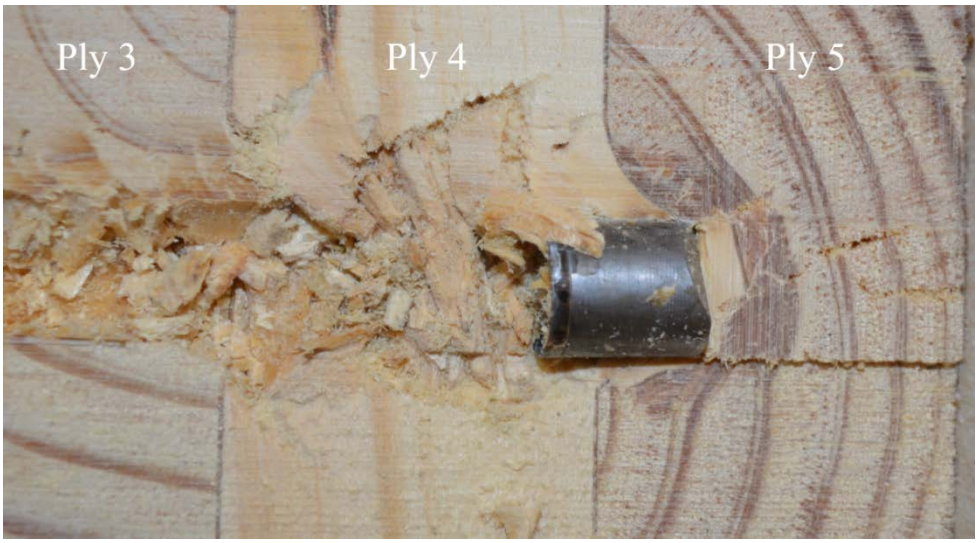

Figure 6-13. A close-up perspective of the embedded projectile and ensuing damage.

The cavity left behind the projectile is initially filled with various sized fragments of wood including large loose chunks and still attached splintery sections bent in the direction of the projectile movement. Even in a perforated shot, with the projectile and some debris ejected, it is not possible to see through the specimen with the ½-inch projectiles used in this research due to this residual debris field filling the cavity. The cross-sectional cut with the band saw adds sawdust to the void as well. Much of the debris is loose and will fall free when the cross-section is cut and separated. When the projectile is embedded in the specimen, there tends to be more debris still attached to the walls of the cavity close to the round as shown in Figure 6-14. This may be attributable to the slower velocity of the projectile prior to stopping embedded in the CLT.

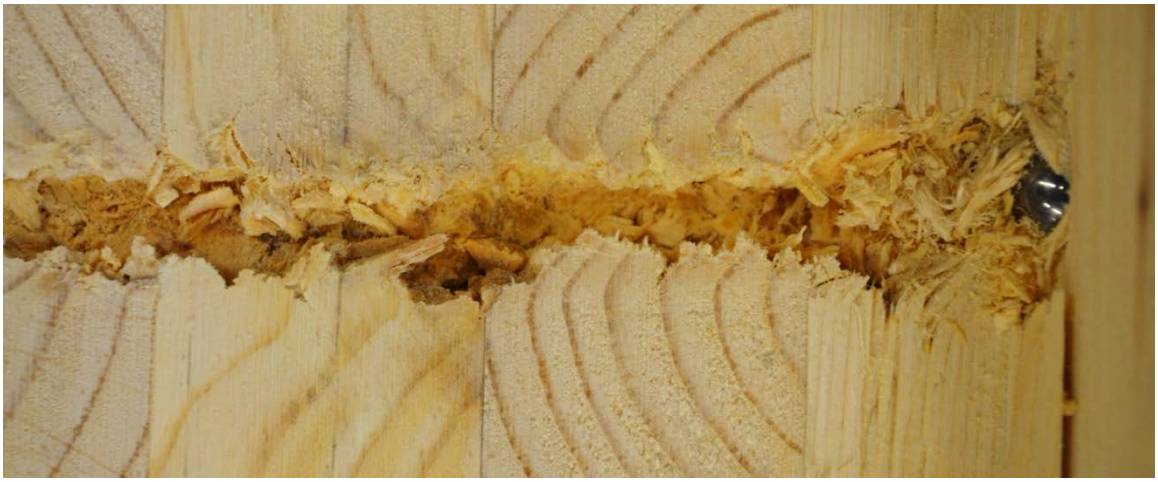

Figure 6-14. Debris fills the cavity behind the embedded projectile in the test specimen.

When the projectile exits the back face of the specimen, debris is pushed out as well. Figure 6-15 shows the splintering fracture of the back face as well as the debris being forced out along with the projectile. The series of still photos were extracted from an ultra-

high-speed video shot at one million frames per second. They illustrate the progression from the hint of a white vertical line through splintering tension fractures that expand to allow for the ejection of wood debris and the projectile. It is interesting to note the initial formation of cracks on the exit face appear to align with the earlywood-latewood boundary. The amount of wood debris is not the equivalent volume of the evacuated cavity, as a significant portion of the separated debris remained in loose in the cavity, or stays attached to the newly formed cavity walls. This means the debris fractured after the projectile passed or was pushed back behind the round as it passed through the target. The continuous petals protruding into the cavity from the walls appear to compress as the material stresses past its elastic limit and experiences post-elastic deformation.

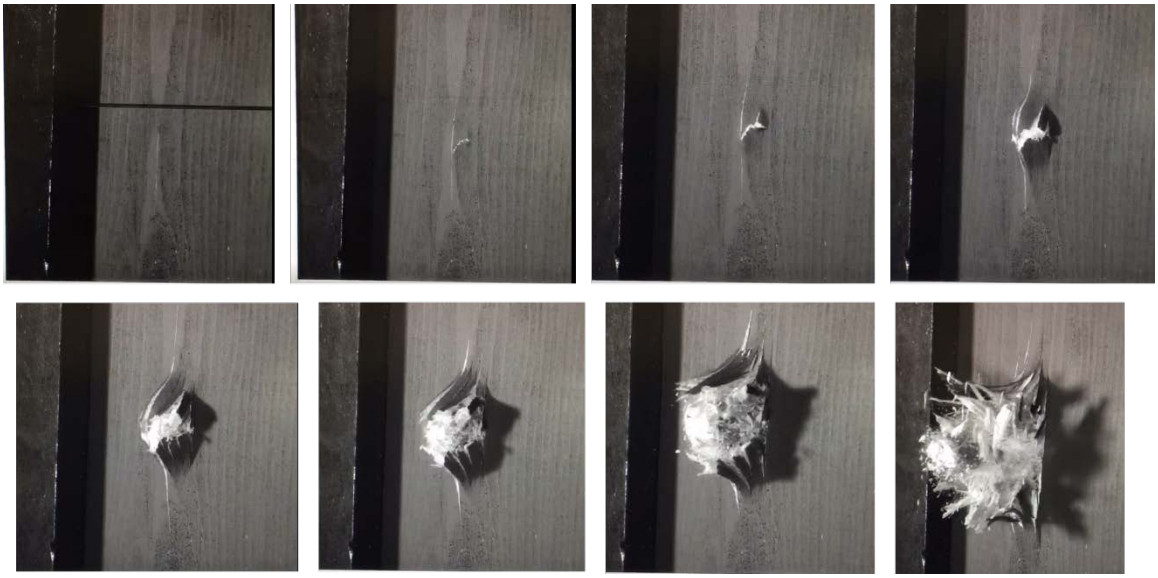

Figure 6-15. A progression of still photos from a high-speed video capturing a complete penetration.

6.5.3 Influence of knots

Knots will be present in CLT as the performance standard (PRG 320) allows for manufacture of the panels with grades of lumber that have knots. The minor strength direction, or transverse, plies typically allow for even lower quality wood than the major strength or longitudinal plies, which means they could have an increased number as well as larger knots as allowed by lumber grading rules [12, 35]. Knots in a board are the result of branches in the tree; they appear in a sawn timber as round and generally darker colored wood perpendicular to the grain of the board [96]. The presence of a knot can disrupt the straightness of the wood grain and influence the wood properties of the board. Knots and the wood around them are often the location of failure in the wood. However, as the hardness testing indicated (Chapter 4), knots are also much harder than the normal straight-grained wood. Depending on the location of the knot relative to the projectile's path through the specimen, the knot is believed to either alter the otherwise straight-line path or to require more energy for the projectile to pass through. Lower residual velocities and reduced depths of penetration were commonly observed to have knots in close proximity to the projectile path. Figure 6-16a shows a projectile path with two knots, where the larger knot was included in the material the projectile passed through. The two knots are perpendicular to the board's grain direction running vertically. Figure 6-16b shows a single knot exposed by the projectile. Unusually, the knot is parallel to the board grain direction, which is still believed to result in a less than expected residual velocity.

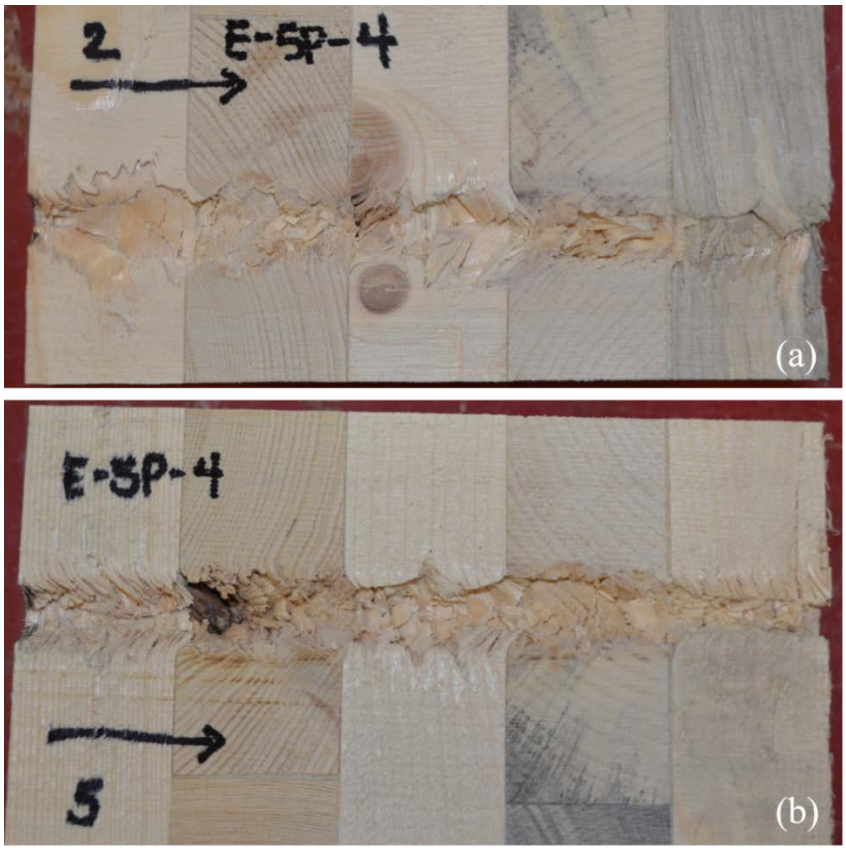

Figure 6-16. Two projectile paths with visible knots, (a) path tracks between two knots, (b) path exposes a knot.

6.6 Outliers

Occasionally with a ballistic test shot, a projectile doesn't travel as deep as expected or exit the target as fast as expected, or conversely, the depth of penetration is deeper or residual velocity is faster than expected. With CLT, the dissection of the projectile path can help explain variation from the mean behavior. Potential outliers were first identified in the context of specimen and outlier type. For example, all SYP specimens with outlying residual velocities or all SPF-S specimens with outlying depths of penetration were investigated. The list of potential outliers was then further examined in the context of the individual specimen. For example, if the outlier was the fifth shot in specimen E-5P-3,

then all then the data was re-examined for all the shots taken on E-5P-3 to determine if the potential outlier deviated from the expected result given that particular specimen.

For outliers with deeper penetrations and higher residual velocity values, a common observation was that the projectile path was aligned tangential to the growth rings and occurred primarily within the earlywood. For lower residual velocity values and shallow depths of penetration, knots were often observed in the path or in close proximity to the path. For these unexpectedly "better" data points, dense growth rings and an increased percentage of latewood were also common. Table 6-2 shows the details of identified outliers. Figure 6-17 shows an example where a higher residual velocity was found with shot #2 into specimen E-5P-12. The longitudinal plies were observed with the path tangential to growth ring orientation as well as near the board edges. Additionally, the pithy center of the tree can be seen in ply 4 with dominant earlywood presence.

Figure 6-17. Shot 2 of specimen E-5P-12 was examined for potential indicators contributing to a higher residual velocity than expected.

Table 6-2. Outliers from ballistic testing.

Specimen	Shot #	Reason identified as outlier	Dissection Observation
Better than expected performance			
E-Base	1	very low residual velocity	even distribution of latewood and earlywood
E-3P-12	3	lower residual velocity	even distribution of latewood and earlywood, 3rd ply: potentially curved grain
E-5P-4	2	lower residual velocity	3rd ply: knot in path
E-Base	10	lower residual velocity	1st ply: knot; 2nd and 4th plies: path tangential to growth rings, even distribution of latewood and earlywood, close to pith
E-Base	9	lower residual velocity	4th ply: potential heartwood; 5th ply: proximity to knot
E-Base	8	lower residual velocity	2nd and 4th plies: knots; 1st, 3rd and 5th plies: path all tangential to growth rings
E-10P-1	5	shallow depth	1st ply: dense growth rings; 4th ply: curved grain; 6th ply (w/ embedded projectile): dense growth rings
E-10P-6	6	shallow depth	3rd and 5th plies: possible knots
E-10P-6	8	shallow depth	2nd ply: close proximity to knot; even distribution of latewood and earlywood
E-10P-6	5	shallow depth	no obvious indicator; even distribution of latewood and earlywood
E-5P-13	1	shallow depth	no obvious indicator; even distribution of latewood and earlywood
E-5P-3	5	shallow depth	1st and 2nd plies: dense growth rings; 2nd ply: possible knot
E-5P-3	4	shallow depth	2nd ply: close proximity curved path of projectile; dense growth rings
Worse than expected performance			
E-9P-4	5	deeper depth	1st, 3rd, 4th plies: path aligned nearly tangential to growth rings, significant earlywood
E-5P-12	2	higher residual velocity	2nd and 4th plies: path tangential to growth rings; 4th ply: significant earlywood (fast growing), also near pith/center and near board edge
E-5P-2	2	higher residual velocity	no obvious indicator; 2nd ply: significant earlywood, alignment close to tangential to growth ring
E-Base	3	higher residual velocity	1st and 5th plies: path aligned tangential to growth rings and also cavity walls lined up with ring transitions; significant earlywood
E-Base	6	higher residual velocity	1st and 5th plies: path aligned tangential to growth rings and also cavity walls lined up with ring transitions; significant earlywood

6.7 Summary

As a natural material, wood has a high degree of variability. To some extent this variability is reduced when the wood is used in a product with multiple plies like CLT. While the individual boards in the material may have a weakness-inducing defect or may be denser than the characteristic species value, the effect of this variability in a composite product is lessened for many material characteristics because all of the pieces would have to possess that defect or increased density for it to significantly affect the overall performance. However, with a ballistic impact the presence of knots, even in a single ply, can serve to resist or deflect the projectile as compared to shots fired through specimens consisting of clear wood. It is possible that lower graded wood, with more knots, would be preferable for panels in a design seeking improved ballistic resistance. Designers and manufacturers would need to verify that the lower quality wood still met the required strength and stiffness characteristics as outlined in PRG 320. Alignment of the grain direction and the distribution of earlywood and latewood also appear to influence the ability of the wood to absorb the energy of the projectile. The localized dynamic impact of the projectile creates complex stress states in the wood and result in a multiple failure modes in many cases as the wood experiences crushing, tensile splintering, and shear. The nature of CLT is such that the tests can be dissected post-test allowing for the close examination of the material response to the ballistic event.

CHAPTER 7
ENHANCED CLT (ECLT)

7.1 Introduction

The laminate nature of the CLT panels lends itself well to the concept of introducing other non-wood materials into the composite. This idea is especially attractive for specialized design requirements like enhanced ballistic resistance. While some materials, such as steel, may offer increased ballistic resistance they are not effective building materials for other reasons such as thermal efficiency of the building envelope. Additionally, design specifications may only need the increased ballistic resistance in specific high threat locations, so the structure could be built from CLT with ECLT panels in designated locations as determined by the threat analysis. CLT's use as a building material is relatively new and the idea of ECLT had not previously been explored by other researchers.

While ECLT is a new concept, hybrid CLT has been investigated although it is not recognized by the wood or mass timber industries. The use of the term hybrid references replacing a layer of sawn timber in the conventional CLT with laminated strand lumber (LSL), laminated veneer lumber (LVL) or hardwood species mixed with softwood species in alternating layers [22, 40, 116, 117]. No prior research was found examining a non-wood layer within the CLT composite construction, such as in ECLT.

The ECLT discussed in this research is distinct in that it introduced a special purpose enhancing layer with the intent of providing improved ballistic resistance. Other purposes could drive the inclusion of other types of materials. A key component of ECLT

is the adhesion of the enhancing layer to the wood layers. Because enhanced CLT involves adding layers to the layup, the increased weight, cost, and impact to overall structural performance such as strengths and stiffness should be considered.

7.2 Methodology

7.2.1 Enhancing layer materials

For the purposes of increased ballistic resistance, several different enhancing materials were selected, as shown in Table 7-1.

Table 7-1. Variations of ECLT investigated.

Nomenclature	Enhancing layer	Abbreviation	Thickness (in.)	Section with full description
Type 1	Perforated steel plate, P900	PM-1	0.50	7.2.2.1
Type 2	Expanded metal plate	PM-2	0.50	7.2.2.2
Type 3	Aramid epoxy panel	K-1, K-2, K-2	0.56	7.2.2.3
Type 4	Mild steel plate	MS-1, MS-2	0.25	7.2.2.4
Type 5	High-hard steel plate	HHS-1, HHS-2	0.25	7.2.2.5
Type 6	Ultra-high-molecular-weight polyethylene (UHMWPE)	D-1	1.00	7.2.2.6
Type 7	Fiberglass fabric, 4-ply consolidated	FF-4-1, FF-4-2	0.12	7.2.2.7
Type 8	Fiberglass fabric, separated 4-plies	FF-1-1, FF-1-2	0.12	7.2.2.7
*Several of the materials were donated by the Army Research Laboratory, at their request the manufacturer information is not disclosed due to proprietary concerns.				

The supplemental layer was selected with the intent of improving ballistic resistance through one of two methods. In the first method, some materials were selected because

they had strengths and hardness that it would overmatch the projectile and prevent perforation or slow the projectile down so much that the remaining wood layers would then not be perforated. The other method selected materials on the basis that they could act as a "net" within the composite, deforming and perforating and also providing significant energy loss to the projectile by dissipating its energy over a larger area and thus reducing its ability to penetrate. The materials selected for an enhancing layer in the ECLT specimens include the following: perforated steel plate; expanded metal plate; an aramid epoxy matrix panel; a 0.25-inch thick mild steel plate; a 0.25-inch thick high hard steel plate, an ultra-high-molecular-weight polyethylene (UHMWPE) panel, and two configurations of a fiberglass fabric woven roving. For one fiberglass fabric configuration, there were 4-plies of the fabric co-located for a thicker fabric layer between the 2- and 3-ply CLT sections. For the second arrangement, a single ply of fabric was placed between two cross-wise oriented wood layers, creating four total single-ply layers spaced evenly between each of the wood layers.

7.2.2 Production of ECLT

The CLT base of the ECLT specimens was a 5-ply Southern Yellow Pine (SYP) CLT specimen sized 12-inches high by 12-inches wide. For most of the enhancing layers, the non-wood material was sandwiched between 2-ply and 3-ply sections. The specimen was oriented so the 2-ply section was the first in contact with the projectile. The intent with sandwiching the enhancing layer at that location was to place the enhanced layer as close to the center of the panel as position to reduce the impact on the CLT specimens other characteristics such as strength and stiffness. Future testing could examine different locations for optimal location based on the CLT and enhancing material characteristics and

combined performance. The 2- and 3-ply sections of CLT were produced in the same manner as the standard CLT specimens using the press and polyurethane adhesive as discussed in Chapter 4, Section 4.3.2.

The perforated steel plate, expanded metal mesh and UHMWPE panel were all mechanically affixed to the two CLT sections due to concerns with bonding the materials. The mechanical connections used were washer hex drive screws sized 3/16-inch diameter and 6-inches long, like the one shown in Figure 7-1. For the perforated steel plate and expanded metal mesh, the screws were predrilled through the 2-ply to line up with the void spaces in the metal. The 3-ply CLT, metal plate and 2-ply CLT were stacked and the connections were driven into place, mechanically attaching all three pieces with eight screws. The UHMWPE panel was also predrilled and the same procedure was followed.

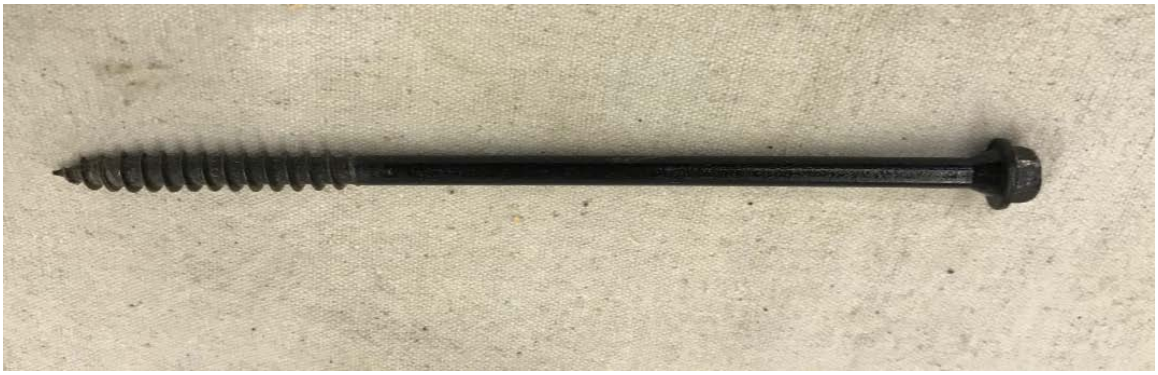

Figure 7-1. Example of the washer hex drive screw used for mechanical connection with ECLT types 1, 2, and 6.

For the other materials, the enhancing layer was adhered to the two CLT sections using a two-part, resin and hardener, epoxy system. The enhancing layer was surface

treated to provide a good adhering surface for the epoxy; the steel plates were media blasted and the aramid panels were lightly sanded. Epoxy was applied to the wood surface and the enhancing layer surface in a thin layer and then the materials were stacked with the 2-ply CLT section on top. No pressure was required for this adhesive method. For the woven roving, the fiberglass fabric was saturated with the epoxy and then laid into place. For the single-ply fabric configuration, the CLT sections were not pre-manufactured into 2- and 3-ply sections as with the other materials as the fabric layer was arranged in between each wood layer.

The epoxied ECLT specimens were left in place for over 24-hours to allow the adhesives to cure undisturbed. The specimens were then sanded on the edges to remove excess epoxy that had pooled and dried in place to create flat surfaces on the specimen sides for placement in the ballistic test set-up. Some shear block specimens were also produced using the fiberglass fabric and a piece of stainless steel for testing bond quality between the wood and enhancing materials using the epoxy. Those shear test results were discussed in Chapter 4.

7.2.2.1 Type 1 - Perforated steel plate

Perforated metal plates have been one advancement in armor technologies with the aim of using less metal for both material and weight considerations while also maintaining the ballistic resistance similar to that achieved with a solid plate. One perforated metal layer trialed was P900 perforated armor. Originally the holes were punched or drilled but the armor evolved to a manufacturing technique known as the lost foam process of casting metal [55]. The steel alloy perforated plate comes in a variety of thicknesses with the intent of being used as applique or add-on armor. It was originally designed to counter Soviet

small arms threats during the Cold War [64]. One advantage of perforated plates over lightweight ceramic armor plates is the ability of the metal plate to handle multiple threats. Some modern armors with high strength-to-weight ratios, such as ceramic plate, may be compromised with one shot and then defeated with additional impacts.

Perforations can significantly reduce the weight of the panel without reducing the strength. The staggered slotted holes in the plate serve to redirect the projectile within the target, thus absorbing more of its energy. Figure 7-2, from the military performance specification for perforated homogeneous steel armor, *MIL-PRF-32269*, shows a schematic of the perforated plate design [6]. The specification outlines hardness and ballistic standards that the perforated panels must meet for prospective manufacturers.

The size of the holes is important relative to the projectile threat as a projectile smaller than the opening may pass through on a carefully placed shot. For the perforated metal used in this research, the hole size was 1.1875-in. wide by 0.375-in. high, with a solid metal width of 0.1875-in. between the holes. The solid metal sections, depending on the projectile type and velocity, may help to defeat a projectile larger than the opening. The holes are also oriented at an angle, which helps with the deflection and limiting pass-through shots. Figure 7-3 is a photo of the perforated steel plate removed from the ECLT specimen after testing.

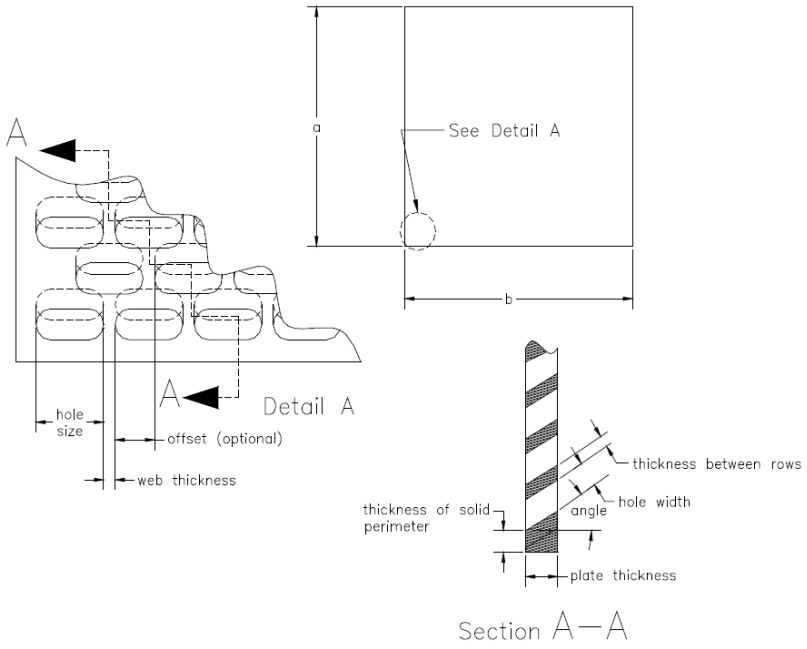

Figure 7-2. Schematic from performance specification document, MIL-PRG-32269, for perforated homogeneous steel armor.

Figure 7-3. A close-up view of the P900 steel plate removed from the ECLT block post-test.

The perforated steel used in this research measured 12-in. wide by 12-in. high and 0.50-in. thick. By the performance specifications of *MIL-PRF-32269*, the required ballistic limit (V_{50}) for the perforated plate with 0.50-in. thickness is 2,295 fps (700 m/s) for a 0.30 caliber armor piercing munition. This is smaller in diameter than the test sphere projectile and also has the armor piercing nose design. The minimum thickness for 0.50 caliber armor piercing munition and 20 mm armor piercing round are both greater than 0.50-inch. While the test projectile is larger in diameter, it does not have the armor piercing design. The test striking velocity was designed to be 2,500 fps (762 m/s) for comparison with the other series of tests to the standard CLT specimens.

7.2.2.2 Type 2 - Expanded metal plate

Expanded metal is typically a carbon steel sheet that has been both slit and stretched into a rigid mesh with diamond shaped openings. The expanded metal is comprised of strands of metal with intersections called bonds. The bonds form a sharp angle from the original flat sheet of metal, as shown in Figure 7-4. Expanded metal products are often made from both hot and cold rolled steel, galvanized steel as well as aluminum and other softer metals. It is used for a variety of purposes from industrial and commercial to decorative uses with thinner strands. Key specification measurements include width of mesh, length of mesh, width of strand, and weight per square foot for the heavier products. Figure 7-5, from the military specification for steel expanded metal, *MIL-M-17194D*, shows how those dimensions are measured.

For the expanded metal plate used in this research the width of mesh was 0.875-in., the length of mesh was 1.0625-in. and the width of strand was 0.25-in. Based on the strand thickness, the metal was likely heat treated prior to slitting and stretching for armored use

in accordance with *MIL-A-46177C*, the military specification for wrought homogeneous steel plate armor less than 0.25-in. thick with an average surface Brinell hardness of 362 to 400. According to this specification the minimum ballistic limit for a steel plate, 0.25-in. thick against a 0.30-caliber ball round fired at 30 degrees obliquity, is 2,544 fps (775 m/s).

Figure 7-4. A bond, the intersection of metal strands, on an expanded metal plate.

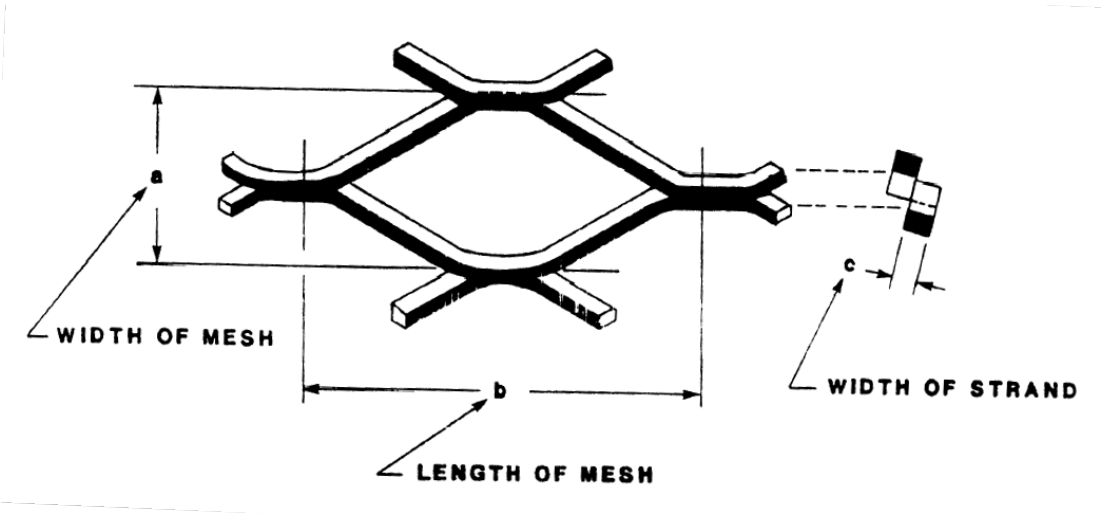

Figure 7-5. Key dimensional characteristics of expanded metal plate from the military specification standard, MIL-M-17194D.

Similar to Type 1, P900 perforated steel plate, Type 2, expanded metal plate has a favorable strength-to-weight ratio. The expanded metal plate used to make an ECLT specimen was not flattened, a common secondary finish completed by the manufacturer of processing it through a rolling mill creating a smooth flat sheet. Instead, the plate was uneven, as shown in Figure 7-6, with the intent of redirecting, slowing down or stopping the projectile when impacted within the ECLT. The individual strands were approximately 0.50-in. thick, with the openings less than 0.50-in. wide making it impossible for the 0.50-in. sphere projectile to pass unimpeded by the expanded metal plate. The heavy gauge of the plate used is similar to catwalk grating. The concept of using the expanded metal product was the same as the perforated steel plate. Expanded metal features a different style of manufactured perforations and different type of steel. As a result, the projectile would be diverted from a straight trajectory through the metal or stopped at the metal plate

when striking the expanded metal plate. Figure 7-7 shows the 12-in. by 12-in. plate removed from the ECLT specimen after the test shots.

Figure 7-6. The expanded metal plate shown assembled in the ECLT test specimen.

Figure 7-7. Expanded metal petal removed from the ECLT specimen post-test.

7.2.2.3 Type 3 - Aramid Epoxy Panel

An aramid epoxy panel is a rigid board approximately 0.5625-in. thick comprised of layers of aramid fabric with a polyvinyl butyral (PVB) phenolic resin. Aramid fibers are the manufactured fibers of the aromatic polyamide used as raw materials in body armors, fireproof clothing and racecar tires originally discovered by a DuPont scientist in the early 1970s. The fibers have a high strength-to-weight ratio, high structural rigidity and offer good resistance to abrasion and cutting. The aramid fabric layers are coated in the resin, stacked and then heated, which produced the rigid composite product. PVB resin is typically used when a strong bond, toughness and flexibility are required. A major application of the product is automobile windshield safety glass. This aramid- PVB resin composite product can be molded into various shapes during production or manufactured as flat sheets. It is also commonly used as a spall liner in armored vehicles to protect the occupants from the spall of the metal armor upon impact.

Based on the military detail specification, *MIL-DTL-62474F, Laminate: Aramid-Fabric-Reinforced, Plastic*, the panels used in the ECLT specimen were categorized as Class B with nominal 3,000 Denier, minimal 1300 filaments, and basket weave for the yarn fibered fabric. The Denier is a unit of measure for the linear density with the quantity annotating the mass in grams per 9,000 meter of fiber. For this fabric, the 3,000 Denier represents thick, heavy threads, which translates to a thick and durable material. Heavy-duty nylon materials for outdoor use are typically in the range of 1,000 Denier. The filament refers to a single continuous fiber strand. A basket weave fabric is a type of fiber weaving where the fiber strands running both longitudinal (warp) and transverse directions (weft) are woven together with at least two threads for each direction, interlaced over and

under each other, producing a checkboard or basket pattern. It provides an increased strength and durability to the fabric.

Based on the number of aramid fabric plies in the panels tested, the military specification calls for a ballistic limit of 1,924 fps (586 m/s) for a 0.30-caliber fragment simulating projectile (FSP) at zero degrees obliquity. This FSP round is typically blunt nosed and lighter at 44 grains than the 0.50-in. sphere test projectile used in this research. This would mean the CLT would be required to also reduce the energy of the projectile in order to prevent perforation of the ECLT specimen. Figure 7-8 shows the aramid panels before they were surface sanded for improved adhesion within the ECLT specimen. Three test specimens were made with the enhanced layer of aramid epoxy panel.

Figure 7-8. Aramid epoxy panels prior to production of ECLT panel.

7.2.2.4 Type 4 - Mild steel plate

Two ECLT specimens were produced with an enhancing layer of 0.25-inch mild steel plate. The characteristics of mild steel are strength and easy formability. Tensile ultimate strengths are typically in the range of 58-80 ksi (400-550 MPa) with a yield strength based on the 2% offset method of 36 ksi (250 MPa). Mild steel has a Brinell hardness in the range of 119-159 and a modulus of elasticity of 29,000 ksi (200 GPa). This type of steel is common for use in construction; it is not typically used as a modern armor material. The intent of using the mild steel was to investigate its performance within the ECLT as a relatively ductile steel.

A previous study conducted by Gupta and Madhu that included mild steel plates approximately 0.25-in. thick with a striking velocity in the range of 2,690 fps (820 m/s) observed petaling on the impact face of the plates and complete perforation by ogive-shaped armor-piercing projectiles. Additionally, crater diameters of measurable depth were formed on the front and back face of the mild steel targets. Thicker mild steel targets, up to almost 1-in., yielded similar results with slower residual velocities, and increased petal height on the front face [57].

7.2.2.5 Type 5 - High-hard steel plate

Two ECLT specimens were made using a 0.25-in. high-hard steel plate. The main difference between mild and high-hard steel are the hardness values for the two materials. Hardened steel such as the plates embedded within the ECLT specimens is typically used in military vehicles as wrought armor plate and covered by the detail specification, *MIL-A-46100D, High-hardness Wrought Steel Armor Plate*. It is typically heat treated to develop increased resistance to penetration. The military specification requires 0.25-in.

thickness to have a Brinell hardness value in the range of 477-534. High hard steels typically have higher yield stresses with strengths in the range of 87 to 130 ksi (600 to 900 MPa) but less ductility compared to mild steel.

The ballistic test standards for the minimum thickness require a 0.30-caliber armor-piercing munition at 30 degrees obliquity. The minimum required ballistic limit for the armored vehicle class with that projectile is 2,237 fps (682 m/s). A harder steel, with a minimum Brinell hardness of 570, known as ultra high-hard steel also exists with its own standard specifications for armor plate but was not included in this research. The failure mode commonly exhibited in high hard steel under a ballistic impact is plugging, where the plate experiences high localized shear forces and a disk, slightly larger than the diameter of the projectile, is ejected in a perforating event. Figure 7-9 shows a steel plug created with the 0.50-inch sphere projectile as an example (not produced with the ECLT specimens).

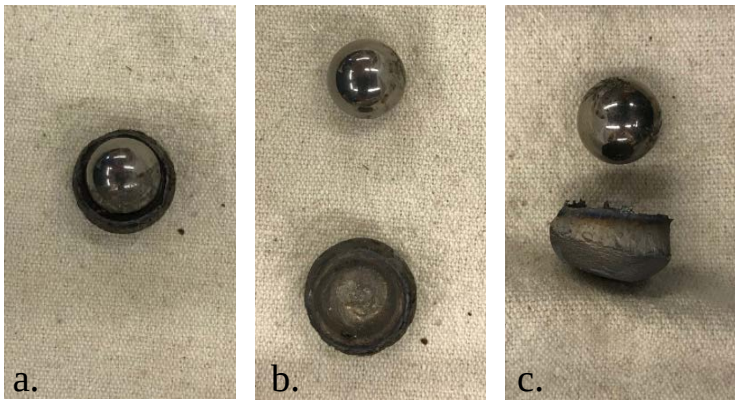

Figure 7-9. Example of the failure mode plugging in a steel plate (a) the projectile embedded in the ejected plug, (b) top view of plug, (c) side view of plug.

Steel, especially high-hard steel, is known for having great strength and the ability to provide an increased resistance against a ballistic threat; high-hard steel is commonly used as applique armor for hardening vehicles for this reason. The goal of embedding the steel plates in the CLT was to investigate the feasibility of such a composite using simple production techniques. Additionally, the research wanted to explore the effect of that a combination of materials presented in terms of delamination potential and effects of the ballistic impact at the CLT-steel interface. While the steel could potentially stop the projectile on its own, it would be unfeasible to make a structure out of high-hard steel on its own. Both the mild and high-hard steel plates enabled cost and weight comparisons between different types of steel and between non-steel enhancing layers.

7.2.2.6 Type 6 - Ultra-High Molecular Weight Polyethylene (UHMWPE)

One test specimen of ECLT contained an enhancing layer of ultra-high molecular weight polyethylene (UHMWPE) plastic panel. This panel was one-inch thick and placed between the 2-ply and 3-ply sections of CLT as shown in Figure 7-10. Based on military detail specification, *MIL-DTL-32398, Cross-plied Ultra-High Molecular Weight Polyethylene (UHMWPE) Unidirectionally Reinforced Plastic Armor* and the weight of the panel, the tested specimen contained a Class C UHMWPE, with a minimum ballistic limit of 1,082 fps (330 m/s). The panel is a fiber based, low weight composite laminate with four unidirectional sheets cross plied, much like CLT, and held together with a polyurethane based matrix. While the exact production details are proprietary, the general process involves the fiber manufacture in a high temperature gel-spinning process and then coated in resin, stacked crosswise to the desired thickness, and hot pressed. With a tensile

strength of 392 ksi (2.7 GPa), manufacturers claim the product as the strongest fiber on the market [112].

Many commercial manufacturers advertise body armor inserts made of UHMWPE with ballistic resistance against standard military munitions including 7.62-mm and 5.56-mm rifle ammunition with striking velocities of 2,780 fps (847 m/s) and 3,150 fps (960 m/s) respectively. Manufacturers of UHMWPE products claim the material has the impact strength equivalent to steel. The material is commonly produced through extrusion and compression molding. It is a unique material that has high tensile strength at high strain rates, which makes it a good lightweight product for body armors.

Figure 7-10. Side view of UHMWPE layer in ECLT specimen.

7.2.2.7 Types 7 and 8 - Fiberglass fabric

A woven roving fiberglass fabric was selected as an enhancing layer for an ECLT specimen due to its low cost, high strength reinforcement, impact resistance and high compatibility for bonding with the CLT sections. Much like the aramid fabric, the woven roving is comprised of bundled threads oriented in two orthogonal directions with a basket style weave. The fabric used was 18 ounces per square yard (582.5 grams per square meter), with a nominal thickness of 0.030-inches. Fiberglass fabric has a high tensile strength and low weight with a history of manufacture as quality ballistic panels capable of meeting many threat level ratings. Ballistic panels are commonly made with resin-saturated layers of woven roving designed to absorb impact as well as trap shrapnel and spall in the plies. The material is often combined with other materials including foam core and concrete to form composite panels. Hybrid products using both carbon and glass fibers are have also been the subject of ballistic impact studies [87, 111, 122].

The concept behind incorporating the fiberglass fabric into ECLT was to add lightweight, thin plies with the capacity to absorb and catch the projectile as it moved through the test specimen. Like UHMWPE, the fiberglass-epoxy panels have shown higher energy absorption capacity at higher impact velocities than at lower velocities. Failure modes with the fiberglass panels demonstrate elastic deformation, delamination between plies and subsequent brittle failure of the fibers.

Two specimens of two distinct layups using the fiberglass fabric were produced for a total of four fiberglass fabric ECLT specimens. One layup placed 4-plies of the fabric between a 2-ply and a 3-ply section of CLT. Figure 7-11 shows the side view of this 4-ply layup. Alternatively, the second layup placed a single ply between each wood layer of the

5-ply specimen block. Figure 7-12 illustrates the single ply layup. The 2-ply CLT, 4-ply fabric, 3-ply CLT layup had both a polyurethane adhesive bonding the wooden layers and an epoxy resin adhesive for bonding the fabric to the wood. The single-ply fabric alternating with wood layup utilized just the epoxy resin adhesive. This difference was not designed to create different strengths or impact resistance but was a necessity of production methods.

Figure 7-11. Close-up side view of 4-ply layer of fiberglass fabric in ECLT specimen.

Figure 7-12. Single-ply layers of fiberglass fabric between each wood layer in ECLT specimen.

7.3 Results and Discussion

Eighty-four tests were conducted on the eights types of ECLT specimens were tested using the same experimental setup at the U.S. Army Corps of Engineers' Engineer Research and Development Center (ERDC) in the Survivability Engineering Branch fragment simulating facility as described in Section 5.3 of this thesis. Fifteen test shots were also conducted on the one baseline traditional 5-ply Southern Pine (SYP) CLT specimen, since the testing was conducted at a different time from the bulk of the traditional CLT specimen testing. The target velocity for all tests was 2,500 fps (762 m/s). It is likely that the relatively small number of shots in the different specimens is not a large enough number of tests to draw any definitive recommendations. While ballistic testing is costly both financially and in time, this initial experimental work can provide a path forward for

additional research for both additional tests and empirical models which represent the behavior.

7.3.1 Perforated metal plates

For both of the perforated metal plates, the P900 and the expanded metal plate, there were no complete perforations. Upon disassembly of the ECLT specimens through the removal of the hex screws, the depth of penetration could be determined and damage assessment could be made. The previously used method of measuring depth of penetration with the drill bit in the projectile entry hole was not effective due to the metal plate; it was difficult to determine if the bit was in contact with the projectile or the plate or if the projectile had potentially been deflected as intended. Therefore, the results should be used with some caution.

7.3.1.1 Type 1 - P900 perforated steel plate

For the P900 perforated plate, seven shots were completed with the 0.50-in. sphere projectile with an average (mean) striking velocity of 2,528 fps (770 m/s). The perforated plate showed visible damage in the form of enlarged perforation holes but the metal was still intact with no fragments, as shown in Figure 7-13. One round, which happened to have the slowest striking velocity at 2,288 fps (697 m/s), was stopped at the front face of the perforated plate. A second round was lodged in the metal plate and became dislodged when the plate was removed from the CLT. It left a projectile-sized indentation in the 3-ply CLT behind the plate but the sphere was not embedded into the wood. The five other rounds were embedded in the first ply of the 3-ply CLT section mounted behind the perforated plate with the deepest depth of penetration measured at 3.75-inches, which is 0.50-in. past the perforated plate. Table 7-2 summarizes the details of the seven test shots

on the P900 plate specimen. Figure 7-14 shows a close-up view of the damage to the P900 plate and the CLT behind it for all seven shots.

Table 7-2. Details of the test shots on the P900 perforated steel plate ECLT specimen.

Specimen/Shot	v_s (chrono) (fps)	v_s (chrono) (m/s)	Partial Penetration (PP)/Complete Penetration (CP)	Measured Depth of Penetration (T_w) (in)	Location of projectile (upon dissection)
E-PM-1 Shot 1	2,642	805	PP	3.72	15/32" in 3-ply
E-PM-1 Shot 2	2,636	803	PP	3.75	1/2" in 3-ply
E-PM-1 Shot 3	2,288	697	PP	2.75	in front of plate
E-PM-1 Shot 4	2,565	782	PP	3.59	11/32" in 3-ply
E-PM-1 Shot 5	2,501	762	PP	3.59	11/32" in 3-ply
E-PM-1 Shot 6	2,514	766	PP	3.53	9/32" in 3-ply
E-PM-1 Shot 7	2,547	776	PP	3.00	in perforation hole

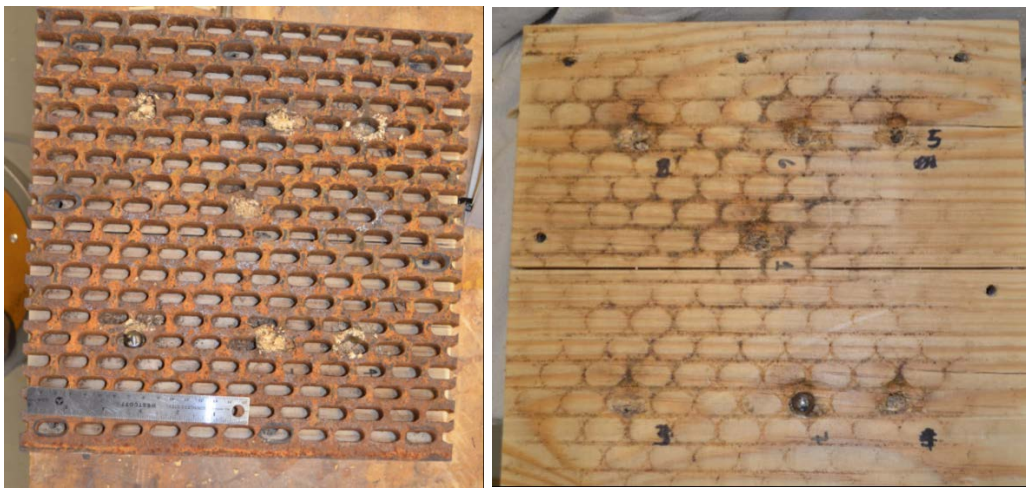

Figure 7-13. Disassembled ECLT: (left) P900 perforated steel plate; (right) 3-ply CLT positioned behind P900 plate.

Generally, the P900 performed well as there were no complete perforations through the ECLT specimen. However, the hole size was sufficiently large that at the given striking

velocities, the projectile was able to expand the hole and continue on into the 3-ply CLT. With the 0.50-inch thick perforated steel, the energy required to expand the hole did limit how much further the projectile traveled as none of the penetrations into the 3-ply were over 0.50-in. The location of the penetration with respect to the perforation influenced the penetration depth, as shots that lined up well with the perforation opening were the deeper penetrations.

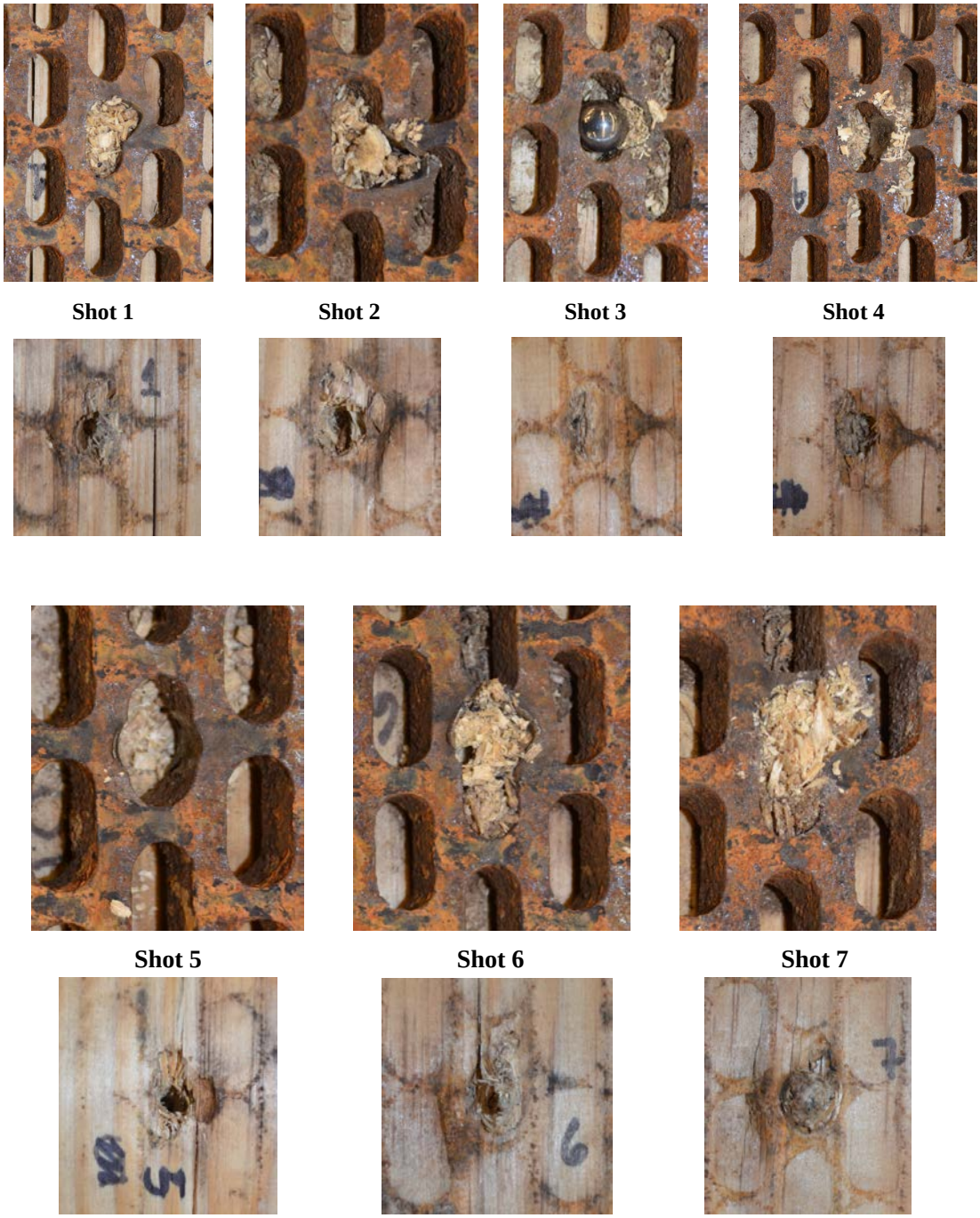

Figure 7-14. Close-up of shots 1-7 on perforated steel plate; for each labeled shot (top) front of steel plate, (bottom) face of 3-ply behind steel plate.

7.3.1.2 Type 2 - Expanded metal plate

For the expanded metal plate, eight shots were taken with the 0.50-in. sphere projectile with an average (mean) striking velocity of 2,543 fps (775 m/s). The perforated plate showed visible damage in the form of enlarged perforation holes and broken metal segments along with metal shrapnel loose and embedded in wood. Three shots were stopped at the front of the metal plate as shown in Figure 7-15.

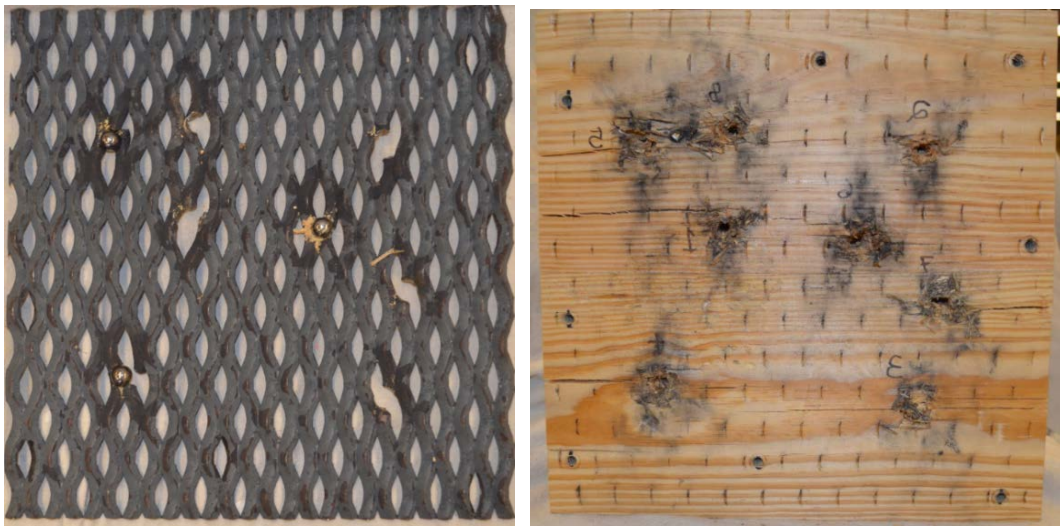

Figure 7-15. Disassembled ECLT: (left) expanded metal plate; (right) 3-plt CLT positioned behind the expanded metal plate shows damage from metal fracturing.

In contrast to the P900 plate, the three projectiles found in front of the metal plate did not coincide with the slowest striking velocities. Two other rounds fell free when the plate was removed but there was embedded shrapnel damage from those shots, which was measured for depth of penetration. One shot was noticeably deflected at an angle of approximately 45 degrees from the initial shot trajectory due to contact with the expanded metal. The angular surface of the expanded metal likely caused the diversion. Table 7-3

shows the details of the eight test shots on the expanded metal specimen. Figure 7-16 shows a close-up view of the damage to the expanded metal plate and the CLT behind it for all eight shots.

Minor damage to the spherical projectile was observed on several of the non-embedded rounds, as shown in Figure 7-17. This, combined with the brittle fracturing of the expanded metal, are caused by the hardness of the metal. This perforated product, in contrast to the P900, was likely heat-treated for increased hardness. The hardness of the spheres was given by the seller as Rockwell C55, which converts to a Brinell hardness of 560. The metal in the expanded product may have been a high-hard steel with an equivalent or higher hardness value. In general, the projectiles that made it past the expanded metal layer were not embedded deeply. The embedded projectiles can be observed in a few of the close-ups in Figure 7-16.

Table 7-3. Details of the test shots on the expanded metal plate ECLT specimen.

Specimen/Shot	v_s (chrono) (fps)	v_s (chrono) (m/s)	Partial Penetration (PP)/Complete Penetration (CP)	Measured Depth of Penetration (T_w) (in)	Location of projectile (upon dissection)
E-PM-2 Shot 1	2,524	769	PP	3.656	0.406-in. in 3-ply
E-PM-2 Shot 2	2,555	779	PP	3.750	0.500-in. in 3-ply
E-PM-2 Shot 3	2,520	768	PP	4.531	1.281-in. in 3-ply, angled 45 degrees left
E-PM-2 Shot 4	2,635	803	PP	2.750	in front of plate
E-PM-2 Shot 5	2,569	783	PP	2.750	in front of plate
E-PM-2 Shot 6	2,503	763	PP	2.750	in front of plate
E-PM-2 Shot 7	2,429	740	PP	4.031	shrapnel depth, sphere just behind plate (3.25")
E-PM-2 Shot 8	2,610	795	PP	4.625	shrapnel depth, sphere just behind plate (3.25")

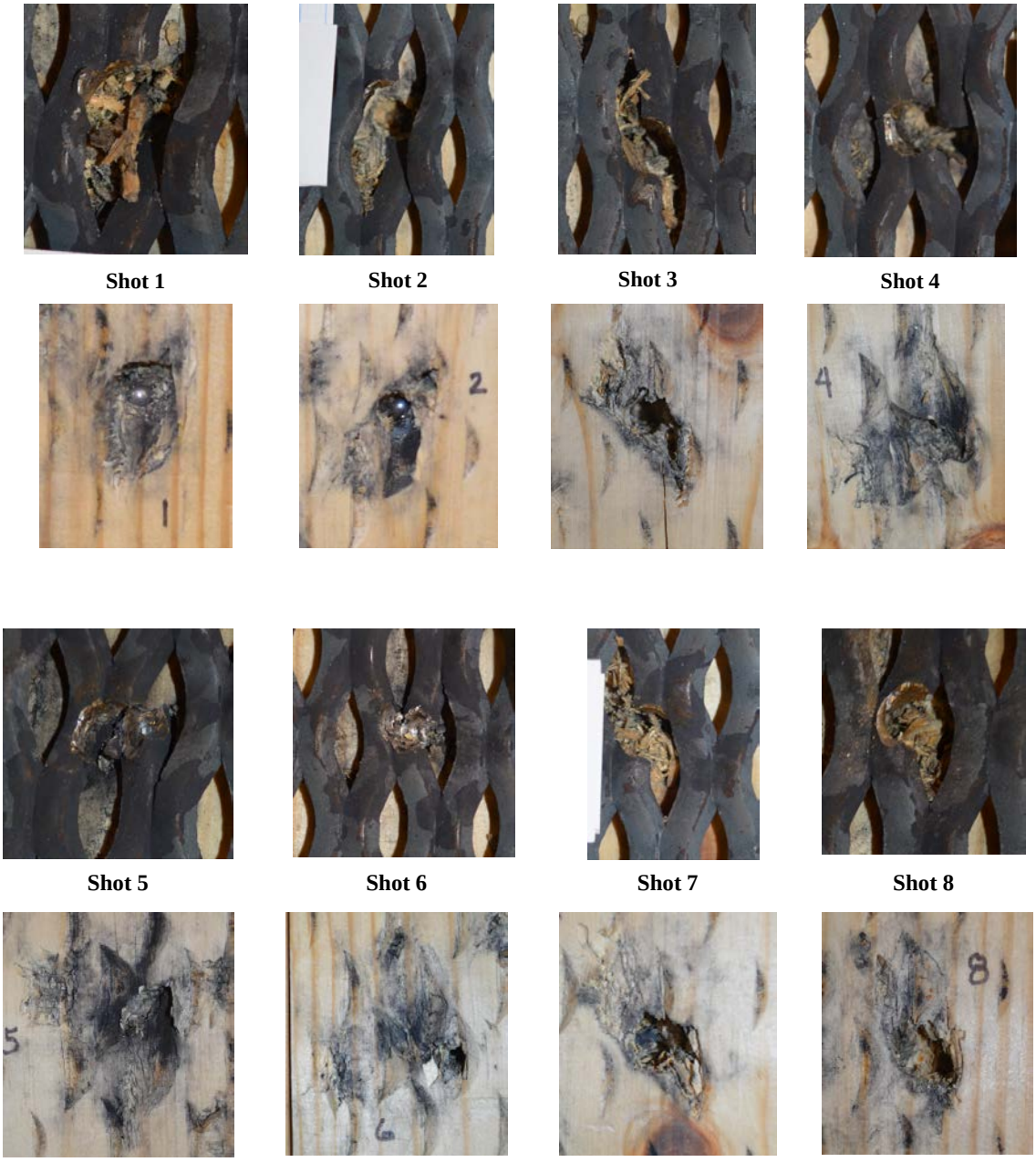

Figure 7-16. Close-up of shots 1-8 on expanded metal plate; for each shot (top) front of expanded metal plate, (bottom) face of 3-ply behind expanded metal plate.

Figure 7-17. Minor damage to sphere projectiles observed from expanded metal plate impact.

Overall, the expanded metal product performed well in that it stopped multiple shots at the face of the enhancing layer and had no complete perforations. The slightly smaller perforations compared to the P900 plate and the harder steel both contributed to its performance. Similar to the P900, the location of the shot with respect to the perforation pattern contributed to the results of the shot as projectiles that impacted a bond were more effective than those that hit a single strand. The shrapnel created from the fracturing metal may be a concern but all pieces were caught within the first ply of wood in the 3-ply CLT section behind the plate. The energy required to fracture the expanded product clearly limited the capacity of the projectile to continue penetrating. Additionally, an angled deflection of the projectile was observed.

7.3.2 Type 3 - Aramid epoxy panels

Three specimens of aramid epoxy panel ECLT were tested. For two of the specimens, the intended striking velocity was held constant with an average (mean) of 2,512 fps (765 m/s). For those two specimens, E-K1 and E-K2, there were no complete

penetrations with the seven and eight test shots respectively. The average depth of penetration for E-K1 was 4.36-in. and for E-K2 that value was 4.73-in. There were no indications of delamination on the top or sides of the specimen and the back face showed no signs of damage. Table 7-4 shows the details for striking velocity and depth of penetrations for the two specimens.

Table 7-4. Aramid epoxy panel ECLT tests for two specimens with no complete penetrations.

Specimen/Shot	v_s (chrono) (fps)	v_s (chrono) (m/s)	v_r (hi-speed) (fps)	v_r (hi-speed) (m/s)	Partial Penetration (PP)/Complete Penetration (CP)	Measured Depth of Penetration (T_w)
E-K1 Shot 1	2,443	745	0	0	PP	4.0000
E-K1 Shot 2	2,413	735	0	0	PP	3.4375
E-K1 Shot 3	2,481	756	0	0	PP	4.3125
E-K1 Shot 4	2,606	794	0	0	PP	5.4375
E-K1 Shot 5	2,502	763	0	0	PP	3.2500
E-K1 Shot 6	2,600	792	0	0	PP	4.6875
E-K1 Shot 7	2,621	799	0	0	PP	5.3750
E-K2 Shot 1	2,407	734	0	0	PP	4.2500
E-K2 Shot 2	2,347	715	0	0	PP	4.0313
E-K2 Shot 3	2,510	765	0	0	PP	4.1250
E-K2 Shot 4	2,435	742	0	0	PP	4.6250
E-K2 Shot 5	2,625	800	0	0	PP	5.8125
E-K2 Shot 6	2,601	793	0	0	PP	5.6250
E-K2 Shot 7	2,483	757	0	0	PP	3.8750
E-K2 Shot 8	2,619	798	0	0	PP	5.5000

A third specimen, E-K3 was subjected to higher striking velocities in order to determine how fast the projectile needed to be in order to result in a complete penetration of the ECLT target, like that shown in Figure 7-18. Six shots were taken with a minimum

striking velocity of 2,851 fps (869 m/s) and a maximum of 3,041 fps (927 m/s) and the three fastest shots achieved complete penetration while the three slower shots had partial penetrations of various depths. Table 7-5 shows the test details from the specimen subjected to the increased striking velocities.

Figure 7-18. Aramid epoxy panel ECLT with projectile path cut-away.

Table 7-5. Aramid epoxy panel ECLT tests of increased striking velocities for complete penetration.

Specimen/Shot	v_s (chrono) (fps)	v_s (chrono) (m/s)	v_r (hi-speed) (fps)	v_r (hi-speed) (m/s)	Partial Penetration (PP)/Complete Penetration (CP)	Measured Depth of Penetration (T_w)
E-K3 Shot 1	3,041	927	343	105	CP	-
E-K3 Shot 2	2,992	912	429	131	CP	-
E-K3 Shot 3	2,851	869	0	0	PP	6.4375
E-K3 Shot 4	2,866	874	0	0	PP	6.1250
E-K3 Shot 5	2,952	900	426	130	CP	-
E-K3 Shot 6	2,878	877	0	0	PP	6.7500

Residual velocities were recorded in values of 350 to 430 fps (105 to 131 m/s) despite striking velocities close to 3,000 fps (915 m/s). The lowest striking velocity for a complete penetration was recorded as 2,952 fps (900 m/s). Dissection of the specimen with complete penetrations showed the bulge of stretching and eventual fracture of the aramid fibers as visible in Figure 7-19.

Figure 7-19. Dissection of aramid panel ECLT: (left) close-up of projectile path; (right) fracture of aramid fibers.

In general, the aramid epoxy panel ECLT specimens did very well with no perforations until the striking velocity was elevated to almost 3,000 fps (915 m/s). For the initial two specimens shot at the constant velocity, the depths of penetration measure indicated that the projectile was stopped just beyond the aramid panel in the first ply of the 3-ply CLT section behind the enhancing layer. The aramid fiber is known for excellent ballistic resistance so this outcome was expected. The lack of evidence of delamination with attachment to the CLT sections was an additional positive measure of performance for this ECLT layup.

7.3.3. Steel plates (solid)

The adhesion of the plate to the wood proved to be challenging due to the natural curvature of the wood surface in contrast to the flat steel plate. While both the steel and wood surfaces were coated with the epoxy mixture, gaps were observed between the two materials. This would be a challenge in manufacturing this particular type of ECLT. Another adhesive or potentially mechanical connections like those used with the perforated metals could be alternatives to explore. Despite the gaps, the overall specimen once the epoxy dried appeared securely adhered and there was no movement upon application of static load to the test specimen.

7.3.3.1 Type 4 - Mild steel

Five test shots were taken as each of the two specimens constructed with the 0.25-inch mild steel plate, as shown in Figure 7-20. With an average striking velocity of 2,585 fps (788 m/s), the average depth of penetration was 2.7875-inches. The thickness of the 2-ply CLT on the specimen face was 2.7500-inches so the measured depths of penetration indicate that the 0.50-in. sphere projectile was stopped right at the front of the mild steel plate. The difference in depths of penetration were relatively minor and attributable to the variation in striking velocity along with the wood variance. Table 7-6 shows the test data.

While not observed after the first shot, upon successive shots, very small fractures (i.e., hairline cracking) were observed on the top and sides of the specimen in the wood near the steel interface, as shown in Figure 7-21. The cracks occurred in the wood on both the front and back face of the steel plate with respective to the impact direction. These cracks grew with each additional shot. Although not a delamination occurring strictly within the epoxy between the steel and wood, this cracking indicated the high stresses

occurring in the interface between the two materials. The gaps observed with the adhering challenges likely contributed to this effect.

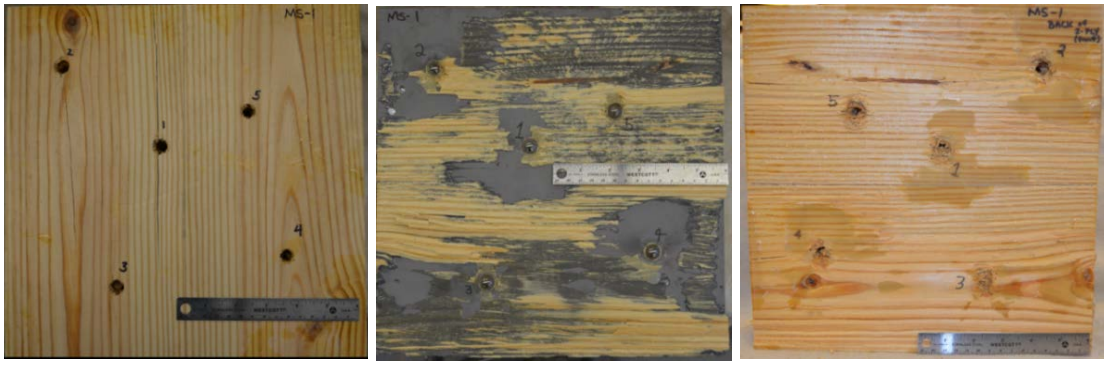

Figure 7-20. Mild steel ECLT post-test: (left) front face, 2-ply CLT; (center) mild steel plate face; (right) back of 2-ply CLT.

Table 7-6. Mild steel plate ECLT test details.

Specimen/Shot	v_s (chrono) (fps)	v_s (chrono) (m/s)	Partial Penetration (PP)/Complete Penetration (CP)	Measured Depth of Penetration (T_w) (in)
E-MS-1 Shot 1	2,556	779	PP	2.6875
E-MS-1 Shot 2	2,649	807	PP	2.7500
E-MS-1 Shot 3	2,470	753	PP	2.6250
E-MS-1 Shot 4	2,515	767	PP	2.7500
E-MS-1 Shot 5	2,548	777	PP	2.6875
E-MS-2 Shot 1	2,554	778.42	PP	2.6875
E-MS-2 Shot 2	N/R*	N/R*	PP	2.8125
E-MS-2 Shot 3	2,637	803.72	PP	2.9375
E-MS-2 Shot 4	2,675	815.30	PP	2.9375
E-MS-2 Shot 5	2,661	811.03	PP	3.000
* N/R – not recorded, chronograph did not read				

Figure 7-21. Evidence of wood fracturing at wood-mild steel interface: (left), top perspective, (right) side perspective.

Upon dissection of the mild steel ECLT specimens, it was observed that the projectiles were all embedded in the mild steel plate. The steel plate had slight bulging on the front face around the projectile but showed significant bulging on the back face of the plate as shown in Figure 7-22. The metal bulge also measurably indented the wood face of the 3-ply CLT section adhered behind the steel plate.

The mild steel plate performed as expected with prevention of complete penetration. The bulging was interesting to note and the increasing wood fractures indicated that another connection method between the wood and metal sections might be better suited for this type of ECLT. While there was enough adhesion between the two materials to hold together as one composite, the stresses caused by the impact lead to

noteworthy fracture in the wood closest to the steel. An additional option besides changing the connection is to add in a shock absorbing layer between the steel plate or and wood surfaces that dissipate that stress.

Figure 7-22. Bulge formed in mild steel and indentation in 3-ply CLT affixed behind steel.

7.3.3.2 Type 5 - High-hard steel

For the two ECLT specimens with embedded 0.25-in. high-hard steel plate, testing consisted of five test shots in each block, as shown in Figure 7-23. The average striking velocity was 2,525 fps (770 m/s) with an average depth of penetration of 2.53-in. This is approximately 0.25-in. less than the mild steel plate ECLT specimens' average depth of penetration. Similar to the mild steel ECLT, the variance in the depths of penetration were relatively small indicating that the projectiles were all stopped at the steel plate as anticipated. Table 7-7 provides the specific striking velocity and depth of penetration measurements.

Figure 7-23. High-hard steel ECLT specimen post-test: (left) back of 2-plt CLT, (center) front of 1/4-inch high-hard steel plate, (right) front of 3-ply CLT positioned behind steel plate.

Upon disassembly of the ECLT, which involved prying the wood away from the steel plate along the pre-existing gaps, the failure mechanism of plugging for the high-hard steel plate could be observed. The high-hard steel has no bulging but instead holes in the steel plate for all five shots that were slightly larger than the projectile diameter. The missing steel could be found as small disks embedded in the face of the 3-ply CLT section positioned behind the steel plate, as shown in Figure 7-24. The projectiles also shown in Figure 7-24, demonstrate damage caused from the impact with the high-hard steel, which was likely of equivalent or greater hardness than the spheres. Two of the projectiles were entrenched in the back face of the 2-ply CLT front section, which was positioned in front of the steel plate.

Table 7-7. Results from hard-hard steel ECLT testing.

Specimen/Shot	v_s (chrono) (fps)	v_s (chrono) (m/s)	Partial Penetration (PP)/Complete Penetration (CP)	Measured Depth of Penetration (T_w) (in)
E-HHS-2 Shot 1	2,602	793	PP	2.6250
E-HHS-2 Shot 2	2,569	783	PP	2.5000
E-HHS-2 Shot 3	2,389	728	PP	2.4375
E-HHS-2 Shot 4	2,541	774	PP	2.5625
E-HHS-2 Shot 5	2,397	731	PP	2.5000
E-HHS-1 Shot 1	2,533	772	PP	2.3750
E-HHS-1 Shot 2	2,693	821	PP	2.5000
E-HHS-1 Shot 3	2,598	792	PP	2.5625
E-HHS-1 Shot 4	2,362	720	PP	2.6250
E-HHS-1 Shot 5	2,572	784	PP	2.6250

Figure 7-24. Post-test on high-hard steel ECLT (left) Plugging failure of steel plate embeds projectile sized plug into 3-ply face; (right) Damage to sphere projectiles.

Some wood fracture was observed in the high-hard steel ECLT specimens and is shown in Figure 7-25. Unlike the cracking seen in the mild steel ECLT, it was not observed until the third or fourth shot on the same test specimen. This could be attributed to more global damage occurring within the specimen. The majority of the fracture cracking was

observed in the wood behind the steel plate. This material interface also had a significant gap due to the slightly irregular surface of the wood, which could have contributed to difference in wood fracture patterns.

Similar to the mild steel, the high-hard steel performed well with all the shots being stopped at the enhancing layer. While less fracture in the wood was observed, this phenomena still creates concern on the best practices for production of this type of ECLT product. The plugging failure mode of the high-hard steel was noticeably different from the bulging of the mild steel but both materials achieved the intent of stopping the projectile. While the depth of penetration was slightly less with the high-hard steel, the embedded steel plug in the 3-ply CLT was notable.

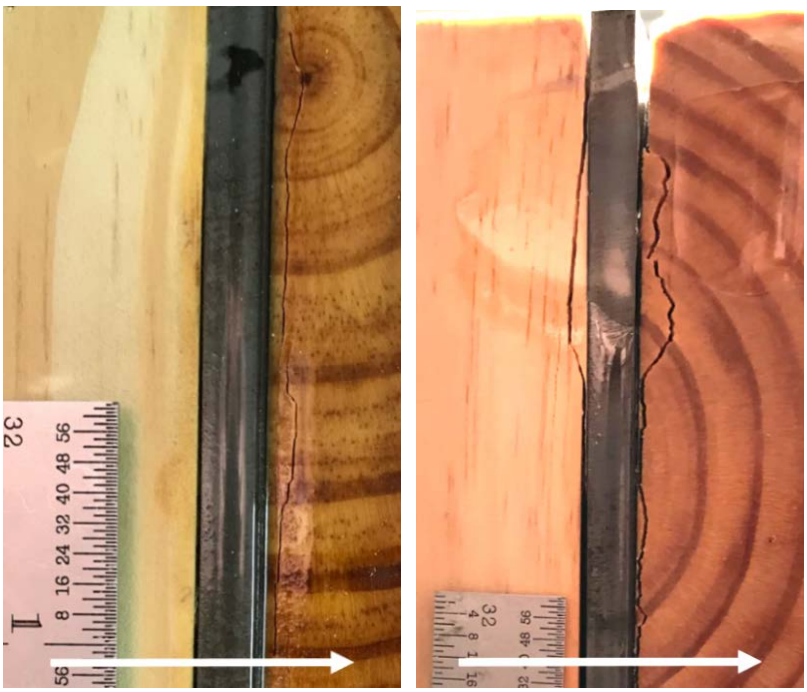

Figure 7-25. Wood fracture observed after test shots at wood-steel interface: (left) top perspective, (right) side perspective.

7.3.4 Type 6 - Ultra-high molecular weight polyethylene (UHMWPE) panel

The UHMWPE ECLT specimen was subjected to a total of eight shots as shown in Figure 7-26 and Figure 7-27. The first five shots had an average striking velocity of 2,503 fps (763 m/s) with an average depth of penetration of 2.3500-inches. This average depth means the projectile was stopping at the back of the 2-ply CLT section as the front of the sphere came into contact with the UHMWPE panel. There were no signs of cracking or damage to the back face of the target.

After the second shot, a small crack on the side of the 2-ply CLT section was observed. This crack aligned with the entry hole of that shot. This suggests that the dissipation of the projectiles energy by the UHMWPE may still be causing stresses in the wood sections. Alternatively, the crack could have simply propagated from the projectiles path in the 2-ply CLT section along a flaw or grain line to the edge of the specimen. After the first five shots, an additional three shots were taken at the specimen to determine the complete penetration striking velocity. Table 7-8 shows the testing specifics for all eight shots. The residual velocity is reported in the depth of penetration column for the one complete penetration achieved as a striking velocity of 4,169 fps (1,271 m/s).

With the last three shots of higher velocities, damage to the UHMWPE could be seen from the edges of the specimen as the high strength fibers pulled in from the edge. The pulling within the UHMWPE panel as well as observed radial and tangential cracking within the wood plies is shown in Figure 7-28. Once disassembled, it was observed that two projectiles were embedded in the 2-ply CLT and three others were in the UHMWPE.

Figure 7-26. UHMWPE ECLT dissected: (left) back of front 2-ply CLT; (right) front of UHMWPE panel.

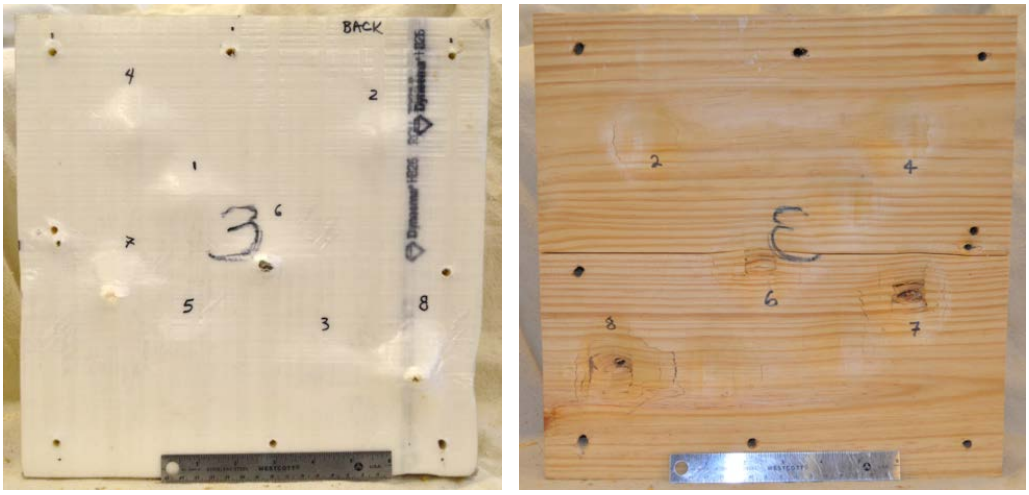

Figure 7-27. UHMWPE ECLT dissected part two: (left) back of UHMWPE section; (right) front of 3-ply CLT behind UHMWPE.

Figure 7-28. Damage to UHMWPE panel within ECLT specimen.

Table 7-8. UHMWPE ECLT test results.

Specimen/Shot	v_s (chrono) (fps)	v_s (chrono) (m/s)	Partial Penetration (PP)/Complete Penetration (CP)	Measured Depth of Penetration (T_w) (in)
E-D1 Shot 1	2,624	800	PP	2.2500
E-D1 Shot 2	2,402	732	PP	2.3750
E-D1 Shot 3	2,563	781	PP	2.4375
E-D1 Shot 4	2,512	766	PP	2.4375
E-D1 Shot 5	2,416	736	PP	2.2500
E-D1 Shot 6	3,610	1,100	PP	3.6875
E-D1 Shot 7	4,169	1,271	CP	v_r =560 fps (171 m/s)
E-D1 Shot 8	3,907	1,191	PP	5.3125

Bulging of the UHMWPE panel occurred on both the front and back faces. Close-up perspectives of the back of the 2-ply CLT and front of the UHMWPE panel can be seen in Figure 7-29. Much like the mild steel, the enhancing layer back face bulging caused indentations in the 3-ply CLT positioned behind that layer. The projectile was not visible

on the back face of the UHMWPE until the striking velocity was increased to values over 3,600 fps (1,097 m/s).

The high impact strength of UHMWPE was clear with the testing of this version of ECLT. The specimen withstood high velocities with minimal impact to the CLT. The UHMWPE panel may have had similar results on its own due to its specific design for increased ballistic resistance, but it lacks the overall strength and stiffness for use as a structural panel. Concerns with adhering the material to the wood sections led to using mechanical connections, which demonstrated the ability to hold the composite together without issue. Further investigation into adhering the panel could be interesting and produce more cost- and labor-effective designs.

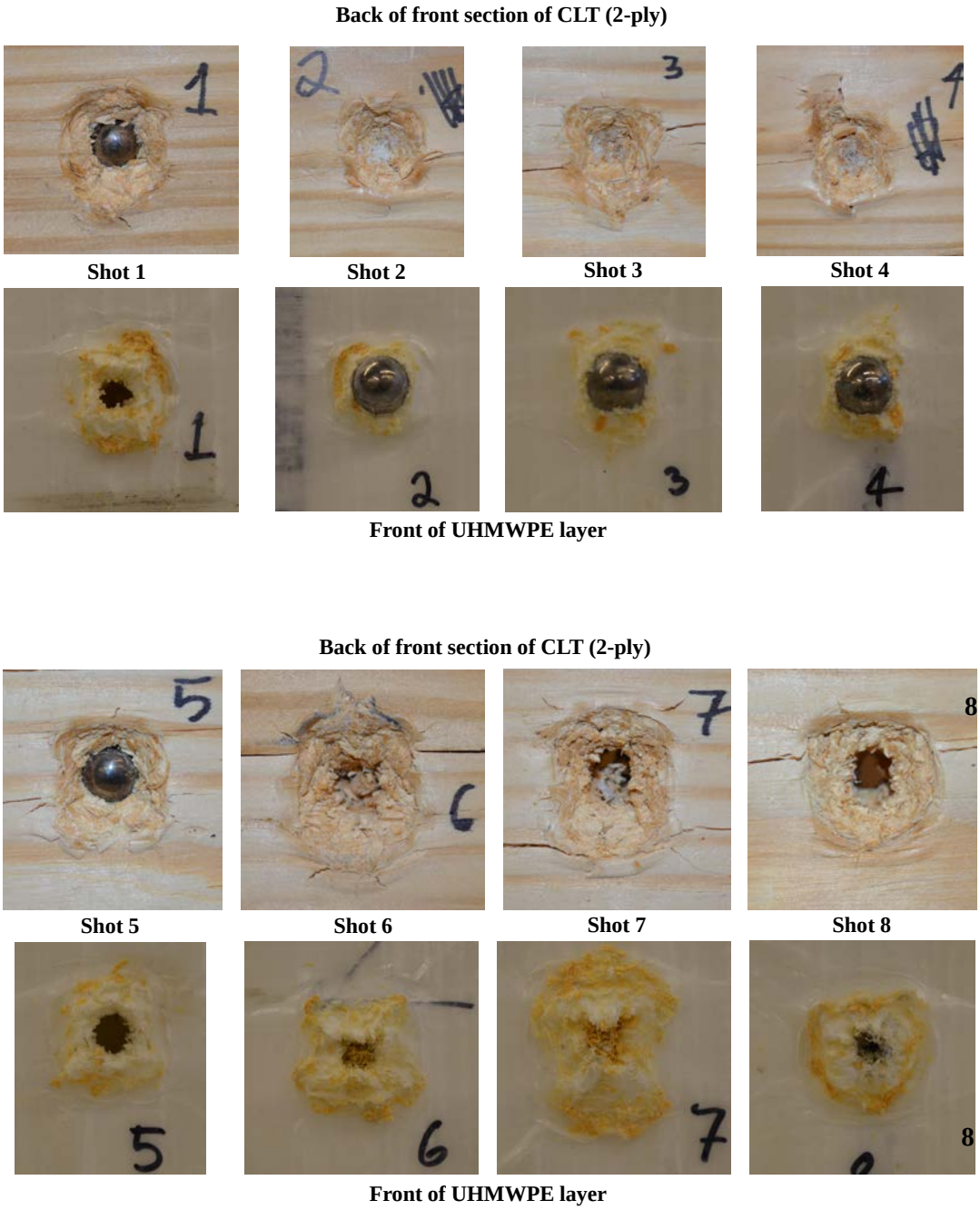

Figure 7-29. Close-up of shots 1-8 on UHMWPE ECLT specimen; for each shot (top) back of 2-ply CLT positioned in front of UHMWPE panel, (bottom) front face of UHMWPE panel.

7.3.5 Fiberglass fabric

The two different layups of ECLT using fiberglass fabric as an enhancing layer showed mixed results in terms of partial and complete penetrations. All four specimens, two of each layup, were shot five times each. Based on this limited number of tests, the consolidated 4-ply version performed better than the separated 4-ply version.

7.3.5.1 Type 7 - Consolidated 4-ply fiberglass fabric

The two specimens with the 4-ply fiberglass fabric consolidated layup resulted in eight partial penetrations and two complete penetrations. One specimen is shown in Figure 7-30. The average striking velocity was 2,469 fps (753 m/s) and the average depth of penetration for partial penetration results was 6.1300-inches. The residual velocities for the two complete penetrations were 301 fps (92 m/s) and 327 fps (100 m/s). Test data can be found in Table 7-9. Despite not being a complete penetration, in shot 5 of the test specimen in Figure 7-30 there was visible back face damage in the form of splintering of the wood, which is effectively petaling of the wood material. The projectile could be seen within the splintered wood but did not have the energy to exit the damaged specimen.

The two shots that resulted in complete penetrations were in the same specimen, E-FF4-2, and one occurred with the fastest velocity that block experienced, 2,492 fps (760 m/s). However, the second complete penetration shot in that specimen was the slowest striking velocity for that specimen at 2,462 fps (750 m/s). The other test specimen with the same enhancing layer composition experienced multiple shots at higher velocities but only had partial penetrations.

Figure 7-30. Consolidated fiberglass fabric ECLT (left) impact face, (right) back face shows damage.

Table 7-9. Results of consolidated 4-ply fiberglass fabric ECLT testing.

Specimen/Shot	v_s (chrono) (fps)	v_s (chrono) (m/s)	v_r (hi-speed) (fps)	v_r (hi-speed) (m/s)	Partial Penetration (PP)/Complete Penetration (CP)	Measured Depth of Penetration (T_w)
E-FF4-1 Shot 1	2,498	761	0	0	PP	6.1875
E-FF4-1 Shot 2	2,547	776	0	0	PP	6.3750
E-FF4-1 Shot 3	2,390	728	0	0	PP	5.7500
E-FF4-1 Shot 4	2,449	746	0	0	PP	5.4375
E-FF4-1 Shot 5	2,432	741	0	0	PP	6.0000
E-FF4-2 Shot 1	2,463	751	0	0	PP	6.4375
E-FF4-2 Shot 2	2,462	750	301	92	CP	-
E-FF4-2 Shot 3	2,484	757	0	0	PP	6.2500
E-FF4-2 Shot 4	2,492	760	327	100	CP	-
E-FF4-2 Shot 5	2,468	752	0	0	PP	6.6250

A cross-section cut of the projectile path through a consolidated 4-ply fiberglass fabric specimen shows the petaling of the wood as well as the stretch and brittle failure of the fiberglass fibers in Figure 7-31. It is not unlike the aramid panel failure except there is a thinner layer of fabric. In comparison to 5-ply CLT made from the same wood type, the four consolidated layers of fiberglass outperforms the 'unenhanced' CLT. Eight shots in two different 5-ply CLT specimens, in the range of 2,428 fps (740 m/s) to 2,560 fps (780 m/s), all resulted in complete penetrations with an average residual velocity of 780 fps (238 m/s). Eight of ten shots on the ECLT with consolidated 4-ply layup only had partial penetrations and the two residual velocities were less than half of the average residual velocity for the baseline CLT.

Figure 7-31. Close-up view of the projectile path through the four plies of fiberglass fabric.

7.3.5.2 Type 8 - Separated 4-ply fiberglass fabric

The two specimens with 4-ply fiberglass fabric separated between each wood layer layup resulted in six complete penetrations and four partial penetrations. One specimen is

shown in Figure 7-32. The average striking velocity was 2,467 fps (752 m/s) and the average depth of penetration for partial penetration was 5.7600-inches. The average residual velocity was 301 fps (92 m/s). Test data can be found in Table 7-10. The visible back face damage occurred the form of brittle failure of the wood, much like the consolidated 4-ply fiberglass fabric layup but the damaged area appeared more localized whereas the consolidated fabric comprised test block seemed to have longer spanning splintering damage. This observation could be a product of the different organization of the fiberglass fabric and its impacts on dissipating energy or on the wood elements in the ECLT specimens. More testing would be required to definitively make that determination.

Figure 7-32. Separated fiberglass fabric plies (left) impact face, (right) back face damage.

A cross-section cut of the projectile path through the separated 4-ply fiberglass fabric specimen displays less obvious stretching in the first two layers of fabric compared to the consolidated 4-ply. A cross-section cutaway of a complete penetration shot is shown in Figure 7-33. A more apparent stretch of the fabric appears in the third and fourth plies.

Table 7-10. Results of consolidated 4-ply fiberglass fabric ECLT testing.

Specimen/Shot	v_s (chrono) (fps)	v_s (chrono) (m/s)	v_r (hi-speed) (fps)	v_r (hi-speed) (m/s)	Partial Penetration (PP)/Complete Penetration (CP)	Measured Depth of Penetration (T_w)
E-FF1-1 Shot 1	2,484	757	0	0	PP	5.7500
E-FF1-1 Shot 2	2,632	802	176	54	CP	-
E-FF1-1 Shot 3	2,402	732	0	0	PP	5.3438
E-FF1-1 Shot 4	2,472	753	0	0	PP	5.8125
E-FF1-1 Shot 5	2,527	770	0	0	PP	6.1250
E-FF1-2 Shot 1	2,491	759	411	125	CP	-
E-FF1-2 Shot 2	2,626	800	944	288	CP	-
E-FF1-2 Shot 3	2,297	700	380	116	CP	-
E-FF1-2 Shot 4	2,382	726	593	181	CP	-
E-FF1-2 Shot 5	2,356	718	510	155	CP	-

A cross-section of the projectile path for a partial penetration shot, shown in Figure 7-34, shows the projectile stopped at the last fabric ply with the fiberglass visibly stretched. While the fewer number of partial penetrations seemingly indicates less ballistic resistance than the consolidated 4-ply, more testing would be required to draw that conclusion definitively. Compared to the baseline CLT, the separated 4-ply fiberglass fabric still stopped four of the ten test shots and had a residual velocity, similar to the complete penetrations of the consolidated 4-ply, less than half the average residual velocity of the 5-ply CLT without the fiberglass fabric.

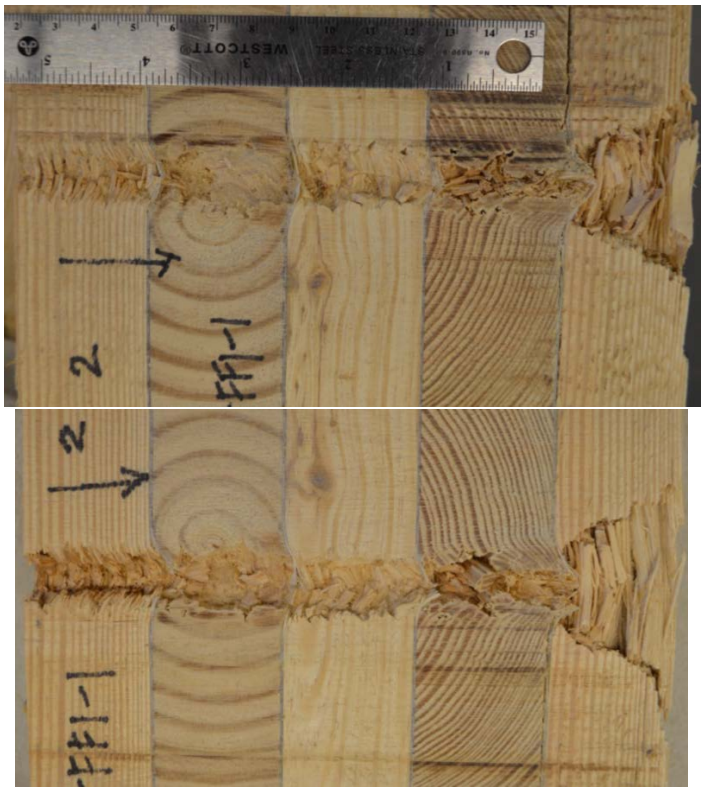

Figure 7-33. Cross-section of projectile path through ECLT specimen with separated fiberglass fabric layer between wood layers.

Figure 7-34. Close-up perspective of projectile stopped within ECLT made with separated layers of fiberglass fabric.

Generally, the fiberglass fabric performed well. While the new technology fiber-based panels such as aramid and UHMWPE had more ballistic resistance, they were also a

lot thicker in composition. As stated, the fiberglass layers did result in less complete penetrations and slower residual velocities than the CLT without it. The thin layers of fiberglass show the potential of adding a lightweight and relatively inexpensive product to the composite material could enhance the design specifications of CLT.

7.4 Weight analysis

A challenge with improved force protection through adding armor is keeping the material as lightweight as possible for logistical reasons while also achieving a high level of protection. Perforated metals work towards this aim by reducing the actual amount of steel with designed void spaces while keeping the general resistance level of the metal plate. New technologies in the fiber-based composite laminates also provide new lightweight options. While hardening a structure does not necessarily have the same weight limitations as a vehicle or person, there are still weight considerations with both the logistics of the construction materials discussed in Chapter 2 as well as the structural design.

7.4.1 Areal density

A key metric for armor is known as the areal density of the material, which is in units of weight per unit area. The logic behind this characteristic is that there is a finite amount of surface area on a vehicle, aircraft, structure or person to protect and the areal density describes the weight over that area. Manufacturers cite areal density as a material characteristic of their composite ballistic panels. The areal density also often gives an indication of the energy absorbing capacity of the material.

For comparison, armors are often described by performance measures such as thickness required for protection, or the distance at which a bullet can perforate. A

compromise between weight and performance is common in armor plate, with improvements in technology often coming in the form of a lighter weight armor with equivalent performance for ballistic threat resistance. Areal density does not measure effectiveness but it does factor into the calculation. Table 7-11 provides the areal density and weight of each of the enhancing layers trialed in this research. The layer thickness for the expanded metal was measured as 0.50-in. as that is how thick it measured with the expanded strands and bonds; the metal stock used to manufacture it was 0.25-in. thick.

Mass efficiency is used to measure effectiveness of armor materials. It is calculated relative to the areal density of rolled homogeneous armor (RHA), the steel plate typically used on tanks. The areal density of the RHA steel plate of the designated thickness required to stop a specified threat is divided by the areal density of the armor material under consideration. The higher the mass effectiveness, the lighter the weight of the armor for the same threat.

The enhancing layers in this research, from highest to lowest areal density are: mild steel plate; high-hard steel plate; P900 perforated steel; expanded metal; aramid epoxy panel; UHMWPE fiberglass fabric. This order is close to the rating of weight from heaviest to lightest except that the perforated plate is third in areal density and second in weight. The areal densities of the entire selection of materials show a wide spectrum of options for enhancing layers with metal, either thin solid plate or perforated plates at one end, advanced technology fiber-based epoxy panels made up of many or thick plies in the middle and very thin, lightweight, low ply count fiberglass fabric on the other end.

Table 7-11. Areal density values for the various enhancing layers trialed in ECLT specimens.

Enhancing layer	Layer thickness (in)	Weight of layer (lb.)	Weight of layer (kg)	Mass density ($lb./in^3$)	Areal density of enhancing layer(s) ($lb./in^2$)	Areal density of enhancing layer (kg/m^2)
Perforated Steel (P900)	0.50	10.00	4.54	719.96	20.00	97.64
Expanded Metal	0.50	6.23	2.82	448.21	12.45	60.79
Aramid Epoxy Panel	0.5625	3.56	1.61	288.31	6.33	30.89
Mild Steel Plate	0.25	10.26	4.66	369.52	41.06	200.46
High-hard Plate	0.25	9.74	4.42	350.62	38.96	190.21
UHMWPE	1.00	5.12	2.32	737.79	5.12	25.02
Fiberglass fabric (4-ply x 1)	0.12	0.51	0.23	8.79	4.24	20.70
Fiberglass fabric (1-ply x 4)*	0.12	0.13	0.0577	8.79	4.24	20.70
* thickness and weight values multiplied by the 4 layers for total provided by fiberglass layers						

7.5 Cost benefit analysis

In conducting a cost to benefit analysis, it is important to define the benefit. Many contributing factors could be used to assess the benefit such as ease of production, ease of constructability, availability of material, ballistic resistance, and weight for logistical considerations if applicable. For simplicity, the cost benefit analysis presented here limits the assessment to a ballistic resistance ranking and two different cost values, cost by weight and the cost by area. Many armor materials are priced by their cost per pound but the area requiring the armored protection should also be considered.

It should be noted that a cost for potential casualties, fatalities or injuries, is not included in this cost benefit analysis. This is because in military decision-making, the assessment of probable casualties is conducted in the risk assessment and composite risk management. In the case of material selection, it is likely that a military commander would make a determination of risk and acceptable mitigation measures. This would be a separate process from the cost benefit analysis detailed in this work. This risk assessment and mitigation would affect the cost benefit analysis by influencing the minimum acceptable levels of protection or setting a maximum damage threshold for some of the protection criteria as discussed in Chapter 9.

Prices listed in Table 7-12 came from 2018 vendor quotes or from experienced researchers for some of the military specific materials, which were donated by the Army Research Laboratory (ARL) [100]. The prices are approximate estimates and do not take into account any quantity discounts or shipping costs, which could significantly change the overall cost. The newer advanced technology fiber-based materials such as aramid and UHMWPE are significantly more costly than the metal plates and fiberglass fabric.

Table 7-12. Cost comparison for enhancing layers.

Enhancing layer	Cost/lb.	Thickness Basis(in.)	Cost/ft^2
Perforated Steel	$ 9.00	0.50	$ 90.00
Expanded Metal	$ 3.23	0.50	$ 20.10
Aramid Epoxy Panel	$ 20.00	0.56	$ 71.19
Mild Steel Plate	$ 0.98	0.25	$ 10.10
High-hard Plate	$ 5.24	0.25	$ 51.05
UHMWPE	$ 40.00	1.00	$204.94
Fiberglass fabric (4-ply x 1)	$ 6.92	0.12	$ 3.52
Fiberglass fabric (1-ply x 4)	$ 6.92	0.12	$ 3.52

A ballistic resistance ranking was subjectively determined for each layer for the purposes of this comparison based on the quantity of complete and partial penetrations, the percentage of penetrations beyond the enhancing layer, and maximum depth of penetration. This assessment is based solely on the experimental testing of this research with the 0.50-in. sphere. Other approaches for ranking the ballistic performance of the materials could incorporate the mass effectiveness using the RHA areal density required to stop the specified projectile. Table 7-13 shows the relevant data for the assessment and ranking of the various materials. The baseline CLT is included in the comparison because not having an enhancing layer is also an option with zero additional cost. Additionally, only test shots in the aimed striking velocity of 2,500 fps (762 m/s) were included in this comparison. The increased velocity shots to test the material limits were excluded.

Table 7-13. A comparison of ballistic resistance based on testing.

Enhancing layer	Ballistic resistance				
	Complete Penetrations	Partial Penetrations	% of penetrations beyond enhancing layer (v_s = 2500 fps)	Maximum depth of penetration (in)	Ranking (low = better performance)
Perforated Steel	0	7	71%	3.72	5
Expanded Metal	0	8	63%	4.625	4
Aramid Epoxy Panel	0	15	93%	5.8125	6
Mild Steel Plate	0	10	0%	3	3
High-hard Plate	0	10	0%	2.625	2
UHMWPE	0	5	0%	2.4375	1
Fiberglass fabric (4-ply x 1)	2	8	100%	6.875	7
Fiberglass fabric (1-ply x 4)	6	4	100%	6.875	8
Baseline CLT	8	0	100%	6.875	9

For the calculation of the benefit cost ratio (BCR), with higher values representing a better situation, the benefit ranking is divided by the cost ranking. In this scenario the ballistic resistance ranking, with low values representing a better performance serves as the benefit metric. This ratio was calculated for both the cost per weight and the cost per area. Each ratio was then ranked to show the highest to lowest BCR materials where a high value is better. Table 7-14 displays the rankings for ballistic resistance and cost as well as the BCR and rank of the BCR for both pricing options.

Table 7-14. Benefit cost ratio assessment for various enhancing materials.

Enhancing layer	Ballistic Resistance Ranking	Cost per weight ($/lb.)			Cost per area ($/ft^2)		
		Cost per weight ranking	Benefit Cost Ratio (BCR)	Rank of BCR	Cost per area ranking	Benefit Cost Ratio	Rank of BCR
Perforated Steel	5	7	0.71	7	8	0.63	7
Expanded Metal	4	3	1.33	5	5	0.80	5
Aramid Epoxy Panel	6	8	0.75	6	6	1.00	4
Mild Steel Plate	3	2	1.50	3	4	0.75	6
High-hard Plate	2	4	0.50	8	7	0.29	8
UHMWPE	1	9	0.11	9	9	0.11	9
Fiberglass fabric (4-ply x 1)	7	5	1.40	4	2	3.50	3
Fiberglass fabric (1-ply x 4)	8	5	1.60	2	2	4.00	2
Baseline CLT	9	1	9.00	1	1	9.00	1

Using this technique with the ballistic resistance as the assessed benefit, the baseline CLT achieved the highest BCR. Despite the lowest ballistic resistance, it had no additional cost. The separated 4-ply fiberglass fabric was second after the baseline CLT.

For the cost per weight, the third best BCR is the mild steel plate ECLT while for the cost per area, the third ranked BCR is the consolidated 4-ply fiberglass fabric ECLT. If the need for ballistic resistance to a specified threat were a requirement to the building design, then materials not meeting that resistance level could be eliminated as options. For example, if the 0.50-in. sphere with a striking velocity of 2,500 fps (762 m/s) were the specified threat and the requirement was no perforations, then the baseline CLT and both 4-ply fiberglass fabric ECLT versions would be eliminated. This criteria would make the mild steel plate ECLT the best option for cost by weight and the aramid epoxy panel the top choice for cost by area.

A variation to the benefit cost ratio assessment would be the incorporation of additional factors beyond just cost and this simplified ballistic resistance ranking. Another option would be to weight the costs or benefits depending on their relative importance. If the cost is less important and the ballistic resistance is very important than the ballistic ranking could be multiplied by two and the cost ranking multiplied by 0.5 as shown in weighted version A of Table 7-15. Conversely, if cost were more important, it could be weighted with a value over one and the ballistic resistance could stay weighted as 1 or a value less than one as shown in weight version B of Table 7-15. Stakeholders in the design and planning need to determine what evaluation criteria are important to include in the costs and benefits categories, how to best assess value to those criteria and what, if any, comparative weights each criteria should have in the final benefit-cost ratio.

As an example of including additional criteria, two additional costs categories were ranked for the different material options. The two added measures were ease of production and transportation cost. The materials were qualitatively ranked based on the ease of

production for the test specimen fabrication. The ranking for transportation costs was based on the weight of the materials with the heaviest having the highest cost and the lightest the lowest cost. Table 7-16 shows the cost and benefit standings for the incorporated criteria.

Table 7-15. Examples of a weighted benefit-cost analysis for the various ECLT versions.

Enhancing layer	**Weighted Version A** *(Ballistic Resistance =2, cost/wt =0.5)*	**Weighted Version B** *(Ballistic resistance = 0.75, cost/wt = 1.5)*
Perforated Steel	0.71	0.80
Expanded Metal	1.33	1.50
Aramid Epoxy Panel	0.75	0.84
Mild Steel Plate	1.50	1.69
High-hard Plate	0.50	0.56
UHMWPE	0.11	0.13
Fiberglass fabric (4-ply x 1)	1.40	1.58
Fiberglass fabric (1-ply x 4)	1.60	1.80
Baseline CLT	9.00	10.13

Two BCR were then calculated. Now, with three cost factors each needs to be multiplied by a percentage for the ratio. In this example, one option, Option A, weighted the three cost criteria unevenly with product cost as 0.5, transportation cost as 0.3 and ease of production as 0.2, and the other, Option B, evenly weighted the three parameters with a 0.33 multiplier for each cost. The multiplier is another way of weighting contributing factors. For the uneven cost weights, the multipliers made the product cost the most important with half of the weight and then transportation cost slightly more important than

the ease of production. Table 7-17 displays the two additional BCRs and their respective rankings from 1 to 9.

Table 7-16. Rankings of multiple cost criteria included in the cost-benefit assessment.

Enhancing layer	BENEFIT	COST		
	Ballistic Resistance	Ease of production	Product cost ($/weight)	Transportation cost
Perforated Steel	5	2	7	8
Expanded Metal	4	2	3	6
Aramid Epoxy Panel	6	5	8	4
Mild Steel Plate	3	7	2	9
High-hard Plate	2	7	4	7
UHMWPE	1	2	9	5
Fiberglass fabric (4-ply x 1)	7	6	5	2
Fiberglass fabric (1-ply x 4)	8	9	5	2
Baseline CLT	9	1	1	1

Table 7-17. Benefit cost ratios and rankings for various ECLT material options based on multiple cost criteria.

Enhancing layer	Option A BCR (uneven cost weights)	Ranking of Option A BCR (uneven cost weights)	Option B BCR (even weighted costs)	Ranking of Option B BCR (even cost weights)
Perforated Steel	0.794	6	0.882	6
Expanded Metal	1.081	4	1.091	4
Aramid Epoxy Panel	0.968	5	1.059	5
Mild Steel Plate	0.588	7	0.500	7
High-hard Plate	0.364	8	0.333	8
UHMWPE	0.156	9	0.188	9
Fiberglass fabric (4-ply x 1)	1.628	3	1.615	2
Fiberglass fabric (1-ply x 4)	1.633	2	1.500	3
Baseline CLT	9.000	1	9.000	1

A simple comparison between the materials can be conducted by just adding the ballistic resistance ranking and the cost ranking of the material, as shown in Table 7-18. Since the lower rankings are defined as better in terms of performance and expense, the materials with the lower total ranking are favored over the higher total rankings. This technique can be useful for comparison of options. Now the lowest cost option, in this scenario the baseline CLT, is not the "automatic" best choice when it has the lowest level of ballistic resistance. Instead the baseline and the UHMWPE are equally ranked because they both have the highest and lowest rankings for the two criteria. Employing the rankings for evaluation can skew a typical benefit cost ratio.

Table 7-18. Total Cost-Benefit rankings.

Enhancing layer	**Total Cost-Benefit ranking** (Ballistic resistance ranking + Cost ranking) [$/lb]	**Total Cost-Benefit ranking** (Ballistic resistance ranking + Cost ranking) [$/ft^2]
Perforated Steel	12	13
Expanded Metal	7	9
Aramid Epoxy Panel	14	12
Mild Steel Plate	5	7
High-hard Plate	6	9
UHMWPE	10	10
Fiberglass fabric (4-ply x 1)	12	9
Fiberglass fabric (1-ply x 4)	13	10
Baseline CLT	10	10

7.6 Summary

The layered composite nature of CLT lends the product well to the idea of modifying the composite composition for special design requirements, such as ballistic resistance. Various materials were fabricated and tested for ballistic resistance using the same test set-up as the baseline CLT ballistic testing. This research limited the enhancing layer placement to one near centrally placed location for all but one variation of the ECLT test specimens. Additional testing could examine different layups with the materials to optimize the placement of the enhancing layer.

The perforated metal plates offered excellent performance with less weight than the solid steel plates, which also performed well. Fabricating the solid steel plates into the composite was a challenge due to the lack of even surfaces with the CLT for good adhesion. Mechanical connections worked well but more research is needed to determine connection spacing and other design factors. Commercially produced fiber-based ballistic panels also greatly increased the ballistic resistance of the panel while adding less weight to the product than the metal options. They also conformed well with an epoxy binder to the CLT sections. Lastly, a small number of very thin fiberglass fabric layers showed marked improvement to the ballistic resistance over the baseline CLT, although some perforating shots were observed.

Cost-benefit assessment examples provided insight into the tradeoffs between the expense of enhancing materials and the perceived benefit. The high cost of the fiber-based ballistic panels made them less attractive choices despite their excellent ballistic resistance. The baseline CLT consistently achieved the best BCR based on cost and resistance

rankings as it added no cost. The total ranking technique identified the steel plates as the best option followed by the expanded metal.

CHAPTER 8
CLT BLAST PERFORMANCE AND ANALYSIS

8.1 Fundamentals of blast loading

8.1.1 Blast loads

In addition to ballistic threats, force protection design specifications include explosive threats. With the prevalence of vehicle, mail and person-borne explosive threats, a structure designed to enhance force protection must also include protective blast design considerations. Commonly, maximized standoff distance is used to mitigate the impact of a potential explosive threat with more sensitive and vulnerable areas, such as fenestrations and mailrooms, designed to be located as far as possible away from exterior walls. However, in some cases large standoff distances cannot be achieved and structures must be designed and analyzed to withstand the explosive load.

The typical static and even quasi-static load analysis completed for live, dead, wind, and seismic loads, is different from blast loading analysis. A blast load is characterized by a large pressure over an extremely short duration, especially when compared to the structure's natural frequency. The detonation of an explosion is a high-energy event that creates these high pressures. Air around the explosive source rapidly compresses to form a shock wave, which moves away from the blast origin faster than the speed of sound. It creates a nearly instantaneous rise in pressure, followed by an exponential decay in pressure. As the air at the blast origin cools, the pressure decreases below the ambient pressure, creating a negative pressure or suction effect.

A typical pressure-time history of a blast wave in the free air, with no reflection is shown in Figure 8-1. The peak positive and negative pressures are represented with p_{peak}^{+} and p_{peak}^{-}, respectively, while the ambient air pressure before the blast event is p_0. The time when the shock wave makes contact with the object is the time of arrival, annotated as $t_{arrival}$. The duration of the positive pressure phase is marked with T_p and the negative pressure phase is labeled T_n. The negative phase is typically less in pressure quantity but may be longer in duration. With a free-air blast with no reflection, the peak pressure is known as the peak static overpressure, $p_{so,}$ or blast pressure relative to the ambient pressure, at the shock front. It is also known as the incident pressure, p_i [104].

The non-linear decay of pressure over time after the initial positive peak, is often expressed with the Friedlander equation, an exponential function shown in Equation 8.1. In this expression, a waveform parameter, *b*, is used. This parameter describes the shape of the pressure decay and is dimensionless.

$$p(t) = p_{peak+}\left[1 - \frac{t}{T_p}\right]e^{\left(-\frac{bt}{T_p}\right)} \tag{8.1}$$

Another important blast parameter is the specific impulse, *i*, which is defined as the area under the pressure-time history curve from arrival to the end of the positive pressure phase, as shown in Equation 8.2. The units are pressure-time.

$$i = \int_{t_{arrival}}^{t_{arrival}+T_p} p(t)dt \tag{8.2}$$

The approximate value of the specific impulse may also be estimated with a simplifying assumption of linear decay of pressure and triangular area calculation.

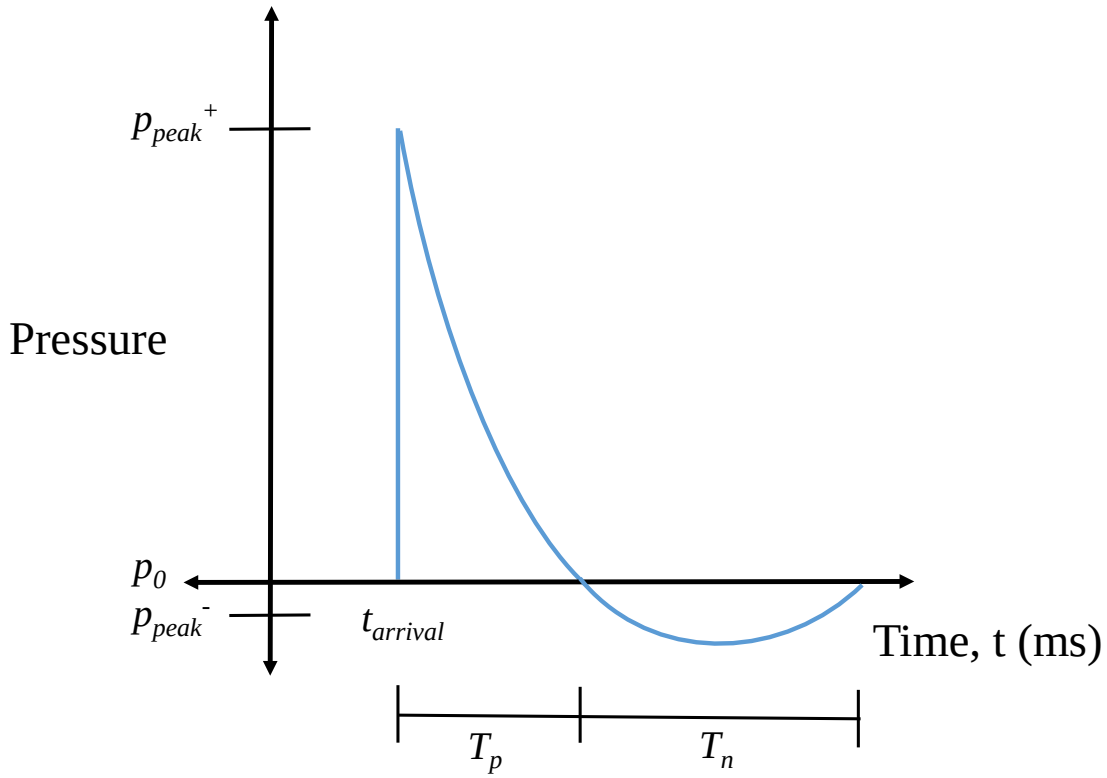

Figure 8-1. Pressure-time history of a blast wave in the free air.

Air bursts and surfaces bursts, where shock waves reflect off the ground are common. Upon contact with an object, such as the ground or a building, the shock front is reflected, creating additional shock waves. The incident shock wave and its reflections raise the applied pressures as the reflected waves merge with the incident wave. Peak reflected pressure, p_r, and reflected impulse, i_r, magnitudes can be significantly higher than the incident pressure wave because the shock front is reinforced by the additional reflected waves [105]. These two values can be derived from the peak static overpressure or found graphically from charts in *UFC 3-340-02, Structures to Resist the Effects of Accidental Explosions* [17, 104].

The negative phase is analyzed separately from the positive pressure phase with its own set of blast wave parameters, if it is not neglected. In general, the majority of the damage in a blast event is caused by the positive pressure phase, so the negative pressure phase is often ignored. Flexible type structures, such as lightweight steel-frame structures, create conditions were the negative blast wave parameters are needed for the full blast wave effects on a structure [42].

The standoff distance, or distance from the explosion to the building or other object of design concern, is an important consideration in force protection planning, as is the type and weight of the explosive. For convenience, TNT is used as a common reference and other high explosive charges are converted to an equivalent TNT weight based on a ratio using weights and specific energies of the two explosives. These key variables are often estimated based on local threats and risk assessments. These values are used to calculate a scaled distance parameter, *Z*. The Hopkinson-Cranz, or cube root, is a commonly used scaling method for spherical charges as shown in Equation 8.3 [104, 105].

$$\mathrm{Z} \equiv \frac{R_d}{\sqrt[3]{w}} \tag{8.3}$$

where Z = scaled distance
R_d = standoff distance
w = explosive charge weight

Scaled distance also aids in classification of the blast event with respect to proximity as follows:

Far field:	$Z > 10$
Near field:	$3 < Z < 10$
Near contact:	$0 < Z < 3$
Contact:	$Z = 0$

Proximity to a blast explosion, as well as design and material characteristics of the structure determine the response and amount of damage sustained. With such extreme loads, blast design often results in high levels of damage, and even unrepairable destruction to the structure. Therefore, it is typical for design to focus on protection of the occupants and other assets within the structure. The blast parameters are determined based on an estimated threat of a given explosive type and weight as well as the distance of the structure to the potential target. The standoff distance is typically achieved through the use of barriers to restrict encroachment by the threat. At points farther away from the source of the explosion, the peak pressure is lower and the duration of the loading is greater, which is why standoff distance is a critical measurement.

Like ballistic penetration, explosions that occur where the load is not perpendicular to the structure require the inclusion of an angle of incidence for analysis and design. An angle of incidence results in a peak scaled reflected pressure, reflected impulse, and reflection coefficient. These values may be found based on the peak static overpressure of a normal loading event and the angle of incidence through equations or graphically with charts from *UFC 3-340-20*.

The blast load felt by a wall panel, depending on distance and orientation, will be a combination of blast effects including reflected overpressure, static overpressure, dynamic wind pressure, and negative pressure. When the shock wave hits the front facing wall, the pressure spikes from zero (ambient) to the peak reflected pressure. The pressure then decays to the stagnation pressure, p_s, over time. The duration of the decay is known as the clearing time, t_c, which is a function of the structure's wall height and width [42, 104]. The resulting load on the wall is dependent on the explosive weight, the standoff distance, and the orientation of the component to the direction of the blast.

8.1.2 Single Degree of Freedom (SDOF) model

In blast-resistant design practices, it is common to treat building components as single-degree-of-freedom (SDOF) nonlinear systems. The SDOF model provides insight into the response of an element, such as a structural panel, to a blast threat through a time history analysis. The model uses a mass, which can move in one degree of freedom, with the motion resisted by a spring and damper, as shown in Figure 8-2. Using Newton's Law, the equation of motion of the SDOF system can be derived as shown in Equation 8.4 [104].

$$m\ddot{x}(t) + c\dot{x}(t) + kx(t) = F(t) \tag{8.4}$$

where m = mass
c = damping
k = stiffness
F = applied force
x = displacement

Conservatively, damping is usually ignored for blast because the maximum response of the structure and its components is reached in such a short time and there is little opportunity for damping to influence the system. The element is transformed into an equivalent mass, stiffness, dampening and force, as represented with the subscript *e*. These

values are then used to find factor values, which are the ratio of the equivalent system to the real system. The factors are the equivalent load K_L, mass K_M, and stiffness K_S, as defined in Equation 8.5 [104].

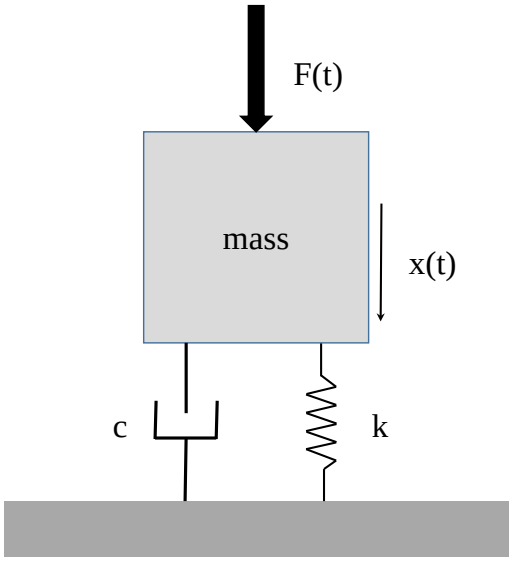

Figure 8-2. Single-degree-of-freedom system.

$$K_L \equiv \frac{F_e(t)}{F(t)}, K_M \equiv \frac{m_e(t)}{m}, K_S \equiv \frac{k_e(t)}{k} \tag{8.5}$$

where
F = force
m = mass
k = stiffness
subscript e = equivalent system

The equation of motion for the equivalent system is used in conjunction with an evaluation of the system with static load, or no acceleration, to find the equivalent load and stiffness

factors are equal. Based on this equality, a load-mass factor is then used in a revised equation of motion for elastic systems, as shown in Equation 8.6.

$$K_{LM} m\ddot{x} + kx = F(t) \tag{8.6}$$

where $K_{LM} \equiv \frac{K_M}{K_L}$ = load-mass factor
m = mass
k = stiffness
F = applied force

Load-mass factor values, K_{LM}, for beams and one-way slabs have been established by previous research by Biggs et al. with respect to boundary conditions and loadings [29].

In Equation 8.6 the stiffness, *k*, varies linearly with displacement, as in an elastic spring. However, the resistance of the force is actually non-linear as plastic behavior is exhibited. Therefore, the stiffness is modified as a non-linear resistance, *R(x)*, as a function of the displacement, shown in Equation 8.7. [29]. The resistance of the element is used to develop the resistance-displacement function [104].

$$K_{LM} m\ddot{x} + R(x) = F(t) \tag{8.7}$$

where K_{LM} = load-mass factor
m = mass
$R(x)$ = resistance as a function of displacement
F = applied force

This type of model assumes structures exhibit elastic-perfectly plastic behavior, loads are uniformly applied and the load shape is triangular or rectangular in nature [75]. SDOF models often are the basis of designs, and if necessary, more in-depth techniques such as high fidelity physics based models can follow. *UFC 3-340-02* provides empirical

charts for blast parameters to be used in an SDOF analysis. The SDOF model offers an approximation without significant computational costs.

In an SDOF analysis, blast loads are applied to the evaluated component using numerical integration tools, such as the linear acceleration method. A common technique used in structural dynamics to find the time-history response for non-linear SDOF systems is Newmark's numerical integration procedure. With this method, the equation of motion is solved using an assumed linear acceleration between time-steps and a displacement value is calculated at each time-step based on the previous and current time-step [104]. This allows for identification of the maximum displacement as well as any residual displacements of the component.

8.1.3 Resistance function

Based on the material characteristics of the CLT panel as outlined by PRG 320, the accepted shear analogy method for design with CLT panels, the procedure of developing resistance functions for other materials such as steel and concrete members, and data from live blast testing, a resistance function for CLT was developed for the elastic region. First, the dynamic moment capacity of the panel was calculated using Equation 8.8. If incorporated, static and dynamic increase factors could be used to factor the bending strength of the material. A static increase factor accounts for the actual strength of the material, versus the required design strength. A dynamic increase factor provides a simplified procedure to account for a dynamic increase in strength, given high rate loading conditions, such as a blast. It is a ratio of the element capacity under dynamic loading to its capacity under static loading. No previously established and industry accepted increase

factors exist for CLT, although some researchers have proposed different values for dynamic increase factors [89, 118].

$$M_{dyn} = f_b S_{eff} \tag{8.8}$$

where M_{dyn} = dynamic moment capacity
f_b = required bending strength
S_{eff} = effective section modulus

The resistance function is dependent on the boundary conditions of the member. The following example uses a simply supported CLT panel, which is loaded until the panel yields at some displacement, x_e. A plastic hinge occurs at the location of maximum stress, also the location of the maximum moment, as shown in Figure 8-3 [104]. The panel has a mass, *m*, modulus of elasticity, *E*, and an area moment of inertia, *I*.

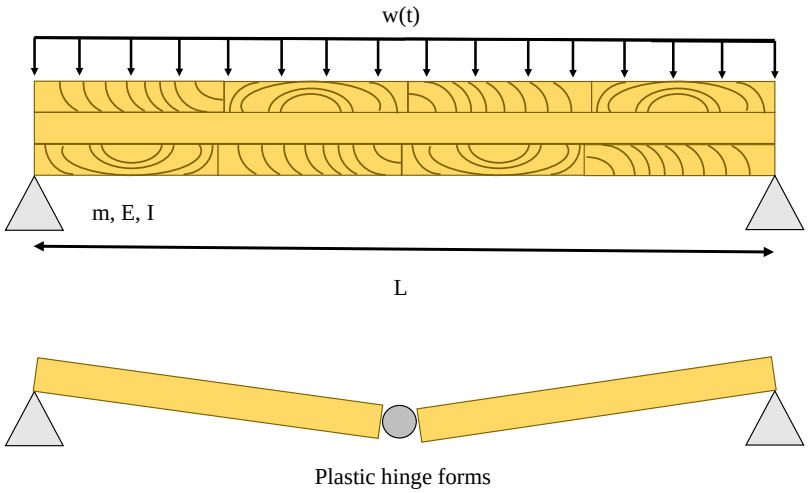

Figure 8-3. CLT panel with blast load and development of plastic hinge.

Based on mechanics, the maximum elastic moment, $M_{max,e}$, for the panel is given by Equation 8.9 and the displacement, x_e, is given by Equation 8.10. The force required to resist this deflection, or elastic resistance of the panel, R_u, can be then be found, by solving for the load, $w(t)$, and dividing by the panel length, L, as shown in Equation 8.11 [104].

$$M_{max,e} = \frac{w(t)L_p^2}{8} \tag{8.9}$$

where $w(t)$ = blast load
L_p = panel length

$$x_e = \frac{5w(t)L_p^3}{384EI} \tag{8.10}$$

where $w(t)$ = blast load
L_p = panel length
E = modulus of elasticity
I = area moment of inertia

$$R_u = \frac{8M_{u,dyn}}{L_p}\ [Force] \tag{8.11}$$

The elastic stiffness, k, can be calculated as shown in Equation 8.12. These three values, the elastic resistance of the panel, R_u, the corresponding displacement for the simply supported panel at midspan, x_e, and the elastic stiffness, k, form the resistance function as shown in Figure 8-4 [104]. Other boundary conditions can be considered, with changes to the equations used to find the maximum moment and displacement as appropriate for the determined conditions.

$$k = \frac{R_u}{x_e} \tag{8.12}$$

A resistance function for CLT will be considerably different from the resistance functions generally used for steel or concrete. Figure 8-4 illustrates the theoretical response

of the wood material in the plastic regime with the dashed line in the plastic regime. Due to the laminated nature of the wood product, the resistance drops as the plies rupture. Experimentally derived static resistance curves for CLT panels from Poulin et al. show this piecewise type failure in the panel [89].

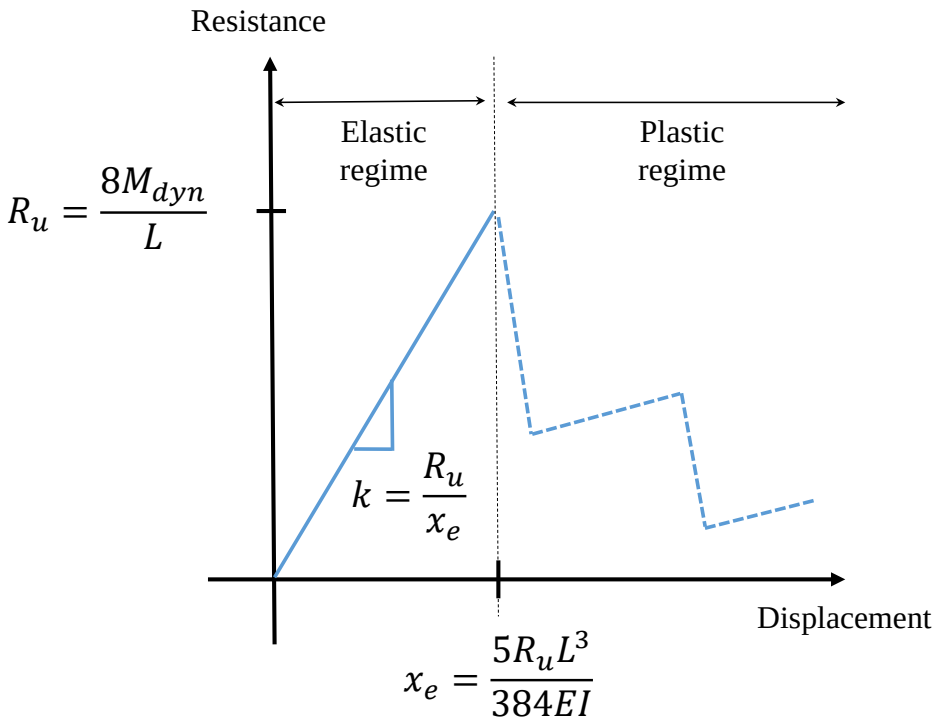

Figure 8-4. Proposed resistance function with simply supported boundary conditions and uniform load.

The flexural strength of the panel typically controls based on typical CLT panel dimensions and loads. However, shear is still checked. The actual shear is evaluated using the shear analogy method and the PRG 320 required design values. The actual shear capacity, V_n, is calculated as shown in Equation 8.13. This value is then compared to the assumed shear capacity, V_u, based on the flexural response, as calculated in Equation 8.14.

If the assumed shear is less than the actual shear, then the flexural response is appropriate. However, if the assumed shear is less than the actual shear, the resistance function must be recalculated based on the shear response. The ultimate shear resistance and corresponding displacement are calculated as shown in Equation 8.15 and 8.16 respectively.

$$V_n = f_v \left(\frac{Ib}{Q}\right)_{eff} \tag{8.13}$$

where f_v = shear strength

$$\left(\frac{Ib}{Q}\right)_{eff} = \frac{EI_{eff}}{\sum_{i=1}^{n/2} E_i h_i z_i}$$

[based on shear analogy method, see Chapter 4]

$$V_u = \frac{R_u}{2} \tag{8.14}$$

where R_u = force required to resist deflection

$$R_{u,shear} = 2V_n \tag{8.15}$$

$$x_{e,shear} = \frac{5R_{u,shear}L^3}{384EI_{app}} \tag{8.16}$$

where EI_{app} = apparent bending stiffness, [based on shear analogy method, see Chapter 4]

With the concerns of rolling shear for the crosswise layers of the CLT, this parameter likely needs to be incorporated into the calculations as well. A methodology of checking for rolling shear does not currently have a standard procedure. In this research, it will be treated as a second shear failure response check unless otherwise detailed.

8.1.4 Blast design and Levels of protection

While blast design is component based, the performance criteria desired is typically tied to goals of the entire building system or structure. Approaches established by ASCE and the U.S. Army Corps of Engineers, Protective Design Center both use building Levels of Protection (LOP), which are performance goals and expected damage levels based on the individual element response. Table 8-1 shows the defined levels associated with desired performance goals. Table 8-2 shows the Level of Protection rating associated with component damage levels. Primary components are elements whose loss could potentially affect the overall structural integrity, and would affect other components, such as columns, girders, and load-bearing components. Secondary components are usually supported by primary components and can fail without widespread damage. Elements that fall into this category include non-load bearing walls, studs, purlins, joists. Nonstructural components are not typically designed specifically for blast loads, they include interior non-load bearing walls, and architectural items affixed to structural components.

Damage levels used in Table 8-2 can be defined as follows:

Hazardous:	likely to fail and produce debris
Heavy:	unlikely to fail, significant permanent deflections, not repairable
Moderate:	unlikely to fail, probably some permanent deflection that is repairable, although replacement may be preferable for economic or aesthetic reasons
Superficial:	unlikely to exhibit any visible damage

Table 8-1. Building Levels of Protection, adapted from [44].

Level of Protection	Building Performance Goals	Overall Building Damage
I (Very low)	*Collapse prevention*: surviving occupants likely able to evacuate, building not reusable; contents may not remain intact	Damage expected, up to onset of total collapse but progressive collapse is unlikely
II (Low)	*Life safety*: surviving occupants likely able to evacuate and return temporarily; contents likely intact for retrieval	Damage expected, such that building is not likely to be economically repairable, but progressive collapse is unlikely
III (Medium)	*Property preservation*: surviving occupants may have to evacuate temporarily, likely able to return after repairs and clean-up; contents likely remain at least partially functional, may be impaired for a time	Damage is expected, but building is expected to be economically repairable, and progressive collapse is unlikely
IV (High)	*Continuous occupancy*: All occupants likely able to stay and maintain operations without interruption; contents will likely remain fully functional	Only superficial damage is expected

Table 8-2. Expected Component Damage for Each Level of Protection, adapted from [44].

	Component Damage Levels		
Level of Protection	Primary Structural Component	Secondary Structural Components	Nonstructural Components
I (Very low)	Heavy	Hazardous	Hazardous
II (Low)	Moderate	Heavy	Heavy
III (Medium)	Superficial	Moderate	Moderate
IV (High)	Superficial	Superficial	Superficial

8.2 Previous work with CLT and blast

As a newer construction material, minimal research has been conducted on CLT performance under blast loading conditions. The majority of dynamic loading research on

CLT has focused on seismic loads with testing effort examining in-plane shear response in the CLT panels as well as a systematic response and appropriate connections [118]. Compared to reinforced concrete and steel, minimal research has been conducted on light-frame timber construction and blast loads resulting in less information on wood response to high strain rate effects in terms of resistance and stiffness. Generally, the damage to wood exposed to a blast is catastrophic and wood has not been seen as a preferable material for protective design.

8.2.1 Load duration factor

Wood is known for greater load capacity for short durations of loading. According to the *National Design Specification for Wood Construction (NDS)* in allowable stress design (ASD), load durations factors, C_D, can be used to adjust reference design values, which apply to normal load durations, when the duration of the full maximum load is less than the normal load duration. With wood, normal load duration typically refers to a full design load for a cumulative duration of ten years. The U.S. design standard also states that the modulus of elasticity, E, modulus of elasticity for beam and column stability, E_{min}, and compression perpendicular to grain, $F_{c\perp}$, should not be factored however. The load duration factor provided for impact loading is 2.0. In LRFD design, the time effect factor for impact is given as 1.25 [19].

8.2.2 Shock tube testing

Lacroix and Doudak used shock tube testing to examine the response of two different light-frame wood construction types, 0.4375-inch (11-mm) oriented strand board (OSB) and 0.75-inch (18.5-mm) plywood sheathed 2x6 studs, under a simulated blast loads. A strong correlation between increase in strain rate and increased strength was

observed. This study yielded a proposed DIF of 1.4 over a strain rate range of 1.67 to 1.65 x 10^3 s^{-1} with the researcher's acknowledgement that more testing is necessary [74].

A recent study published by the same research team in February of 2018, examined shock tube testing to simulate blast loads on CLT test specimens. Their work presented a dynamic increase factor of 1.28 for 3-ply and 5-ply CLT panels for blast resistance. Based on their set-up with simply supported end conditions, free vertical edges, one-way bending and both static and dynamic testing, they found no increase in stiffness. The simulated blast load was designed to replicate far-field conditions with a uniform loading and minimal local damage. Previously, the group had examined differences in failure modes between static and dynamic loading. Other research on high strain rates on wood, in the realm of impact loading, indicated that an increased flexural strength could be expected [89].

The shock tube testing observed failure through rolling shear in some but not all test specimens under the same loading and end conditions. The researchers hypothesized that the increased strength experienced in the high strain loading effectively delayed a flexural mode of failure and allowed the rolling shear failure to occur [89]. However, this does not explain why some specimens experienced rolling shear failure and others did not.

A drawback to the shock tube testing is that the experimental setup induces multiple impulses on the test specimen due to the reflection of the shock waves in the tube apparatus unless the pressurized gas is allowed to vent and dissipate. The pressure-time history plots tend to have multiple peaks demonstrating that repeated blast-type loadings were experienced. While recorded loads, displacements and strain data can be attributed to the

initial impulse by evaluation of the time of the reading, the observed damage and failure modes post-test may be harder to ascribe.

8.2.3 Live-Blast Testing

A cooperative effort between WoodWorks, Karagozian and Case Inc., and the Air Force Civil Engineer Center, funded by the U.S Forest Service, conducted a series of live-blast tests to investigate the resistance of CLT construction to air-blast loads in October 2016. The test set-up included three two-story, single-bay CLT structures, approximate 50 square feet (4.57 square meters) in size, subjected to three different explosive loads of 32-lb (14.5-kg), 67-lb (30.4-kg) and 199-lb (90.3-kg). The objectives of the study included: (1) investigate the system-level response of CLT structures to explosive loads, specifically air-blast explosives; (2) compare response of test structure to predicted single-degree-of-freedom (SDOF) analysis methods and (3) examine responses of the CLT panels around window and door openings and well as various connection configurations under high explosive loading conditions [118].

Prior to the live-blast testing, quasi-static testing was conducted to investigate the bending response of the CLT panels in their major strength direction under a uniformly applied quasi-static load. The test set-up for this loading used rubber water bladders which allowed for the controlled quasi-static pressure application. A series of shock tube tests were also performed within the elastic range of the panel response. Based on these tests, it was concluded that the shear analogy model could compute the stiffness and strengths of the panel response in the elastic range of uniformly-applied transient load. An effective increase factor of 1.25, based on load duration factor, C_D, from the NDS and the PRG 320's

10-minute duration factor, was determined to convert published CLT design values to impact load factored design values [118].

A TNT charge of designated weight was elevated 18-inches off the ground above compacted soil as a standoff distance of 75-feet for all three tests. Using an arena style site plan, the three structures were placed so their front face was an equal distance from the center of the explosive charge, as shown in Figure 8-5. The structures were spaced to limit the shockwave reflections between each other [118].

Each structure was built from a different grade of CLT panel produced by a different manufacturer and certified by a third party for meeting PRG 320 standards. Grades included were E1, V1 and V4. The wall and roof panels were all 3-ply panels and the floor panel for the second story was a 5-ply panel. Each grade of panel varied in lamella width, board length and finger jointing but all were consistent with PRG 320 standards. Panels were jointed with a splice connection of half-lapped joints and self-tapping screws of a length to engage all plies, as shown in Figure 8-6 [118].

The structures were anchored to an existing concrete slab with a generally over-designed connections of steel angles, intending to fix the structure and allow for CLT panel damage as opposed to connection failure at the anchored interface between the concrete slab and mass timber structure. Pressure gauges were placed to measure reflected pressure, internal pressure in each of the three structures and incident overpressure at a gauge places 75-feet away from the explosive charge. Displacement gauges were also used to measure out-of-plane displacement of the wall panels [118].

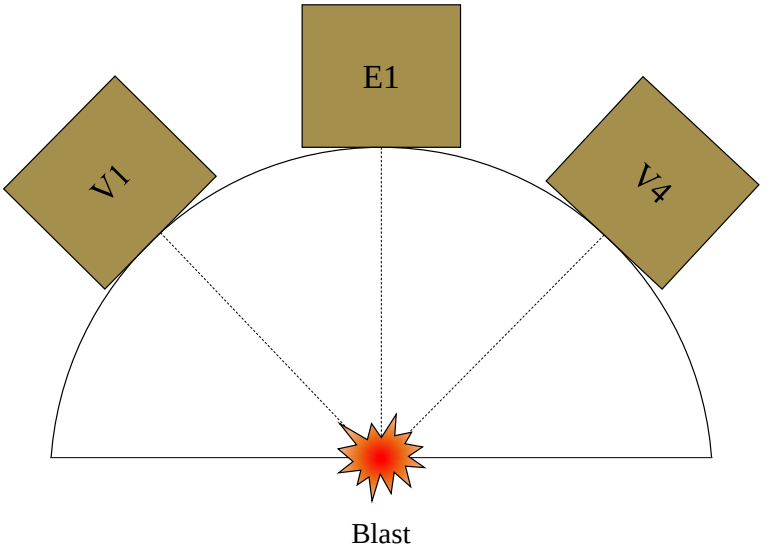

Figure 8-5. Schematic of live-test set-up.

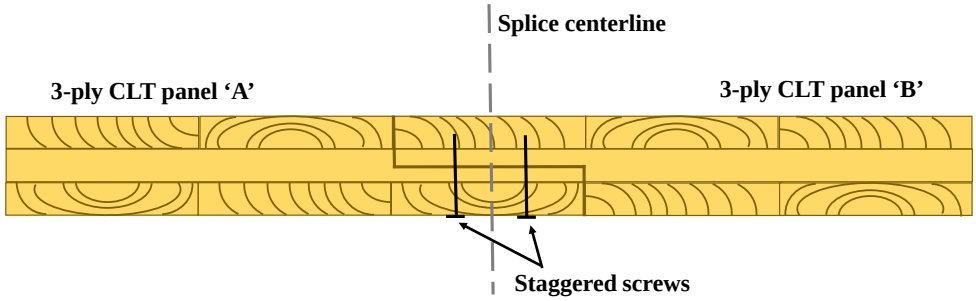

Figure 8-6. Wall panel splice detail.

With the first two explosive loads, which were designed to displace all the grades to their respective elastic limits, based on the quasi-static test results, no damage or permanent deformation was observed. Some knots dislodged from the panels but the CLT structures withstood the blast impact with no signs of damage. The third test was designed

to cause residual displacement of the Grade E1 panel, with the highest bending strength and modulus of elasticity. The explosive weight was selected with the intent of causing displacement up to 1.5 times its elastic limit [118]. Despite those expectations, visible damage to all three structures was only observable after the third test. Both the interior and exterior faces of the first floor wall panels facing the charge experienced visible lamella fracture and plastic deformation on the outermost and innermost plies of the panel.

The parties of the cooperative effort created a SDOF model, independent of the model created in this research. Their model used a DIF of 1.25 and assumed simple pin-roller (simply supported) boundary conditions. General observations on this model included that the predicted displacements exceeded the measured value. Differences between the test data and model predictions for the fundamental period were attributed to the actual test conditions having a level of fixity not well represented by the SDOF model assumption of no rotation restraint with simply supported conditions [118].

8.3 SDOF model development and validation: a CLT blast analysis tool

8.3.1 Model development with incorporation of CLT parameters

Using the computer software Mathcad, a tool was developed for blast load analysis of CLT using an SDOF model. The tool allows for user specified input parameters that include CLT panel properties and dimensions, the explosive threat of concern, and the structure and blast geometry. It incorporates the shear analogy method of CLT design to account for the cross-oriented lamella in the transverse plies, develops a resistance function for the elastic regime of the specified panel and runs a linear acceleration methodology to find the time-history response of the element.

The model currently uses a perfectly plastic response to indicate that the CLT panel experiences rupture of an outer ply. If the model predicts inelastic behavior or residual deformation, that indicates rupture of the outermost ply. It does not accurately predict the behavior of the plastic regime due to a lack of data for the material's response in that regime. The model estimates the displacement that will cause the rupture of a ply based on the CLT panel strengths.

Results produced by the tool include plots of the force-time history, resistance-displacement, displacement-time history and dynamic shear history. Additionally, the maximum displacement of the panel, the maximum rebound displacement, and the maximum dynamic shear load are all identified. The expected damage and level of protection are estimated based ranges of the ductility ratio and support rotation as used for reinforced concrete and steel. These expected behaviors also need to be examined for CLT.

For CLT panel properties, the tool is capable of calculating analysis for four grades or CLT: E1, V1, V3 and V4 based on the PRG 320 allowable design properties. The number of plies in the panel can range in odd numbers from 3-ply to 9-ply. Both of these choices are made with selection of a radio button for the given available options. Additional grades could be added to the model in the future if necessary with slight modification. The ply thickness, panel height and panel volumetric density are all values that the user should specify based on the actual panel specifications. Average values for ply thickness and density are appropriate if there is variability. The member end conditions, panel type and member classification are all selected from radio button options. Figure 8-7 exhibits the panel properties and dimensions section of the user specified input step.

1. User specified input parameters:

a. Panel Properties and Dimensions:

CLT grade:	○ E1 ◉ V1 ○ V3 ○ V4
Number of ply:	◉ 3 Ply ○ 5 Ply ○ 7 Ply ○ 9 Ply
Ply thickness:	$t_{ply} = 1.375\text{in}$
Panel height:	$L = 12\text{ft}$
Panel volumetric density:	$\rho_{clt} = 28 \frac{\text{lbf}}{\text{ft}^3}$
Select member end conditions:	○ Simply Supported ○ Fixed-Fixed ◉ Fixed-Pinned
Select panel type:	○ Floor/Roof Panel ◉ Wall Panel
Select member classification:	◉ Primary Element ○ Secondary Element ○ Nonstructural Element

b. Explosive Threat:

Select design explosive type:	◉ TNT ○ C4 ○ ANFO
Enter explosive weight (in lbs):	$W_{EXP} = 199\text{lb}$

Figure 8-7. Panel properties and dimensional inputs for the CLT blast load analysis tool.

After the panel properties are identified, the user can input the explosive threat information. This includes the explosive type and the explosive weight. The structure and blast geometry must also be specified for the tool to incorporate into the analysis. This includes the orientation of the exposed ply face to the blast, the structural dimensions of the building, the global hazard orientation, the member location with respect to the threat, the story height, the total number of stories above ground level and the selected design story level. For the blast geometry, the perpendicular distance from the explosive threat location to the CLT panel or designed member must be identified as well as the desired load calculation basis with the options of field test data or UFC. If UFC is selected, the load calculations are based on the *UFC 3-340-02* empirical equations and plots given the

explosive weight and identified distance from the hazard to member. Figure 8-8 shows the explosive threat and structure and blast geometry inputs.

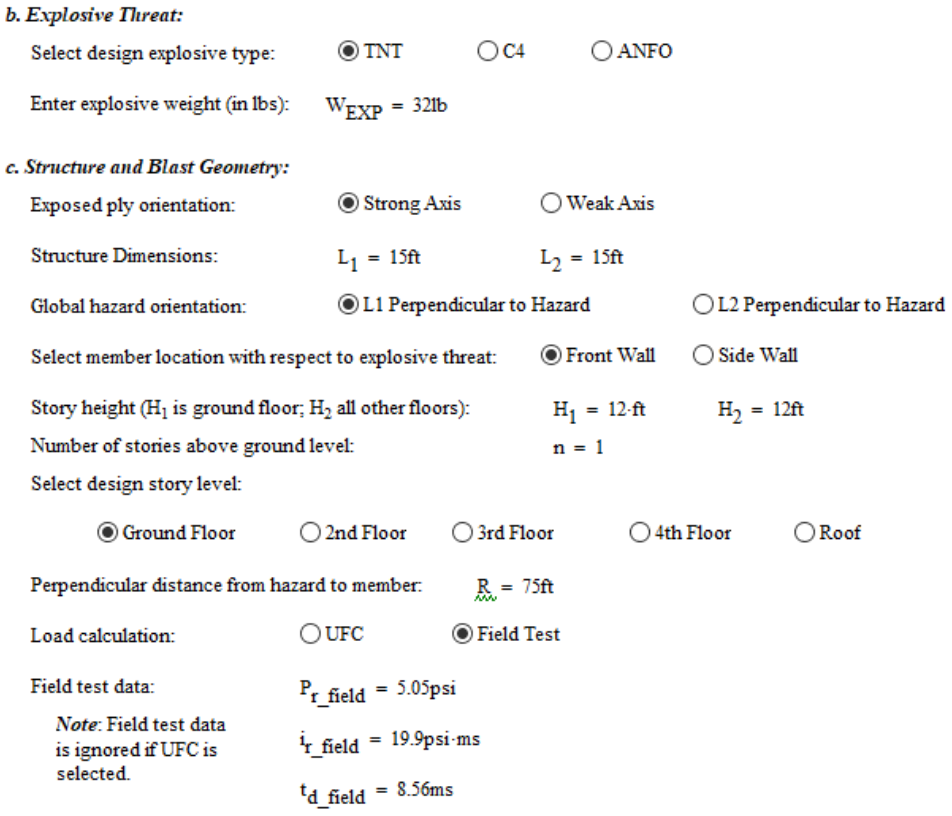

Figure 8-8. Threat and structure geometry inputs for the CLT blast load analysis tool.

The strong and weak axis refer to the direction of the wood lamella on the exposed face of the CLT. The global hazard orientation specifies the structural dimension that is perpendicular to the explosive threat. The designation of the design story level, determines the angle of incidence for the blast parameter calculations.

The user must also specify the member static loads. This includes the number of ply in the floor panel, ranging from 3-ply to 9-ply. Unfactored gravity loads, as any

additional loads applied directly on the panel, which typically occur with roof and floor panels, the tributary area and load eccentricity can all be specified as applicable. Next, the user can specify any desired factoring, like the 0.85 conservatism reduction factor applied in PRG 320 to the calculated moment capacities. The default for this input is 1.0 meaning no factoring is incorporated in the calculations.

Lastly, the user can determine whether to consider rolling shear or not. While it seems intuitive to incorporate rolling shear, further analysis of the failure mode and its occurrence with blast loading is required as inclusion of the parameter tends to predict rolling shear failure more frequently than it occurs in testing. Figure 8-9 shows the static load and other analysis parameter input section of the tool.

Properties of the CLT panel were addressed next. Areal density was calculated based on user inputs. Based on the shear analogy method, detailed in Chapter 4, strength and stiffness section properties were determined for the defined CLT panel. This included section properties such as effective stiffness, apparent stiffness, effective section modulus, effective shear stiffness and effective shear parameters. Additionally, material properties were defined in accordance with the allowable design properties of PRG 320 by CLT grade. Figure 8-10 shows the calculated CLT design parameters for incorporation into the blast load analysis. All values were all calculated based on the user specified inputs for the panel using the shear analogy method.

d. Member Static Loads:

Number of ply (floor panel): ○ 3 Ply ◉ 5 Ply ○ 7 Ply ○ 9 Ply

Gravity loads (unfactored): $W_{gravity} = 0 \cdot psf$

Note: Additional loads directly on panel. Typically for floor/roof panel analysis.

Tributary area: $A_{trib} = 0 ft^2$

Static load eccentricity: $e_{load} = 0 in$

d. Other Analysis Parameters:

Conservative reduction factor: $\lambda = 1.0$

Consider rolling shear: ◉ Yes ○ No

Figure 8-9. Static load and other analysis parameters for the CLT blast load analysis tool.

CLT Panel Properties

[Code to calculate effective stiffness, effective shear stiffness, and material properties]

a. Member properties for analysis:

Areal density: $\rho_A = 9.625 \cdot psf$

Section properties:

Effective stiffness: $EI_{eff} = 1.15 \times 10^8 \cdot lbf \cdot in^2$

Apparent stiffness: $EI_{app} = 1.011 \times 10^8 \cdot lbf \cdot in^2$

Effective section modulus: $S_{eff} = 32.8 \cdot in^3$

Effective shear stiffness: $GA_{eff} = 462363\,lbf$

Effective shear parameters: $IBQ_{eff} = 35.573 \cdot in^2$

Material properties:

Allowable bending stress: $F_b = 1950\,psi$

Required bending stress: $f_b = 2.1 \cdot F_b = 4.095 \times 10^3\,psi$

Allowable shear stress: $F_v = 135\,psi$

Required shear stress: $f_v = 3.15 \cdot F_v = 425.25\,psi$

Allowable rolling shear: $F_s = 45\,psi$

Required rolling shear: $f_s = \frac{1}{3} \cdot f_v = 141.75\,psi$

Figure 8-10. CLT design parameters.

The equivalent TNT explosive weight is calculated if the explosive is another type of explosive based on use of TNT as the reference explosive. This equivalent weight is found based on specific energy and weight ratios between the designated explosive and TNT. The angle of incidence for the blast event is calculated based on the story under consideration and geometry specified for the story height. Figure 8-11 shows the inclusion of these parameters in the CLT blast load analysis tool.

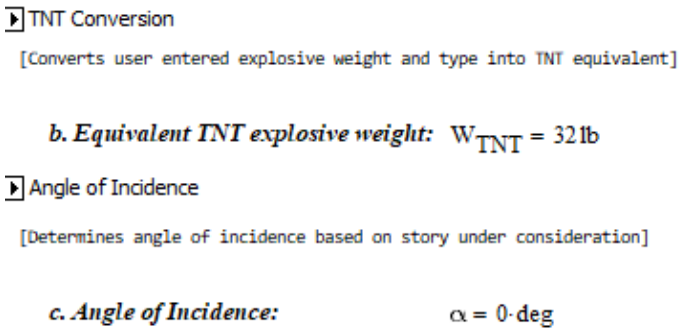

Figure 8-11. Equivalent explosive weight and angle of incidence parameters are determined based on user inputs.

The tool incorporates UFC 3-340-20 figure data so if the user selected UFC as the load calculation source, in the absence of field data, the blast parameters could still be estimated based on the scaled distance. UFC Figure 2-15, *Positive Shock Wave Parameters for a Hemispherical TNT Explosion on the Surface at Sea Level* is reproduced in Figure 8-12. From UFC Figure 2-15, the incident pressure, incident impulse, impulse duration, reflected pressure, reflected impulse, shock front velocity, and length of wave can all be estimated with a given scaled distance.

Additional UFC figures and their parameters built in to the tool include the following:

UFC Figure #	Figure Title	Blast parameter
2-3	Peak Incident Pressure versus Peak Dynamic Pressure, Density of Air Behind the Shock Front, and Particle Velocity	dynamic pressure (blast wind), q
2-196	Peak Equivalent Uniform Roof Pressures	equivalent pressure reduction factor, C_e
2-193	Reflected Pressure Coefficient versus Angle of Incidence	reflected pressure coefficient, $C_{r\alpha}$
2-194b	Reflected Scale Impulse versus Angle of Incidence	reflected scaled impulse, $i_{r\alpha}$

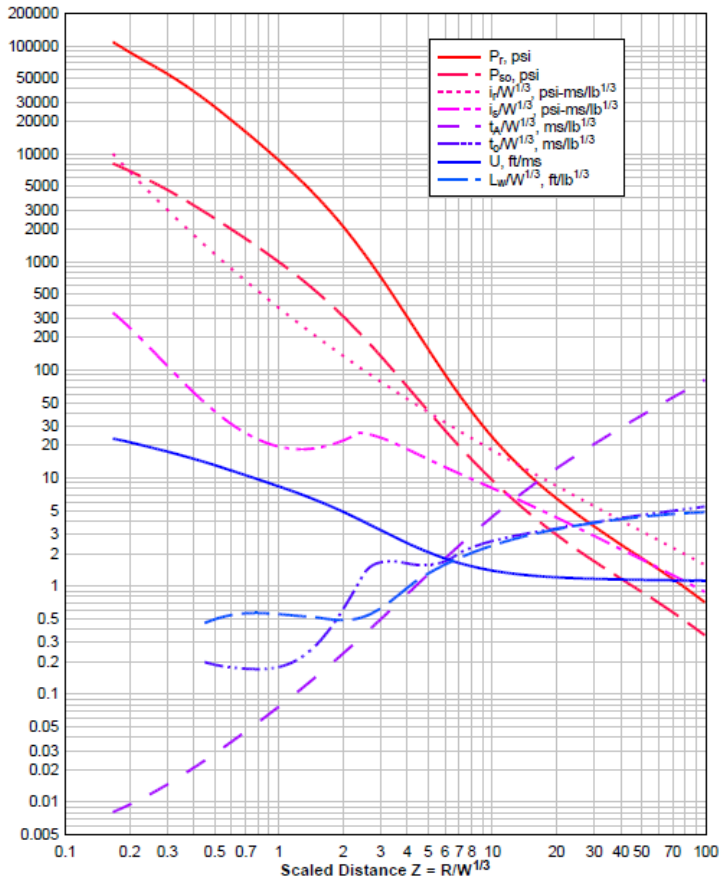

Figure 8-12. Empirically derived curves used to estimate blast parameters in UFC Figure 2-15 [17].

Figure 8-13 shows the blast parameters derived from the UFC figures in the tool. If field data is selected, then those user-specified values supersede the UFC values. The dynamic pressure, *q*, is the air movement caused by the blast and has a corresponding drag coefficient, C_d. The dynamic pressure is dependent on the peak overpressure of the blast wave. The equivalent pressure reduction factor, C_e, accounts for the lessened loaded experienced by the sidewalls and roof, should the analyzed member be one of those panels.

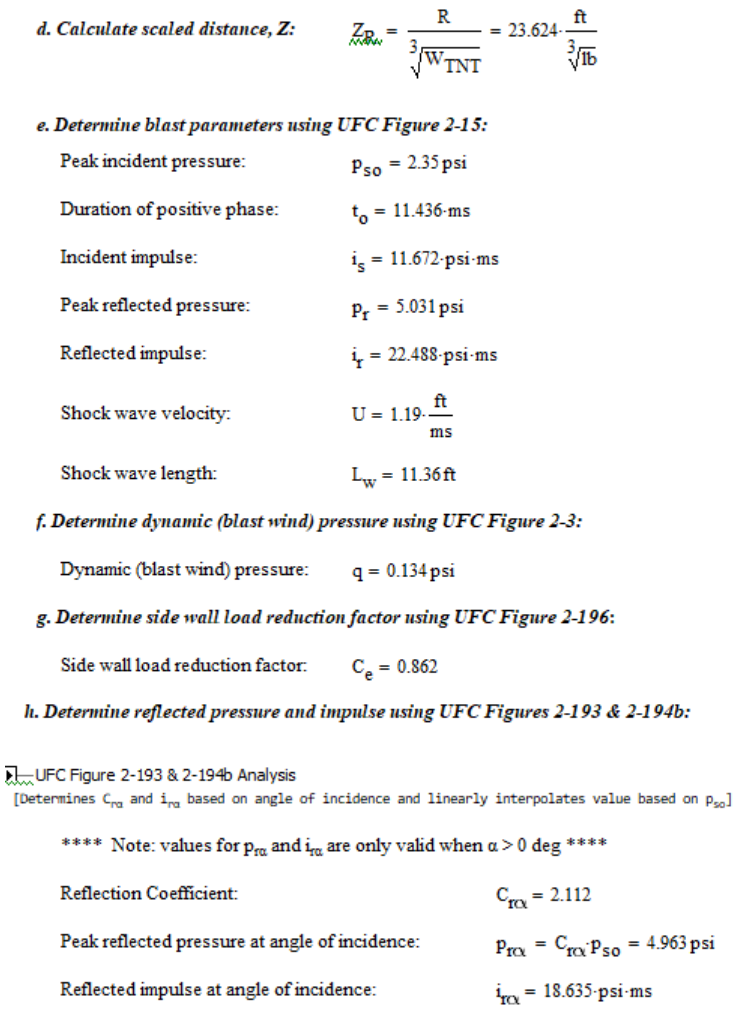

Figure 8-13. Blast parameters based on UFC figures.

Next, the tool determines the design peak pressure, impulse and duration based in the blast environment, building geometry and location of the member under consideration. Clearing effects are checked for applicability and a waveform parameter for Friedlander equation is calculated. Static axially loads are determined based on previous user inputs for self-weight, floor panel weight and any additional gravity loads. Figure 8-14 shows the design loads variables in the tool.

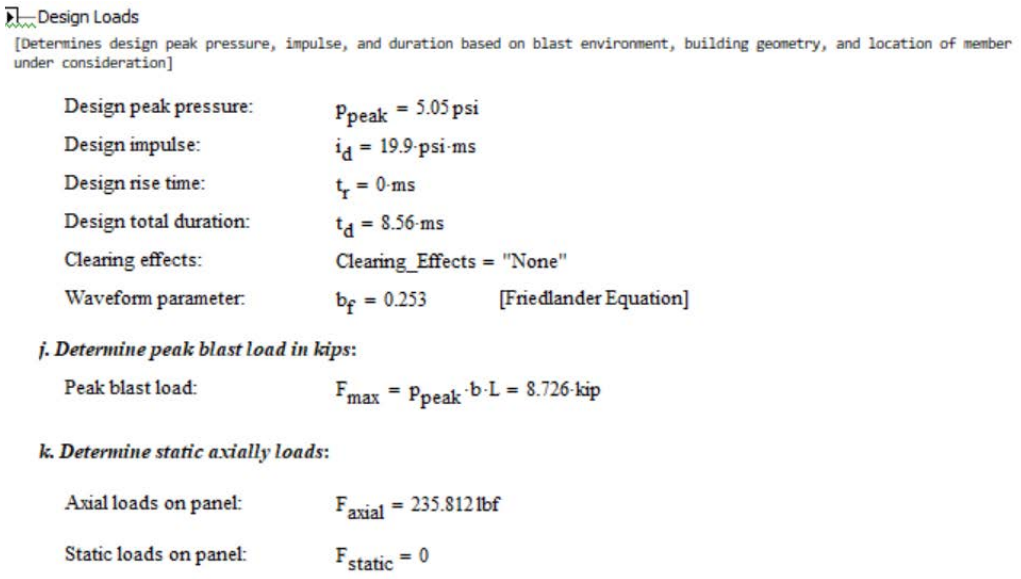

Figure 8-14. Design loads as determined by the CLT blast load analysis tool.

In preparation for the linear acceleration method numerical integration, the member mass was determined based on the density and dimensions of the specified panel. Static loads beyond the self-weight would be included if there were any on the panel. Figure 8-15 shows the tool calculation steps for determining member mass.

3. Determine Member Mass:

Member self weight: $m_{sw} = \frac{\rho_{clt} \cdot L \cdot b \cdot (n_{ply} \cdot t_{ply})}{g} = 0.29915 \cdot \frac{lbf \cdot s^2}{in}$

Static load: $m_s = \frac{F_{static}}{g} = 0 \cdot \frac{kip \cdot s^2}{in}$

Total mass: $m = m_{sw} + m_s = 0.0002992 \cdot \frac{kip \cdot s^2}{in}$

Figure 8-15. Calculation of the member mass in the CLT blast load analysis tool.

The first step of determining the resistance function for the specified CLT panel member is determination of the dynamic moment capacity of the member. The tool is set-up to incorporate specified static and dynamic increase factors if applicable. For this research, the increase factors were both set to 1.0 as definitive factors have not yet been established and more testing is required to evaluate the need for them. The calculated dynamic moment capacity of the member is then used in finding the ultimate resistance, elastic displacement and stiffness based on the specified boundary conditions.

The shear response is then checked. The tool is set-up to include the rolling shear capacity as well. This feature needs more blast testing for validation as when rolling shear is considered, based on a user option, a shear failure prediction occurs when test results do not present that failure mode. The occurrence of rolling shear failure under blast loads has been observed inconsistently in panel testing using shock tubes but was not observed in live blast testing. The absence of rolling shear failure may be attributed to the physical connections at the edges of the front wall with the sidewalls, whereas the panel shock tube testing had free vertical edges. More in-depth analysis and additional testing of CLT for rolling shear failure with blast loading is needed.

Figure 8-16 shows the resistance function development section of the tool. The resistance function is described as bilinear or equivalent bilinear function because the tool is set-up to incorporate the various components of the blast loads experienced by a front wall section. For the initial version of the tool, only the elastic portion is utilized. However, the tool is set-up to allow for future inclusion of the plastic regime once there is data to calibrate it. With the blast load, the pressure acting on the front wall of a structure starts with the jump to the reflected pressure, p_r, a function of the incident pressure, and decays to the stagnation pressure, p_s. The stagnation pressure is the incident pressure added to the net dynamic pressure, $C_d q$ [104].

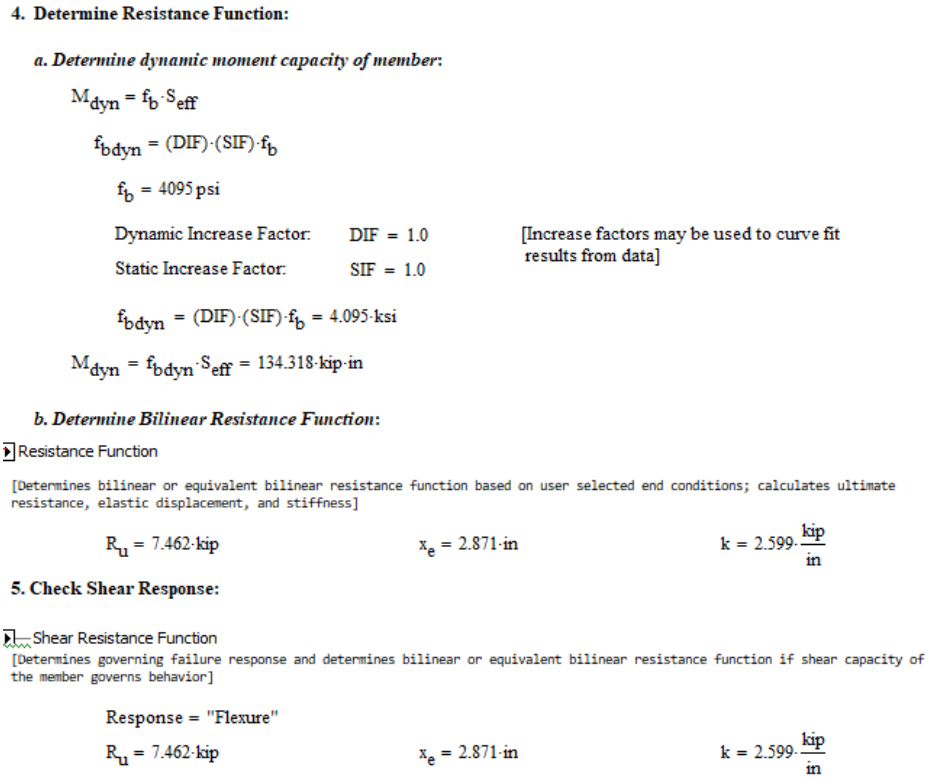

Figure 8-16. Resistance function development in the CLT blast analysis tool.

The front wall pressure-time history can be plotted with a bilinear curve including the different blast load components as shown in Figure 8-17. An equivalent load can be found using the peak reflected pressure, p_r, and the impulse for each load shape or the areas under each section of the curve. This equivalent load will provide an associated equivalent impulse, I_e, and equivalent duration, T_e. The fictitious duration of the positive phase of static overpressure is annotated with $t_{so,f}$. The very short durations in this type of loading require an extra check for accuracy; this check compares the reflected pressure impulse and associated fictitious duration to the equivalent values. The smaller impulse value is used in calculations of the wall blast loading [104].

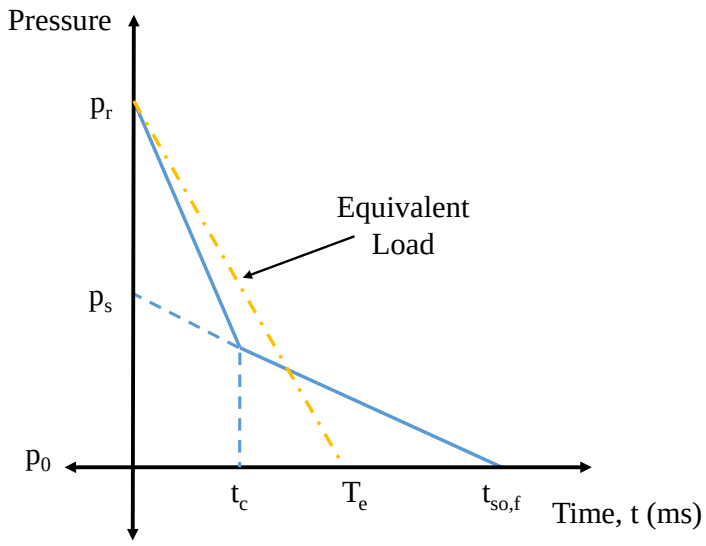

Figure 8-17. Pressure-time history bilinear function for front walls.

The tool then conducts numerical integration running the linear acceleration method with the bilinear resistance functions to produce the time-history response of the member. This means incremental solutions are found at each time step, and results of the

previous and current time step help predict the acceleration and velocity using the equation of motion through the history of the blast load event. Small time periods provide accurate and stable solutions; for an SDOF system this is typically 0.10 of the duration time [104]. The time step in the CLT blast analysis tool is set to 0.00001 sec.

This numerical evaluation of the dynamic response of the member produces the results, which include plots for the Force-Time History, Resistance-Displacement, Displacement-Time History and Dynamic Shear History as shown in Figure 8-18. Additionally, values are determined for the maximum displacement in the positive phase, the maximum rebound displacement, from the negative phase, the residual displacement and the maximum dynamic shear and displayed as shown in Figure 8-19.

While the maximum rebound displacement is displayed, this calculation needs further evaluation due to the lightweight nature of the CLT material. The negative pressure phase generally has limited impact with robust steel and reinforced concrete designs but with flexible materials like wood, the behavior is different. While outside the scope of this research, there is the opportunity to add the negative phase parameters and incorporate them into future work.

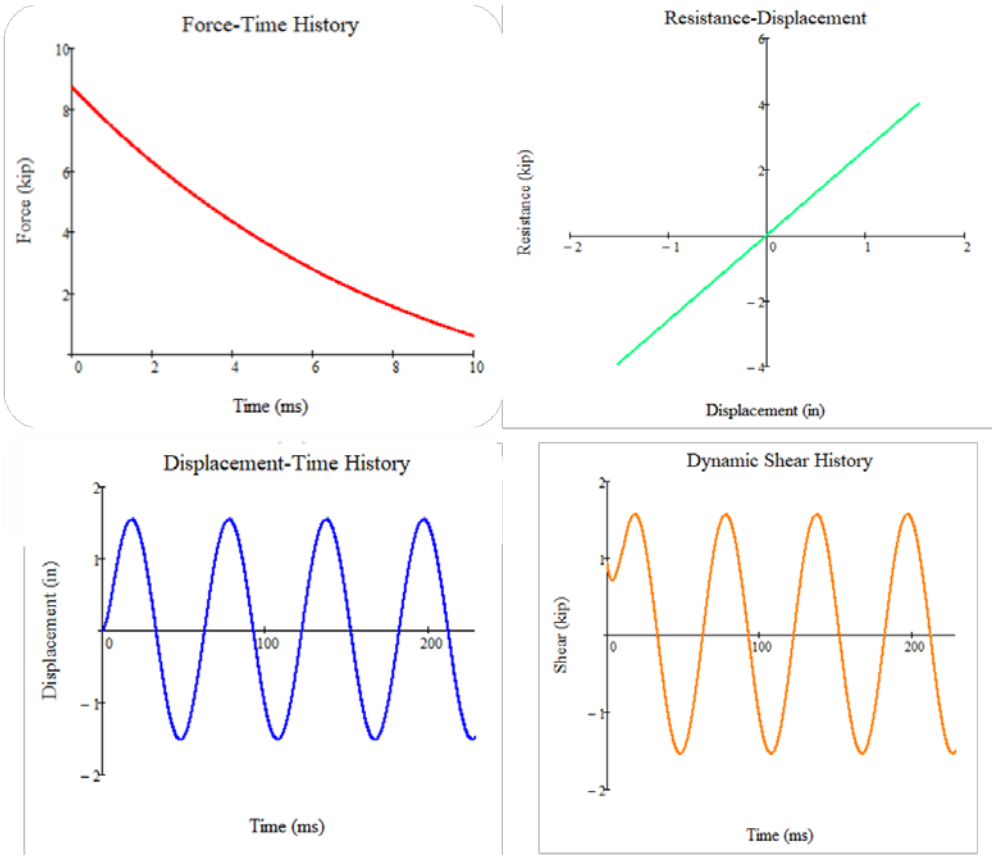

Figure 8-18. Resulting plots from the CLT blast analysis tool.

7. Key Results:

See plots for Force-Time History, Resistance-Displacement, Displacement-Time History, and Dynamic Shear History.

Maximum Displacement (in)	$x_{max} = 1.545 \cdot in$
Maximum Rebound Displacement (in):	$x_{min} = -1.517 \cdot in$
Residual Displacement (in):	$x_r = 0 \cdot in$
Maximum Dynamic Shear (kip):	$V_{max} = \max(V) = 1.572 \cdot kip$

Figure 8-19. Values of key results from the CLT blast analysis tool.

The maximum support rotation, θ_r, and ductility ratio, μ, were computed using Equation 8.17 and Equation 8.18, in order to categorize the expected element damage of the element and Level of Protection provided against the specified explosive threat [104]. These categorizations were based on values associated with reinforced concrete and steel and should be examined more in-depth with CLT.

$$\theta_r = \tan^{-1}\left(\frac{2x_{max}}{L}\right) \tag{8.17}$$

where x_{max} = maximum displacement
L = length of element

$$\mu = \frac{x_{max}}{x_e} \tag{8.18}$$

where x_{max} = maximum displacement
x_e = elastic displacement

Based in the user specified classification of the element type (primary, secondary, nonstructural) and the tool computed values for ductility ratio and maximum support rotation, the expected damage and associated Level of Protection were predicted. Figure 8-20 shows the tool output for Level of Protection.

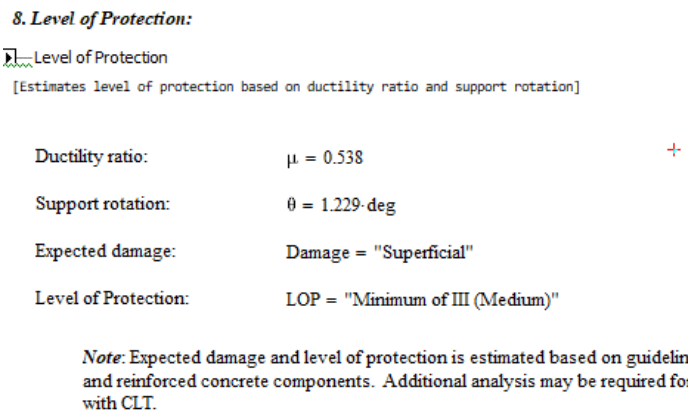

Figure 8-20. Expected Level of Protection as determined by the CLT blast analysis tool.

8.3.2 Validation of the CLT blast analysis tool

The observations and field data from the live blast testing previously detailed provided an opportunity to validate the CLT blast analysis tool. The parameters were set in the tool to the actual physical parameters of the live blast tests and the results in terms of inbound displacement (positive phase) and expected damage were compared to the data gathered observed at the actual tests. A percent difference was calculated to compare the tool predicted displacement based on the UFC load calculations to the actual gauge recorded displacements. The tool predicted displacements based on the input of the field recorded values and calculations for peak reflected pressure, reflected impulse and positive phase duration, were also compared to the gauge recorded displacements. Rolling shear was not considered in the shear response check for the resistance function. Table 8-3 shows the blast parameters used for the three shots for both UFC load calculations and field data based load calculations.

Table 8-3. Blast parameters for load calculations, UFC and field data.

Blast parameter	Shot 1		Shot 2		Shot 3	
	Field Test data	UFC calculated	Field Test data	UFC calculated	Field Test data	UFC calculated
Peak reflected pressure, p_r (psi)	5.05	5.031	7.94	7.361	13.2	14.061
Reflected impulse, i_r (psi-ms)	19.9	22.488	32.9	37.446	65.7	79.992
Duration of positive phase, t_d (ms)	8.56	11.436	9.42	13.507	11.26	17.108

Table 8-4 shows the gauge displacement data, tool UFC based displacement, tool field data based displacement and the percentage differences for each of the three structures and all three test shots for the fixed-pinned member end-conditions for the front wall, ground level. This end condition classification in the blast analysis tool seemed the most applicable based on the rigid steel angle connections used to affix the CLT structures to the concrete slab.

The tool predictions of inbound displacement are generally in good agreement with the actual displacements of the live blast tests for the first two shots because the panels exhibited an elastic response. For the percentage difference based on the UFC load calculations, the majority of differences were less than 10 percent. The field data based displacement values were mostly under-predicted ranging from about 4 percent to 15 percent difference from the actual displacement for the first two shots. The field data based displacements appeared to have slightly higher percent difference across the entire dataset, with most under-predicting the displacement in the range of 4 to 15 percent.

Table 8-4. Tool predicted versus actual displacements using fixed-pinned end conditions.

Shot	TNT Weight [lb.]	Inbound displacement (gauge recorded) [in]	SDOF inbound model displacement (UFC loads) [in]	Percent difference	SDOF inbound model displacement (field data) [in]	Percent difference
		CLT grade E-1, front face, Ground level				
1	32	1.09	1.217	11.65%	1.101	1.01%
2	67	1.96	1.978	0.92%	1.801	-8.11%
3	*199*	*3.9*	*4.029*	*3.31%*	*3.498*	*-10.31%*
		CLT grade V-1, front face, Ground level				
1	32	1.18	1.206	2.20%	1.091	-7.54%
2	67	2.04	1.938	-5.00%	1.773	-13.09%
3	*199*	*4.28*	*5.478*	*27.99%*	*4.095*	*-4.32%*
		CLT grade V-4, front face, Ground level (h= 10-ft)				
1	32	1.07	1.044	-2.43%	0.951	-11.12%
2	67	1.83	1.676	-8.42%	1.551	-15.25%
3	*199*	*4.57*	*4.35*	*-4.81%*	*3.403*	*-25.54%*

With the third shot, highlighted in italics on Table 8-4, the model predicted that the panel ruptured for the two visually graded CLT panels based on the computed displacements. The calculated displacement values are therefore inaccurately predicted because the model has not been validated for response after rupture of an outer ply. This is illustrated with the two percentage differences in excess of 25 percent. More testing and data is needed for response of the panels in the plastic regime to develop a model for that regime. This is necessary to more accurately predict the panel response upon rupture of the outer ply.

The CLT tool predictions for the V4 panel were consistently under-predicted for both the UFC load calculations and the field data based load calculations. Whereas, all but one other displacement value was over-predicted for both V1 and E1 CLT using the UFC

load calculations. Field data based calculations under-predicted the displacement for five of the six values for V1 and E1 CLT.

Based on the CLT blast analysis tool, the expected damage and Level of Protection for the specified panel are rated in accordance with the *ASCE 59-11, Blast Protection of Buildings* as depicted in Table 8-5. It should be noted that the actual observed damaged can be described as superficial for all three structures for the first two blasts with 32-lb and 67-lb TNT weights. There was no visible evidence of damage aside from a few knots displaced from the plies and there was no sign of permanent deformation or ply rupture.

For the third blast of 199-lb, the actual damage was moderate with some visible damage. The extent of the damage was fracture of individual sawn timbers in the outermost plies, with some plastic deformation, as the fractured section did not return to lie flat with the rest of the panel. For the CLT grade V1 and E1 structures, the damage was approximately mid-height and mid-width of the ground floor front panel on both the exterior ply and the interior ply. For the CLT grade V4 structure, the majority of the observed damage was on the interior face, ground floor, front panel and small pieces of debris, not observed in the other two structures was found inside [118]. Residual displacement values were not reported. This may be due to the difficulty in accurately measuring displacement with the individual timbers fracturing – if the gauge was not aligned with the specific timber which fractured, but rather a timber which did not fracture, the measurement would not represent the entire panel.

The tool computed the ductility ratio and support rotation using both the UFC based blast parameters and the field measured data based parameters to determine a corresponding expected damage and Level of Protection rating. For the E1 structure, the

tool predicted moderate damage based on the UFC based parameters and a low Level of Protection for the third blast. However, for the V1 and V4 structures, the tool predicted collapse and hazardous levels of damage with collapse extremely likely for Level of Protection. Both of these expected damage predictions indicate that the model predicted rupture of the panel. It should be noted that while the panels experienced rupture of plies, the overall structure was not in danger of collapse. This furthers the recommendation of future work related to assessing the appropriate values for ductility ratio and support rotation corresponding to expected damage and Levels of Protection.

Table 8-5. Predicted Level of Protection.

Shot	TNT Weight [lb.]	Ductility Ratio (μ) (UFC)	Ductility Ratio (μ) (field)	Support Rotation [degree] (UFC)	Support Rotation [degree] (field)	Expected Damage (UFC/Field)	Level of Protection (UFC/Field)
		CLT grade E-1, front face, Ground level					
1	32	0.327	0.296	0.968	0.876	Superficial/ Superficial	Med/Med
2	67	0.531	0.484	1.574	1.433	Superficial/ Superficial	Med/Med
3	199	1.082	0.94	3.203	2.781	Moderate/ Superficial	Low/Med
		CLT grade V-1, front face, Ground level					
1	32	0.713	0.645	0.959	0.868	Superficial/ Superficial	Med/Med
2	67	1.146	1.049	1.542	1.411	Moderate/ Moderate	Low/Low
3	199	3.24	2.421	4.351	3.255	Collapse/ Hazard	Collapse/ Collapse
		CLT grade V-4, front face, Ground level (h= 10-ft)					
1	32	0.645	0.588	0.997	0.908	Superficial/ Superficial	Med/Med
2	67	1.036	0.959	1.6	1.481	Moderate/ Superficial	Low/Med
3	199	2.69	2.081	4.146	3.21	Hazard/ Hazard	Collapse/ Collapse

Reasons for the discrepancies between the tool prediction and the actual observed effects may include that the panels are stronger than the required design values of PRG 320. A SIF and DIF may need to be determined to account for the additional strength of the panels. Validation of the tool beyond the elastic regime was not possible without blast test data from the plastic regime. Additionally, the negative pressure phase is not accurately represented in the tool. Future modifications to the tool could incorporate more accurate rebound displacements with additional validation using plastic regime data and the calculation of negative phase blast parameters.

8.3.3 Model with proposed Dynamic Increase Factor (DIF)

Using the dynamic increase factor of 1.28 proposed by Poulin et al. the CLT blast analysis tool was re-run [89]. The DIF appears to improve the predicted inbound displacement for larger blast loads but more testing is needed. At the smallest blast weight, the displacement predictions were unchanged for all three grades of CLT. For the second shot, the displacement values were unchanged for the E1 panel, and improved for the V1 panel for both the UFC and field data loads. For the V4 panel, the UFC load provided a smaller percent difference for the second shot. The field data based displacement resulted in the same value calculated without the DIF. The improved percent differences are highlighted in blue on Table 8-6. The addition of the DIF accounts for higher strengths achieved at the high strain rates of the dynamic loading. The model still has the limitation for the third test shot where the panels responded beyond the elastic regime. This means the displacement values for the third shot are still inaccurate.

Based on the inclusion of the DIF, the CLT blast analysis tool predicted that the E1 panel would only experience superficial damage, shown in Table 8-7. Since the actual

damage was fracture of the sawn timbers in the outermost plies at the center of the panel, this revised damage estimate seems to under predict the expected damage for this grade of CLT. The two visually graded panels, V1 and V4, were still expected to receive heavy and hazardous levels of damage which seems excessive given the panel was still standing and appeared structurally sound. The observed damage was most consistent with the moderate damage rating in that there was some fractured timbers but repair seemed possible and the panel appeared unlikely to fail.

Table 8-6. Tool predicted versus actual displacements using fixed-pinned end conditions using DIF.

Shot	TNT Weight [lb.]	Inbound displacement (gauge recorded) [in]	SDOF inbound model displacement (UFC loads) [in]	Percent difference	SDOF inbound model displacement (field data) [in]	Percent difference
		CLT grade E-1, front face, Ground level				
1	32	1.09	1.217	11.65%	1.101	1.01%
2	67	1.96	1.978	0.92%	1.801	-8.11%
3	*199*	*3.9*	*4.066*	*4.26%*	*3.524*	*-9.64%*
		CLT grade V-1, front face, Ground level				
1	32	1.18	1.206	2.20%	1.091	-7.54%
2	67	2.04	1.96	-3.92%	1.785	-12.50%
3	*199*	*4.28*	*4.608*	*7.66%*	*3.666*	*-14.35%*
		CLT grade V-4, front face, Ground level (h= 10-ft)				
1	32	1.07	1.044	-2.43%	0.951	-11.12%
2	67	1.83	1.685	-7.92%	1.551	-15.25%
3	*199*	*4.57*	*3.723*	*-18.53%*	*3.077*	*-32.67%*

Table 8-7. Predicted Level of Protection using DIF.

Shot	TNT Weight [lb.]	Ductility Ratio (μ) (UFC)	Ductility Ratio (μ) (field)	Support Rotation [degree] (UFC)	Support Rotation [degree] (field)	Expected Damage (UFC/Field)	Level of Protection (UFC/Field)
		CLT grade E-1, front face, Ground level					
1	32	0.255	0.231	0.968	0.876	Superficial/ Superficial	Med/Med
2	67	0.415	0.378	1.574	1.433	Superficial/ Superficial	Med/Med
3	199	0.853	0.739	3.232	2.802	Superficial/ Superficial	Med/Med
		CLT grade V-1, front face, Ground level					
1	32	0.557	0.504	0.959	0.868	Superficial/ Superficial	Med/Med
2	67	0.905	0.825	1.559	1.42	Superficial/ Superficial	Med/Med
3	199	2.129	1.694	3.662	2.915	Hazardous/ Heavy	Collapse/ Very Low
		CLT grade V-4, front face, Ground level (h= 10-ft)					
1	32	0.504	0.459	0.997	0.908	Superficial/ Superficial	Med/Med
2	67	0.814	0.749	1.608	1.481	Superficial/ Superficial	Med/Med
3	199	1.799	1.487	3.551	2.936	Heavy/ Heavy	Very Low/ Very Low

8.4 Model predictions

8.4.1 Effect of end conditions

With the boundary conditions adjusted to simply supported, and no other changes are made with the user specifications of the tool, there is significantly worse agreement between the predicted displacements and the actual values as signified by the percent differences in Table 8-8. The smallest percent difference in displacement values is over 10 percent, and the highest is over 160 percent. The tool consistently over-predicted the displacements using the simply supported end conditions. This disagreement between the model and actual displacements makes sense given that the actual end conditions were not

very representative of a simply supported system with the robust connection to the concrete slab.

Table 8-8. Tool predicted versus actual displacements using simply supported end conditions.

Shot	TNT Weight [lb.]	Inbound displacement (gauge recorded) [in]	SDOF inbound model displacement (UFC loads) [in]	Percent difference	SDOF inbound model displacement (field data) [in]	Percent difference
		CLT grade E-1, front face, Ground level				
1	32	1.09	1.545	41.74%	1.387	27.25%
2	67	1.96	2.528	28.98%	2.273	15.97%
3	199	3.9	5.872	50.56%	4.614	18.31%
		CLT grade V-1, front face, Ground level				
1	32	1.18	1.559	32.12%	1.41	19.49%
2	67	2.04	2.891	41.72%	2.454	20.29%
3	199	4.28	11.159	160.72%	7.727	80.54%
		CLT grade V-4, front face, Ground level (h= 10-ft)				
1	32	1.07	1.313	22.71%	1.195	11.68%
2	67	1.83	2.351	28.47%	2.027	10.77%
3	199	4.57	8.821	93.02%	6.208	35.84%

With the boundary conditions changed to a fixed-fixed system, and no other changes made with the user specifications of the tool, there is worse agreement between the predicted displacements and the actual values than the fixed-pinned condition, but better agreement than the simply supported scenario, as illustrated by the percent differences in Table 8-9. The percent differences in displacement values are close to those for the fixed-pinned end condition however, the over-predictions present a slightly higher percent difference and the under-predictions offer a slightly smaller percent difference. As

seen with the fixed-pinned end conditions, the predicted displacements for the V4 structure were consistently under-predicted.

Table 8-9. Tool predicted versus actual displacements using fixed-fixed end conditions.

Shot	TNT Weight [lb.]	Inbound displacement (gauge recorded) [in]	SDOF inbound model displacement (UFC loads) [in]	Percent difference	SDOF inbound model displacement (field data) [in]	Percent difference
		CLT grade E-1, front face, Ground level				
1	32	1.09	1.238	13.58%	1.119	2.66%
2	67	1.96	2.014	2.76%	1.831	-6.58%
3	199	3.9	4.108	5.33%	3.585	-8.08%
		CLT grade V-1, front face, Ground level				
1	32	1.18	1.227	3.98%	1.11	-5.93%
2	67	2.04	1.973	-3.28%	1.806	-11.47%
3	199	4.28	5.516	28.88%	4.178	-2.38%
		CLT grade V-4, front face, Ground level (h= 10-ft)				
1	32	1.07	1.062	-0.75%	0.967	-9.63%
2	67	1.83	1.71	-6.56%	1.578	-13.77%
3	199	4.57	4.389	-3.96%	3.437	-24.79%

8.4.2 Effect of rolling shear

When rolling shear is considered in the tool, the failure response changed for only one of the four considered CLT grades, E1, as shown in Table 8-10. This was the case for both fixed-pinned and fixed-fixed end conditions. For the simply supported condition, all grades of CLT investigated were found to have a failure response in flexure in the development of the resistance function. This shear failure response corresponds with a lower required shear strength for the E1 graded CLT panels per PRG 320 design properties. For the two conditions with E1 shear failure response, the displacement values changed

when the rolling shear response was used for the calculation of the displacement predictions for that grade. For fixed-pinned conditions, the values were over-predicted in the range of almost 42 percent to over 75 percent above the actual observed displacements, as shown in Table 8-11. This high percentage of over-prediction indicates that the expected shear response was likely not experienced in the actual testing. One reason that the rolling shear failure was not experienced may be attributed to the panel edge connections to the side walls.

Table 8-10. Governing failure response for resistance function for fixed-pinned and fixed-fixed end conditions.

Shot	TNT Weight [lb.]	CLT grade - fixed-pinned & fixed-fixed end conditions			
		E1	V1	V4	V3
1	32	shear	flexure	flexure	flexure
2	67	shear	flexure	flexure	flexure
3	199	shear	flexure	flexure	flexure

Table 8-11. Displacement values for E1 CLT based on shear failure response, fixed-pinned end conditions.

Shot	TNT Weight [lb.]	Inbound displacement (gauge recorded) [in]	SDOF inbound model displacement (UFC loads) [in]	Percent difference	SDOF inbound model displacement (field data) [in]	Percent difference
		CLT grade E-1, front face, Ground level				
1	32	1.09	1.911	75.32%	1.709	56.79%
2	67	1.96	3.138	60.10%	2.802	42.96%
3	199	3.9	6.492	66.46%	5.529	41.77%

8.4.3 Predictions for CLT Grade V3, Southern Yellow Pine

Due to the lack of commercially available V3 graded CLT, there was not a fourth structure made of that grade to include in the live blast tests. However, based on the PRG 320 required design properties, this grade was incorporated into the CLT blast analysis tool. This allowed for predictions to be developed for the material. Table 8-12 presents the inbound (positive pressure phase) displacement, ductility ratio, support rotation, expected damage and Level of Protection for the ground floor, front wall panel of a structure build to the same specifications and dimensions as the E1 and V1 graded CLT structures in the live blast tests. The table includes the three variations of end conditions investigated in the tool but consideration for the connection details used must be accounted for in validating agreement to actual test results. The tool also predicts collapse for the V3 structure given the third blast load, as it did with the V1 structure. This indicates that the panel response will likely extend beyond the elastic regime. Generally, the predicted values align close to the model's predictions for the V1 CLT structure. Based on the live test results and lack of damage despite the tool predictions, more testing and calibration is needed for the larger blast loading.

8.4.4. The CLT blast analysis tool – future development

The CLT blast analysis tool was built to allow for exploring a variety of characteristics that could be changed to include but not limited to: ply quantity, wood density, static loading, dimensions of the panel, location of the panel, location of the blast, and size and type of explosive. Based on the validation with the live blast testing, the tool provides good agreement for the front wall, ground level element in terms of maximum displacement in the positive phase of the loading in the elastic regime. Additional

validation could examine the second floor displacement values given the currently available test data. The four largest areas that need further investigation with the CLT blast analysis tool are: 1) testing of CLT panels in the plastic regime, 2) the refinement for inclusion of the negative phase by adjusting the rebound blast parameters, 3) further investigation with rolling shear and blast response, and 4) further exploration of a dynamic increase factor based on the indicated increased strength of CLT under high strain loading such as a blast load.

The hydraulic blast generator set-up like the one at the Georgia Institute of Technology's Structural Engineering and Materials Laboratory can be used in the future to experimentally derive the resistance function of CLT panels in the plastic regime. By applying an impulsive blast-like load to a CLT test panel with a mass in a controlled manner data can be collected on the material response and displacement as the panel enters the plastic regime and experiences rupture in the outermost ply. The blast generator allows for full-scale testing with repeatable load configurations thus multiple CLT grades and panel layups could be tested and used to expand the model and improve its predictions.

.

Table 8-12. CLT blast load analysis tool predictions for V3 grades CLT (Southern Yellow Pine).

Fixed-pin end conditions									
Shot	TNT Weight [lb.]	Inbound model displacement (UFC loads) [in]	Inbound model displacement (field data) [in]	Ductility Ratio (μ) (UFC)	Ductility Ratio (μ) (field)	Support Rotation (degree) (UFC)	Support Rotation (degree) (field)	Expected Damage (UFC/Field)	Level of Protection (UFC/Field)
1	32	1.206	1.091	0.658	0.596	0.959	0.868	Superficial/Superficial	Medium/Medium
2	67	1.944	1.785	1.061	0.975	1.547	1.42	Moderate/Superficial	Low/Medium
3	199	5.148	3.956	2.81	2.16	4.09	3.145	Hazardous/Hazardous	Collapse/Collapse
Simply Supported end conditions									
Shot	TNT Weight [lb.]	Inbound model displacement (UFC loads) [in]	Inbound model displacement (field data) [in]	Ductility Ratio (μ) (UFC)	Ductility Ratio (μ) (field)	Support Rotation (degree) (UFC)	Support Rotation (degree) (field)	Expected Damage (UFC/Field)	Level of Protection (UFC/Field)
1	32	1.566	1.416	1.05	0.949	1.246	1.126	Mod/Super	Low/Medium
2	67	2.783	2.39	1.866	1.602	2.214	1.901	Heavy/Heavy	Very Low/Very Low
3	199	10.276	7.186	6.889	4.817	8.123	5.699	Collapse/Collapse	Collapse/Collapse
Fixed-fixed end conditions									
Shot	TNT Weight [lb.]	Inbound model displacement (UFC loads) [in]	Inbound model displacement (field data) [in]	Ductility Ratio (μ) (UFC)	Ductility Ratio (μ) (field)	Support Rotation (degree) (UFC)	Support Rotation (degree) (field)	Expected Damage (UFC/Field)	Level of Protection (UFC/Field)
1	32	1.227	1.11	0.649	0.587	0.976	0.883	Superficial/Superficial	Medium/Medium
2	67	1.981	1.816	1.049	0.961	1.576	1.444	Moderate/Superficial	Low/Medium
3	199	5.19	3.993	2.747	2.114	4.123	3.147	Hazardous/Hazardous	Collapse/Collapse

8.5 Summary

In order for CLT to be considered as an optional construction material for DoD facilities, temporary or permanent, the material response to blast loading must be determined. This characteristic of the material is just beginning to be explored. Preliminary testing shows positive response, with less damage than generally expected. However, blast testing is resource intensive in both cost and time. Analytic tools, like the CLT blast analysis tool developed in this research, can help provide insight into what might be expected given a blast load against a CLT panel using the fundamental concepts of blast design and CLT design. The objective of this initial version of the tool was to capture the composite wood product behavior to peak resistance in the elastic regime based on existing data from live blast tests. With refinement of the tool and further validations, it can provide important insight in expected CLT response to blast loads for designers.

CHAPTER 9
ASSESSING CLT FOR USE IN TEMPORARY MILITARY STRUCTURES

The overall goal of this dissertation is to assess the suitability of CLT for use in housing for the U.S. military. The majority of the work focuses on issues of force protection, that is, the suitability of CLT structures for ballistic and blast resistance. This chapter introduces a broader set of issues regarding the design and construction of temporary military structures and develops a framework for decision making to assess the overall efficacy of CLT buildings in military applications. The assessment and framework also inform future research on CLT. The chapter reviews decision-making methodologies and tools before introducing a critical set of performance criteria for military structures used in theater. Each of these criterion are then discussed in detail with respect to the specific attributes of CLT.

9.1 Introduction

Decision making can be based on many different inputs including experience, pre-existing knowledge, assessment of alternatives, and/or prioritization of evaluation criteria [37]. Decision making is the selection of a choice based on the alternatives. Optimization is the process of making the optimal or "best" choice based on a pre-determined set of variables and constraints. A multi-criteria or multi-attribute tool provides a means for assessment based on defined evaluation criteria, alternatives, and given objectives or goals. Using tools employed in the construction management and project management industry often used for risk assessment and project evaluation, CLT could be comparatively

assessed as a material for use in temporary military structures or other construction project with unique or challenging requirements and constraints.

The goal of this chapter is to discuss the development of a methodology and preliminary tool to using critical evaluation criteria to assess the choice of construction material for temporary military structures given specific mission scenarios. The focus of this research heretofore has been on force protection with the ultimate goal of contributing to a body of knowledge for the military to consider using CLT in theater. Regardless of the decision tool used, the development of thorough evaluation criteria that pertain to the unusual requirements of military construction is essential to selecting the best systems. Identification of areas where CLT lags competitor systems will guide future work needed with respect to CLT performance.

9.2 Background on decision-making tools

Many of the decision making tools in the field of architecture, engineering and construction (AEC), focus on risk and assessment of risk. Common areas of risk in construction include cost, time to completion and quality of work. Often the tools for evaluating risk focus on a probability-impact (P-I) model. The model requires a rating of the likelihood of an expected event, the probability, and the consequences if the event occurs, the impact. A simplified example of this type of model is shown in Figure 9-1 where the terms very low, low, medium, high and very high are used as variable for rating both the probability and impact. Often in this type of model, the impact is assumed to be negative. These terms can also be assigned a numerical value and a basic calculation of risk computed by multiplying the impact by the likelihood. The resulting value then

represents risk on a numerical scale where lower values are less risk and higher values are riskier.

Impact	Very High	5	10	15	20	25
	High	4	8	12	16	20
	Medium	3	6	9	12	15
	Low	2	4	6	8	10
	Very Low	1	2	3	4	5
		Very Low	Low	Medium	High	Very High
		Probability/Likelihood				

Figure 9-1. Example of a simplified P-I model.

Identifying objective probabilities of occurrence and impact to a project can be challenging, especially for decision spaces with combinations of qualitative and quantitative measurements. Probabilistic theory and Monte Carlo simulations served as one of the early methods to handle risk assessment as related to cost estimates and variance [108]. Mont Carlo simulation requires significant computing time and requires accurate information, which may be unknown in reality [73]. Fuzzy Set Theory (FST) was developed to represent uncertainty in risk assessment. This type of model allows for the use of words, known as linguistic variables, in the fuzzy set. A fuzzy set is a group of numbers that represent those linguistic variables by rating the level of agreement or disagreement to the definition of that variable [108].

In the 1980s, Analytical Hierarchy Process (AHP) emerged as concept for use in multi-attribute decision making based on mathematics and psychology. It included value and weight to assess probability and impact. AHP also allows for judgment of the decision maker and the use of both qualitative and quantitative assessments for a P-I risk model. The process effectively reduces complex decisions with multiple considerations to a series of pairwise comparisons, which can then be combined for overall results to assist a decision maker. The comparisons can be based on measurements or a given scale, called the fundamental scale, representing the strength of preferences [98]. As indicated by its name, the technique uses a hierarchical structure to model the decision. At the top of the hierarchy is the objective, while the second level is criteria for evaluation followed by alternatives at the bottom level. Depending on the complexity of the decision, sub-criteria can be added as additional levels between the first level of criteria and the bottom level of alternatives [76]. Figure 9-2 shows a generic depiction of the hierarchy.

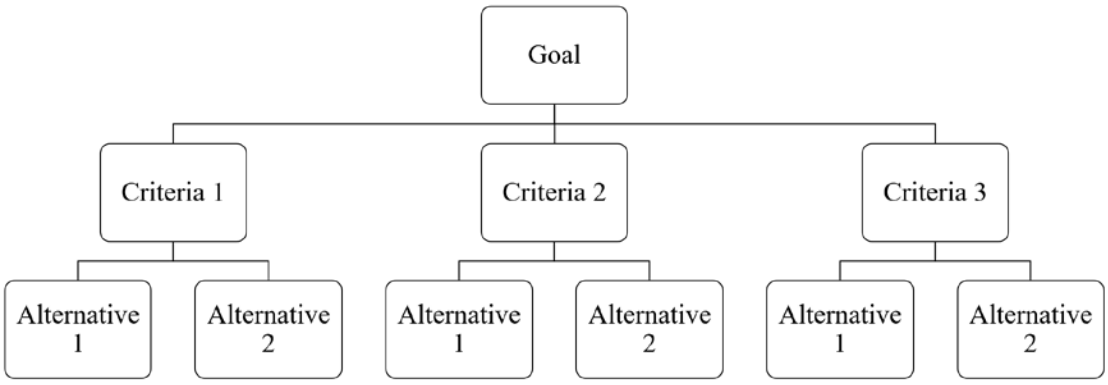

Figure 9-2. A generic hierarchy set-up for AHP application in decision-making.

After the development of the hierarchy, the problem is evaluated with the pairwise comparisons using a scale of relative measurement of priorities or weights for the criteria as determined by decision maker input. Alternatives to reach the objective are compared for each criterion and then a total score is developed through aggregation. AHP and FST became the principle approaches for complex problems that involved subjectivity and were often ill-defined [108].

Risk came to be viewed in the construction industry as a project attribute more than an estimation variance and the risk assessment tools have been found applicable to other attributes besides risk. Tools like the P-I risk model were extended to other aspects of consideration in attempt to better capture the overall decision at hand. Additional attributes or evaluation criteria for a decision required clear definitions with specified ranges of value.

The methodologies used in construction risk assessment may be adjusted to allow for broader application to construction decision making. No existing decision making tool exists for material assessment for temporary military structures. While a military leader may be familiar with risk and general decision making, the challenge with material selection can be the inclusion of relevant technical information by a non-technical decision maker. The leader or group of leaders responsible for making decisions may not have any experience with construction or engineering in general but need to make an informed decision based on complicated interdependences related to material performance and other criteria.

9.3 Evaluation criteria for temporary military structures

In order to make a choice in a multi-attribute problem, the criteria of interest to the decision must be well defined. The performance of each alternatives will be evaluated for each attribute so the description as well as the method of measuring the level of performance should be thoroughly detailed. For temporary military structures, there are several distinctive performance attributes of interest which will be detailed. Generally, in construction risk assessment and decision making criteria may be included or excluded depending on the purpose and environment of the project. Some criteria may have no difference between the given alternatives which makes them non-differentiating factors. These criteria are still important to identify because additional alternatives considered later may introduce differences. The following sections discuss evaluation criteria identified as attributes of critical interest relative to material selection for temporary military structures. A similar process of determining criteria of interest could be used for other decisions related to temporary structures, such as the type, design of the structure, or site layout of a group of structures. The scope of the identified criteria is limited to the decision of material selection for this research.

9.3.1 Material Cost

This criterion is likely one of the least complicated. Construction materials all have an associated cost and in general, the overarching goal is to reduce costs to the greatest extent possible. Material costs are provided in various measurements depending on the material being purchased. Common examples are price per item, price per specific measurement (per linear feet or per square feet) or even price by weight. If alternatives have different cost measurements then this performance metric must be normalized to

allow for direct comparison. One method to address non-uniform pricing is to complete a cost estimate for the material based on the plans of the specific temporary structure.

It is important to note that the lowest price may not always be the most desirable, just as the lowest bidder is not always the most desirable. The material has to be feasible and meet the minimum requirements for other desired performance attributes. With a multi-attribute decision methodology, other characteristics, which may be related to cost, can help determine the most overall cost effective solution. For example, a canvas tent may be the lowest cost material for a temporary structure, and so this alternative would earn a high assessment for the cost criterion. However, other attributes such as blast protection and energy efficiency would earn low performance values thereby countering the cost criterion. Conversely, a net zero energy, blast-proof structure may have very high material costs. Cost must be considered as the situation will likely call for multiple temporary structures, and thus high costs may be prohibitively expensive for a large project such as a basecamp based on fiscal resources available.

It is likely that the cost criterion is a quantitative measurement based on the expense of procuring the construction material. It should also be noted in the criteria description if the cost assessed is purely purchase costs or if transportation associated costs are included. Construction materials can vary in transportation costs based on prefabricated size for delivery, weight of the material, and distance to be transported. Depending on the complexity of the scenario, transportation costs may need to be a separate criterion from material costs, but given that these costs can often be as high as or higher than the material costs alone, their inclusion in any decision-making framework is essential.

9.3.2 Logistics

Each material alternative will have some logistical aspects to consider. These may include time of production, locational availability, and resources required to move the material to the desired end location, such as haul assets, containers, and trailers. Additionally, each of these logistical transport resources have associated constraints relative to volume and weight capacities. This criteria may also include assessing the operational and maintenance requirements of the various material alternatives. This criteria is less objective than cost and will be assessed qualitatively. A performance metric in the form of an assigned numerical value, would need to be tied to a relative scale such as the example shown in Table 9-1 for evaluation. A fully defined measure of the logistics attribute is outside the scope of this work. If the decision tool does not require a numerical value, the assessed linguistic value of high, medium, and low could also be used. However, a clear and concise definition of those ratings is necessary for proper inclusion in the decision-making tool.

Table 9-1. Example of a simplified scale for logistical considerations.

Logistic ease		Definitions by aspect		
Scale	Definition	Production Time Required	Locational Availability	Resource Requirement
1	Very low	Months to years	Unavailable	Intensive, specific requirements
2	Low	Weeks to months	Requires significant shipping time	Many resources required
3	Moderate	Weeks	Moderate shipping time	Some resources required
4	High	Days	Readily available with minimal shipping requirements	Minor resources required, commonly available
5	Very high	On-hand	Immediately available	No resources required

9.3.3 Energy Efficiency

Different measurements can be used in the AEC industry for energy efficiency. For temporary military structures, the circumstances are different from typical construction types in that the standard of comfort is different and the equipment used for heating, air conditioning and ventilation (HVAC) is also temporary in nature. These two facts combine to provide a unique scenario for energy efficiency evaluation. To achieve an accurate energy efficiency valuation of a construction material, a model estimating the building energy performance metrics could be developed for each material type. Alternatively, a simplified assessment could compare the thermal resistance performance using the R-value of the basic material or proposed building envelope assembly [26, 70]. The R-value is a commonly used measure of insulating effectiveness. Both of these methodologies could be employed for temporary military structure evaluation. To accurately model and predict the performance in terms of energy efficiency, additional information would be required such as the environmental operating conditions, the building design, layout and occupancy schedule as well as the available or planned HVAC systems and their specifications [70].

The American Society of Heating, Refrigerating and Air-Conditioning Engineers (ASHRAE), outlines comfort zones for indoor air design conditions as 74 to 80 degrees Fahrenheit at 50 percent relative humidity for summer and 68 to 75 degrees Fahrenheit with a minimum of 30 percent relative humidity for winter [70]. These conditions are unlikely to be the standard for temporary military structures unless the structure has specific functional requirements, such as medical facilities, housing of specialized heat sensitive equipment, or storage of military aircraft.

There is no set standard for HVAC comfort standards outlined in *UFC 1-201-01, Non-Permanent DOD Faculties in Support of Military Operations,* which focuses on the life safety and habitability aspects of temporary military structures [14]. The standard includes reference to ventilation system calculations based on building function and local environmental conditions. The standard further specifies that HVAC systems are to be installed in accordance with manufacturer instructions. The comfort zone of the interior conditions is generally left up to the discretion of the commander. It is important to note this does not necessarily mean no temperature conditioning as military commanders recognize that uninhabitable conditions will contribute to decreased performance from lack of appropriate rest. The threshold of acceptable temperature comfort zone is likely to be significantly outside the range of typical structures in the United States.

The available HVAC equipment can vary depending on location but the military frequently deploys equipment known as Environmental Control Units (ECUs). ECUs either come with a power source or require a power supply such as a generator. Manufacturers build the equipment to be rugged and easily transported to meet military requirements. An in-depth analysis of the energy required to cool and heat a temporary structure could calculate the heating and cooling demand of a single structure in order to determine the number of ECUs and accompanying generators required. The key aspect for deciding on a building material is to evaluate the thermal performance of the structure given the operational environment and expected operating conditions.

9.3.4 Blast protection

Blast protection is generally achieved through a combination of two factors, stand-off distance and the structures response to blast loading. Stand-off distance is the space

between the structure and the detonated explosive which relates to site layout and exterior force protection measures such as bollards and barriers designed to provide defense in depth. The response of the structure is a product of both the building design and material type. A building can be assessed a Level of Protection (LOP) as a qualitative measure related to an explosive event. It is defined by ASCE as the expected performance of the building in terms of structural damage and potential injury to personnel and equipment contained within and around the structure. As detailed in Chapter 8, the expected structural damage is derived from anticipated damage to individual elements of the structure. Table 9-2, from *UFC 4-010-01, DoD Minimum Antiterrorism Standards for Buildings*, outlines the Levels of Protection for expeditionary structures with qualitative descriptions. Temporary military structures are often classified as expeditionary structures for they are used in an overseas or deployed environment.

Knowledge on the expected behavior of building elements and elements made from specific materials can be assessed using analytical models like SDOF models to predict the response. These models can examine different aspects such as material type, connections within the structure, or differing levels of blast threat. The models, through use of a resistance function, predicts the displacement response of the structural element. Based on the classification of the element as either a primary, secondary or non-structural element combined with the model's predicted deformations, a component damage level may be assessed. While blast pressures may be survivable on their own, structures and building components that fail under a blast-loading event may cause injury or fatalities through structural collapse.

In the evaluation of material selection for temporary military structures it is important to ensure the SDOF model used an appropriate resistance function for the material and that the end conditions are representative of the actual structural connections. A higher level of protection is generally preferred although some consideration must be given to the effect on level of protection when the site layout likely implements inherent stand-off distance. For example, if the structure is going to be a set distance from the blast threat by nature of its location within a military compound, then the structure may not need to be as robust to achieve the same LOP. The consideration and incorporation of additional stand-off distance would have the effect of potentially reducing costs while not having to make trade-offs for other criteria.

Table 9-2. Levels of Protection for Expeditionary Structures, from UFC 4-010-01, DoD Minimum Antiterrorism Standards for Buildings [15].

Level of Protection	Potential Structural Damage	Potential Injury
Below AT standards*	Severe damage. Frame collapse/massive destruction. Little left standing.	Majority of personnel in collapse region suffer fatalities. Potential fatalities in areas outside of collapsed area likely.
Very Low	Heavy damage. Major portions of the structure will collapse. A significant percentage of secondary structural members will collapse.	Majority of personnel in damaged area suffer serious injuries with a potential for fatalities. Personnel in areas outside damaged area will experience minor to moderate injuries.
Low	Moderate damage. Damage will be unrepairable. Some sections of the structure may collapse or lose structural capacity.	Majority of personnel in damaged area suffer minor to moderate injuries with the potential for a few serious injuries, but fatalities unlikely. Personnel in areas outside damage areas will potentially experience a minor to moderate injury.
Medium	Minor damage. Damage will be repairable. Minor to major deformations of both structural members and non-structural elements. Some secondary debris will be likely, but the structure remains intact with collapse unlikely.	Personnel in damaged area potentially suffer minor to moderate injuries, but fatalities are unlikely. Personnel in areas outside damaged areas will potentially experience superficial injuries.
High	Minimal damage. No permanent deformation of primary and secondary structural members or non-structural elements.	Only superficial injuries are likely.

* Not a level of protection, should not be used as a design goal. Provided to define a realm of more severe structural response for informational purposes.

9.3.5 Ballistic protection

Much like blast resistance, ballistic resistance is a product of both the munition and the target. Direct fire weapon threats covered in the UFC include small arms weapons and

shoulder fired rockets which all require direct lines of sight. Similar to standoff distance with blast, obscuration or denial of that clear line of sight is the default technique to counter the threat. The Levels of Protection associated with ballistic protection tie to a general design protective system which is a series of countermeasures to mitigate a ballistic threat. The protective system includes site work elements, building elements, building support elements, equipment and manpower and procedures. The selection of a construction material applied only to the building element category of the system. Other categories are outside the scope of this body of work.

Walls and building layout design strategies to achieve the Levels of Protection as specified by *UFC 4-023-07 Design to Resist Direct Fire Weapons Effects* are shown in Table 9-3 [7]. Additional strategies exist for window and door design but given the decision of material selection for temporary military structures, the wall is the primary structural element as windows and doors are minimized. The key to increased protection is energy absorbing materials or hardened construction that stops the penetrating projectile.

Standards related to material performance in stopping different types of munitions include *ASTM F1233, Standard Test Method for Security Glazing Materials and Systems, National Institute of Justice (NIJ) 0108.01, Underwriters Laboratories (UL) 752, and State Department SD-STD-02.01* as well as multiple European standards. The appendix of UFC 4-023-07 includes tables for these standards, which all list the standard or rating levels with associated ammunitions and their weights, diameters, nose shape coefficient, velocities, and the number of shots required. In evaluating and comparing ballistic protection levels of a specified material, its ability to resist ballistic penetration or at least determination of the amount of energy absorbed should be examined. If the material is capable of resisting

rounds without hardening then it should be rated to one of the aforementioned standards, preferably UL 752 as it is a standard specifically for building components and appears to be the universal standard used with materials.

Table 9-3. Design strategy to achieve Levels of Protection against direct fire ballistic threat, based on [7].

Level of Protection	Building layout	Building Element: Wall
Very Low	Main entrances do not face uncontrolled vantage points, or line-of-sight is blocked	No requirement at this level
Low	Line-of-sight minimized; interior layout set to locate critical assets within interior; buildings oriented to minimize exposure	Glass block walls use translucent or otherwise prevent line-of-sight as necessary
Medium	Employment of energy absorption in building shell and/or pre-detonation screens; minimize doors and windows to targeted assets	Select material and thickness for energy absorption screen and design wall to resist residual velocity of round after impact with screen (including resisting spall on interior face as applicable)
High	Building exteriors designed to resist direct impacts; avoid exposure of targeted assets to windows and doors	Design using hardened construction techniques to include retrofit with steel plate and bullet resisting fiberglass

9.3.6 Rapid constructability

One of the more unique criterion for temporary military structures is the assessment of rapid constructability. This feature can be important because the structures may need to be constructed in multiples to house deployed units, and the timeline for desired completion is as soon as possible. Prior to the completed construction of temporary military structures, deployed personnel may have minimal to no shelter from which to live and work. Units may be held at reception and staging areas until the temporary structures are completed.

Additionally, military tents may be used for short-term temporary occupancy until a more robust temporary structure like a B-hut can be occupied.

Military engineers work to project estimated completion dates based on the number of resources available to assign to the project. Evaluating the rapid constructability of a material is similar to traditional construction schedule estimates. The project is analyzed and deconstructed into logical activities related to the work and resources required. Based on the resources and work hours required, a project duration can be estimated. Materials that can be prefabricated into larger components of the structure are favored over stick-built materials that are constructed entirely on-site. The quantity of temporary structures required may also be a factor.

While there is a quantitative portion to assessing this aspect with estimating the project duration, the final assessment can be qualitative like the logistics criterion. A simplified qualitative assessment can also be based on the number of pieces and connections required with a particular material if a full project schedule estimate is more intensive than the time available. Table 9-4 provides an example of a five level qualitative scale for rapid constructability.

Table 9-4. Example of a qualitative rating scale for rapid constructability evaluation.

Scale	Definition	Definition
1	Very low	Stick built; many components, many connections
2	Low	Mostly stick built, minor prefabricated elements; significant number of connections
3	Moderate	Some prefabrication; moderate number of connections
4	High	Large prefabricated sections; minimal connections
5	Very high	Modular; arrives on-site complete

9.3.7 Adaptability

Another unique criterion for temporary military structures is adaptability. Adaptability is defined as the capacity to be altered for a new purpose. This quality is ideal from multiple perspectives with a temporary military structure. One aspect is that the building may need to change functional purpose. For example, a structure that was housing a platoon of Soldiers last week may need to change into a medical facility in the future. Another characteristic of adaptability is the potential for disassembly and relocation of the structure. The ability for the structure to be disassembled, packed up, transported to another location and reassembled would be a highly desirable quality as it would save resources and remove the hassle of disposal. This criterion is one of the more openly defined evaluation metrics. The rating of the materials relative to adaptability would be qualitative, which could then be translated to a numerical scale by outlined definition.

9.3.8 Prioritizing criteria

An important aspect of the decision making tools is setting the priority of criteria, potentially via expert opinion or just based on the given circumstances of the project. For

example, a humanitarian mission in Africa may have different threat parameters than an austere combat outpost in the mountains of Afghanistan and that difference may drive the value of criteria related to protection and threat mitigation, such as blast and ballistic resistance. The ability to adjust to the environment is important for decisions related to temporary military structures due to the wide variety of uses and missions for which they may be employed.

In addition to the case-by-case assessment, trade-offs between criteria and weighing of criteria or alternative advantages is important. This allows for flexibility in application of the tool. The inclusion of multiple stakeholders should also be possible as there will likely be many parties with varied interests and knowledge, providing data, analysis, and opinion. These parties may be the leader or group making the decision or they may be providing a recommendation to a decision maker.

9.4 Case study: material selection for temporary military structures

Temporary military structures may be simple in structural design, but as a construction project there are still complex decisions in terms of risk and assessing standards of performance. Decisions in terms of types of material used, structural design, and site layout all involve attributes such as cost, logistical feasibility, energy efficiency, and force protection capacity (blast resistance and ballistic resistance). Embedded in the decision space are interdependencies and both subjective and objective assessment levels. Often in the construction industry, decision making tools are focused on risk assessment and mitigating risk in terms of cost and project duration. In temporary military structures, those two attributes are important but depending on the intended operating environment, there are many additional attributes of equal or greater importance.

9.4.1 Applying AHP to the problem

A hierarchical design for the decision of material selection for temporary military structures would set the goal of choosing the best material. While the term material is used, the material is representative of a material system which can have significant impacts on the selection of the actual primary construction material. Evaluation criteria would include attributes such as cost, logistics, energy efficiency, and force protection with the sub-criteria of blast resistance, and ballistic resistance. Other parameters could be included depending on the environment in which the structures will be employed. The bottom layer of the design is the alternatives, which in this case are the different material systems. For this simple example, three material systems are included: lightweight steel frame-aluminum skin, CLT, and concrete masonry. The lightweight steel-frame-aluminum skin design represents the K-span type structure shown in Chapter 2, while a CLT replacement for lightweight wood frame construction is used as the wood product. Concrete masonry or CMU is considered as a potentially low-cost, locally-sourced option for temporary military construction. Other alternatives could be considered, including lightweight wood frame, clay masonry brick, and others. There are many sub-criteria for cost, logistics, and energy efficiency, which are excluded for simplicity in this example. Furthermore, criteria can be interrelated. For example, cost is tied to logistics and energy, so there is some relationship between the criteria, which is allowable. Some decision tools handle that interrelatedness better than others; AHP is known for representing that connectivity well [76]. Figure 9-3 shows a possible hierarchy design for the problem set as an example.

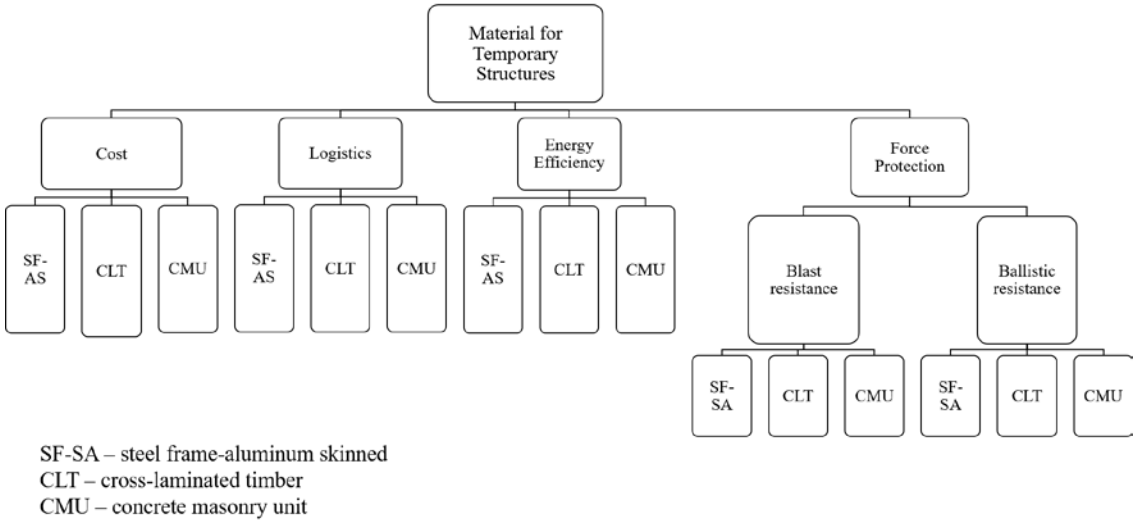

Figure 9-3. Example of hierarchy design for material selection for temporary structures.

With the hierarchy design, information relative to the alternatives and their performance for the determined criteria are gathered. Some of this information will be quantitative such as a cost data while other criteria may be qualitative such as logistical feasibility. Understanding the evaluation criteria for the decision under consideration and then having the technical information on the alternatives relevant to those identified criteria is key.

AHP can utilize all types of criteria. The next step in the process is comparing the criteria with respect to the objective of the decision. This involves the judgment of the decision makers to determine which criteria is more important in the pair and how much more important in reaching the goal. Judgments can be changed later and the model can be re-run. The intensity of importance may be entered into AHP software, if used, based on AHP's fundamental scale for pairwise comparisons, shown in Table 9-5.

Table 9-5. The fundamental scale used in AHP, adapted from [98].

Intensity of important (on absolute scale)	Definition	Explanation
1	Equal importance	Two activities contribute equally to the objective
3	Moderate importance of one over another	Experience and judgment strongly favor one activity over another
5	Essential or strong importance	Experience and judgment strongly favor one activity over another
7	Very strong importance	An activity is strongly favored and its dominance demonstrated in practice
9	Extreme importance	The evidence favoring one activity over another is of the highest possible order of affirmation
2,4,6,8	Intermediate values between two adjacent judgments	When compromise is needed

Using the AHP model, the evaluation criteria are assessed using a pairwise comparison that examines the importance of one relative to another and by how much. Table 9-6 shows an example based on the theoretical problem set with temporary military structures. In this case, the decision makers have determined cost is twice as important as logistics for the given the scenario, so a 2 is entered in the comparison matrix for in row 1, column 2, (cost vs. logistics) and its reciprocal, 1/2 is placed in row 2, column 1 for the opposite perspective (logistics vs. cost). These values are assigned based on personal experience with overseas military construction and perceived value of assessed criteria. They are not meant to accurately represent every scenario for temporary military structures and would need to be evaluated and assigned on a case-by-case basis.

Table 9-6. Example of matrix of pairwise comparisons of evaluation criteria with respect to goal.

GOAL	Cost	Logistics	Energy Efficiency	Blast Resistance	Ballistic Resistance
Cost	1	2	4	1/5	1/5
Logistics	1/2	1	2	1/2	2
Energy Efficiency	1/4	1/2	1	1/5	1/5
Blast Resistance	5	2	5	1	1/2
Ballistic Resistance	5	1/2	5	2	1

Relative weights are assigned to the criteria based on the judged importance and the matrix is normalized. Each alternative under consideration is then assessed with a pairwise comparison for each criteria. This results in an associated weight value for each alternative under each criteria. The matrix of alternative weights and then multiplied by the criteria weight vector to produce a final value for each alternative. The highest valued alternative in that resulting vector is the most preferred choice [98].

9.4.2 Development of the Simplified Multi-Attribute Radar Tool (SMART) assessment

Simplicity is a key factor in tool implementation or adoption [108]. This research employed a radar chart to develop a material selection assessment tool called the Simplified Multi-Attribute Radar Tool, or SMART. A radar chart is a simple graphical method of showing multivariate data, often associated with benchmarking [86]. The two-dimensional plot can be used to graphically depict the performance of an entity for multiple characteristics and if desired, multiple entities can be plotted on the same chart for comparison.

This tool was designed to assist the multi-attribute decision making process of material assessment for use in temporary military structures, specifically for a non-

technical audience. In the military, the team assigned to select the material system may or may not have a technical background or the time necessary to complete a comprehensive technical assessment. The SMART assessment is designed to allow for technical background information on the material and the environment to be pulled into the tool so that the decision maker can determine relevant evaluation criteria to the specific situation, if any prioritization or weights should be assigned. After determining what evaluation criteria and respective weights of the criteria, the decision maker just needs to look at the SMART plot and can then make a rapid judgment on the best fitting alternative.

The key to the radar chart is the selection of evaluation criteria. The criteria must be well defined and consider the methodology for determining a rated value relative to the performance of the criteria by the entity in question. It is difficult to plot sub-criteria with this tool, so it may not work for very complex multi-attribute problems where sub-criteria levels are desired. In addition, the tool does not inherently consider the weighing of different attributes. With the material selection for temporary military structures decision, the two force protection performance measures identified previously as sub-criteria using AHP, blast resistance and ballistic resistance, can be evaluated separately as stand-alone criteria if desired and information is available.

The overall plot represents the decision at hand, such as what construction material to select for temporary military structures for a specific mission or deployment. The axes of the plot, or spokes, represent the metrics of evaluation criteria. The scale of these spokes must be explained in the definition of each criteria. This explanation should include whether a data point assessed closer to the origin of the plot or further from the origin is a positive or negative attribute; this directional assignment should be consistent for all the

spokes evaluated for a given decision. In the radar plot, the scale of the spoke can be set to reflect the weighting or importance value. If criteria A is twice as important as criteria B, then the assigned values relative to criteria A can simply be doubled to account for the increased value of that characteristic of performance.

Each alternative, in this case each material under consideration, is then assessed a value for each of the spokes. The assessed value on each spoke can then be connected to create an area for that particular alternative on the plot, as shown in Figure 9-4. It should be noted that the three material system options shown in the example are light frame wood, CMU and CLT, in contrast to the options in the AHP example. The optimal decision relative to the combined evaluation criteria may either be the largest or smallest area depending on if the outward direction from the origin is determined to be a negative or positive trait. For comparison of alternatives, multiple materials can be plotted on the same radar plot, as shown in Figure 9-5. With the comparison, the decision maker can see by inspection which alternative to select. The individual alternatives on the plot can be shaded, as shown in Figure 9-6, and approximate area calculations could be evaluated to help with the choice between alternatives. Restrictions could also be implemented, often tied to risk, such as specifying that the material cannot rate less than a 2 on the scale for protection, both ballistic and blast, as shown in Figure 9-7.

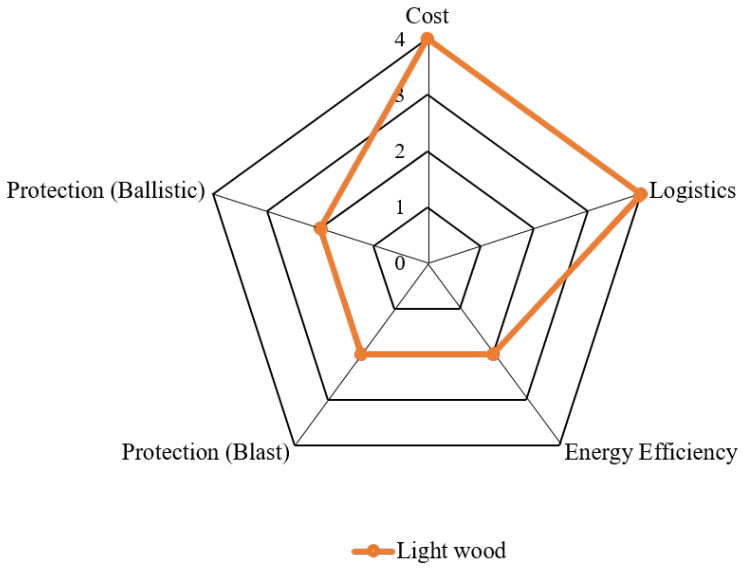

Figure 9-4. An example radar plot for a single alternative is shown with five evaluation criteria metrics.

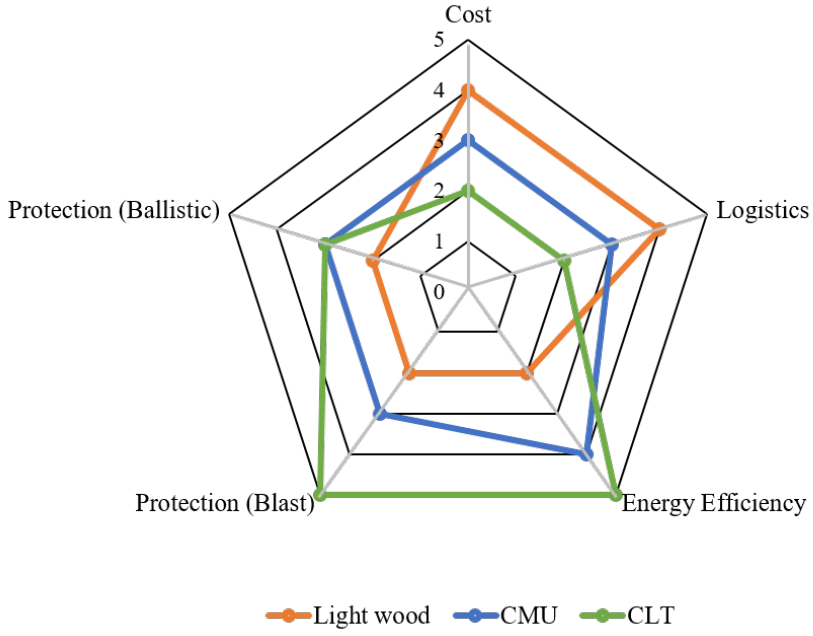

Figure 9-5. An example radar plot with multiple alternatives shown for five evaluation criteria.

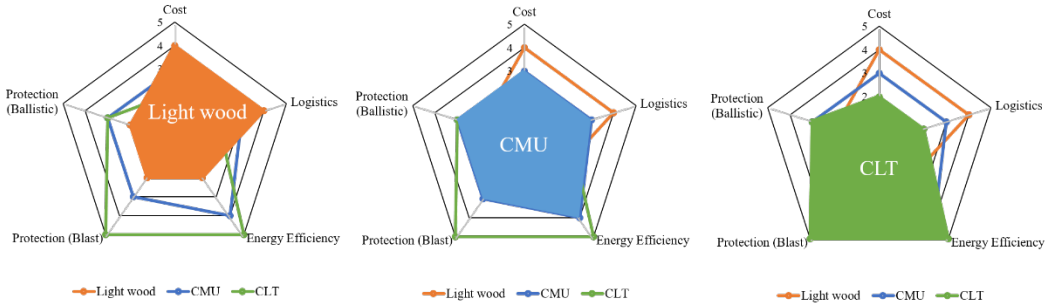

Figure 9-6. An example of shading individual alternatives on the SMART plot for easier assessment between choices.

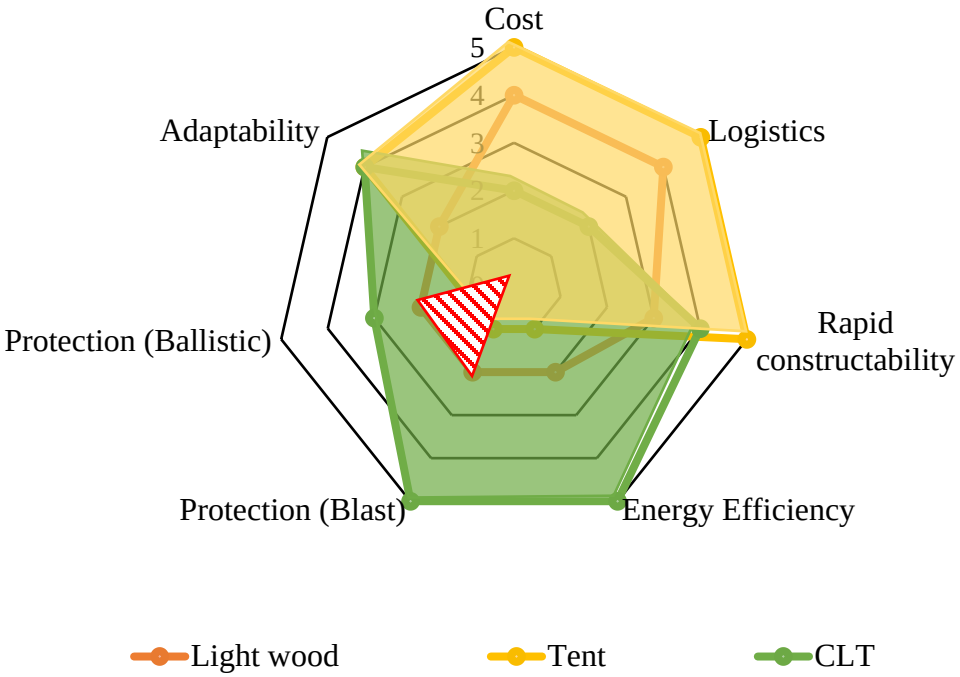

Figure 9-7. An example of a restriction applied to the SMART plot; this case demonstrates that the Protection (Blast) and Protection (Ballistic) criteria must have a rating of 2 or higher for the material system to be in considerations. The red hash marked area represents the restriction.

9.5 Summary

Construction of temporary military structures out of CLT would be a change from current practices. Such a change would require a critical assessment and decision making

process. Many approaches and processes exist to model complex multi-criterion decision making. Construction is one of many fields that employ a variety of tools related to risk assessment and decisions related to project selection or other aspects of design with multiple contributing factors. Analytic hierarchy process is a commonly used approach and could be applied to the decision of material selection for temporary military structures. SMART, a simplified tool, was developed for material selection decision using a radar chart to provide a visual model for military decision makers based on multiple criteria and potential options for construction materials. The evaluation criteria are one of the most important aspects of a decision as they shape the conclusion. The criterion must be thoroughly defined and then methodologies and metrics to assess and evaluate the potential choices should also be outlined. Selection of a material for temporary military structures should include cost, logistical considerations, energy efficiency, blast protection, ballistic protection, rapid constructability, and adaptability.

CHAPTER 10
CONCLUSION

10.1 Summary

CLT is an emerging construction material with significant potential to change the industry. As interest and knowledge in the product gains momentum in the U.S., CLT is being used in more sectors of the industry. One previously unexplored market is temporary military structures, which could potentially expand CLT's use into other military and government projects. Military construction has unique requirements, especially in the realm of force protection measures. Designs incorporating force protection systems require knowledge of a building material's response to ballistic and blast threats.

This research conducted the first experimental testing of CLT for ballistic resistance performance and examined empirical models to determine methods to predict the performance of CLT against ballistic threats posed by conventional small arms weaponry. It identified that current wood penetration models used in military design guides do not accurately predict the performance of CLT, likely due to the fact that the models were calibrated from material systems (e.g., plywood) that behave in a different manner than CLT. Ballistic tests were used to develop and calibrate a model specifically for CLT ballistic performance. Additionally, it recommends a path forward in exploring the ballistic performance of CLT to achieve UL standard performance ratings. The testing conducted for this research was intended to provide preliminary performance capacities to inform future testing related to UL ratings.

Through empirical model development and qualitative analysis of the ballistic test data, CLT and its material characteristics were investigated based on relevant wood properties, including the unique properties of the composite wood product. Characteristics such as hardness and shear strength were explored to provide an understanding of how the material responded to penetration and blast loading events. The qualitative analysis of CLT test specimens based on observed wood properties examined the impact of wood's natural variation on ballistic resistance performance. A lack of existing knowledge for wood and wood products under dynamic and high strain rate loads exposed gaps in fundamental material characterization needed for analytical and numerical models of CLT.

Based on the initial ballistic testing, a new material, ECLT was developed and investigated in terms of constructability and improved ballistic performance. Challenges with adding heavy armor plates to the composite were identified. The advantages of flexible fiber materials developed for use in lightweight armored panels showed promise even with only a few plies of the fabric. Increased ballistic performance can be achieved but typically at either a significant weight or cost increase, and so decisions must be made on acceptable protection levels and trade-offs may be required, such as less protection but at a much lower cost. This work proposed a method to help the decision making process.

This research developed a single-degree-of-freedom model and CLT blast analysis tool to evaluate blast performance of CLT panels. The tool was validated based on live blast test data for CLT response in the elastic regime. Further testing is proposed to investigate and improve the model's predictions in the inelastic regime.

Two decision-making models are considered for determining what construction material to select for use in temporary military structures given the evaluation criteria. The

evaluation criteria for the specific requirements of this type of project were defined in detail. Additionally, a multi-attribute tool named SMART, shown in Figure 10-1, was developed to provide military leaders a quick graphical representation using a radar chart for the decision between material selection based on multiple benchmarks. This tool could be adjusted to other types of construction with other criteria and alternatives.

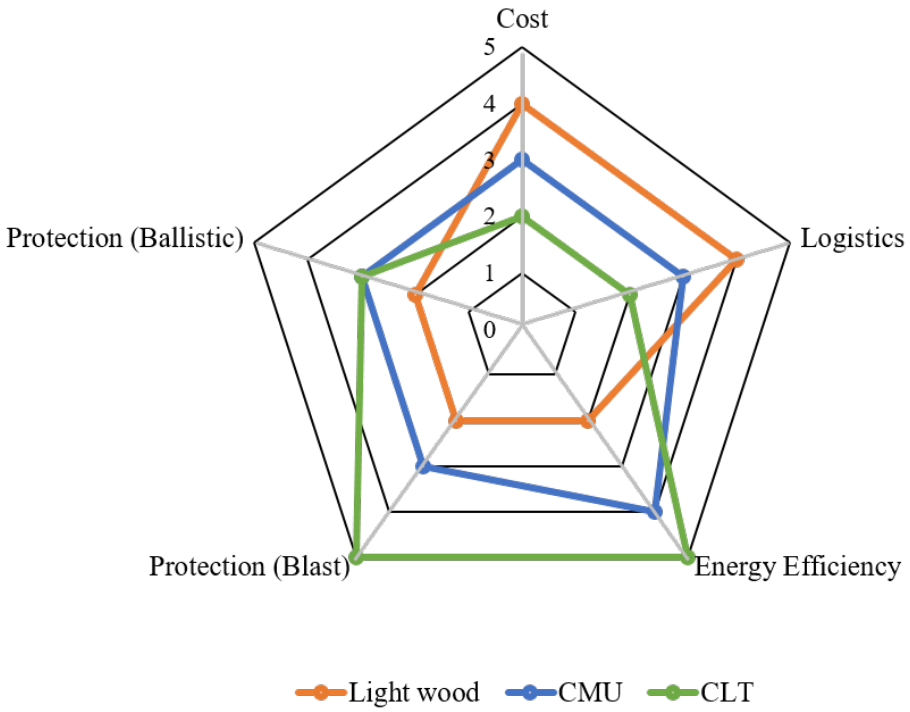

Figure 10-1. An example of the SMART assessment for material selection for temporary military structures.

In summary, the key conclusions from this research with respect to the research questions presented in Chapter 1 include:

1. A new construction material for temporary military structures can be assessed across multiple criteria using a decision making tool that allows for input on alternatives as well as defined evaluation criteria based on the users judgment, and knowledge of the material.
2. The ballistic performance of CLT can be empirically modeled used curve-fitting equations developed from experimental test data. These equations can be expected to reasonably predict the performance as long as the ballistic munition is the same as the experimental round. Re-calibration of the model is required to change munitions, especially for with variations on nose shape, as this parameter was not included in these models.
3. CLT can be altered with modest effort to include an additional enhancing layer to improve its ballistic resistance. Inexpensive fiberglass fabric shows greatest cost-benefit potential of the investigated modified layups of ECLT.
4. Currently, CLT can be modeled for blast performance in the elastic regime using a single-degree-of-freedom model and resistance function. Further blast testing is required to expand this model and resistance function accurately into the inelastic regime.

10.2 Contributions and significance

The contributions and significance of this research exploring CLT for use in temporary military structures include:

1. The first ballistic tests of CLT were conducted from which initial empirical models were developed and calibrated. The testing and analysis showed that

current empirical models in military guidelines for protective design using wood do not apply to CLT.

2. A new variation of CLT, ECLT with an enhanced layer for improved ballistic resistance was prototyped. Testing of several layups using existing armored materials demonstrated the feasibility of manufacturing the product and that improved performance can be achieved even with thin, relatively inexpensive materials such as fiberglass fabric added to the sandwich composite.
3. A tool based on a single-degree-of-freedom model was developed to evaluate the expected performance of CLT panels under blast loading. The tool allows the user to input various parameters related to the CLT panel, including grade and dimensional data as well as blast information. It employs the shear analogy method to estimate the CLT panel structural properties. Currently the tool is validated in the elastic regime based on live blast tests.
4. A multi-attribute decision making tool was developed to provide a simple, visual representation of the material alternatives for temporary military structures based on specified and defined evaluation criteria.

10.3 Recommendations for future work

The foremost recommendation for future work is additional experimental testing for both ballistic resistance and blast performance of CLT to allow for standard ratings to be assigned to the material. The ballistic testing needs to expand into additional munition types with varied nose shapes to allow for empirical models to include that variable. The blast testing needs to extend the material response into the inelastic regime so that the

resistance function can include the expected displacements and associated panel stiffness as plies fracture in the composite material.

Additional ECLT layups based on the test results of this research are another area of research that yield significant developments in terms of hybridizing the composite panel to create a cost-effective, highly ballistic resistant construction material for specialized uses to include, but not limited to, temporary military structures. Each new layup would require not just ballistic testing but also blast testing and other static tests of strength and stiffness for use in constructing a structure.

Additionally, beyond the realm of force protection, other areas related to the evaluation criteria defined for temporary military structures need to be explored for CLT. This includes energy efficiency, logistical feasibility and rapid constructability. Energy efficiency could examine cost-benefit of using the heavier CLT panels in temporary military structures given its thermal performance. The logistical feasibility assessment could include developing a prototype CLT structure similar to a B-hut based on weight and capacity limitations of commonly available equipment for transport and assembly. This would tie to the rapid constructability as well because the structure would need connections between the CLT panels.

In conclusion, this research was intended to explore CLT for use in temporary military structures. As a wood product, the composite is a complex material offering unique characteristics and an expanded use of wood as a structural component. A primary concern with temporary military structures is protection of the occupants from threats in overseas environments such as small arms weapons and explosives. Today, troops are

protected by standoff distances, concrete bunkers and barriers. However, wood has a unique energy absorption capacity and thick wooden panels of CLT may provide a viable material alternative for temporary military structure construction. This investigation into CLT performance has shown that the material has potential for improved performance over currently used materials and serves as a starting point for future work involving ballistic ratings and expected blast performance.

APPENDIX A

Table 1 0.50-cal FSP striking specimen E- 5P-1

Shot	Powder Mass (grains)	Chrono-Based		Chrono-Based		DOP (in)
		v_s (fps)	v_s (m/s)	v_r (fps)	v_r (m/s)	
E-5P-1 Shot 01	124.5	2739	834.81	1427	434.93	--
E-5P-1 Shot 02	127.3	2789	850.05	1571	478.82	--
E-5P-1 Shot 03	81	1989	606.22	588	179.21	--
E-5P-1 Shot 04	74	1781	542.82	639	194.76	--
E-5P-1 Shot 05	67	1554	473.64	214	65.22	--

Table 2 0.50-in. sphere striking specimen E-5P-2

Shot	Powder Mass (grains)	Chrono-Based		Chrono-Based		DOP (in)
		v_s (fps)	v_s (m/s)	v_r (fps)	v_r (m/s)	
E-5P-2 Shot 1	106.5	2527	770.19	1218	371.23	--
E-5P-2 Shot 2	94.5	2060	627.86	934	284.67	--
E-5P-2 Shot 3	70.5	1806	550.44	456	138.98	--
E-5P-2 Shot 4	57	1409	429.44	--	--	4.875
E-5P-2 Shot 5	60.2	1418	432.19	--	--	5.250

Table 3 0.50-in. sphere striking specimen E-5P-3

Shot	Powder Mass (grains)	Chrono-Based		Chrono-Based		DOP (in)
		v_s (fps)	v_s (m/s)	v_r (fps)	v_r (m/s)	
E-5P-3 Shot 1	57	1304	397.44	--	--	4.000
E-5P-3 Shot 2	57	1388	423.04	--	--	5.125
E-5P-3 Shot 3	57	1382	421.21	--	--	4.875
E-5P-3 Shot 4	57	1407	428.83	--	--	3.250
E-5P-3 Shot 5	57	1307	398.35	--	--	3.500

Table 4 0.50-in. sphere striking specimen E-5P-4

Shot	Powder Mass (grains)	Chrono-Based		Chrono-Based		DOP (in)
		v_s (fps)	v_s (m/s)	v_r (fps)	v_r (m/s)	
E-5P-4 Shot 1	106.5	2564	781.47	1169	356.29	--
E-5P-4 Shot 2	106.5	2427	739.71	1082	329.78	--
E-5P-4 Shot 3	106.5	2522	768.67	1225	373.36	--
E-5P-4 Shot 4	106.5	2373	723.26	1143	348.37	--
E-5P-4 Shot 5	106.5	2632	802.19	1324	403.54	--

Table 5 0.50-in. sphere striking specimen E-5P-5

Shot	Powder Mass (grains)	Chrono-Based		Chrono-Based		DOP (in)
		v_s (fps)	v_s (m/s)	v_r (fps)	v_r (m/s)	
E-5P-5 Shot 1	30.9	985	300.21	--	--	1.25
E-5P-5 Shot 2	67.2	1888	575.43	564	171.90	--
E-5P-5 Shot 3	37.6	1226	373.67	--	--	3.625
E-5P-5 Shot 4	33.7	1153	351.42	--	--	2.875
E-5P-5 Shot 5	27.1	986	300.52	--	--	1.75
E-5P-5 Shot 6	21.9	838	255.41	--	--	1.5
E-5P-5 Shot 7	16.7	507	154.53	--	--	0.375
E-5P-5 Shot 8*	18.3	624	190.19	--	--	0.75
E-5P-5 Shot 9	20.7	629	191.71	--	--	0.375
E-5P-5 Shot 10	21.5	664	202.38	--	--	0.75

Note: * Shot 8 was about 1-1/8-inch from Shot 7 due to error in not resetting the target.

Table 6 0.50-cal FSP striking specimen E- 5P-8

Shot	Powder Mass (grains)	Chrono-Based		Hi-speed camera		DOP (in)
		v_s (fps)	v_s (m/s)	v_r (fps)	v_r (m/s)	
E-5P-8 Shot 1	136.0	1883	573.91	573	174.64	--
E-5P-8 Shot 2	119.0	1719	523.93	471	143.55	--
E-5P-8 Shot 3	106.0	1641	500.15	266	81.07	--
E-5P-8 Shot 4	90.5	1536	468.15	--	--	5.125
E-5P-8 Shot 5	150.5	2015	614.14	628	191.41	--

Table 7 0.50-cal FSP striking specimen E- 5P-9

Shot	Powder Mass (grains)	Chrono-Based		Hi-speed camera		DOP (in)
		v_s (fps)	v_s (m/s)	v_r (fps)	v_r (m/s)	
E-5P-9 Shot 1	156	2280	694.91	1108	337.70	--
E-5P-9 Shot 2	151	1952	594.94	708	215.79	--
E-5P-9 Shot 3	152	2213	674.49	1029	313.62	--
E-5P-9 Shot 4	152	2198	669.92	1031	314.23	--
E-5P-9 Shot 5	126	2003	610.48	848	258.46	--

Table 8 0.50-cal FSP striking specimen E- 5P-11

Shot	Powder Mass (grains)	Chrono-Based		Chrono-Based		DOP (in)
		v_s (fps)	v_s (m/s)	v_r (fps)	v_r (m/s)	
E-5P-11 Shot 01	127.3	2753	839.07	1344	409.63	--
E-5P-11 Shot 02	81	1954	595.55	553	168.55	--
E-5P-11 Shot 03	67	1585	483.08	--	--	5.1875
E-5P-11 Shot 04	75	1846	562.63	364	110.94	--
E-5P-11 Shot 05	69.5	1659	505.64	--	--	4.6875

Table 9 0.50-in. sphere & 0.50-cal FSP striking specimen E- 5P-12

Shot	Powder Mass (grains)	Chrono-Based		Chrono-Based		DOP (in)	Projectile type
		v_s (fps)	v_s (m/s)	v_r (fps)	v_r (m/s)		
E-5P-12 Shot 1	150	2183	665.35	796	242.61	--	1/2" sphere
E-5P-12 Shot 2	167.5	2428	740.02	1297	395.31	--	1/2" sphere
E-5P-12 Shot 3	181.5	2552	777.81	1193	363.61	--	1/2" sphere
E-5P-12 Shot 4	205.5	2796	852.18	1252	381.59	--	1/2" sphere
E-5P-12 Shot 5	175	2408	733.92	1029	313.62	--	0.50-cal FSP
E-5P-12 Shot 6	109.0	1132	345.02	--	--	3.000	0.50-cal FSP
E-5P-12 Shot 7	132.5	1866	568.73	--	--	NR	0.50-cal FSP
E-5P-12 Shot 8	127.5	1803	549.53	498	151.78	0.750	0.50-cal FSP
E-5P-12 Shot 9	119.5	1766	538.25	153	46.63	0.375	0.50-cal FSP

Note: Shot 7 fully perforated the specimen at a residual velocity that was too low to be captured.

Table 10 0.50-cal FSP striking specimen E- 5P-15

Shot	Powder Mass (grains)	Chrono-Based		Hi-speed camera		DOP (in)
		v_s (fps)	v_s (m/s)	v_r (fps)	v_r (m/s)	
E-5P-15 Shot 1	146.0	1937	590.37	274	83.51	--
E-5P-15 Shot 2	149.5	1984	604.69	--	--	6.125
E-5P-15 Shot 3	157.0	2063	628.77	553	168.55	--
E-5P-15 Shot 4	177.0	2222	677.23	576	175.56	--
E-5P-15 Shot 5	185.0	2311	704.36	857	261.20	--

Table 11 0.50-in. sphere striking specimen E-5P-13

Shot	Powder Mass (grains)	Chrono-Based		Chrono-Based		DOP (in)
		v_s (fps)	v_s (m/s)	v_r (fps)	v_r (m/s)	
E-5P-13 Shot 1	89	2158	657.73	--	--	4.750
E-5P-13 Shot 2	78.2	2053	625.72	--	--	4.500
E-5P-13 Shot 3	75	1999	609.27	--	--	4.625
E-5P-13 Shot 4	63	1709	520.88	--	--	3.500
E-5P-13 Shot 5	55.5	1573	479.43	--	--	3.000
E-5P-13 Shot 6	44.1	1381	420.91	--	--	1.750
E-5P-13 Shot 7	32	1044	318.20	--	--	1.625
E-5P-13 Shot 8	24.5	830	252.97	--	--	0.375
E-5P-13 Shot 9	18	656	199.94	--	--	0.250

Table 12 0.50-in. sphere striking specimen E-9P-2

Shot	Powder Mass (grains)	Chrono-Based		Chrono-Based		DOP (in)
		v_s (fps)	v_s (m/s)	v_r (fps)	v_r (m/s)	
E-9P-2 Shot 1	51.5	1445	440.41	--	--	4.375
E-9P-2 Shot 2	53.6	1479	450.78	--	--	4.500
E-9P-2 Shot 3	64.3	1765	537.95	--	--	6.500
E-9P-2 Shot 4	66.5	1821	555.01	--	--	6.750
E-9P-2 Shot 5	83.5	2188	666.87	--	--	8.625
E-9P-2 Shot 6	78	2071	631.21	--	--	7.500
E-9P-2 Shot 7	60	1631	497.10	--	--	5.375
E-9P-2 Shot 8	61.8	1689	514.78	--	--	6.250
E-9P-2 Shot 9	55	1555	473.94	--	--	5.500

Table 13 0.50-in. sphere striking specimen E-9P-4

Shot	Powder Mass (grains)	Chrono-Based		Chrono-Based		DOP (in)
		v_s (fps)	v_s (m/s)	v_r (fps)	v_r (m/s)	
E-9P-4 Shot 1	92	2388	727.83	--	--	8.500
E-9P-4 Shot 2	88.5	2291	698.26	--	--	8.000
E-9P-4 Shot 3	99	2483	756.78	--	--	8.875
E-9P-4 Shot 4	105.5	2533	772.02	--	--	9.125
E-9P-4 Shot 5	118	2900	883.88	--	--	10.25
E-9P-4 Shot 6	111.5	2744	836.33	--	--	9.250
E-9P-4 Shot 7	106.8	2380	725.39	--	--	8.500
E-9P-4 Shot 8	89.5	2056	626.64	--	--	7.000
E-9P-4 Shot 9	95.6	2101	640.35	--	--	7.375

Table 14 0.50-in. sphere striking specimen E-10P-1

Shot	Powder Mass (grains)	Chrono-Based		Chrono-Based		DOP (in)
		v_s (fps)	v_s (m/s)	v_r (fps)	v_r (m/s)	
E-10P-1 Shot 1	120	2772	844.86	--	--	12.5
E-10P-1 Shot 2	108	2602	793.05	--	--	11
E-10P-1 Shot 3	99.5	2329	709.84	--	--	9.25
E-10P-1 Shot 4	105.3	2438	743.07	--	--	9.625
E-10P-1 Shot 5	106.5	2275	693.39	--	--	7.75

Table 15 0.50-in. sphere striking specimen E-10P-5

Shot	Powder Mass (grains)	Chrono-Based		Chrono-Based		DOP (in)
		v_s (fps)	v_s (m/s)	v_r (fps)	v_r (m/s)	
E-10P-5 Shot 1	106.9	2546	775.98	--	--	10.375
E-10P-5 Shot 2	86.2	1982	604.08	--	--	7.25
E-10P-5 Shot 3	111.5	2603	793.36	--	--	11.5
E-10P-5 Shot 4	114	2660	810.73	--	--	11
E-10P-5 Shot 5	98.6	2331	710.45	--	--	7.625

Table 16 0.50-in. sphere striking specimen E-10P-6

Shot	Powder Mass (grains)	Chrono-Based		Chrono-Based		DOP (in)
		v_s (fps)	v_s (m/s)	v_r (fps)	v_r (m/s)	
E-10P-6 Shot 1	120	2938	895.46	--	--	9.625
E-10P-6 Shot 2	136	3143	957.94	--	--	10.625
E-10P-6 Shot 3	152	3415	1040.84	--	--	11.750
E-10P-6 Shot 4	169	3683	1122.52	--	--	12.250
E-10P-6 Shot 5	106.5	2625	800.06	--	--	7.625
E-10P-6 Shot 6	99	2388	727.83	--	--	6.500
E-10P-6 Shot 7	92	2372	722.95	--	--	6.500
E-10P-6 Shot 8	106.5	2566	782.08	--	--	8.000
E-10P-6 Shot 9	121.5	2930	893.02	--	--	9.250

Table 17 Various 3-P specimens

Shot	Powder Mass (grains)	Chrono-Based		Chrono-Based		DOP (in)	Projectile type
		v_s (fps)	v_s (m/s)	v_r (fps)	v_r (m/s)		
E-3P-11	109	2469	752.51	1569	478.21	--	0.50-cal FSP
E-3P-12 shot 1	100.0	2526	769.89	1587	483.69	--	1/2" sphere
E-3P-12 shot 2	100.0	2392	729.05	1452	442.55	--	1/2" sphere
E-3P-12 shot 3	100.0	2400	731.48	1352	412.07	--	1/2" sphere
E-3P-12 shot 4	104.5	2453	747.64	1504	458.40	--	1/2" sphere
E-3P-12 shot 5	106.5	2597	791.53	1651	503.20	--	1/2" sphere
E-3P-17 Shot 1	103.0	2429	740.32	1186	361.48	--	1/2" sphere
E-3P-17 Shot 2	103.5	2416	736.36	1308	398.66	--	1/2" sphere
E-3P-17 Shot 3	104.0	2544	775.37	1487	453.22	--	1/2" sphere
E-3P-17 Shot 4	103.0	2550	777.20	1327	404.45	--	1/2" sphere
E-3P-16	103.0	2538	773.54	1363	415.42	--	1/2" sphere

Table 18 Fog room weathered specimens

Shot	Powder Mass (grains)	Chrono-Based		Chrono-Based		DOP (in)
		v_s (fps)	v_s (m/s)	v_r (fps)	v_r (m/s)	
E-5P-18 Shot 1	106.5	2247	685.06	--	--	5.1875
E-5P-18 Shot 2	118.5	2697	822.26	1209	368.60	--
E-5P-18 Shot 3	113.5	2615	797.26	1026	312.80	--
E-5P-18 Shot 4	110	2486	757.93	867	264.33	--
E-5P-18 Shot 5	110	2490	759.15	864	263.41	--
E-5P-7 Shot 1	110	2627	800.91	1271	387.50	--
E-5P-7 Shot 2	105	2440	743.90	1309	399.09	--
E-5P-7 Shot 3	106.1	2607	794.82	1339	408.23	--
E-5P-7 Shot 4	102	2455	748.48	1149	350.30	--
E-5P-7 Shot 5	103	2389	728.35	1243	378.96	--

Table 19 Water submerged weathered specimens

Shot	Powder Mass (grains)	Chrono-Based		Chrono-Based		DOP (in)
		v_s (fps)	v_s (m/s)	v_r (fps)	v_r (m/s)	
E-5P-17 - Shot 1	171	2421	7940.88	816	2676.48	--
E-5P-17 - Shot 2	176	2516	8252.48	1061	3480.08	--
E-5P-17 - Shot 3	176	2426	7957.28	938	3076.64	--
E-5P-17 - Shot 4	176	2400	7872.00	1002	3286.56	--
E-5P-17 - Shot 5	176	1919	6294.32	284	931.52	--
E-5P-17 - Shot 6	182	2592	8501.76	N/A	N/A	--
E-5P-17 - Shot 7	179	2478	8127.84	N/A	N/A	--
E-5P-17 - Shot 8	180	2519	8262.32	945	3099.60	--
E-5P-6 - Shot 1	208	2504	8213.12	1144	3752.32	--
E-5P-6 - Shot 2	205	2874	9426.72	1653	5421.84	--
E-5P-6 - Shot 3	178	2501	8203.28	743	2437.04	--
E-5P-6 - Shot 4	178	2545	8347.60	1146	3758.88	--
E-5P-6 - Shot 5	178	2243	7357.04	1015	3329.20	--
E-5P-6 - Shot 6	178	2527	8288.56	1461	4792.08	--

Note: N/A represents data that could not be collected due to equipment malfunction or user error

Table 20 0.50-in. sphere striking specimen E-Base

Shot	Powder Mass (grains)	Chrono-Based		Chrono-Based		DOP (in)
		v_s (fps)	v_s (m/s)	v_r (fps)	v_r (m/s)	
E-Base Shot 1	105.5	2560	780.25	236	478.21	--
E-Base Shot 2	105.0	2628	800.98	1017	309.97	--
E-Base Shot 3	104.5	2512	765.62	1131	344.71	--
E-Base Shot 4	104.5	2723	829.93	1158	352.94	--
E-Base Shot 5	104.5	2595	790.92	1156	352.33	--
E-Base Shot 6	104.0	2692	820.48	1225	373.36	--
E-Base Shot 7	104.0	2745	836.64	993	302.65	--
E-Base Shot 8	100.0	2668	813.17	691	210.61	--
E-Base Shot 9	96.0	2498	761.35	319	97.23	--
E-Base Shot 10	96.0	2469	752.51	598	182.26	--
E-Base Shot 11	96.0	2408	733.92	710	216.40	--
E-Base Shot 12	97.0	2409	734.23	709	216.09	--
E-Base Shot 13	100.0	2579	786.04	832	253.58	--
E-Base Shot 14	99.0	2441	743.98	746	227.37	--
E-Base Shot 15	100.0	2532	771.72	726	221.27	--

Table 21 0.50-in. sphere striking E-glass, woven roving (4-ply consolidated) ECLT specimens

Shot	Powder Mass (grains)	Chrono-Based		Chrono-Based		DOP (in)
		v_s (fps)	v_s (m/s)	v_r (fps)	v_r (m/s)	
E-FF4-1 Shot 1	99.5	2498	761.35	--	--	6.1875
E-FF4-1 Shot 2	99.5	2547	776.29	--	--	6.3750
E-FF4-1 Shot 3	99.5	2390	728.44	--	--	5.7500
E-FF4-1 Shot 4	99.5	2449	746.42	--	--	5.4375
E-FF4-1 Shot 5	100.5	2432	741.24	--	--	6.0000
E-FF4-2 Shot 1	103.0	2463	750.69	--	--	6.4375
E-FF4-2 Shot 2	103.0	2462	750.38	301	91.74	--
E-FF4-2 Shot 3	103.0	2484	757.09	--	--	6.2500
E-FF4-2 Shot 4	103.0	2492	759.52	327	99.66	--
E-FF4-2 Shot 5	103.0	2468	752.21	--	--	6.6250

Table 22 0.50-in. sphere striking E-glass, woven roving (4-ply separated) ECLT specimens

Shot	Powder Mass (grains)	Chrono-Based		Chrono-Based		DOP (in)
		v_s (fps)	v_s (m/s)	v_r (fps)	v_r (m/s)	
E-FF1-1 Shot 1	103.0	2484	757.09	--	--	5.7500
E-FF1-1 Shot 2	103.5	2632	802.19	176	53.64	--
E-FF1-1 Shot 3	103.0	2402	732.09	--	--	5.3438
E-FF1-1 Shot 4	103.0	2472	753.43	--	--	5.8125
E-FF1-1 Shot 5	103.0	2527	770.19	--	--	6.1250
E-FF1-2 Shot 1	103.0	2491	759.22	--	--	6.4375
E-FF1-2 Shot 2	103.0	2626	800.37	301	91.74	--
E-FF1-2 Shot 3	103.0	2297	700.09	--	--	6.2500
E-FF1-2 Shot 4	103.0	2382	726.00	327	99.66	--
E-FF1-2 Shot 5	103.0	2356	718.07	--	--	6.6250

Table 23 0.50-in. sphere striking perforated metal, P900, ECLT specimens

Shot	Powder Mass (grains)	Chrono-Based		Chrono-Based		DOP (in)
		v_s (fps)	v_s (m/s)	v_r (fps)	v_r (m/s)	
E-PM-1 Shot 1	105.0	2642	805.24	--	--	3.72
E-PM-1 Shot 2	103.5	2636	803.41	--	--	3.75
E-PM-1 Shot 3	100.0	2288	697.35	--	--	2.75
E-PM-1 Shot 4	103.0	2565	781.77	--	--	3.59
E-PM-1 Shot 5	103.0	2501	762.27	--	--	3.59
E-PM-1 Shot 6	103.0	2514	766.23	--	--	3.53
E-PM-1 Shot 7	103.0	2547	776.29	--	--	3

Table 24 0.50-in. sphere striking expanded metal, ECLT specimens

Shot	Powder Mass (grains)	Chrono-Based		Chrono-Based		DOP (in)
		v_s (fps)	v_s (m/s)	v_r (fps)	v_r (m/s)	
E-PM-2 Shot 1	105.0	2524	769.28	--	--	3.656
E-PM-2 Shot 2	105.0	2555	778.73	--	--	3.750
E-PM-2 Shot 3	105.0	2520	768.06	--	--	4.531
E-PM-2 Shot 4	105.0	2635	803.11	--	--	2.750
E-PM-2 Shot 5	104.0	2569	782.99	--	--	2.750
E-PM-2 Shot 6	103.5	2503	762.88	--	--	2.750
E-PM-2 Shot 7	103.5	2429	740.32	--	--	4.031
E-PM-2 Shot 8	104.0	2610	795.49	--	--	4.625

Table 25 0.50-in. sphere striking mild steel plate, ECLT specimens

Shot	Powder Mass (grains)	Chrono-Based		Chrono-Based		DOP (in)
		v_s (fps)	v_s (m/s)	v_r (fps)	v_r (m/s)	
E-MS-1 Shot 1	104.0	2556	779.03	--	--	2.6875
E-MS-1 Shot 2	104.0	2649	807.38	--	--	2.7500
E-MS-1 Shot 3	103.5	2470	752.82	--	--	2.6250
E-MS-1 Shot 4	103.7	2515	766.53	--	--	2.7500
E-MS-1 Shot 5	103.7	2548	776.59	--	--	2.6875
E-MS-2 Shot 1	103.7	2554	778.42	--	--	2.6875
E-MS-2 Shot 2	103.7	N/R		--	--	2.8125
E-MS-2 Shot 3	103.7	2637	803.72	--	--	2.9375
E-MS-2 Shot 4	103.7	2675	815.30	--	--	2.9375
E-MS-2 Shot 5	103.0	2661	811.03	--	--	3.0000

Note: N/R represents data that could not be collected due to equipment malfunction or user error

Table 26 0.50-in. sphere striking high-hard steel plate, ECLT specimens

Shot	Powder Mass (grains)	Chrono-Based		Chrono-Based		DOP (in)
		v_s (fps)	v_s (m/s)	v_r (fps)	v_r (m/s)	
E-HHS-1 Shot 1	103.7	2533	772.02	--	--	2.3750
E-HHS-1 Shot 2	103.7	2693	820.79	--	--	2.5000
E-HHS-1 Shot 3	103.7	2598	791.83	--	--	2.5625
E-HHS-1 Shot 4	103.7	2362	719.90	--	--	2.6250
E-HHS-1 Shot 5	103.7	2572	783.91	--	--	2.6250
E-HHS-2 Shot 1	103.0	2602	793.05	--	--	2.6250
E-HHS-2 Shot 2	101.0	2569	782.99	--	--	2.5000
E-HHS-2 Shot 3	100.0	2389	728.13	--	--	2.4375
E-HHS-2 Shot 4	101.5	2541	774.46	--	--	2.5625
E-HHS-2 Shot 5	101.5	2397	730.57	--	--	2.5000

Table 27 0.50-in. sphere striking ultra-high molecular weight polyethylene (UHMWPE), ECLT specimens

Shot	Powder Mass (grains)	Chrono-Based		Chrono-Based		DOP (in)
		v_s (fps)	v_s (m/s)	v_r (fps)	v_r (m/s)	
E-D1 Shot 1	102.0	2624	799.76	--	--	2.2500
E-D1 Shot 2	102.0	2402	732.09	--	--	2.3750
E-D1 Shot 3	103.0	2563	781.16	--	--	2.4375
E-D1 Shot 4	103.0	2512	765.62	--	--	2.4375
E-D1 Shot 5	103.0	2416	736.36	--	--	2.2500
E-D1 Shot 6	103.0	3610	1100.27	--	--	3.6875
E-D1 Shot 7	103.0	4169	1270.65	560	170.68	--
E-D1 Shot 8	103.0	3907	1190.80	--	--	5.3125

Table 28 0.50-in. sphere striking aramid epoxy plate, ECLT specimens

Shot	Powder Mass (grains)	Chrono-Based		Chrono-Based		DOP (in)
		v_s (fps)	v_s (m/s)	v_r (fps)	v_r (m/s)	
E-K1 Shot 1	102.0	2443	744.59	--	--	4.0000
E-K1 Shot 2	102.0	2413	735.45	--	--	3.4375
E-K1 Shot 3	103.0	2481	756.17	--	--	4.3125
E-K1 Shot 4	103.0	2606	794.27	--	--	5.4375
E-K1 Shot 5	103.0	2502	762.57	--	--	3.2500
E-K1 Shot 6	103.0	2600	792.44	--	--	4.6875
E-K1 Shot 7	103.0	2621	798.84	--	--	5.3750
E-K2 Shot 1	103.0	2407	733.62	--	--	4.2500
E-K2 Shot 2	103.0	2347	715.33	--	--	4.0313
E-K2 Shot 3	103.0	2510	765.01	--	--	4.1250
E-K2 Shot 4	103.0	2435	742.15	--	--	4.6250
E-K2 Shot 5	103.0	2625	800.06	--	--	5.8125
E-K2 Shot 6	103.0	2601	792.75	--	--	5.6250
E-K2 Shot 7	103.0	2483	756.78	--	--	3.8750
E-K2 Shot 8	103.0	2619	798.23	--	--	5.5000
E-K3 Shot 1	124.0	3041	926.85	343	104.54	--
E-K3 Shot 2	118.0	2992	911.92	429	130.75	--
E-K3 Shot 3	114.5	2851	868.94	--	--	6.4375
E-K3 Shot 4	116.5	2866	873.51	--	--	6.1250
E-K3 Shot 5	119.0	2952	899.73	426	129.84	--
E-K3 Shot 6	118.0	2878	877.17	--	--	6.7500

Woven Roving

Part # - 223

18 oz/sq yd, 50" Wide, .030" Thick
Woven Roving is used in laminating large fiberglass parts such as boats and tanks where an inexpensive, high impact, high strength reinforcement is required. Woven roving should be used with mat whenever bonding to plywood or making repairs.

(Typical full roll length is 100 yards)

Specific Product Properties	
Finish	Compatible with Polyester, Vinyl Ester and Epoxy
Weave Pattern	Plain
Count: Ends x Picks (in)	4.5-5.5 x 3-4
Tensile Strength	27-33 ksi
Compressive Strength	27-30 ksi
Weight	16.0-18.5 oz/yd^2
Thickness	.030 in
Roll Length	100 yd

DESCRIPTION
Woven fabrics are strong reinforcements because the fibers are bundled into yarns oriented in just two directions. The warp and fill yarns run at 0 and 90 degrees respectively. Thus, fabrics are anisotropic, or strong in only two directions.

Fabrics need to be oriented so the fiber yarns run parallel to the expected loads. If extra strength is needed in a different direction, another ply must be added at an angle to the first. The most common angles are +/- 45 degrees.

Resin Compatibility:
223 is compatible with Polyester, Vinyl Ester, and Epoxy

Fibre Glast Developments Corporation
385 Carr Drive
Brookville, Ohio 45309
Phone – 800.214.8572
Fax – 937.833.6555
www.fibreglast.com

PDCT-PDS-00088-E-01/18-BE

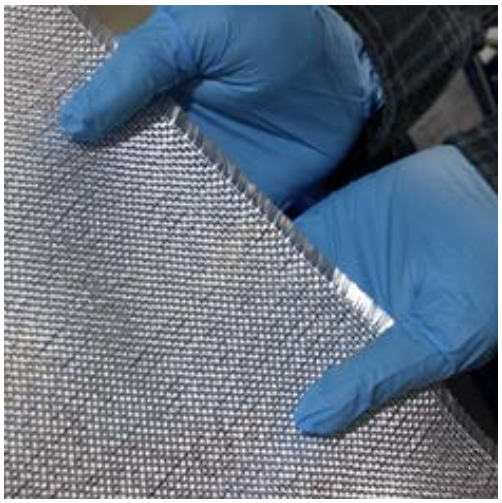

10 oz Fabric

Part # - 245, 247, 271

10 oz/sq yd 38", 50" and 60" Wide .014" Thick, 16 x 14 Plain Weave Frequently used in mold building, sandwich core panels, and high strength layups. 8 plies of 10 oz fabric will produce a strong 1/8" laminate weighing 1 lb per sq ft. This Style 7500 fabric meets AMS-C-9084 Type XII-A (Class 1 & 2).

Specific Product Properties	
Style	7500
Finish	Compatible with Polyester, Vinyl Ester and Epoxy
Weave Pattern	Plain
Yarn Description	Warp: ECG 37 1/2
	Fill: ECG 37 1/2
Count: Ends x Picks (in)	13-17 x 11-15
Breaking Strength	Warp: >100 lb/in Fill: >85 lb/in
Weight	9.0-10.2 oz/yd^2
Thickness	.011-.017 in

DESCRIPTION

Woven fabrics are strong reinforcements because the fibers are bundled into yarns oriented in just two directions. The warp and fill yarns run at 0 and 90 degrees respectively. Thus, fabrics are anisotropic, or strong in only two directions. Fabrics need to be oriented so the fiber yarns run parallel to the expected loads. If extra strength is needed in a different direction, another ply must be added at an angle to the first. The most common angles are +/- 45 degrees

This material can be certified to meet:

-AMS-C-9084 Type XII-A (Class 1 & 2)

*exception: G37 ½ replaces K75 2/2

Fibre Glast Developments Corporation
385 Carr Drive
Brookville, Ohio 45309
Phone – 800.214.8572
Fax – 937.833.6555
www.fibreglast.com

PDCT-PDS-00345-C-01/18-BE

REFERENCES

[1] "Ceiling/ Wood Construction Ceiling Plan, Wood Frame Building," ed. Washington, DC: Contingency Standard Designs U.S. Army Corps of Engineers.

[2] "The Resistance of Various Metallic Materials to Perforation by Steel Fragments; Empirical Relationships for Fragment Residual Velocity and Residual Weight," Ballistic Analysis Laboratory, Baltimore, MD1961.

[3] U.S. Department of Justic, National Institute of Justice, Ballistic Resistant Protective Materials, NIJ 0108.01, 1985.

[4] American Institute of Timber Construction AITC 405-2005, Standard for Adhesives for Use in Structural Glued Laminated Timber, 2005.

[5] American Society of Testing and Materials, ASTM D143 - 94 Standard Test Methods for Small Clear Specimens of Timber, 2007.

[6] "Performance Specification: Perforated Homogeneous Steel Armor," D. o. t. Army, Ed., ed. Aberdeen Proving Ground, MD: Army Research Laboratory, Weapons and Materials Research Directorate, Materials Applications Branch, Specifications and Standards Office, 2007.

[7] U.S. Army Corps of Engineers, Unifed Facilities Criteria (UFC) 4-023-07 Design to Resist Direct Fire Weapons Effects, 2008.

[8] U.S. Army Corps of Engineers, Unified Facilities Criteria (UFC) 4-020-01 DoD Security Engineering Facilities Planning Manual, UFC 4-020-01, 2008.

[9] U.S. Department of Housing and Urban Development, HUD Noise Guidebook, 2009.

[10] American Society of Testing and Materials, ASTM D3499-11 Standard Test Method for Toughness of Wood-Based Structural Panels, 2011.

[11] American Society for Testing and Materials, ASTM D 1037-12 Standard Test Methods for Evaluating Properties of Wood-Base Fiber and Particle Panel Materials, 2012.

[12] American National Standards Institute; APA - The Engineered Wood Association, Standard for Performance-Rated Cross-Laminated Timber ANSI/APA PRG 320-2012, 2012.

[13] Underwriters Laboratory, UL 752 Standard for Safety Bullet-Resisting Equipment, 11th Ed., 2013.

[14] U.S. Army Corps of Engineers, Unified Facilities Criteria (UFC) 1-201-02 Non-Permanent DoD Facilities in Support of Military Operations, 2013.

[15] U.S. Army Corps of Engineers, Unified Facilities Criteria (UFC) 4-010-01 DoD Minimum Antiterrorism Standards for Buildings with Change 1, 2013.

[16] International Code Council, 2015 International Building Code, 2014.

[17] U.S. Army Corps of Engineers, Unified Facilities Criteria (UFC) 3-340-02 Structures to Resist the Effects of Accidental Explosions, 2014.

[18] American Society for Testing and Materials, ASTM D905 - 08 Standard Test Method for Determining Strength of Gap-Filling Adhesive Bonds in Shear by Compression Loading, 2015.

[19] American Wood Council, National Design Specification for Wood Construction, 2015.

[20] Ahrens, T.J., "Equation of State," in *High Pressure Shock Compression of Solids*, J. R. Asay and M. Shahinpoor, Eds., ed New York: Springer-Verlag, 1993, pp. 75-1114.

[21] Aicher, S. and G. Dill-Langer, "Basic Considerations to Rolling Shear Modulus in Wooden Boards," *Annual Journal on Research and Testing of Materials*, vol. 11, pp. 157-165, 2000.

[22] Aicher, S., M. Hirsch, and Z. Christian, "Hybrid cross-laminated timber plates with beech wood cross-layers," *Construction and Building Materials*, vol. 124, pp. 1007-1018, 2016.

[23] Allen, W.A. and J.W. Rogers, "Penetration of a Rod into a Semi-Infinite Target," *Journal of the Franklin Institute*, vol. 272, pp. 275-284, 1961.

[24] Andrews, C. (2012, September 17, 2012) Wood in warfare. *Engineering & Technology*. Available: https://eandt.theiet.org/content/articles/2012/09/wood-in-warfare/

[25] Asay, J.R. and M. Shahinpoor, *High-Pressure Shock Compression of Solids*. New York: Springer-Verlag, 1993.

[26] Awad, H., M. Gül, H. Zaman, H. Yu, and M. Al-Hussein, "Evaluation of the thermal and structural performance of potential energy efficient wall systems for mid-rise wood-frame buildings," *Energy and Buildings*, vol. 82, pp. 416-427, 2014.

[27] Backman, M. and W. Goldsmith, "The Mechanics of Penetration of Projectiles into Targets," *International Journal of Engineering Science*, vol. 16, pp. 1-99, 1978.

[28] Bartlett, F.M. and J.G. MacGregor, "Statistical Analysis of the Compressive Strength of Concrete in Structures," *ACI Materials Journal*, 1996.

[29] Biggs, J.M. and J.M. Biggs, *Introduction to structural dynamics*: McGraw-Hill College, 1964.

[30] Birkhoff, G., D.P. MacDougall, E.M. Pugh, and S.G. Taylor, "Explosives with Lined Cavities," *Journal of Applied Physics*, vol. 19, pp. 563-582, 1948.

[31] Bodig, J. and B.A. Jayne, *Mechanics of Wood and Wood Composites*. New York, NY: Van Nostrand Reinhold Company, 1982.

[32] Brandner, R., "Production and Technology of Cross Laminated Timber (CLT): A state-of-the-art Report," presented at the Focus Solid Timber Solutions - European Conference on Cross Laminated Timber (CLT), Graz, Austria, 2013.

[33] Brandner, R., G. Flatscher, A. Ringhofer, G. Schickhofer, and A. Thiel, "Cross laminated timber (CLT): overview and development," *European Journal of Wood and Wood Products*, 2016.

[34] Breyer, D.E., K.J. Fridley, K.E. Cobeen, and D.G. Pollock, *Design of wood structures - ASD/LRFD*, 6th ed. New York, NY: McGraw-Hill, 2007.

[35] Export Grading for Southern Pine Lumber, 1981.

[36] Ceccotti, A., C. Sandhaas, M. Okabe, M. Yasumura, C. Minowa, and N. Kawai, "SOFIE project - 3D shaking table test on a seven-storey full-scale cross-laminated timber building," *Earthquake Engineering & Structural Dynamics,* vol. 42, pp. 2003-2021, 2013.

[37] Chachere, J.M. and J.R. Haymaker, "Framework for Measuring the Rationale Clarity of AEC Design Decisions," *Journal of Architectural Engineering,* vol. 17, pp. 86-96, 2011.

[38] Christman, D.R. and J.W. Gehring, "Analysis of High-Velocity Projectile Penetration Mechanics," *Journal of Applied Physics,* vol. 37, pp. 1579-1587, 1966.

[39] Dalheim, R., "International Beams says its upcoming CLT plant will be the biggest in U.S.," in *Woodworking Network*, ed. Dothan, Alabama, 2017.

[40] Davids, W.G., N. Willey, R. Lopez-Anido, S. Shaler, D. Gardner, R. Edgar, *et al.*, "Structural performance of hybrid SPFs-LSL cross-laminated timber panels," *Construction and Building Materials,* vol. 149, pp. 156-163, 2017.

[41] Doyle, J. and J.C.F. Walker, "Indentation Hardness of Wood," *Wood and Fiber Science,* vol. 17, pp. 369-376, 1985.

[42] Dusenberry, D.O., *Handbook for blast resistant design of buildings*: John Wiley & Sons, 2010.

[43] Eberhardt, T.L. and L.J. Samuelson, "Collection of wood quality data by X-ray densitometry: a case study with three southern pines," *Wood Science and Technology,* vol. 49, pp. 739-753, 2015.

[44] ASCE, Blast Protection of Buildings (ASCE/SEI 59-11), 2011.

[45] Espinoza, O., V.R. Trujillo, M.F.L. Mallo, and U. Buehlmann, "Cross-Laminated Timber Status and Research Needs in Europe," *BioResources,* vol. 11, pp. 281-295, 2016.

[46] Falk, A., "Cross-Laminated timber: driving forces and innovation," in *2nd International Conference on Structures and Architecture*, Guimaraes, Portugal, 2013, pp. 511-518.

[47] Fellmoser and H.J. Blaß, "Influence of Rolling Shear Modulus on Strength and Stiffness of Structural Bonded Timber Members," Edinburgh, UKAugust 2004 2004.

[48] Fernández, M., A. Martínez, A. Alonso, and L. Lizondo, "A mathematical model for the sustainability of the use of cross-laminated timber in the construction industry: the case of Spain," *Clean Technologies and Environmental Policy,* vol. 16, pp. 1625-1636, 2014.

[49] Forbes, J.W., *Shock Wave Compression of Condensed Matter: A Primer*. New York: Springer, 2012.

[50] Forrestal, M.J., K. Okajima, and V.K. Luk, "Penetration of 6061-T651 Aluminum Targets with Rigid Long Rods," *Journal of Applied Mechanics,* vol. 55, pp. 755-760, 1988.

[51] Frangi, A., M. Fontana, E. Hugi, and R. Jübstl, "Experimental analysis of cross-laminated timber panels in fire," *Fire Safety Journal,* vol. 44, pp. 1078-1087, 2009.

[52] Garratt, G., *The Mechanical Properties of Wood*. New York, NY: Wiley & Sons, Inc., 1931.

[53] Gebo, K.M., "A Comparison of the Lifecycle Cost and Environmental Impact of Military Barracks Huts in Deployed Environments Constructed from Structural Insulated Panels (SIPs) versus Traditional Techniques," Master of Science, Department of Industrial and Systems Engineering, Rochester Institute of Technology, Rochester, NY, 2014.

[54] Gilbertson, C.G. and W.M. Bulleit, "Load Duration Effects in Wood at High Strain Rates," *Journal of Materials in Civil Engineering,* vol. 25, pp. 1647-1654, 2013.

[55] Gooch, W.A., M.S. Burkins, L.F. Mills, J.W. Ogilvy, and A.J. Ricchiazzi, "Cast Single Plate P900 Armor," United States Patent 5,007,326, 1991.

[56] Green, D., M. Begel, and W. Nelson, "Janka Hardness Using Nonstandard Specimens," FPL-RN-0303, 2006.

[57] Gupta, N.K. and V. Madha, "An Experimental Study of Normal and Oblique Impact of Hard-Core Projectile on Single and Layered Plates," *International Journal of Impact Engineering*, vol. 19, pp. 395-414, 1997.

[58] Hasburgh, L., K. Bourne, P. Peralta, P. Mitchell, S. Schiff, and W. Pang, "Effect of Adhesive and Ply Configuration on the Fire Performance of Southern Pine Cross-Laminated Timber," in *World Conference on Timber Engineering*, Vienna, Austria, 2016.

[59] Heil, M. and L. Tune, "UMD Researchers Create Super Wood Stronger Than Most Metals," ed, 2018.

[60] Hess, P.E., D. Bruchman, I. Assakkaf, and B.M. Ayyub, "Uncertainties in Material and Geometric Strength and Load Variable," *Naval Engineers Journal*, 2002.

[61] Hill, R., "Cavitation and the influence of headshape in attack of thick targets by non-deforming projectiles," *Journal of Mechanics of Physical Solids*, vol. 28, pp. 249-263., 1980.

[62] Hindman, D.P. and J.C. Bouldin, "Mechanical Properties of Southern Pine Cross-Laminated Timber," *Journal of Materials in Civil Engineering*, vol. 27, p. 04014251, 2015.

[63] Hough, R., J. Kell, and J. Koopman, "CLT Apartment Blocks for the Sydney Affordable Housing Market," in *World Conference on Timber Engineering*, Auckland, New Zealand, 2012.

[64] Howell, R.A., J.S. Montgomery, and D.C. Van Aken, "Advancements in Steel for Weight Reduction of P900 Armor Plate," in *Army Science Conference*, Orlando, FL, 2008.

[65] U.S.Navy Office of Information. *USS Constitution*. Available: http://www.navy.mil/ah_online/constitution/.

[66] Jacques, E., A. Lloyd, A. Braimah, M. Saatcioglu, G. Doudak, and O. Abdelalim, "Influence of high strain-rates on the dynamic flexural material properties of spruce–pine–fir wood studs," *Canadian Journal of Civil Engineering*, vol. 41, pp. 56-64, 2014.

[67] Jonas, G.H. and J.A. Zukas, "Mechanics of Penetration: Analysis and Experiment," *International Journal Engineering Science,* vol. 16, pp. 879-903, 1978.

[68] Karacabeyli, E. and B. Douglas. (2013). *CLT Handbook (Cross-Laminated Timber) U.S. Edition*.

[69] Kaufmann, C., D. Cronin, M. Worswick, G. Pageau, and A. Beth, "Influence of material properties on the ballistic performance of ceramics for personal body armour," *Shock and Vibration,* vol. 10, pp. 51-58, 2003.

[70] Kavanaugh, S.P., *HVAC Simplified*. Atlanta, GA: ASHRAE, 2006.

[71] Kipfer, A. (2017, July 14, 2017) Cross-laminated timber fire testing sees promising results. *Woodworking Network*. Available: http://www.woodworkingnetwork.com/architectural-products/cross-laminated-timber-fire-testing-sees-promising-results

[72] Kreiger, M., D. Chu, S. Shrestha, K.J. Hay, M.R. Kemme, A.C. Johannes, *et al.*, "The Stuctural Insulated Panel "SIP Hut"," 2015.

[73] Kwak, Y.H. and L. Ingall, "Exploring Monte Carlo Simulation Applications for Project Management," *Risk Management,* vol. 9, pp. 44-57, 2007.

[74] Lacroix, D.N. and G. Doudak, "Investigation of Dynamic Increase Factors in Light-Frame Wood Stud Walls Subjected to Out-of-Plane Blast Loading," *Journal of Structural Engineering,* vol. 141, p. 04014159, 2015.

[75] Lee, K. and J. Shin, "Equivalent single-degree-of-freedom analysis for blast-resistant design," *International Journal of Steel Structures,* vol. 16, pp. 1263-1271, 2016.

[76] Lee, S., "Determination of Priority Weights under Multiattribute Decision Making Situations: AHP versus Fuzzy AHP," *Journal of Construction Engineering and Management,* vol. 141, pp. 05014015-1, 2015.

[77] LeVan, S.L. and R.M. Rowell, *The Chemistry of Solid Wood* vol. 207. Washington, D.C.: American Chemical Society, 1984.

[78] Lui, J.Y. and L.H. Floeter, "Shear Strength in Principal Plane of Wood," *Journal of Engineering Mechanics,* vol. 110, pp. 930-936, 1984.

[79] Mahamid, M., T. Brindley, N. Triandafilou, and S. Domagala, "Behavior and Strength Characteristics of Cross-Laminated Timber Mats: Experimental and Numerical Study," presented at the Structures Congress, Denver, Colorado, 2017.

[80] Malick, D., "The Resistance of Various Woods to Perforation by Steel Fragments and Small Caliber Projectiles," Ballistic Analysis Laboratory, Institute for Cooperative Research, Johns Hopkins University, Baltimore, MD BAL Technical Report No. 62, 1966.

[81] Mallo, M.F.L. and O. Espinoza, "Outlook for Cross-Laminated Timber in the United States," *BioResources,* vol. 9, pp. 7427-7443, 2014.

[82] Marquardt, D.W., "An algorithm for least-squares estimation of nonlinear parameters," *Journal of the Society for Industrial and Applied Mathematics,* vol. 11, pp. 431-441, 1963.

[83] Mestek, P., H. Kreuzinger, and S. Winter, "Design of cross laminated timber (CLT)," in *10th World Conference on Timber Engineering*, 2008.

[84] Meyer, L., C. Brischke, and C.R. Welzbacher, "Dynamic and static hardness of wood: method development and comparative studies," *International Wood Products Journal,* vol. 2, pp. 5-11, 2013.

[85] Moon, F.C., "A Critical Survey of Wave Propagation and Impact in Composite Materials," National Aeronautics and Space Administration1973.

[86] Mosley, H. and A. Mayer, "Benchmarking national labour market performance: A radar chart approach," No. FS | 99-202, 1999.

[87] Pandya, K.S., J.R. Pothnis, G. Ravikumar, and N.K. Naik, "Ballistic impact behavior of hybrid composites," *Materials & Design*, vol. 44, pp. 128-135, 2013.

[88] Payne, B., "D.R. Johnson Passes Two Critical Tests for Safety of its Cross-Laminated Timber Panels - Flame Spread and Fire Resistance," ed. Riddle, Oregon, 2016.

[89] Poulin, M., C. Viau, D.N. Lacroix, and G. Doudak, "Experimental and Analytical Investigation of Cross-Laminated Timber Panels Subjected to Out-of-Plane Blast Loads," *Journal of Structural Engineering,* vol. 144, p. 04017197, 2018.

[90] Rao, C.L., V. Narayanamurthy, and K.R.Y. Simha, *Applied Impact Mechanics*. West Sussex, United Kingdom: John Wiley & Sons Ltd, 2016.

[91] Recht, R.F. and T.W. Ipson, "Ballistic Perforation Dynamics," *Journal of Applied Mechanics,* pp. 384-390, 1963.

[92] Reid, S.R. and C. Peng, "Dynamic Uniaxial Crushing of Wood," *International Journal of Impact Engineering,* vol. 19, pp. 531-570, 1997.

[93] Rosenberg, Z., S.J. Bless, and N.S. Brar, "On the Influence of the Loss of Shear Strength on the Ballistic Performance of Brittle Solids," *International Journal of Impact Engineering,* vol. 9, pp. 45-49, 1990.

[94] Rosenberg, Z. and E. Dekel, "The penetration of rigid long rods – revisited," *International Journal of Impact Engineering,* vol. 36, pp. 551-564, 2009.

[95] Rosenberg, Z. and E. Dekel. (2016). *Terminal Ballistics (Second ed.)*.

[96] Ross, R.J., "Wood handbook: Wood as an engineering material," F. S. U.S. Department of Agriculture, Forest Products Laboratory, Ed., Centennial Edition ed. Madison, WI: US, 2010.

[97] Rottman, G.L., *Japanese Pacific Island Defenses 1941-45*. Oxford, UK: Osprey Publishing, 2003.

[98] Saaty, R.W., "The Analytic Hierarchy Process - What it is and how it is used," *Mathematical Modelling,* vol. 9, pp. 161-176, 1987.

[99] Saavedra Flores, E.I., K. Saavedra, J. Hinojosa, Y. Chandra, and R. Das, "Multi-scale modelling of rolling shear failure in cross-laminated timber structures by homogenisation and cohesive zone models," *International Journal of Solids and Structures,* vol. 81, pp. 219-232, 2016.

[100] Scott, B., Mechanical/Materials Engineer,Multi-Threat Armor Branch, RDRL-WMP-D, US Army Research Laboratory, Personal Communication, January 25, 2018.

[101] Shiling, P., J.W. van de Lindt, and M. Popovski, "Approximate R-Factor for CLT Walls in Multistory Buildings," *Journal of Architectural Engineering*, vol. 19, pp. 245-255, 2013.

[102] Showalter, J., B. Douglas, and M. Kam-Biron, "Changes to the 2015 National Design Specification (NDS) for Wood Construction and the Inclusion of Cross-Laminated Timber," presented at the Structures Congress, Portland, OR, 2015.

[103] Sikora, K.S., D.O. McPolin, and A.M. Harte, "Shear Strength and Durability Testing of Adhesive Bonds in Cross-laminated Timber," *The Journal of Adhesion*, vol. 92, pp. 758-777, 2015.

[104] Stewart, L., *Course Notes CEE 8813: Multi-hazard Analysis and Design*. Atlanta, GA: Georgia Institute of Technology, 2015.

[105] Stewart, L.K., A. Freidenberg, T. Rodriguez-Nikl, M. Oesterle, J. Wolfson, B. Durant, *et al.*, "Methodology and validation for blast and shock testing of structures using high-speed hydraulic actuators," *Engineering Structures*, vol. 70, pp. 168-180, 2014.

[106] Stürzenbecher, R., K. Hofstetter, and J. Eberhardsteiner, "Structural design of Cross Laminated Timber (CLT) by advanced plate theories," *Composites Science and Technology*, vol. 70, pp. 1368-1379, 2010.

[107] Sukontasukkul, P., F. Lam, and S. Mindess, "Fracture of parallel strand lumber (PSL) under impact loading," *Materials and Structures*, vol. 33, pp. 445-449, 2000.

[108] Taroun, A., "Towards a better modelling and assessment of construction risk: Insights from a literature review," *International Journal of Project Management*, vol. 32, pp. 101-115, 2014.

[109] Tobin, W., Operations Director, Timber & Innovations Group, Lendlease, Personal Communication, October 12, 2016.

[110] Tudhope, R., Vice President of Product Development, SmartLam, Personal Communication, February 9, 2017.

[111] Vaidya, U.K., S. Pillay, M. Magrini, and P.R. Mantena, "Ballistic Impact Testing of Balsa, PVC Foam, Glass Reinforces Polyurethane Core Sandwich Structures," presented at the 17th International Conference on Composite Materials, Edinburgh, UK, 2009.

[112] van Dingenen, J.L.J., "High performance dyneema fibres in composites," *Materials & Design*, vol. 10, pp. 101-104, 1989/03/01/ 1989.

[113] Vural, M. and G. Ravichandran, "Dynamic response and energy dissipation characteristics of balsa wood: experiment and analysis," *International Journal of Solids and Structures*, vol. 40, pp. 2147-2170, 2003.

[114] Waller, J.C.C. (2011) From Manufacturer to Forward Operating Base. *Army Sustainment*. Available: http://www.almc.army.mil/alog/issues/JulAug11/spectrum_forward_operating%20base.html

[115] Walley, S.M. and J.E. Field, "Elastic Wave Propagation in Materials," in *Encyclopedia of Materials: Science and Technology*, ed: Elsevier Ltd, 2001, pp. 1-7.

[116] Wang, Z., H. Fu, M. Gong, J. Luo, W. Dong, T. Wang, *et al.*, "Planar shear and bending properties of hybrid CLT fabricated with lumber and LVL," *Construction and Building Materials*, vol. 151, pp. 172-177, 2017.

[117] Wang, Z., M. Gong, and Y.-H. Chui, "Mechanical properties of laminated strand lumber and hybrid cross-laminated timber," *Construction and Building Materials*, vol. 101, pp. 622-627, 2015.

[118] Weaver, M.K., C. O'Laughlin, and C.M. Newberry, "Blast Resistance of Cross-Laminated Timber Construction," presented at the International Symposium on the Interactions of the Effects of Munitions with Structures (17th ISIEMS), Bad Neuenahr, Germany, 2017.

[119] Weirer, W., "History and Development of CLT using the example of KLH," in *WoodWorks website*, KLH, Ed., ed. http://www.woodworks.org/wp-content/uploads/CLT-Weirer.pdf, 2012.

[120] Widehammar, S., "Stress-Strain Relationships for Spruce Wood: Influence of Strain Rate, Moisture Content and Loading Direction," *Experimental Mechanics*, vol. 44, pp. 44-48, 2004.

[121] Wilkins, M.L., "Mechanics of Penetration and Perforation," *International Journal Engineering Science*, vol. 16, pp. 793-807, 1978.

[122] Wonderly, C., J. Grenestedt, G. Fernlund, and E. Cěpus, "Comparison of mechanical properties of glass fiber/vinyl ester and carbon fiber/vinyl ester composites," *Composites Part B: Engineering*, vol. 36, pp. 417-426, 2005.

[123] Wouts, J., G. Haugou, M. Oudjene, D. Coutellier, and H. Morvan, "Strain rate effects on the compressive response of wood and energy absorption capabilities – Part A: Experimental investigations," *Composite Structures*, vol. 149, pp. 315-328, 2016.

[124] Zukas, J., *Introduction to Hydrocodes*: Elsevier Science, 2004.

[125] Zukas, J.A., "Impact Dynamics: Theory and Experiment," US Army Armament Research and Development Command, Ballistic Research Laboratory, Aberdeen Proving Ground, MD ARBRL-TR-02271, 1980.

[126] Zukas, J.A., *High velocity impact dynamics*. New York: Wiley, 1990.